



**UNSTEADY SPECIFIC WORK AND ISENTROPIC  
EFFICIENCY OF A RADIAL TURBINE DRIVEN BY  
PULSED DETONATIONS**

DISSERTATION

Kurt P. Rouser, Lieutenant Colonel, USAF

AFIT/DS/ENY/12-25

**DEPARTMENT OF THE AIR FORCE  
AIR UNIVERSITY**

**AIR FORCE INSTITUTE OF TECHNOLOGY**

**Wright-Patterson Air Force Base, Ohio**

APPROVED FOR PUBLIC RELEASE; DISTRIBUTION UNLIMITED

The views expressed in this dissertation are those of the author and do not reflect the official policy or position of the United States Air Force, Department of Defense, or the United States Government. This material is declared a work of the U.S. Government and is not subject to copyright protection in the United States.

AFIT/DS/ENY/12-25

**UNSTEADY SPECIFIC WORK AND ISENTROPIC EFFICIENCY OF A  
RADIAL TURBINE DRIVEN BY PULSED DETONATIONS**

DISSERTATION

Presented to the Faculty  
Department of Aeronautics and Astronautics  
Graduate School of Engineering and Management  
Air Force Institute of Technology  
Air University  
Air Education and Training Command  
in Partial Fulfillment of the Requirements for the  
Degree of Doctor of Philosophy in Aeronautical Engineering

Kurt P. Rouser, BS, MS

Lieutenant Colonel, USAF

June 2012

APPROVED FOR PUBLIC RELEASE; DISTRIBUTION UNLIMITED.



## **Abstract**

There has been longstanding government and industry interest in pressure-gain combustion for use in Brayton cycle based engines. Theoretically, pressure-gain combustion allows heat addition with reduced entropy increase. The pulsed detonation combustor (PDC) is a device that can provide such pressure-gain combustion and possibly replace typical steady deflagration combustors. The PDC is inherently unsteady, however, and comparisons with conventional steady deflagration combustors must be based upon time-integrated performance variables. In this study, the radial turbine of a Garrett automotive turbocharger was coupled directly to and driven, full admission, by a PDC in experiments fueled by hydrogen or ethylene. Data included pulsed cycle time histories of turbine inlet and exit temperature, pressure, velocity, mass flow, and enthalpy. The unsteady inlet flowfield showed momentary reverse flow, and thus unsteady accumulation and expulsion of mass and enthalpy within the device. The coupled turbine-driven compressor provided a time-resolved measure of turbine power. Peak power increased with PDC fueled fraction, and duty cycle increased with PDC frequency. Cycle-averaged unsteady specific work increased with fueled fraction and frequency. An unsteady turbine efficiency formulation is proposed and evaluated, accounting for heat transfer effects and including extensively weighted total pressure ratio and ensemble averaging over multiple cycles. Turbine efficiency increased with frequency but was lower than the manufacturer reported conventional steady turbine efficiency.

## **Acknowledgments**

I am sincerely grateful for guidance I received from my advisor, Dr. Paul King, and my research committee members: Drs. Marc Polanka, Glen Perram, Fred Schauer, and Rolf Sondergaard. Additionally, I am forever indebted to Drs. Larry Goss and Drew Caswell for instrumentation support.

Special thanks are due to the Detonation Engine Research Facility team for technical and fabrication support that made this research possible, especially Dr. John Hoke, Curtis Rice, Andrew Naples, Chris Stevens, Justin Goffena, and David Burris. I am particularly thankful for the technical leadership afforded to me by Drs. Robert Hancock and Joseph Zelina. Funding was provided by the Air Force Research Laboratory and the Air Force Office of Scientific Research.

Kurt P. Rouser

## Table of Contents

	Page
Abstract .....	iv
Acknowledgments.....	v
Table of Contents .....	vi
List of Figures .....	x
List of Tables .....	xx
List of Symbols .....	xxi
I. Introduction.....	1
I.A. Objectives .....	2
I.B. Outline.....	3
II. Previous Pulsed Detonation Driven Turbine Research.....	5
III. Unsteady Thermodynamics and Unsteady Turbine Model .....	10
III.A. Unsteady Flow in Conventional Brayton Cycle Turbines .....	10
III.B. Unsteady Flow in Pulsed Detonation Driven Turbines .....	12
III.C. Unsteady Turbine Model with Heat Transfer .....	18
IV. Facility and Procedures .....	25
IV.A. Detonation Engine Research Facility.....	26
IV.A.1. Air Supply.....	28
IV.A.2. Fuel Supply .....	29
IV.B. Pulsed Detonation Combustor.....	29
IV.B.1. Operating Procedure.....	31
IV.B.2. Operating Conditions .....	31
IV.B.3. Instrumentation .....	33
IV.C. Radial Turbine.....	34
IV.D. Turbine Inlet and Exit Flowfield Instrumentation .....	37
IV.D.1. Laser Absorption Spectroscopy .....	38
IV.D.2. Static Pressure Transducers .....	39
IV.D.3. Two-Band Optical Pyrometry .....	40
IV.D.4. Particle Streak Velocimetry .....	41
IV.E. Power Instrumentation.....	42
IV.F. Rotor Speed Instrumentation .....	43

V.	Data Reduction and Uncertainty Analysis .....	45
V.A.	Turbine Inlet and Exit Flowfields .....	48
V.A.1.	Ensemble Averaging .....	49
V.A.2.	Uncertainty .....	49
V.B.	Turbine Power .....	56
V.B.1.	Ensemble Averaging .....	56
V.B.2.	Uncertainty .....	58
V.C.	Sources of Error.....	58
VI.	Results.....	61
VI.A.	Turbine Cycle-Average Specific Work.....	61
VI.A.1.	Sensitivity Study .....	63
VI.A.2.	Time-Resolved Turbine Power: Effect of PDC Frequency .....	66
VI.A.3.	Time-Resolved Turbine Power: Effect of Fueled Fraction.....	68
VI.A.4.	Time-Resolved Turbine Power: Effect of Purge Fraction .....	69
VI.B.	Cycle-Average Isentropic Turbine Efficiency.....	70
VI.B.1.	Sensitivity Study .....	74
VI.B.2.	Time-Resolved Turbine Inlet and Exit Flowfields: Temperature.....	78
VI.B.3.	Time-Resolved Turbine Inlet and Exit Flowfields: Pressure .....	81
VI.B.4.	Time-Resolved Turbine Inlet and Exit Flowfields: Velocity.....	84
VI.B.5.	Time-Resolved Turbine Inlet and Exit Flowfields: Mass Flow.....	86
VI.B.6.	Time-Resolved Turbine Inlet and Exit Flowfields: Total Enthalpy Rate .....	90
VII.	Discussion .....	95
VII.A.	General Application of the Unsteady Turbine Efficiency Formulation.....	95
VII.B.	Steady and Unsteady Turbine Operation .....	97
VII.C.	Radial and Axial Turbines .....	102
VIII.	Conclusions.....	104
IX.	Recommendations.....	106
Appendix A: Development History of Pressure-Gain Combustion and Gas Turbine		
Integration .....		108
Early Developments with Pressure Gain Combustion .....		109
Developments in the 1950's and 1960's with Pulsed Detonations.....		110
Developments in the 1970's with Pressure-Gain Combustion Driven Turbines.....		110
Developments in the 1980's with Detonation Engines.....		112
Developments in the 1990's with Wave Rotors .....		112
Developments in the 21 <sup>st</sup> Century with Pulsed Detonation Driven Turbines .....		114

Two-Dimensional Detonation-Turbine Interaction Studies.....	116
Mixed-Flow, Detonation-Driven Axial Turbine Studies.....	117
Thermodynamic Analysis of a Pulsed Detonation Driven Cycle.....	120
Appendix B: Theory of Confined Detonations.....	126
Rayleigh Line and Rankine-Hugoniot Relations.....	126
Chapman-Jouguet Conditions.....	130
Zeldovich, von Neumann and Döring One-Dimensional Model.....	130
Three-Dimensional Structure of Confined Detonations.....	131
Appendix C: Pulsed Detonation Combustor Operation.....	135
Fire Phase.....	136
Fill and Purge Phases.....	138
Rotating Detonation Configuration.....	139
Key Operating Parameters.....	141
Appendix D: Comparison of Pulsed Detonation and Steady Deflagration Turbine, Presented at the 2010 AIAA Aerospace Sciences Meeting (AIAA-2010-1116).....	142
Performance Figures of Merit.....	143
Experimental Arrangement and Methodology.....	147
Turbocharger Instrumentation.....	149
Phase One: Cold Flow Driven Turbine.....	151
Phase Two: Steady Deflagration-Driven Turbine.....	152
Phase Three: Pulsed Detonation-Driven Turbine.....	153
Operating Conditions.....	155
Results.....	156
Cold Flow Driven Turbine.....	156
Steady Deflagration Combustor Driven Turbine.....	158
Pulse Detonation Combustor Driven Turbine.....	158
Comparison of SDC and PDC Driven Turbine Performance.....	160
Summary.....	162
Appendix E: Preliminary Parametric Study of PDC Operating Parameters, Presented at the 2010 AIAA Joint Propulsion Conference (AIAA-2010-6536).....	163
PDC-Turbine Arrangement with Orifice Plates for DDT.....	163
Power and Rotor Speed Instrumentation.....	166
Results.....	166
Comparison of SDC and PDC Turbine Performance.....	167
Average Specific Work.....	168
Rotor Speed Response to Pulsed Cold Flow ( $\phi = 0.0$ ).....	169

Rotor Speed Response to Pulsed Detonations .....	171
Summary .....	174
Appendix F: Preliminary PDC-Turbine Flowfield and Rotor Speed Measurements, Presented at the 2011 AIAA Aerospace Sciences Meeting (AIAA-2011-0577) .....	175
PDC-Turbine Arrangement with Internal Spiral for DDT .....	175
Rotor Speed Measurement Techniques.....	176
Turbine Inlet and Exit Flowfield High-Speed Measurement Techniques .....	177
Optical Pyrometry .....	179
Particle Streak Velocimetry .....	181
Background Oriented Schlieren .....	182
Comparison of Rotor Speed Results .....	185
Initial High-Speed Flowfield Results.....	188
Turbine Inlet Temperature and Pressure Spatial Variation.....	191
Summary of Initial High-Speed Measurements and Rotor Speed Results.....	193
Appendix G: Performance of a PDC-Turbine with a Pre-Detonator Configuration, Presented at the 2011 ASME Turbo Expo (GT2011-45396).....	194
PDC Arrangement with a Pre-detonator .....	195
Results for PDC-Turbine with a Pre-Detonator.....	197
Summary and Conclusions.....	199
Appendix H: PDC-Turbine Energy Conservation Analysis .....	200
Appendix I: Time-Resolved PDC-Turbine Power Results .....	203
Appendix J: Time-Resolved PDC-Turbine Inlet and Exit Flowfield Results.....	209
Appendix K: Alternate Unsteady Turbine Efficiency Results .....	220
Instantaneous Turbine Efficiency.....	220
Mean Effective Instantaneous Turbine Efficiency.....	222
Summary and Conclusions.....	225
Appendix L: Turbine Inlet Rayleigh Line Flow Analysis.....	226
Bibliography.....	229

## List of Figures

	Page
Figure 1. Normalized rotor speed time history for stoichiometric hydrogen-fueled PDC operation at 10 Hz, 15 Hz, and 20 Hz operating frequencies	8
Figure 2. Time-average specific work from 10 Hz to 25 Hz operation, fueled fractions of 0.5 to 0.8 and 0.5 purge fraction	9
Figure 3. Schematic of 1 <sup>st</sup> Law thermodynamic analysis for a steady flow turbine	11
Figure 4. Notional Mollier diagram for a steady flow turbine	11
Figure 5. Notional Mollier diagram for a pulsed detonation driven turbine	13
Figure 6. Schematic of unsteady model for a pulsed detonation driven turbine	19
Figure 7. Notional Mollier diagram for an pulsed detonation driven turbine with heat transfer	19
Figure 8. Compressor operating map for Garrett GT28R automotive turbocharger (used with permission from Honeywell)	23
Figure 9. Block diagram of AFRL Detonation Engine Research Facility engine test rig	26
Figure 10. Detonation engine head, fill and purge lines, and fill and purge valves	27
Figure 11. Notional ideal temperature-entropy diagram of experimental test configuration	28
Figure 12. Side view schematic of PDC-turbine test section arrangement	30
Figure 13. PDC-turbine arrangement with inlet and exit diagnostic sections	30
Figure 14. Locations of PDC thermocouples and ion probes	33
Figure 15. Garrett GT28R journal bearing turbocharger (used with permission from Advanced Tuning Products, Inc.)	35
Figure 16. Turbine operating map for Garrett GT28 journal bearing turbocharger (used with permission from Honeywell)	35
Figure 17. Turbine housing and inlet wall temperatures with 10 and 20 Hz hydrogen-fueled PDC with 0.75 fueled and purge fractions	36

Figure 18. Top and side view schematics of laser absorption instrumentation	39
Figure 19. Side view schematic of optical access arrangement for pyrometry and velocimetry measurements	40
Figure 20. Single pyrometry frame of a detonation travelling from left to right at the turbine inlet, such that black represents unburned fuel-air	41
Figure 21. Single particle streak velocimetry image during blowdown at the turbine inlet	42
Figure 22. Top view schematic of test section	43
Figure 23. Garrett speed sensor arrangement (used with permission from Advanced Tuning Products, Inc.)	44
Figure 24. Schematic of data acquisition systems	45
Figure 25. Schematic of facility data acquisition system	46
Figure 26. Schematic of high-speed data acquisition system	46
Figure 27. Schematic of laser absorption data acquisition system	47
Figure 28. Comparison of inlet static pressure results for optical pyrometry and laser absorption experiments with 20 Hz ethylene-fueled PDC with 0.9 fueled fraction and 0.5 purge fraction. Transducer stand-off distance was 38 mm greater in the optical experiment.	51
Figure 29. Comparison of inlet static temperature results from optical pyrometry and laser absorption during 6 ms of blowdown with ethylene-fueled PDC at 20 Hz with 0.9 fueled fraction and 0.5 purge fraction	52
Figure 30. Comparison of inlet velocity results from soot particle velocimetry and laser absorption Doppler shift during 6 ms of blowdown with ethylene-fueled PDC at 20 Hz with 0.9 fueled fraction and 0.5 purge fraction	53
Figure 31. Schematic of energy conservation analysis for PDC-turbine arrangement	55
Figure 32. Time-resolved power over 5 cycles at 30 Hz with 0.75 fueled and purge fractions	57
Figure 33. Ensemble-average power over 5 cycles at 30 Hz with 0.75 fueled and purge fractions	57

Figure 34. Summary of turbine cycle-average specific work with hydrogen-fueled PDC	62
Figure 35. Time-resolved power with 10, 20, and 30 Hz hydrogen-fueled PDC with 0.75 fueled and purge fractions	67
Figure 36. Normalized time-resolved turbine power with 10, 20, and 30 Hz hydrogen-fueled PDC with 0.75 fueled and purge fractions	68
Figure 37. Time-resolved power with 10 Hz hydrogen-fueled PDC with fueled fractions of 0.60, 0.75, and 0.90 and with 0.75 purge fraction	69
Figure 38. Time-resolved power with 20 Hz hydrogen-fueled PDC with 0.90 fueled fraction and 0.50 and 0.75 purge fractions	70
Figure 39. Comparison of inlet heat transfer fraction for turbine efficiency with 30 Hz hydrogen-fueled PDC with 0.75 fueled and purge fractions, using Eq. (29) and ensemble-averaged efficiency	72
Figure 40. Comparison of averaging techniques for turbine efficiency with 30 Hz hydrogen-fueled PDC with 0.75 fueled and purge fractions, using Eq. (29) with constant total pressure heat transfer at the inlet only ( $\psi = 1$ )	73
Figure 41. Comparison of averaging techniques for turbine efficiency with 20 Hz hydrogen-fueled PDC with 0.75 fueled and purge fractions, using Eq. (29) with constant total pressure heat transfer at the inlet only ( $\psi = 1$ )	74
Figure 42. Turbine inlet and exit static temperature over 5 cycles with 30 Hz hydrogen-fueled PDC with 0.75 fueled and purge fractions	79
Figure 43. Ensemble average of turbine inlet and exit static temperature over 13 cycles with 30 Hz hydrogen-fueled PDC with 0.75 fueled and purge fractions	79
Figure 44. Turbine inlet and exit total temperature over 2 cycles with 20 and 30 Hz hydrogen-fueled PDC with 0.75 fueled and purge fractions	80
Figure 45. Turbine inlet and exit static pressure over 5 cycles with 30 Hz hydrogen-fueled PDC with 0.75 fueled and purge fractions	81
Figure 46. Turbine inlet and exit static pressure ensemble averaged over 13 cycles with 30 Hz hydrogen-fueled PDC with 0.75 fueled and purge fractions	83
Figure 47. Turbine inlet and exit total pressure over 2 cycles with 20 and 30 Hz hydrogen-fueled PDC with 0.75 fueled and purge fractions	84

Figure 48. Turbine inlet and exit velocity over 5 cycles with 30 Hz hydrogen-fueled PDC with 0.75 fueled and purge fractions	85
Figure 49. Turbine inlet and exit velocity over 2 cycles with 20 and 30 Hz hydrogen-fueled PDC with 0.75 fueled and purge fractions	86
Figure 50. Turbine inlet and exit mass flow rate over 5 cycles with 30 Hz hydrogen-fueled PDC with 0.75 fueled and purge fractions	87
Figure 51. Turbine inlet and exit mass flow rate over 2 cycles with 20 and 30 Hz hydrogen-fueled PDC with 0.75 fueled and purge fractions	88
Figure 52. Turbine inlet and exit aggregate mass over 2 cycles with 10 and 30 Hz hydrogen-fueled PDC with 0.75 fueled and purge fractions	89
Figure 53. Turbine inlet and exit aggregate mass over 14 cycles with 30 Hz hydrogen-fueled PDC with 0.75 fueled and purge fractions	90
Figure 54. Turbine inlet total enthalpy rate over 13 cycles with 30 Hz hydrogen-fueled PDC with 0.75 fueled and purge fractions	91
Figure 55. Turbine exit total enthalpy rate over 13 cycles with 30 Hz hydrogen-fueled PDC with 0.75 fueled and purge fractions	92
Figure 56. Turbine inlet and exit total enthalpy rate ensemble-averaged over 13 cycles with 30 Hz hydrogen-fueled PDC with 0.75 fueled and purge fractions	93
Figure 57. Turbine inlet and exit total enthalpy rate over 2 cycles with 10 and 30 Hz hydrogen-fueled PDC with 0.75 fueled and purge fractions	94
Figure 58. Simulated test case for evaluating the proposed unsteady turbine efficiency formulation with a steady operation including a single transient condition	96
Figure 59. Simulated test case for time-varying turbine efficiency, with equal steps in time, turbine efficiency drop, and total specific enthalpy expansion	97
Figure 60. Compressor dynamometer map with instantaneous and average operating points with 30 Hz hydrogen-fueled PDC with 0.75 fueled and purge fractions and with average operating points for other frequencies, fueled fractions, and purge fractions	98
Figure 61. Steady turbine model operating points for the condition equivalent to the steady compressor dynamometer map with 30 Hz hydrogen-fueled PDC with 0.75 fueled and purge fractions	100

Figure 62. Instantaneous turbine model operating points with 30 Hz hydrogen-fueled PDC with 0.75 fueled and purge fractions	101
Figure 63. Development timeline of pressure-gain combustion driven turbines	108
Figure 64. Cross section of the Holzwarth pressure-gain combustion gas turbine (Holzwarth 1912)	109
Figure 65. Relative improvement in net power output per percent pressure gain in the combustor, varying with of cycle pressure ratio, cycle temperature ratio, and combustor temperature ratio (Kentfield, et al. 1979).	112
Figure 66. Schematic of a wave rotor used as a topping cycle for jet engines (Wilson and Fronck 1993)	113
Figure 67. Schematic of NASA self-cooled, four-port wave rotor (Welch, et al. 1999)	114
Figure 68. Schematic of constant volume combustion wave rotor (Akbari, Szpynda and Nalim 2007)	114
Figure 69. Heiser and Pratt comparison of ideal PDE, Humphrey, and Brayton cycles on a temperature-entropy diagram (Heiser and Pratt 2002)	121
Figure 70. Comparison of ideal PDE and ramjet cycles on a temperature-entropy diagram (Dyer and Kaemming 2002)	122
Figure 71. Comparison of ideal PDE, ramjet and Brayton cycle thermal efficiencies (Dyer and Kaemming 2002)	123
Figure 72. Comparison of ideal Fickett-Jacobs, Humphrey and Brayton cycle thermal efficiencies (Wintenberger and Shepherd 2004)	124
Figure 73. Schematic of stationary, one-dimensional, confined combustion wave model	126
Figure 74. Hugoniot curve with solution domains of different combustion conditions	129
Figure 75. Notional variation of temperature, pressure, and density through a ZND 1-D detonation wave model (not to scale)	131
Figure 76. Components of detonation wave cell structure (Porowski and Teodorczyk 2009)	132
Figure 77. Measured cell sizes of different fuels (Guirao, et al. 1982:583-590; Knystautas 1984:23-37)	133

Figure 78. Pulsed detonation combustor cycle with timing for 11 Hz operation with equal phase times	135
Figure 79. Notional timeline of events in fire phase (adapted from Hopper 2008)	136
Figure 80. Notional diagram of a rotating detonation combustor (adapted from Daniau, Falempin and Zhdan 2005)	140
Figure 81. Garrett GT2860RS automotive turbocharger (used with permission)	142
Figure 82. Turbocharger components (used with permission)	143
Figure 83. Schematic of one-dimensional, adiabatic thermodynamic analysis of a radial turbine	144
Figure 84. Compressor map for GT2860RS (used with permission)	146
Figure 85. Notional ideal temperature-entropy diagram of PDC and SDC configurations	148
Figure 86. Turbocharger experimental arrangement	149
Figure 87. Turbocharger compressor instrumentation and control valve	150
Figure 88. Schematic of turbocharger tachometer arrangement	151
Figure 89. Schematic of laser tachometer	151
Figure 90. Schematic of steady deflagration turbine experimental arrangement with GT2860RS turbocharger	152
Figure 91. Schematic of PDC-turbine experimental arrangement with GT2860RS turbocharger	154
Figure 92. Compressor tachometer signal with 10 Hz cold flow operation	157
Figure 93. Rotor speed response over 2 cycles with 10 Hz cold flow operation	157
Figure 94. Rotor speed response with 10 Hz PDC	160
Figure 95. Comparison of specific work for SDC and PDC configurations	161
Figure 96. Compressor power response over 2 cycles driven by PDC at 11 Hz with cycle turbine air flow of 3.65 kg/min	162
Figure 97. Schematic of PDC-turbine rig with orifice plate DDT obstacles	165

Figure 98. Variation in average rotor speed with increasing PDC frequency	167
Figure 99. Comparison of average specific work at four equivalence ratios and two operating frequencies	169
Figure 100. Rotor speed periodicity for 10 Hz cold flow operation ( $\phi = 0.0$ ) with 1.0 fueled fraction and zero purge fraction	170
Figure 101. Normalized rotor speed time history with 10 and 15 Hz cold flow operation ( $\phi = 0.0$ ) with 1.0 fueled fraction and zero purge fraction	171
Figure 102. Rotor speed time history with 10 Hz PDC with 1.0 fueled fraction and 0.40 purge fraction	172
Figure 103. Rotor speed periodicity with 10 Hz PDC with 1.0 fueled fraction and 0.40 purge fraction	172
Figure 104. Normalized rotor speed time history with 10, 15, and 20 Hz PDC with overall equivalence ratio of 0.70	173
Figure 105. Rotor speed history with 15 Hz PDC with overall equivalence ratios of 0.58, 0.64, 0.70, and 0.78	174
Figure 106. Schematic of PDC-turbine test rig arrangement for preliminary high-speed flowfield measurements	176
Figure 107. Schematic of optical access for preliminary high-speed measurements	179
Figure 108. Preliminary arrangement of turbine inlet and exit optical access high-speed flowfield measurements	180
Figure 109. Left graph: PCO Dimax camera relative responsivity for the blue, green and red channels as a function of wavelength. Right graph: ratio of the various color channels for a PCO Dimax camera as a function of temperature for a black or gray body emitter	180
Figure 110. Schematic of background oriented Schlieren arrangement utilized for high-speed visualization, density and velocity measurements at the PDC-turbine exit	184
Figure 111. Six sequential frames of BOS vector magnitude plots for a pulsed detonation turbine exhaust flow field. Flow in each image is from bottom to top, and the sequence proceeds from left to right with 0.12 ms time step.	184
Figure 112. Rotor speed history using the compressor laser tachometer with 10 Hz PDC with 1.0 fueled fraction and 0.3 purge fraction	185

Figure 113. Compressor rotor speed history using a Garrett speed sensor with 15 Hz PDC with 1.0 fueled fraction and 0.5 purge fraction	186
Figure 114. Time history of rotational energy and net shaft torque with 15 Hz PDC with 1.0 fueled fraction and 0.5 purge fraction	187
Figure 115. Time history of rotational energy and power with 15 Hz PDC with 1.0 fueled fraction and 0.5 purge fraction	188
Figure 116. Turbine inlet and exit wall static pressures with 15 Hz PDC with 1.0 fueled fraction and 0.5 purge fraction	189
Figure 117. Turbine inlet and exit velocities from PSV and BOS measurements, respectively, with 15 Hz PDC with 1.0 fueled fraction and 0.5 purge fraction	190
Figure 118. Turbine inlet and exit static temperatures from pyrometry measurements with 15 Hz PDC with 1.0 fueled fraction and 0.5 purge fraction	191
Figure 119. Axial turbine inlet velocity variation in the x-direction along the centerline at two moments during blowdown	192
Figure 120. Turbine inlet temperature variation in the y-direction at two moments during blowdown	192
Figure 121. Garrett T3/T4E Turbocharger (used with permission from Advanced Tuning Products, Inc.)	194
Figure 122. Schematic of PDC-turbine arrangement using a pre-detonator and small to large diameter pipe transition	195
Figure 123. Pre-detonator and PDC arrangement at the engine head	196
Figure 124. Variation in corrected rotor speed with 25 Hz PDC with 0.8 fueled fraction and 0.5 purge fraction	198
Figure 125. Time-average specific work with 10 to 25 Hz operation with 0.5 to 0.8 fueled fractions and 0.5 purge fraction	199
Figure 126. Time-resolved power with 10 Hz hydrogen-fueled PDC with 0.60 fueled fraction and 0.75 purge fraction	203
Figure 127. Time-resolved power with 10 Hz hydrogen-fueled PDC with 0.75 fueled fraction and 0.75 purge fraction	203
Figure 128. Time-resolved power with 10 Hz hydrogen-fueled PDC with 0.90 fueled fraction and 0.75 purge fraction	204

Figure 129. Time-resolved power with 20 Hz hydrogen-fueled PDC with 0.60 fueled fraction and 0.50 purge fraction	204
Figure 130. Time-resolved power with 20 Hz hydrogen-fueled PDC with 0.60 fueled fraction and 0.75 purge fraction	205
Figure 131. Time-resolved power with 20 Hz hydrogen-fueled PDC with 0.75 fueled fraction and 0.75 purge fraction	205
Figure 132. Time-resolved power with 20 Hz hydrogen-fueled PDC with 0.90 fueled fraction and 0.50 purge fraction	206
Figure 133. Time-resolved power with 20 Hz hydrogen-fueled PDC with 0.90 fueled fraction and 0.75 purge fraction	206
Figure 134. Time-resolved power with 30 Hz hydrogen-fueled PDC with 0.60 fueled fraction and 0.75 purge fraction	207
Figure 135. Time-resolved power with 30 Hz hydrogen-fueled PDC with 0.75 fueled fraction and 0.75 purge fraction	207
Figure 136. Time-resolved power with 20 Hz ethylene-fueled PDC with 0.90 fueled fraction and 0.50 purge fraction	208
Figure 137. Time-resolved turbine inlet and exit flowfield properties with 10 Hz hydrogen-fueled PDC with 0.60 fueled fraction and 0.75 purge fraction	209
Figure 138. Time-resolved turbine inlet and exit flowfield properties with 10 Hz hydrogen-fueled PDC with 0.75 fueled fraction and 0.75 purge fraction	210
Figure 139. Time-resolved turbine inlet and exit flowfield properties with 10 Hz hydrogen-fueled PDC with 0.90 fueled fraction and 0.75 purge fraction	211
Figure 140. Time-resolved turbine inlet and exit flowfield properties with 20 Hz hydrogen-fueled PDC with 0.60 fueled fraction and 0.50 purge fraction	212
Figure 141. Time-resolved turbine inlet and exit flowfield properties with 20 Hz hydrogen-fueled PDC with 0.60 fueled fraction and 0.75 purge fraction	213
Figure 142. Time-resolved turbine inlet and exit flowfield properties with 20 Hz hydrogen-fueled PDC with 0.75 fueled fraction and 0.75 purge fraction	214
Figure 143. Time-resolved turbine inlet and exit flowfield properties with 20 Hz hydrogen-fueled PDC with 0.90 fueled fraction and 0.50 purge fraction	215

Figure 144. Time-resolved turbine inlet and exit flowfield properties with 20 Hz hydrogen-fueled PDC with 0.90 fueled fraction and 0.75 purge fraction	216
Figure 145. Time-resolved turbine inlet and exit flowfield properties with 30 Hz hydrogen-fueled PDC with 0.60 fueled fraction and 0.75 purge fraction	217
Figure 146. Time-resolved turbine inlet and exit flowfield properties with 30 Hz hydrogen-fueled PDC with 0.75 fueled fraction and 0.75 purge fraction	218
Figure 147. Time-resolved turbine inlet and exit flowfield properties with 20 Hz ethylene-fueled PDC with 0.90 fueled fraction and 0.50 purge fraction	219
Figure 148. Time resolved turbine efficiency with 30 Hz hydrogen-fueled PDC with 0.75 fueled and purge fractions and $\psi = 0.75$ , using Eq. (79)	221
Figure 149. Ensemble averaged turbine efficiency over 14 cycles with 30 Hz hydrogen-fueled PDC with 0.75 fueled and purge fractions and $\psi = 0.75$ , using Eq. (79)	222
Figure 150. Cycle average turbine efficiency over 14 cycles with 30 Hz hydrogen-fueled PDC with 0.75 fueled and purge fractions and $\psi = 0.75$ , using Eq. (82)	224
Figure 151. Time-resolved turbine efficiency and inlet total enthalpy rate over one cycle with 30 Hz hydrogen-fueled PDC with 0.75 fueled and purge fractions and $\psi = 0.75$ , using Eq. (82)	224
Figure 152. Time-resolved turbine efficiency using Eq. (82) and turbine power using Eq. (80) for one cycle with 30 Hz hydrogen-fueled PDC with 0.75 fueled and purge fractions and $\psi = 0.75$	225
Figure 153. Schematic of unsteady model for Rayleigh analysis of a pulsed detonation driven turbine	226

## List of Tables

	Page
Table 1. Summary of PDC operating conditions	32
Table 2. Summary of laser absorption configuration	37
Table 3. Summary of pyrometry and PSV configuration	38
Table 4. Average percent standard deviation of turbine inlet and exit ensemble data	50
Table 5. Summary of mass flow uncertainty analysis	54
Table 6. Energy conservation analysis with 30 Hz hydrogen-fueled PDC with 0.75 fueled and purge fractions	56
Table 7. Summary of turbine cycle-average power and specific work	62
Table 8. Sensitivity study for cycle-average specific work with hydrogen-fueled PDC	65
Table 9. Comparison of weighting parameters and inlet heat transfer models for unsteady turbine efficiency with 30 Hz hydrogen-fueled PDC with 0.75 fueled and purge fractions, using Eq. (29) and ensemble-averaged efficiency	71
Table 10. Sensitivity of cycle-average turbine efficiency to measurement error	75
Table 11. Sensitivity of cycle-average turbine efficiency to time-shifted turbine exit flowfield pressures, temperatures, and velocities	77
Table 12. Comparison of detonation and deflagration (Kuo, 1986:234)	129
Table 13. Summary of SDC and PDC operating conditions	155
Table 14. Results from steady deflagration operation	158
Table 15. Results from pulsed detonation operation	159
Table 16. Summary of PDC operating conditions with orifice plate DDT obstacles	165
Table 17. Summary of results with PDC having orifice plate DDT obstacles	167
Table 18. Preliminary turbine inlet and exit flowfield measurement techniques	178
Table 19. Summary of PDC operating conditions using a pre-detonator	197

## List of Symbols

### Acronyms

1-D	=	one dimensional
2-D	=	two dimensional
3-D	=	three dimensional
AFIT	=	Air Force Institute of Technology
AFOSR	=	Air Force Office of Scientific Research
AFRL	=	Air Force Research Laboratory
AIAA	=	American Institute of Aeronautics and Astronautics
ASME	=	American Society of Mechanical Engineers
BOS	=	background oriented Schlieren
BSFC	=	brake specific fuel consumption
C-J	=	Chapman-Jouguet
DAQ	=	data acquisition
DDT	=	detonation to deflagration transition
DERF	=	Detonation Engine Research Facility
FF	=	fueled fraction
FJ	=	Fickett-Jacobs
LED	=	light emitting diode
LHV	=	lower heating value
MAF	=	mass air flow
NASA	=	National Aeronautics and Space Administration
NPSS	=	Numerical Propulsion Systems Simulation
PDC	=	pulsed detonation combustor
PDE	=	pulsed detonation engine
PF	=	purge fraction
PIV	=	particle image velocimetry
PSV	=	particle streak velocimetry
RDC	=	rotating detonation combustor
RDE	=	rotating detonation engine
SDC	=	steady deflagration combustor
SiC	=	silicon carbide
TDLAS	=	tunable diode-laser absorption spectroscopy
TFP	=	thin filament pyrometry
WPAFB	=	Wright-Patterson Air Force Base
ZND	=	Zeldovich, von Neumann and Döring

### Symbols

A	=	area ( $m^2$ )
c	=	speed of sound (m/s)
$c_D$	=	nozzle discharge coefficient
$c_p$	=	specific heat at constant pressure (kJ/ kg K)

$d$	=	nozzle throat diameter (m)
$E$	=	energy (kJ)
$f$	=	operating frequency (Hz), fuel-air ratio
$g$	=	acceleration due to gravity ( $\text{m/s}^2$ )
$Gr$	=	Grashof number
$h$	=	convective heat transfer coefficient ( $\text{W/m}^2 \text{K}$ )
$h_t$	=	total specific enthalpy (kJ/kg)
$\dot{H}_t$	=	total enthalpy rate (kW)
$I$	=	moment of inertia ( $\text{kg m}^2$ )
$k$	=	thermal conductivity ( $\text{W/m K}$ )
$KE_{\text{rot}}$	=	rotational energy (kJ)
$m$	=	mass (kg)
$\dot{m}$	=	mass flow rate (kg/s)
$Nu$	=	Nusselt number
$P$	=	pressure (bar)
$Pr$	=	Prandtl number
$q$	=	heat release per unit mass (kJ/kg)
$R$	=	gas constant (kJ/kg K)
$Ra$	=	Rayleigh number
$T$	=	temperature (K), cycle time (s)
$u$	=	specific internal thermal energy (kJ/kg), axial velocity (m/s)
$s$	=	specific entropy (J/kg K)
$t$	=	time (s)
$v$	=	specific volume ( $\text{m}^3/\text{kg}$ ), velocity (m/s)
$V$	=	velocity magnitude (m/s)
$\forall$	=	volume ( $\text{m}^3$ )
$W$	=	work (kJ)
$\dot{W}$	=	power (kW)
$W_s$	=	specific work (kW/kg/s)

### Greek

$\alpha$	=	thermal diffusivity ( $\text{m}^2/\text{s}$ )
$\beta$	=	coefficient of volumetric expansion ( $1/\text{K}$ )
$\varepsilon$	=	emissivity
$\phi$	=	equivalence ratio, cycle temperature ratio
$\gamma$	=	ratio of specific heats
$\eta$	=	efficiency
$\lambda$	=	thermal conductivity ( $\text{W/m K}$ ), detonation wave cellular width (m)
$\mu$	=	dynamic viscosity (Pa s)
$\mu'$	=	bulk viscosity (Pa s)
$\nu$	=	kinematic viscosity ( $\text{m}^2/\text{s}$ )
$\pi$	=	pressure ratio

$\theta$	= combustor temperature ratio
$\rho$	= density ( $\text{kg/m}^3$ )
$\sigma$	= Boltzmann constant ( $\text{m}^2 \text{kg/s}^2 \text{K}$ )
$\tau$	= torque (N m)
$\omega$	= rotor speed (rad/s)
$\xi$	= inlet weighting parameter
$\psi$	= inlet heat transfer fraction parameter

# UNSTEADY SPECIFIC WORK AND ISENTROPIC EFFICIENCY OF A RADIAL TURBINE DRIVEN BY PULSED DETONATIONS

## I. Introduction

Gas turbine engines may achieve higher specific work with pulsed detonation combustors (PDCs), reducing the entropy associated with heat addition. PDCs are inherently unsteady with large, rapid transients occurring in less than a millisecond typically with peak gas pressures ratios greater than 25, peak gas temperatures greater than 2,900 K, peak gas velocities near Mach 1 and detonation wave speeds exceeding Mach 3. Incorporating a PDC into a steady Brayton cycle introduces unsteady flow behavior with potential negative effects on rotating machinery performance. Practical implementation of a PDC in a gas turbine engine must ensure that performance improvements in the combustor are not overcome by performance deterioration in the turbine. Comparisons between conventional steady and pulsed detonation operation require time-integrated formulations for specific work and isentropic turbine efficiency.

Evaluation of pulsed detonation driven turbine performance requires full-cycle, time-resolved measurements. There have been few previous experiments conducted with pulsed detonation driven turbines. Hoke, et al. (2002), Schauer, et al. (2003), and Sakurai, et al. (2005) conducted experiments with radial turbines. Hoke, et al. (2002) demonstrated the capability of an automotive turbocharger radial turbine to extract unsteady work from a PDC consisting of two simultaneously firing detonation tubes. Schauer, et al. (2003) reported a 6.8% thermal efficiency with a single tube PDC-turbocharger with an initial absolute tube pressure of 2.5 bar and proved that the radial

turbine was able to survive more than 50,000 detonations and a 25 minute continuous run. The thermal efficiency was lower than that of the equivalent ideal Brayton cycle, which is 23% thermally efficient with an overall pressure ratio of 2.5. Sakurai, et al. (2005) experimented with a single tube PDC driven turbocharger and showed that power output improved with increasing operating frequency. None of the above studies included time-resolved measurements of turbine inlet and exit pressures, temperatures and velocities with full-admission pulsed detonation operation.

Currently, there is no widely accepted method for characterization of ideal unsteady turbine performance, in particular unsteady turbine efficiency. Suresh, et al. (2009) proposed and evaluated two formulations from a two-dimensional (2-D) numerical simulation with a full-admission array of PDC tubes feeding a translating axial turbine cascade. One formulation was based on integrated turbine inlet and exit total enthalpy and assumed instantaneous expansion, and the other formulation was based on mass-averaged inlet and exit total temperature and work-averaged inlet and exit total pressure. There was a significant difference between efficiency results from the two formulations, using the same flowfield data. An industry standard, unsteady turbine efficiency formulation is needed. A practical formulation for unsteady turbine efficiency must account for differences in experimental pulsed detonation operation and conventional steady deflagration operation.

#### **I.A. Objectives**

The current objective, to evaluate pulsed detonation driven turbine performance, is accomplished in two parts: 1) time-resolved measurements of power and turbine inlet

and exit flowfield properties, and 2) evaluation of cycle-averaged unsteady specific work and isentropic turbine efficiency. Time-resolved power and turbine inlet and exit flowfield properties show the interaction between the PDC and turbine. Time-integrated turbine power is necessary to compute cycle-averaged specific work. To compute cycle-averaged turbine efficiency, measured flowfield properties must include pressure, temperature, velocity, mass flow, and enthalpy. A standard formulation for turbine efficiency is proposed, accounting for heat transfer effects and including cycle-average terms for work, enthalpy, and pressure ratio.

A comparison of cycle-averaged specific work and isentropic efficiency over a range of PDC operating parameters shows the full relationship between the coupled PDC operation and turbine performance. Key PDC operating parameters include frequency, fueled fraction, purge fraction, and fuel type. The operating hypothesis was that unsteady specific work and isentropic efficiency increase with PDC frequency and fueled fraction due to shorter quiescent periods in the flowfield and that isentropic efficiency is lower than comparable conventional deflagration operation due to fluctuations away from the designed steady operating condition.

### **I.B. Outline**

The first section of this document introduced the motivation and objectives of this research. Section II includes previous research of unsteady flow in conventional and pulsed detonation driven turbines. Section III addresses unsteady thermodynamics associated with conventional and pulsed detonation driven turbines and introduces an unsteady turbine model for the proposed isentropic efficiency formulation. Section IV

describes the experimental research facility, test article and instrumentation. Section V includes a discussion of the data reduction and uncertainty analysis. Section VI contains results from pulsed detonation driven turbine experiments. Section VII entails a discussion of the results as related to comparisons between steady and unsteady turbines and axial and radial turbines. Section VIII includes conclusions drawn from experimental results. Section IX includes recommendations for continued research.

## II. Previous Pulsed Detonation Driven Turbine Research

The PDC-turbine arrangement used in this study was developed from recent pulsed detonation driven turbine research, as described below. A more detailed history of previous research is provided in Appendix A, relating the current research to the development history of pressure-gain combustion and gas turbine integration. Theory and operation of pulsed detonation combustors are discussed in Appendices B and C, respectively.

The radial turbine of a Garrett automotive turbocharger was selected for this research due to previously proven pulsed detonation driven performance and durability. Schauer, et al. (2003) conducted an experiment with a single-tube, hydrogen-fueled, pulsed detonation driven radial turbine from a Garrett T3 automotive turbocharger. Power output was measured with the turbocharger coupled compressor, and maximum cycle-average thermal efficiency was 6.8%. Operating frequencies ranged from 20 to 40 Hz. The current study also used the turbocharger compressor for power measurements and explored a range of operating frequencies from 10 to 30 Hz. Testing at higher frequencies was not possible due to back-fire.

Schauer, et al. (2003) reported that peak pressure was attenuated through the turbine from 27.6 bar to 6.9 bar, indicating that the amplitude of unsteadiness was smaller at the turbine exit than at the inlet. The choice of 50 bar pressure transducers for this current experiment was determined to be sufficient for the expected peak pressures.

A full-admission PDC-turbine arrangement was selected for this current research to eliminate the effect of viscous mixing between the PDC exhaust and steady bypass

flow associated with partial-admission arrangements. Rasheed, et al. (2005), Glaser, et al. (2007), and Caldwell, et al. (2006 and 2008) experimented with axial turbine arrangements driven by a partial-admission, annular, multi-tube PDC array and a steady flow of cooling “bypass” air that mixed with PDC exhaust before entering the turbine. The cooling air allowed conventional measurement techniques for turbine inlet and exit pressures, temperatures, and velocities. Glaser, et al. (2007) reported that work output and turbine efficiency from this arrangement were comparable to that of steady deflagration operation. Caldwell and Gutmark (2008) investigated the inlet flowfield of the same PDC-turbine arrangement. Shadowgraph images showed a shock-jet interaction between the primary and secondary flow that induced a vortex ring, attenuating the exiting PDC shock before entering the turbine and reducing the energy available for shaft work due to viscous mixing. The results indicated that a full-admission PDC-turbine arrangement is necessary to eliminate energy mixing losses at the turbine inlet.

The flowfield of a full-admission PDC-turbine arrangement was previously studied by Rasheed, et al. (2004) to observe the interaction of a single-tube full-admission pulsed detonation with a 2-D turbine cascade. Shadowgraph images showed strong shocks reflected from blade leading edges and weaker shocks passed through the cascade. Rasheed, et al. (2004) also conducted an unsteady numerical study of the full-admission cascade arrangement and concluded that multi-cycle measurements and calculations are necessary to evaluate detonation driven turbine performance.

Appendices D, E, F, and G include preliminary results from experiments using different test articles, PDC configurations, and instrumentation techniques and were

presented at various conferences (Rouser, et al. 2010a, Rouser, et al. 2010b, Rouser, et al. 2011a, Rouser, et al. 2011b). The initial experiments were essential to the development of the current test configuration; however, they did not contain a complete full-cycle evaluation of specific work and turbine efficiency.

Appendix D includes a preliminary comparison of pulsed detonation and steady deflagration turbine performance with the radial turbine in a GT2860RS ball bearing turbocharger (similar to the GT28 journal bearing turbocharger used in the current study). With a combustor inlet pressure of about 2 bar, there was a 41.3% relative improvement in specific work with PDC operation. There was also a 28.7% relative improvement in brake specific fuel consumption (BSFC) at the same baseline operating condition. The conclusions drawn from this initial experiment demonstrated potential for improved performance; however, the rudimentary steady deflagration arrangement was not representative of a typical gas turbine engine.

Appendix E includes a parametric study of a PDC driven GT28 radial turbine using orifice plates as obstacles for deflagration-to-detonation transition (DDT). Results showed that cycle-average specific work increased with frequency, and rotor speed behavior was steadier at higher frequencies, as shown in Fig. 1 with instantaneous rotor speed normalized by maximum cycle rotor speed and time normalized by total cycle time. The orifice plates were effective for DDT; however, they also incurred significant total pressure loss.

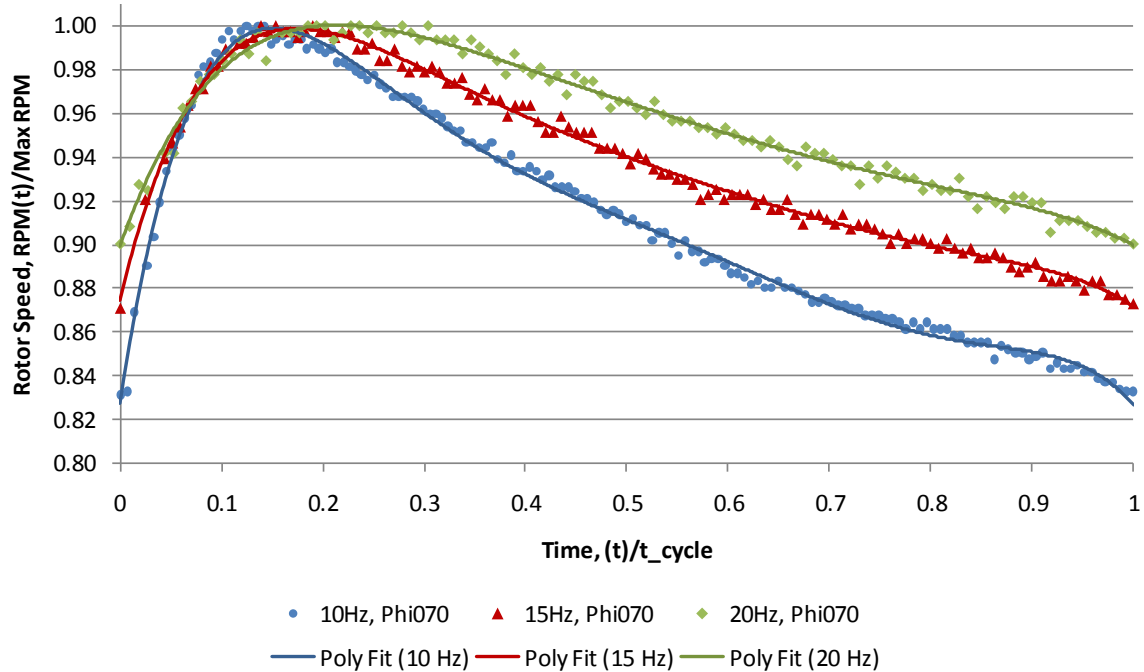


**Figure 1. Normalized rotor speed time history for stoichiometric hydrogen-fueled PDC operation at 10 Hz, 15 Hz, and 20 Hz operating frequencies**

Appendix F includes preliminary GT28 radial turbine inlet and exit flowfield measurements using high-speed cameras and silicon-carbide seed particles. Results for turbine inlet and exit flowfield properties during 6 ms of blowdown were comparable to results obtained in this current study, including peak inlet static temperature greater than 2,500 K, peak inlet static pressure about 10 bar, and peak inlet velocity about 1,000 m/s. The optical measurement technique was limited by the particle emission threshold and could not be used for full-cycle measurements; however, the technique was used in this current study to increase confidence in laser-based measurements.

Appendix G includes results from a PDC driven T3/T4E turbocharger radial turbine arrangement with a pre-detonator for detonation initiation. Results showed increased cycle-average specific work with increasing frequency, as well as with

increasing fueled fraction, as shown in Fig. 2. Performance improvements were more strongly related to frequency than fueled fraction. The pre-detonator arrangement eliminated the total pressure loss incurred by DDT obstacles; however, initiation was not consistent.

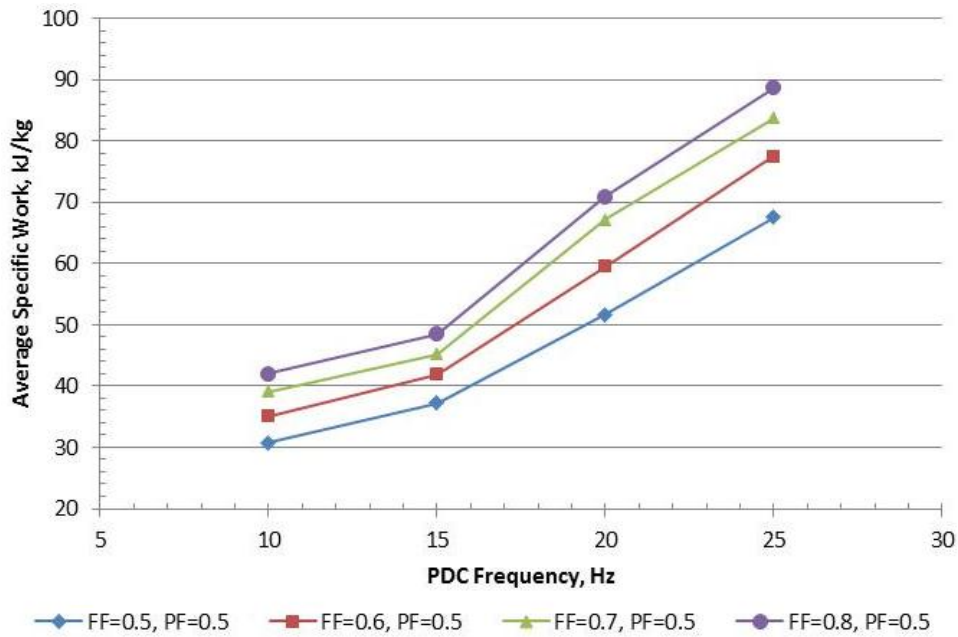


**Figure 2. Time-average specific work from 10 Hz to 25 Hz operation, fueled fractions of 0.5 to 0.8 and 0.5 purge fraction**

Appendices D, E, and G show that average specific work improved with a pulsed detonation driven radial turbine and increased with increasing frequency and fueled fraction. Average isentropic efficiency, however, must also be known to ensure that improvements in specific work were not overcome by deterioration in turbine efficiency.

### **III. Unsteady Thermodynamics and Unsteady Turbine Model**

Unsteady flows in turbomachinery have been the subject of many experimental, numerical, and analytical studies. The main motivation has been to gain understanding of unsteady flow effects on operability, durability, and performance in order to improve engine design. Glaser, et al. (2007) noted from experiments that PDC driven turbine performance was comparable to that of steady deflagration; however, the comparison was based on conventional steady formulations for specific work and turbine efficiency. Formulations for specific work and turbine efficiency are developed below, starting from conventional turbine thermodynamic analysis and accounting for unsteady effects.

#### **III.A. Unsteady Flow in Conventional Brayton Cycle Turbines**

Conventional turbine thermodynamic analysis usually involves an Eulerian approach that assumes uniform steady flow. Figure 3 illustrates the energy interactions in a typical control volume 1st Law formulation for turbine power. Steady shaft power is related to the rate change of enthalpy across the device and the rate of energy lost to heat transfer, as shown in Eq. (1). In many cases, heat transfer effects can be neglected or estimated as a second order effect and the power related directly to the net total enthalpy rate across the turbine. Steady turbine efficiency is the ratio of actual and ideal net total enthalpy rate across the turbine. Figure 4 illustrates a notional Mollier enthalpy-entropy diagram for a conventional turbine. A typical formulation for steady isentropic turbine efficiency is shown in Eq. (2), relating actual change in total specific enthalpy rate to ideal using an isentropic relationship for a calorically perfect gas.

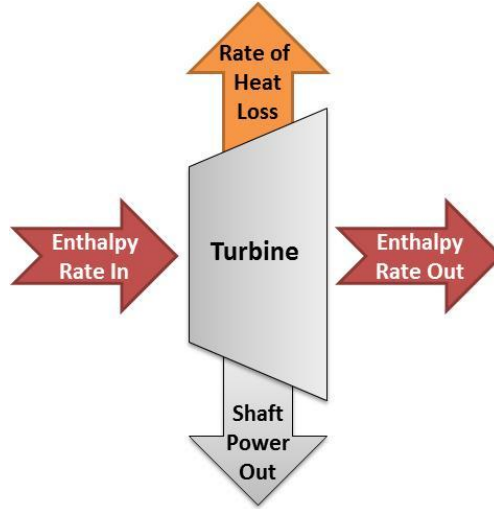


Figure 3. Schematic of 1<sup>st</sup> Law thermodynamic analysis for a steady flow turbine

$$\dot{W}_{out} = \dot{m}(h_{t,in} - h_{t,out}) - \dot{E}_{loss} \quad (1)$$

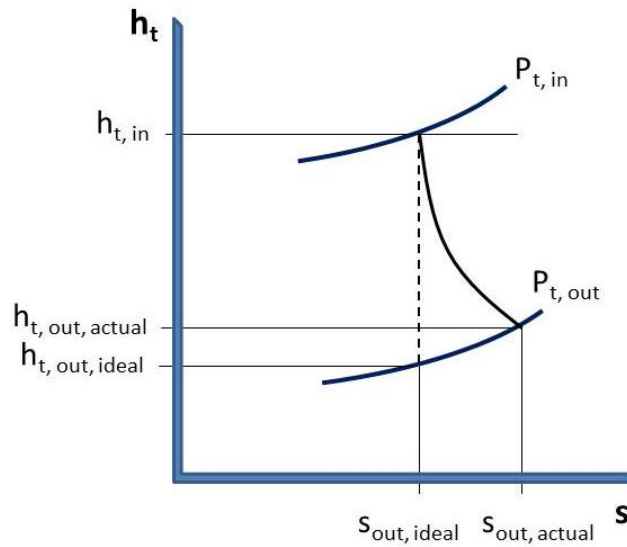


Figure 4. Notional Mollier diagram for a steady flow turbine

$$\eta_{turb,steady} = \frac{h_{t,in} - h_{t,out,actual}}{h_{t,in} - h_{t,out,ideal}} = \frac{h_{t,in} - h_{t,out,actual}}{h_{t,in} \left( 1 - \left( \frac{P_{t,out}}{P_{t,in}} \right)^{\frac{\gamma-1}{\gamma}} \right)} \quad (2)$$

Though steady formulations are typically used for conventional gas turbines, unsteady flow can be caused by potential field interactions, wake-blade interactions, rotor-stator shock interactions, blade flutter, turbulence, blade tip leakage, and vortex shedding, all of which can affect enthalpy and total pressure at the turbine inlet and exit. Oro, et al. (2009) identified various unsteady flow structures within conventional gas turbine engines, classifying the structures by length and time scales and by deterministic or stochastic behavior (i.e., forced or unforced behavior). Sieverding, et al. (2004), Sharma, et al. (1992), Greitzer, et al. (1993) and Fritsch and Giles (1992) examined various unsteady flow effects in conventional turbomachines and concluded that performance losses from secondary flow effects are small because the time scales are fast compared to the mean through-flow time and energy content is low compared to that of the mean flow.

### **III.B. Unsteady Flow in Pulsed Detonation Driven Turbines**

Steady performance formulations are not appropriate for turbines operating in unsteady flowfields with rapid, large excursions in pressure, temperature, and velocity, such as those associated with pulsed detonation combustion. A complicating feature is unsteady mass storage, and thus, specific power must be integrated over a full-cycle to obtain cycle-average specific work,  $\overline{W_{s,turb}}$ . In this study, turbine power and mass flow measurements were expected to have different characteristic response times regarding pulsed detonation inputs. Thus, the formulation for cycle-average specific work proposed here includes separate time-integrals for the numerator and denominator, seen in Eq. (3).

$$\overline{W}_{s,turb} = \frac{\int_{cycle} (\dot{m}_{in} h_{t,in} - \dot{m}_{out} h_{t,out}) dt}{m_{air,in,cycle}} = \frac{\int_{cycle} \dot{W}_{out} dt}{\int_{cycle} \dot{m}_{air,in} dt} \quad (3)$$

A formulation for unsteady isentropic turbine efficiency must include integrated properties over at least one full-cycle but better over many cycles to account for unsteady mass and energy storage effects. Figure 5 illustrates a notional Mollier diagram for a pulsed detonation driven turbine. Due to the unsteady nature of pulsed detonation operation, the thermodynamic state at the turbine inlet changes over cycle time, illustrated by a large circle. The amplitude and time scales at the turbine exit differ from that at the inlet. Preliminary results (Rouser et al., 2011a) showed that fluctuations in temperature, pressure, and velocity are attenuated at the turbine exit, and thus the time variation for actual and ideal conditions are shown as smaller circles.

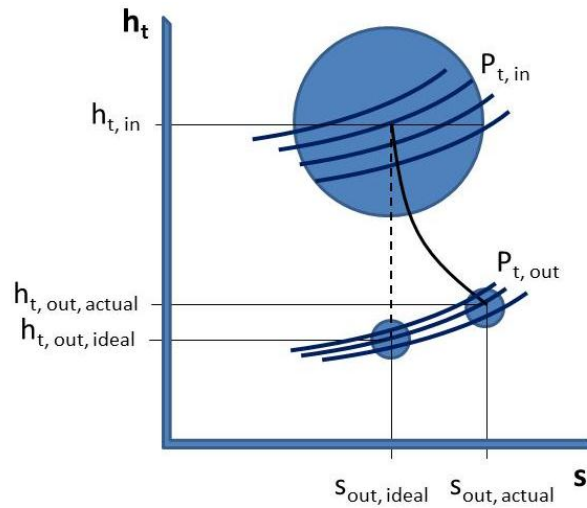


**Figure 5. Notional Mollier diagram for a pulsed detonation driven turbine**

Two general methods can be used to evaluate cycle average unsteady turbine efficiency: average instantaneous efficiency and average net efficiency. The first

method yields a time-integrated formulation of Eq. (2) and includes instantaneous inlet and exit total enthalpy rate and total pressure, as shown in Eq. (4). In a steady machine, the instantaneous isentropic relationship between the inlet and exit is unambiguous and is associated with a fixed mass travelling through the turbine. The unsteady thermodynamic model is complicated in pulsed detonation driven operation due to the time-uncoupled states of the gas at the inlet and exit, as shown by Rouser, et al. (2011a). Thus, the time-integrated instantaneous formulation was impractical for this experimental study in which pressure, temperature, and velocity measurements at the turbine inlet and exit were not correlated for each fixed mass passing the turbine.

$$\overline{\eta_{turb, instant}} \equiv \int_{cycle} \frac{\dot{H}_{t, in} - \dot{H}_{t, out, actual}}{\dot{H}_{t, in} \left( 1 - \left( \frac{P_{t, out}}{P_{t, in}} \right)^{\frac{\gamma-1}{\gamma}} \right)} dt \quad (4)$$

The second method evaluates the cycle average unsteady turbine efficiency based on the net total enthalpy entering and exiting the turbine. A general form of the proposed formulation, based on 1-D measurements of stagnation pressure and total enthalpy rate, is shown in Eq. (5). The formulation does not require total enthalpy rate at the turbine inlet and exit to be correlated to a fixed mass. Rouser, et al. (2011a) showed that the exit total pressure is nearly steady at ambient conditions. Thus, a simple and accurate procedure is to assume instantaneous-like expansion and employ the isentropic relation in the denominator of Eq. (5). In this study, the exponent of the isentropic relation is based on an average specific heat across the turbine, as a function of temperature.

$$\overline{\eta}_{turb,net} \equiv \frac{\int_{cycle} \dot{H}_{t,in} dt - \int_{cycle} \dot{H}_{t,out,actual} dt}{\int_{cycle} \dot{H}_{t,in} \left( 1 - \left( \frac{P_{t,out}}{P_{t,in}} \right)^{\frac{\gamma-1}{\gamma}} \right) dt} \quad (5)$$

$$\frac{\gamma-1}{\gamma} \equiv \frac{R}{c_{p,avg}(T)} \quad (6)$$

An averaging method, shown in Eq. (7), is applied to the collective pressure ratio term in the denominator of Eq. (5) based on an extensive weighting parameter,  $\xi$ , which is required due to the extensive property of the enthalpy rate terms of Eq. (5). Thus, the efficiency formulation shown in Eq. (8) is based on mean effective pressure. Two different weighting parameters were considered in this study to model the large rapid excursions associated with the detonation arrival at the turbine inlet: inlet total enthalpy rate and inlet mass flow rate, both of which can be used to determine the thermodynamic state on a Mollier diagram. A sensitivity study is presented in the results discussion to show the effect of weighting parameter on unsteady turbine efficiency.

$$\left( \frac{P_{t,out}}{P_{t,in}} \right)^{\frac{\gamma-1}{\gamma}} \equiv \frac{\int_{cycle} \xi \left( \frac{P_{t,out}}{P_{t,in}} \right)^{\frac{\gamma-1}{\gamma}} dt}{\int_{cycle} \xi dt} \quad (7)$$

$$\overline{\eta}_{turb,eff} \equiv \frac{\int_{cycle} \dot{H}_{t,in} dt - \int_{cycle} \dot{H}_{t,out,actual} dt}{\int_{cycle} \dot{H}_{t,in} \left( 1 - \left( \frac{P_{t,out}}{P_{t,in}} \right)^{\frac{\gamma-1}{\gamma}} \right) dt} \quad (8)$$

Suresh, et al. (2009) proposed two formulations for periodic isentropic efficiency for a turbine driven by pulsed detonations. Their first formulation was similar to Eq. (5), based on net total enthalpy entering and exiting the turbine. Shown in Eq. (9), their formulation was predicated on shaft power equal to change in total enthalpy rate across the turbine, with negligible heat transfer. Equation (9) includes temporal and spatial integration with constant specific heat, where  $T$  is PDC cycle time,  $T_t$  is stagnation temperature,  $P_t$  is stagnation pressure,  $A_i$  is turbine inlet area, and  $A_e$  is turbine exit area.

$$\overline{\eta}_{turb,net}^{Suresh} = \frac{\int_0^T \int_{A_i} (\rho \cdot u \cdot T_t) dA dt - \int_0^T \int_{A_e} (\rho \cdot u \cdot T_t) dA dt}{\int_0^T \int_{A_i} (\rho \cdot u \cdot T_t) dA dt - \int_0^T \left( \int_{A_i} \frac{(\rho \cdot u \cdot T_t)}{P_t^{\frac{\gamma-1}{\gamma}}} dA \cdot \frac{1}{|A_e|} \int_{A_e} P_t^{\frac{\gamma-1}{\gamma}} dA \right) dt} \quad (9)$$

For simplification, the formulation in Eq. (9) can be expressed in terms of inlet and exit net total enthalpy and average total pressure to show similarity with the Eq. (5) formulation proposed in this study.

$$\overline{\eta}_{turb,net}^{Suresh} = \frac{H_{t,net,in} - H_{t,net,out}}{H_{t,net,in} - \left( \left( \frac{H_{t,in}}{P_{t,in}^{\frac{\gamma-1}{\gamma}}} \right)_{net\_area} \left( P_{t,out}^{\frac{\gamma-1}{\gamma}} \right)_{area\_avg} \right)_{net\_time}} \quad (10)$$

Suresh, et al. (2009) applied Eq. (9) to a numerical study of a 2-D, translating turbine rotor cascade with inlet conditions from 1-D numerical simulations of a 30 Hz pulse detonation tube and nozzle with adiabatic walls. The simulation started from a uniform flow condition and evolved into a periodic state. Rotor blade passing frequency

was 778 blades per PDC cycle (23,575 Hz). The resulting integrated isentropic efficiency was 84%.

Suresh, et al. (2009) also proposed a work-averaged formulation, shown in Eq. (11), that yielded a 73.5% turbine efficiency under the same PDC-cascade conditions, indicating that the averaging technique has a significant effect on efficiency results. The work-averaged formulation included mass-averaged inlet and exit total specific enthalpy, work-averaged inlet and exit total pressure, and constant specific heat.

$$\overline{\eta}_{turb,work-avg}^{Suresh} = \frac{(h_{t,in})_{mass\_avg} - (h_{t,out})_{mass\_avg}}{(h_{t,in})_{mass\_avg} \left[ 1 - \frac{\left( \frac{P_{t,out}}{P_{t,in}} \right)^{\frac{\gamma-1}{\gamma}}_{work\_avg}}{\left( \frac{P_{t,in}}{P_{t,in}} \right)^{\frac{\gamma-1}{\gamma}}_{work\_avg}} \right]} \quad (11)$$

The work-averaged total pressure terms proposed by Suresh, et al. (2009) are expressed in Eq. (12) in terms of enthalpy weighted inlet total pressure and time-average exit total pressure to show similarity with the Eq. (8) formulation in this study, with inlet total enthalpy rate as the weighting parameter. The formulation proposed by Suresh, et al. (2009) differs in that exit total pressure is not enthalpy weighted.

$$\overline{\eta}_{turb,work-avg}^{Suresh} = \frac{(h_{t,in})_{mass\_avg} - (h_{t,out})_{mass\_avg}}{(h_{t,in})_{mass\_avg} \left[ 1 - \frac{\left( \frac{\dot{m} h_{t,in}}{P_{t,in}} \right)^{\frac{\gamma-1}{\gamma}}_{net\_time}}{\left( \frac{\dot{m} h_{t,in}}{P_{t,in}} \right)^{\frac{\gamma-1}{\gamma}}_{net\_time}} \left( \frac{P_{t,out}}{P_{t,in}} \right)^{\frac{\gamma-1}{\gamma}}_{time\_avg} \right]} \quad (12)$$

### **III.C. Unsteady Turbine Model with Heat Transfer**

Due to short run times, experiments in this study did not reach thermal equilibrium, thus requiring a formulation for turbine efficiency that accounts for unsteady heat transfer and storage, unlike the formulations proposed by Suresh, et al (2009). The proposed formulation is based on the model shown in Fig. 6. Turbine efficiency is obtained from the thermodynamic states at stations 2 and 3; however, flowfield temperature, pressure and velocity measurements were made at stations 1 and 4. Heat transfer and storage within the turbine and housing occurs between stations 2 and 3, shown in the Fig. 3 steady model on page 11, at a rate that is expected to decrease from the turbine inlet to the exit, with decreasing temperature potential. Heat transfer and storage across the turbine reduces enthalpy available for turbine work and must be taken into account for turbine efficiency. Station 1 enthalpy measurements overestimate actual enthalpy available for turbine work, and station 4 enthalpy measurements underestimate actual enthalpy at the turbine exit. Thus, the analysis in this study splits the amount of heat transfer across the turbine, modeling the inlet duct and housing as a heat exchanger upstream of the turbine, between stations 1 and 2, and the turbine exit duct and housing as a downstream heat exchanger, between stations 3 and 4. In the analysis, the upstream heat exchanger accounts for reduced total enthalpy available for shaft work due to heat transfer at the turbine inlet, and the downstream heat exchanger accounts for the additional drop in enthalpy by heat rejection at the turbine exit. Thus, evaluation of unsteady turbine efficiency is based on inferred thermodynamic states at stations 2 and 3.

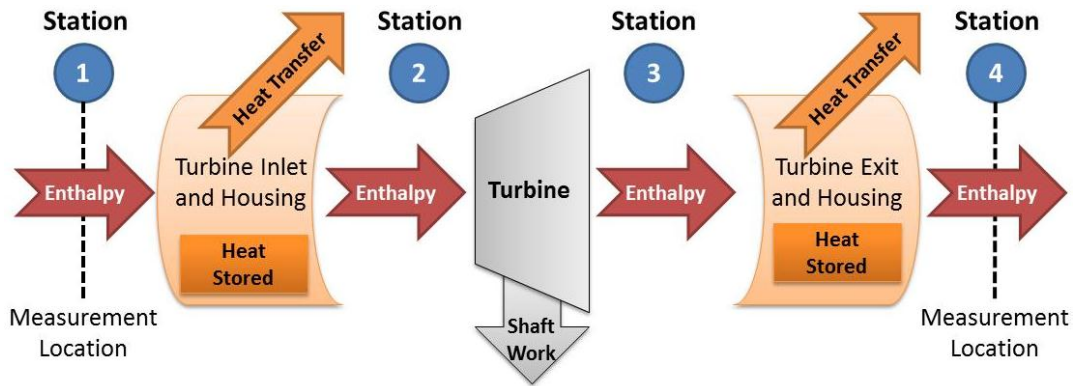


**Figure 6. Schematic of unsteady model for a pulsed detonation driven turbine**

The new model for average isentropic turbine efficiency assumes constant total pressure between stations 1 and 2 and stations 3 and 4, as indicated in the notional Mollier diagram included in Fig. 7. A Rayleigh flow analysis was conducted at the turbine inlet to validate the constant pressure heat transfer assumption, as will be shown in the results discussion.

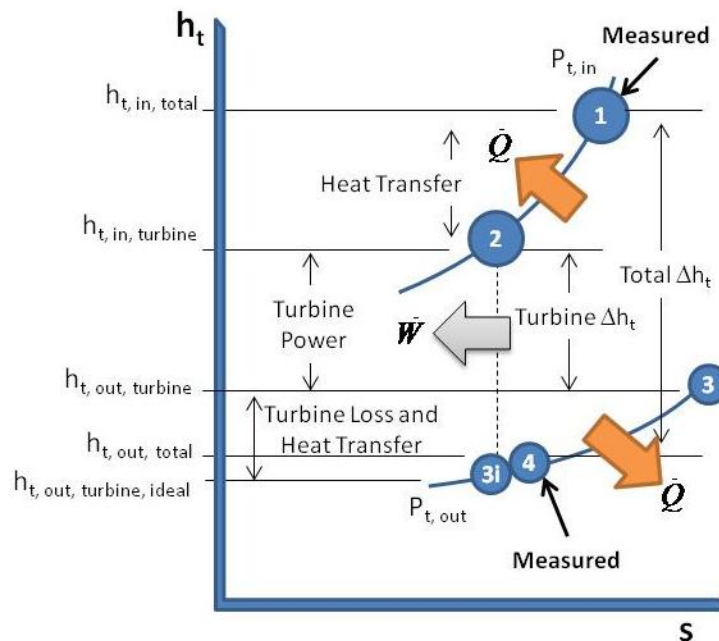


**Figure 7. Notional Mollier diagram for an pulsed detonation driven turbine with heat transfer**

Drop in total enthalpy between stations 1 and 2 in Fig. 7 is due to the fraction of heat transfer and storage in the turbine inlet duct and housing. Drop in total enthalpy between stations 2 and 3 is due to expended power. The difference in total enthalpy between stations 3 and 3i is associated with loss in turbine efficiency. Ideal enthalpy at the exit, 3i, is computed from the isentropic pressure ratio between stations 2 and 3i. Without accounting for heat transfer between stations 3 and 4, the apparent efficiency would falsely approach unity, as shown by the close proximity of stations 4 and 3i.

Turbine inlet total enthalpy rate at station 2 is obtained from measurements of shaft power output via shaft-coupled compressor power and total enthalpy rate at stations 1 and 4. The derivation for turbine inlet total enthalpy rate begins with a calculation of total heat transfer and storage rate between stations 1 and 2 and between 3 and 4, as shown in Eq. (13).

$$\dot{Q}_{total} = \dot{Q}_{1 \rightarrow 2} + \dot{Q}_{3 \rightarrow 4} = \dot{H}_{t,1} - \dot{H}_{t,4} - \dot{W}_{out} \quad (13)$$

A fraction of the total heat transfer and storage rate is attributed to the inlet, between stations 1 and 2, through the inlet heat transfer fraction parameter,  $\psi$ . A sensitivity study is shown later for the effect of  $\psi$  on unsteady turbine efficiency.

$$\dot{Q}_{1 \rightarrow 2} = (\psi) \dot{Q}_{total} \quad (14)$$

Turbine inlet total enthalpy rate at station 2 is obtained from measurement of total enthalpy rate at station 1 and the inferred heat transfer rate between stations 1 and 2.

$$\dot{H}_{t,in,turb} = \dot{H}_{t,2} = \dot{H}_{t,1} - \dot{Q}_{1 \rightarrow 2} = \dot{H}_{t,1} - (\psi) \dot{Q}_{total} \quad (15)$$

The Eq. (16) formulation is obtained by substituting Eq. (13) into Eq. (15).

$$\dot{H}_{t,in,turb} = \dot{H}_{t,1} - (\psi) (\dot{H}_{t,1} - \dot{H}_{t,4} - \dot{W}_{out}) \quad (16)$$

Turbine exit total enthalpy rate at station 3 is inferred from the remaining fraction of total heat transfer and storage rate and measurement of total enthalpy at station 4.

$$\dot{Q}_{3 \rightarrow 4} = (1 - \psi) \dot{Q}_{total} \quad (17)$$

$$\dot{H}_{t,out,turb} = \dot{H}_{t,3} = \dot{H}_{t,4} + \dot{Q}_{3 \rightarrow 4} = \dot{H}_{t,4} + (1 - \psi) \dot{Q}_{total} \quad (18)$$

The Eq. (19) formulation is obtained by substituting Eq. (13) into Eq. (18), and the Eq. (20) formulation is obtained by distributing terms.

$$\dot{H}_{t,out,turb} = \dot{H}_{t,4} + (1 - \psi) (\dot{H}_{t,1} - \dot{H}_{t,4} - \dot{W}_{out}) \quad (19)$$

$$\dot{H}_{t,out,turb} = \dot{H}_{t,1} - \dot{W}_{out} - (\psi) (\dot{H}_{t,1} - \dot{H}_{t,4} - \dot{W}_{out}) \quad (20)$$

Thus, the difference between inlet total enthalpy rate in Eq. (16) and exit total enthalpy rate in Eq. (20) is equal to turbine power output, and the integrated turbine power output over one or more full pulsed detonations is equal to the integrated power into the coupled compressor.

$$\dot{H}_{t,in,turb} - \dot{H}_{t,out,turb} = \dot{W}_{out} \quad (21)$$

$$\int_{cycle} \dot{H}_{t,in,turb} dt - \int_{cycle} \dot{H}_{t,out,turb} dt = \int_{cycle} \dot{W}_{out,turb} dt \quad (22)$$

$$\int_{cycle} \dot{W}_{out,turb} dt = \int_{cycle} \dot{W}_{in,compr} dt \quad (23)$$

Cycle integrated turbine power output is equal to compressor power input (less mechanical losses), because the two components are coupled to the same shaft. Typical turbocharger mechanical efficiency at high-power is above 95%. In this study, the efficiency was assumed to be 100%. A formulation for cycle integrated compressor power input, shown in Eq. (24), is developed from a one-dimensional, adiabatic thermodynamic analysis. The formulation assumes constant average specific heat across the compressor, which is reasonable for the temperatures in these experiments.

$$\int_{cycle} \dot{W}_{in,compr} dt = \int_{cycle} \left( \dot{m}_{compr} c_{p,avg} (T_{t,out} - T_{t,in})_{compr} \right) dt \quad (24)$$

Equation (24) assumes steady-state, uniform compressor inlet and exit temperatures; however, in this current study exit temperature measurements do not reach steady-state during short run times. Duration of combustor run times is restricted by instrumentation temperature limits. A formulation for cycle integrated compressor power is developed using isentropic relations for a calorically perfect gas and compressor efficiency. Compressor efficiency is obtained from the manufacturer compressor map (Fig. 8).

$$\int_{cycle} \dot{W}_{in,compr} dt = \int_{cycle} \left( \dot{m}_{compr} c_{p,avg} T_{t,in,compr} \left( \left( \frac{T_{t,out}}{T_{t,in}} \right)_{compr} - 1 \right) \right) dt \quad (25)$$

$$\left( \left( \frac{T_{t,out}}{T_{t,in}} \right)_{compr} - 1 \right) = \frac{1}{\eta_{compr}} \left( \left( \frac{P_{t,out}}{P_{t,in}} \right)_{compr}^{\frac{\gamma-1}{\gamma}} - 1 \right) \quad (26)$$

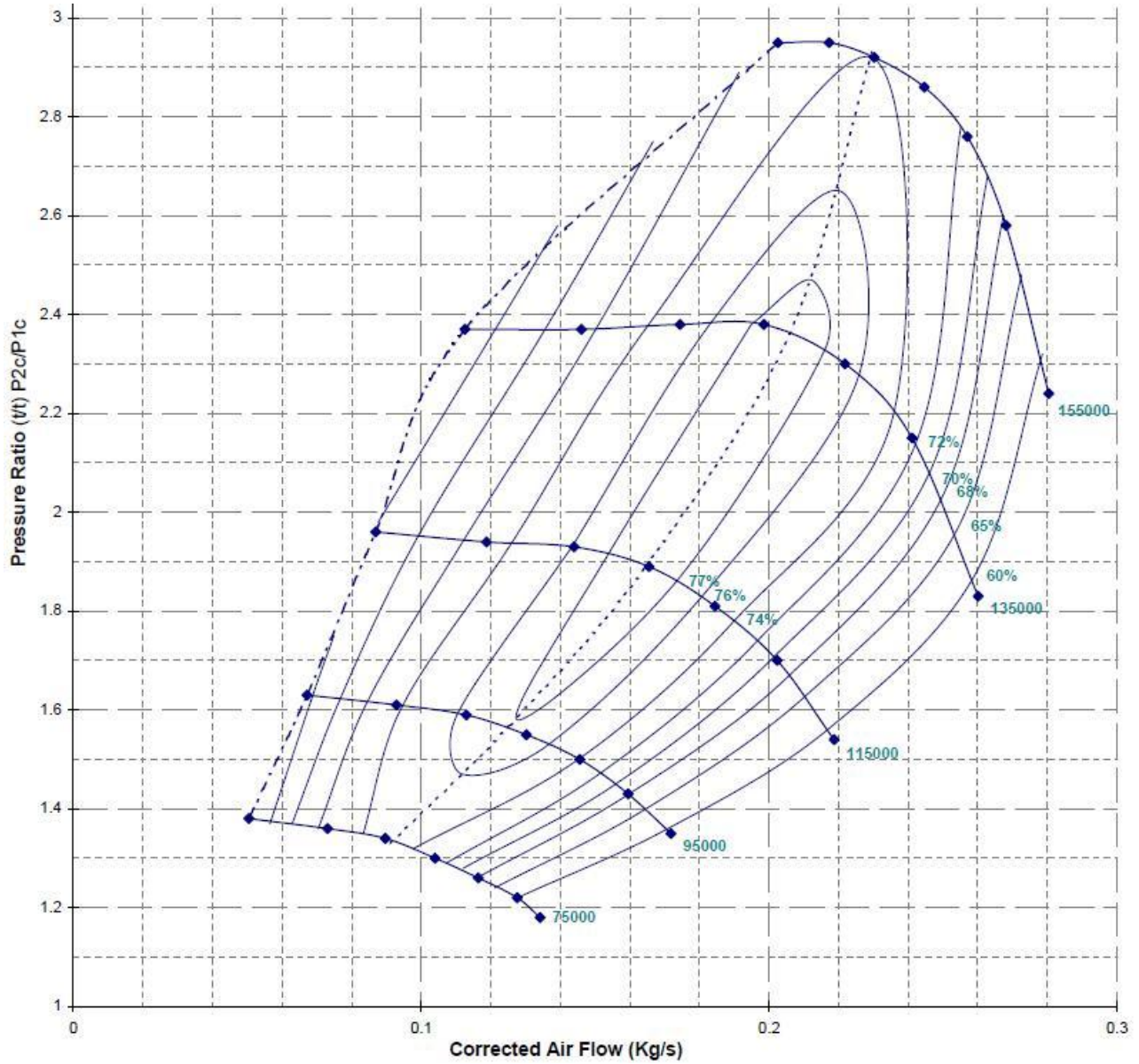


**Figure 8. Compressor operating map for Garrett GT28R automotive turbocharger (used with permission from Honeywell)**

The Eq. (27) formulation is obtained by substituting Eq. (26) into Eq. (25).

$$\int_{\text{cycle}} \dot{W}_{in,compr} dt = \int_{\text{cycle}} \left( \dot{m}_{compr} c_{p,avg} \frac{T_{t,in,compr}}{\eta_{compr}} \left( \left( \frac{P_{t,out}}{P_{t,in}} \right)_{compr}^{\frac{\gamma-1}{\gamma}} - 1 \right) \right) dt \quad (27)$$

The Eq. (28) formulation for cycle-average specific work is obtained by combining Eqs. (27) and (3) on page 13.

$$\overline{W}_{s,turb} = \frac{\int_{cycle} \dot{W}_{in,compr} dt}{\int_{cycle} \dot{m}_{air,in,turb} dt} = \frac{\int_{cycle} \frac{\dot{m}_{compr} C_{p,avg} T_{t,in,compr}}{\eta_{compr}} \left( \left( \frac{P_{t,out}}{P_{t,in}} \right)_{compr}^{\frac{\gamma-1}{\gamma}} - 1 \right) dt}{\int_{cycle} \dot{m}_{air,in,turb} dt} \quad (28)$$

Substituting Eqs. (16) and (27) into the formulation of turbine efficiency in Eq. (8) on page 15 yields a proposed formulation for cycle-average mean effective isentropic efficiency that account for heat transfer effects.

$$\overline{\eta}_{turb,eff} \equiv \frac{\int_{cycle} \dot{W}_{in,compr} dt}{\int_{cycle} \left[ \dot{H}_{t,1} - (\psi) (\dot{H}_{t,1} - \dot{H}_{t,4} - \dot{W}_{out}) \right] \left[ 1 - \left( \frac{P_{t,out}}{P_{t,in}} \right)^{\frac{\gamma-1}{\gamma}} \right] dt} \quad (29)$$

A sensitivity study is presented in the results discussion section to show the effects of three different methods for evaluating Eq. (29) over multiple cycles. In the first method, the cycle-average efficiency for each full cycle is computed, followed by an ensemble average of the cycle-averaged efficiencies. In the second method, the pressures, temperatures and velocities are ensemble-averaged before computing cycle-average efficiency. In the third method, the cycle-average efficiency is computed from ensemble-average mass flow, enthalpy and total pressure ratio terms. As will be shown, the difference in efficiency results between ensemble averaging methods is between 2.1% and 7.2%.

#### **IV. Facility and Procedures**

The following detailed description of the experimental arrangement includes the final configuration tested. Initial tests, as discussed in Appendix D, compared steady deflagration driven turbine operation to pulsed detonation turbine operation using a Garrett GT2860RS ball bearing turbocharger, spark ignition, and an internal spiral for detonation transition. During subsequent testing, the PDC-turbine experimental arrangement was refined. The ball-bearing turbocharger was supplanted by a journal bearing turbocharger to better withstand high axial thrust loads. Two other detonation initiation configurations were tested, as described in Appendices E and G: spark ignition with two orifice plate detonation transition obstacles and pre-detonator initiation with transition from a small to large diameter detonation tubes. Whereas the pre-detonator configuration offered the greatest potential for reduced total pressure loss, the spark-spiral arrangement offered the best initiation consistency, which was preferred for high-speed optical instrumentation techniques employed in this experiment. Appendix F includes initial results from optical flowfield measurements using silicon carbide seed particles; however, subsequent testing determined that a simplified approach using soot particles from ethylene-air operation provided sufficient emission for optical measurements.

To date, there have been no time-resolved experimental measurements of PDC-turbine inlet and exit flowfields from which to calibrate or confirm measurement accuracy. Therefore, different flowfield measurement techniques were utilized, as described below, to increase confidence in measurement accuracy. Comparison of results from the two techniques is discussed in the uncertainty section of the next chapter.

#### IV.A. Detonation Engine Research Facility

Experiments were carried out in the AFRL Detonation Engine Research Facility (DERF), using similar configurations as previous work by Hoke, et al. (2002) and Schauer, et al. (2003). Formerly a full-scale turbine engine test cell, the facility has been modified to enable pulsed detonation engine tests.

The facility supplies compressed air to the main fill and purge manifolds as seen in Fig. 9. Fuel is mixed at the main manifold entrance. Fill distribution and ignition takes place using an automotive engine head, shown in Fig. 10, with camshafts to operate intake and exhaust poppet valves for a desired operating frequency. The fill mixture enters the engine head from the top, and the purge air enters from the bottom. The detonation rig is capable of mounting and operating up to four detonation tubes at one time. However, in this current experiment, a single detonation tube was mounted in the first position from the left (Port #1), and the main and purge lines to the three other ports were capped during testing.

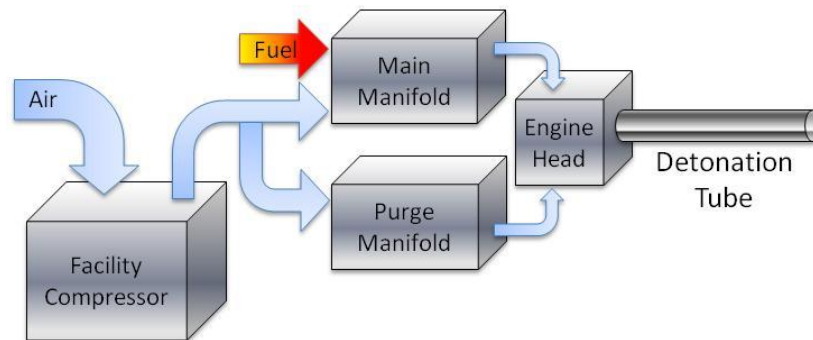


**Figure 9. Block diagram of AFRL Detonation Engine Research Facility engine test rig**

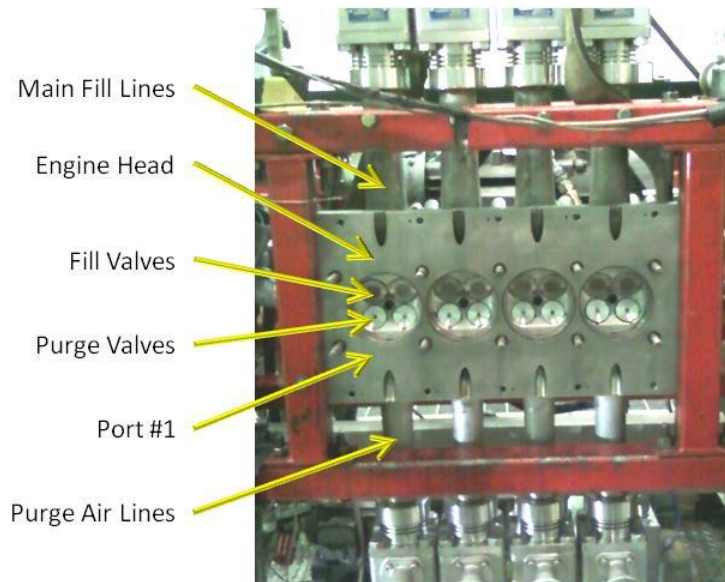


**Figure 10. Detonation engine head, fill and purge lines, and fill and purge valves**

The camshafts are driven by an electric motor and are aligned to provide approximately equal time with main valves open, all valves closed, and purge valves open (corresponding to the fill, fire and purge phases of PDC operation) in each tube. The intake valves are used for the main fill fuel-air mixture, and the exhaust valves are used to inject purge air. During the fire phase, intake and exhaust valves are closed. Ignition timing is based on the stock cam design, with a variable spark delay for optimal detonation operability.

Combustion products and purge flow expand through the turbocharger turbine, which is coupled to the detonation tube exit. Turbine exhaust passes through a 77.9 mm diameter 90 degree elbow, followed by a 77.9 mm to 52.5 mm reducer coupling, and finally through a 52.5 mm exhaust pipe. A notional temperature-entropy diagram in Fig. 11 illustrates the experimental configuration as an ideal cycle in which the turbocharger turbine does not drive the air supply compressor.



where  $P_0$  and  $T_0$  are the stagnation pressure and temperature,  $C_D$  is the nozzle discharge coefficient,  $d$  is the nozzle throat diameter,  $\gamma$  is the ratio of specific heats, and  $R$  is the gas constant.

#### ***IV.A.2. Fuel Supply***

Gaseous fuel is fed to the combustor from pressurized bottles. Fuel flow is controlled by a Tescom electromagnetic controller that actuates a pressure regulator and is metered through a calibrated converging-diverging nozzle. Gaseous fuel mass flow rate is also governed by Eq. (30). Fuel is injected into the main manifold approximately 5.9 m (19.5 ft) upstream of the poppet valves. Fuel was added to the main manifold at a rate to achieve a desired equivalence ratio ( $\phi = 1.0$  for hydrogen and 1.2 for ethylene in these experiments).

#### **IV.B. Pulsed Detonation Combustor**

The PDC assembly shown in Figs. 12 and 13 consists of schedule-40 round steel pipe with a 52.5 mm inner diameter. The detonation tube, 1092 mm in length, was coupled to the engine head and included an internal spiral-type obstacle, 457 mm in length, which extended from the engine head and assisted with deflagration to detonation transition. The turbine inlet diagnostic section, 178 mm in length, was coupled to the detonation tube exit. The diagnostic section includes non-intrusive laser instrumentation and a wall-mounted static pressure transducer, the details of which are provided later. A transition section, 178 mm in length, coupled the diagnostic section to the turbine inlet, adapting the round pipe to a rectangular T3 turbocharger inlet flange. The total combustor length was 1.4 m, and the volume was 0.003 m<sup>3</sup>.

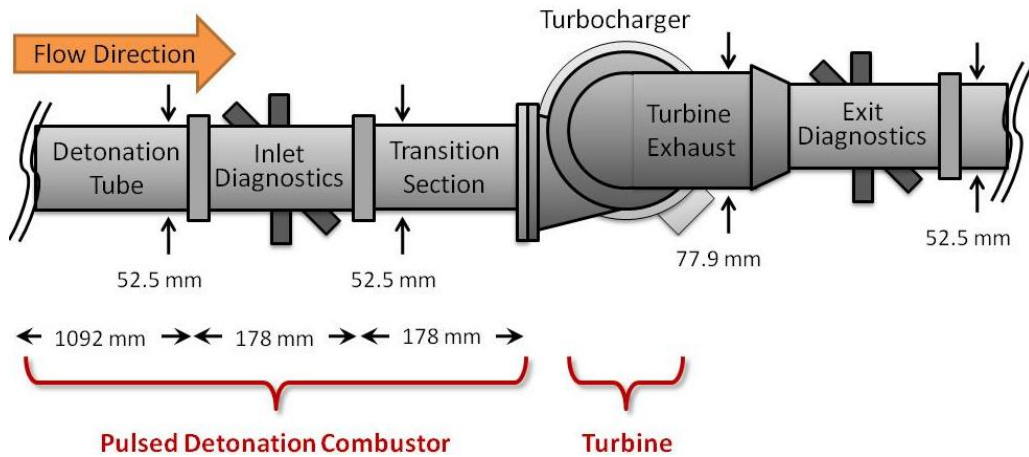


**Figure 12. Side view schematic of PDC-turbine test section arrangement**

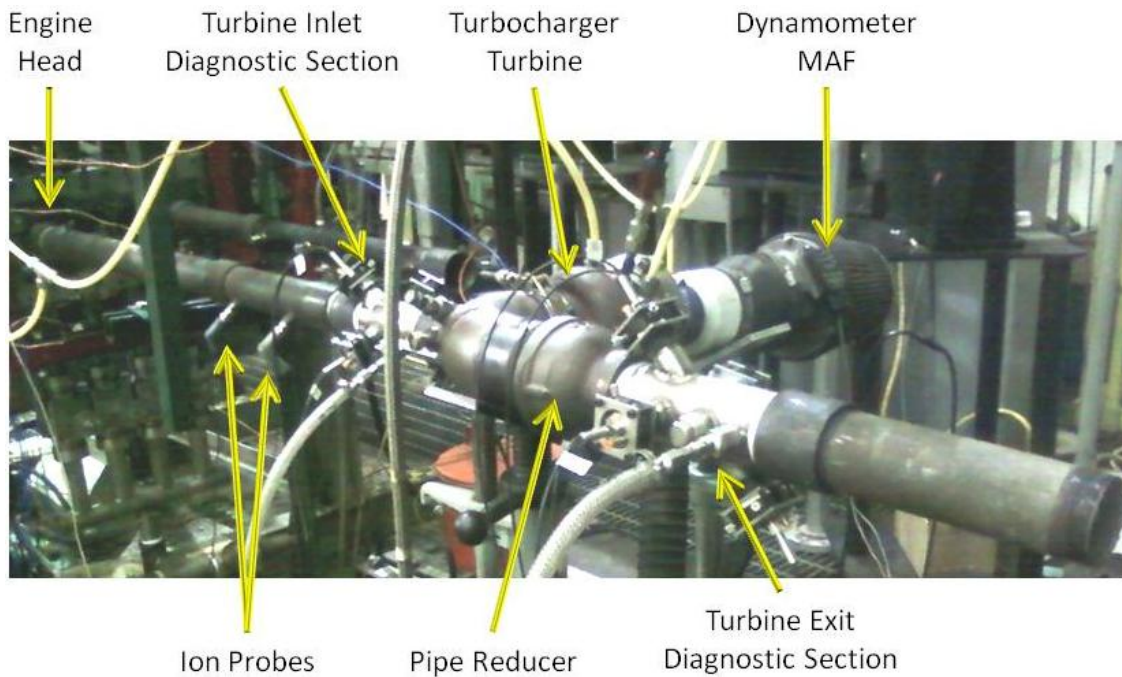


**Figure 13. PDC-turbine arrangement with inlet and exit diagnostic sections**

The turbine exit diagnostic section, 178 mm in length, with a 52.5 mm inner diameter, was coupled with a pipe reducer to the turbine exhaust elbow, which had a 77.9 mm inner diameter. Exit diagnostics were the same as that of the inlet, as will be

discussed later. A straight 52.5 mm inner diameter exhaust nozzle, 229 mm in length, was coupled downstream of the exit diagnostic section.

#### ***IV.B.1. Operating Procedure***

PDC operation was attained by first setting desired fill and purge air flows and operating frequency. Thus, the turbine was spinning before pulsed detonation operation was achieved. After fill and purge air flows were established, spark operation was started, and then fuel flow commenced in the main fill manifold and increased until a desired fuel-air ratio was attained. Typically, the desired equivalence ratio was achieved within five seconds, during which time intermittent detonations occurred. Once the start-up sequence was complete and desired operating conditions were achieved, measurements were taken and then fuel was shut-off. Most run times were less than 30 seconds and included about 500 detonation cycles.

#### ***IV.B.2. Operating Conditions***

Table 1 includes the range of operating conditions explored in this study. Total turbine airflow ranged from 2.35 kg/min to 7.45 kg/min, and frequency ranged from 10 to 30 Hz. Two key PDC operating parameters are fueled fraction (FF) and purge fraction (PF). These volumetric fractions of the detonation tube are associated with the respective phases of the PDC cycle. For a 0.75 fueled fraction, the volume of fuel-air mixture extended to a nominal location 1016 mm downstream from the engine head, just upstream of the inlet diagnostic section, shown in Fig.12. For a 0.90 fueled fraction, the volume of fuel-air mixture extended to a nominal location 1270 mm from the engine

head, just downstream of the inlet diagnostic section. Larger fueled fractions were possible; however, 0.90 was chosen to avoid over-filling and burning in the turbine.

**Table 1. Summary of PDC operating conditions**

Hydrogen ( $\phi = 1.0$ )							
Frequency (Hz)	Fueled Fraction	Purge Fraction	Main Air Flow (kg/min)	Purge Air Flow (kg/min)	Main Manifold Pressure (bar)	Purge Manifold Pressure (bar)	Total Air Flow (kg/min)
10	0.60	0.75	0.85	1.50	1.19	1.38	2.35
10	0.75	0.75	1.05	1.50	1.27	1.37	2.55
10	0.90	0.75	1.26	1.50	1.37	1.37	2.76
20	0.60	0.50	1.67	1.97	1.52	1.66	3.64
20	0.60	0.75	1.67	2.98	1.55	2.04	4.65
20	0.75	0.75	2.08	2.97	1.74	2.04	5.05
20	0.90	0.50	2.50	1.97	1.88	1.57	4.46
20	0.90	0.75	2.50	2.97	1.92	2.06	5.46
30	0.60	0.75	2.48	4.41	2.07	2.55	6.89
30	0.75	0.75	3.09	4.36	2.33	2.60	7.45

Ethylene ( $\phi = 1.2$ )							
Frequency (Hz)	Fueled Fraction	Purge Fraction	Main Air Flow (kg/min)	Purge Air Flow (kg/min)	Main Manifold Pressure (bar)	Purge Manifold Pressure (bar)	Total Air Flow (kg/min)
20	0.90	0.50	2.89	1.75	1.94	1.57	4.64

$$FF = \frac{(\dot{V}_{air} + \dot{V}_{fuel}) \cdot t_{fill}}{V_{tube}} \quad PF = \frac{(\dot{V}_{air}) \cdot t_{purge}}{V_{tube}} \quad (31)$$

Volumetric flow rate is governed by manifold pressure and mass flow rate.

Volumetric flow rate was controlled by adjusting tube volume, frequency and fueled and purge fractions input into the PDC controls. The tube volume was set to 0.00287 m<sup>3</sup> for the hydrogen runs and 0.00254 m<sup>3</sup> for the ethylene runs. The difference in tube volume settings between hydrogen and ethylene runs accounts for the different stoichiometric fuel-air ratio and fuel density of the two fuels. Total air mass flow rates for hydrogen and

ethylene runs were within 5% of each other at 20 Hz with 0.90 fueled and 0.5 purge fractions. Ambient tube volume was the same for hydrogen and ethylene runs; however, back-pressure from the turbine affected the volumetric flow rate. The tube volume input to the PDC controls was adjusted to ensure accurate fueled and purge fractions, as described in the next section.

### ***IV.B.3. Instrumentation***

Fuel flow rates and main and purge air flow rates, as well as main and purge manifold pressures and temperatures were recorded at 1 Hz. J-type thermocouples were mounted to the exterior wall of the PDC tube at locations 558 mm and 1422 mm downstream of the engine head (see Fig. 14). Tube wall temperatures were equal to test cell ambient temperature at the start of each run, and maximum wall temperature was limited to 500 K to avoid overheating instrumentation.

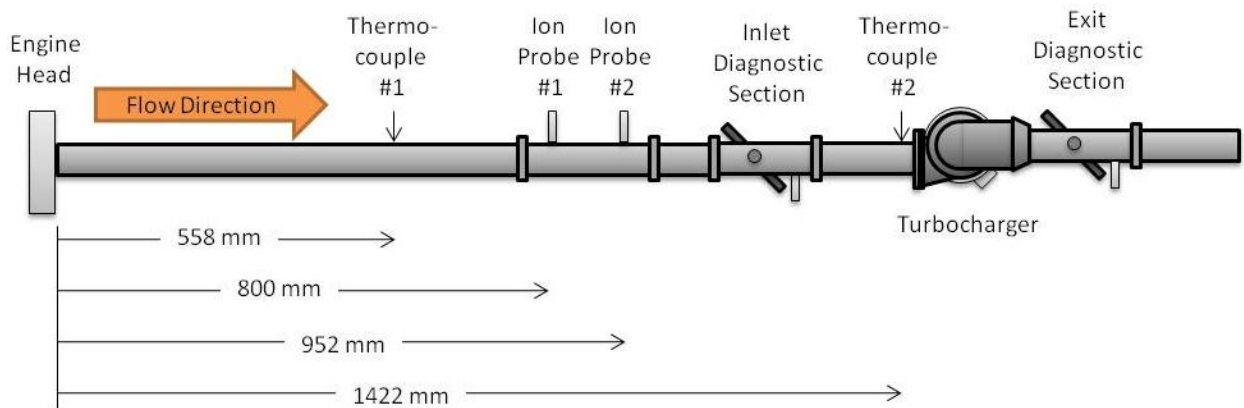


**Figure 14. Locations of PDC thermocouples and ion probes**

Ion probes were installed along the length detonation tube, as shown in Fig. 13, at 800 mm and 952 mm from the engine head (see Fig. 14). The probes are automotive

spark plugs that short circuit in the presence of ionized gas associated with a detonation front, indicating the detonation arrival time. Flame speeds were determined from the transit time between probes, confirming that detonations were achieved with observed Chapman-Jouguet (C-J) velocities (approximately 1800 m/s for ethylene-air).

Ion probes were also used to confirm fueled fraction. When the main fill volumetric flow rate was set too low, a detonation was not detected by the ion probe at the location associated with corresponding fueled fraction. Volumetric flow rate was adjusted until the fueled fraction was confirmed. The volumetric flow rate adjustment was made by changing the apparent tube volume input to the PDC controls, affecting the manifold pressure and density. The presence of a turbine downstream of the PDC generated back-pressure, requiring a higher volumetric flow rate than without the turbine. Therefore, the apparent tube volume with the coupled turbine was larger than the calculated ambient tube volume without the turbine.

#### **IV.C. Radial Turbine**

The nine-blade, radial turbine used in this study is part of a Garrett GT28R journal bearing automotive turbocharger, pictured in Fig. 15. According to the manufacturer, the rotating assembly has a moment of inertia of  $3.2\text{E-}5 \text{ kg m}^2$  and a maximum conventional steady turbine efficiency of 61%. The manufacturer's steady turbine operating map is included in Fig. 16 and is addressed later in the results discussion with regard to operating points in this current study. Turbine efficiency plateaus above a pressure ratio of 2.0 on the steady operating map, indicating choked flow under normal automotive conditions.

The turbine wastegate, shown in Fig. 15, was capped so that all combustor exhaust passed through the turbine.

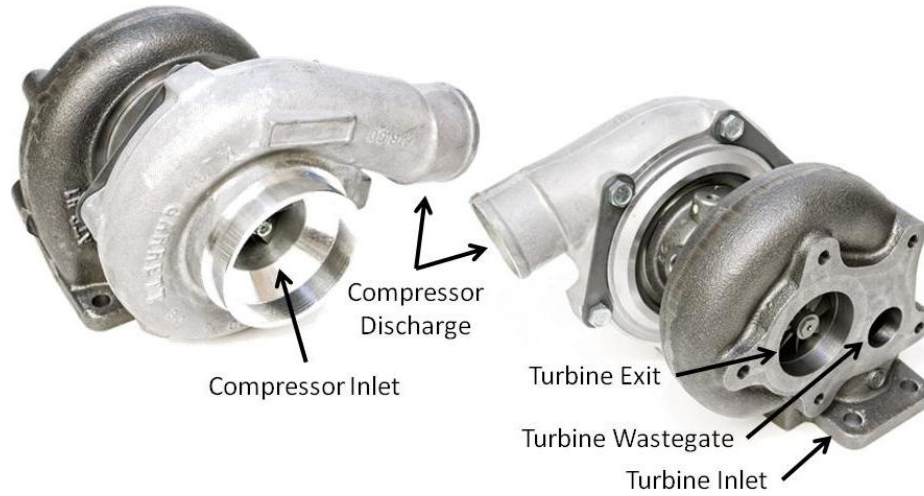


**Figure 15. Garrett GT28R journal bearing turbocharger (used with permission from Advanced Tuning Products, Inc.)**

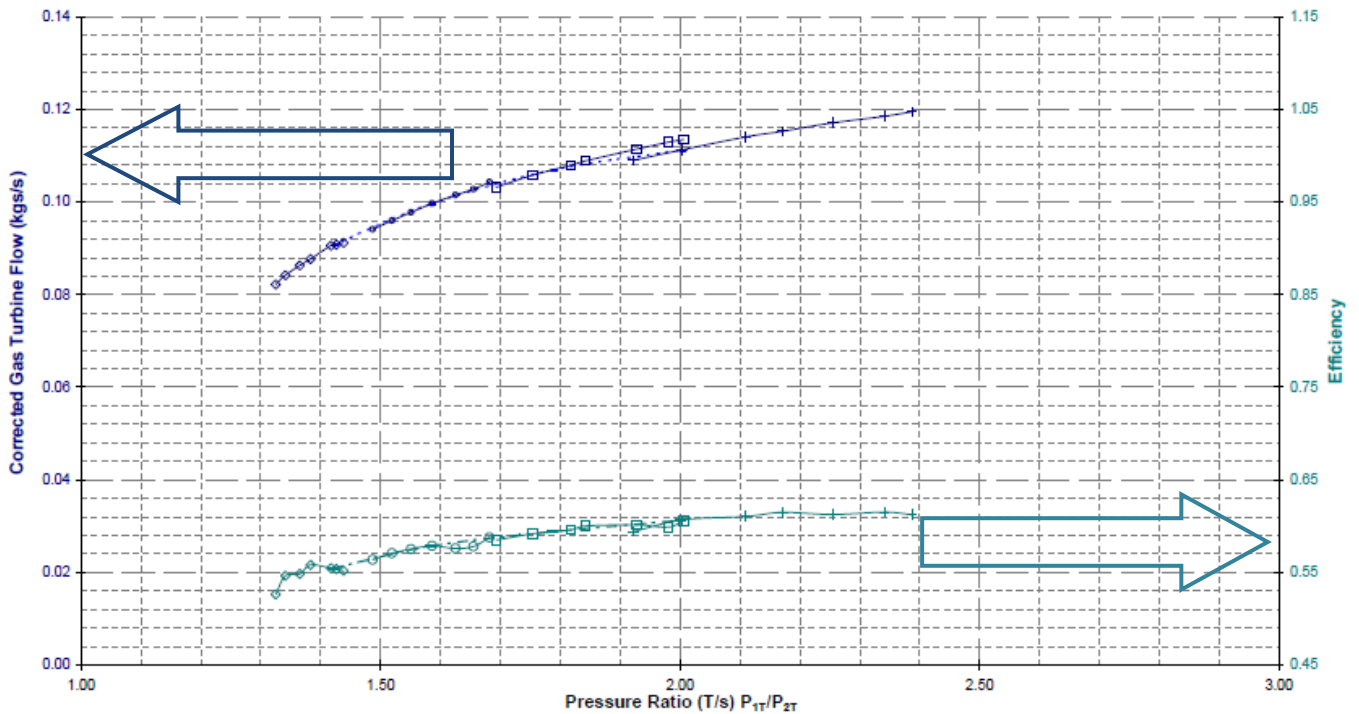


**Figure 16. Turbine operating map for Garrett GT28 journal bearing turbocharger (used with permission from Honeywell)**

The GT28R is equipped with a radial compressor having 12 blades, 6 primary impeller blades and 6 splitter blades. The compressor was used as a dynamometer to measure shaft power output from the turbine, as described later. J-type thermocouples were attached to the exterior of the turbine and compressor housings. Temperature measurements of center housing inlet and exit cooling water were also taken. Cooling water flow rate was set at 5.7 liters per minute. Housing and cooling water temperatures were sampled at 1 Hz. Figure 17 includes a time history of turbine housing and inlet wall temperatures with 10 and 20 Hz hydrogen-fueled PDC with 0.75 fueled and purge fractions, indicating significant heat storage between the inlet measurement location and turbine, as discussed later in the data analysis and uncertainty section.

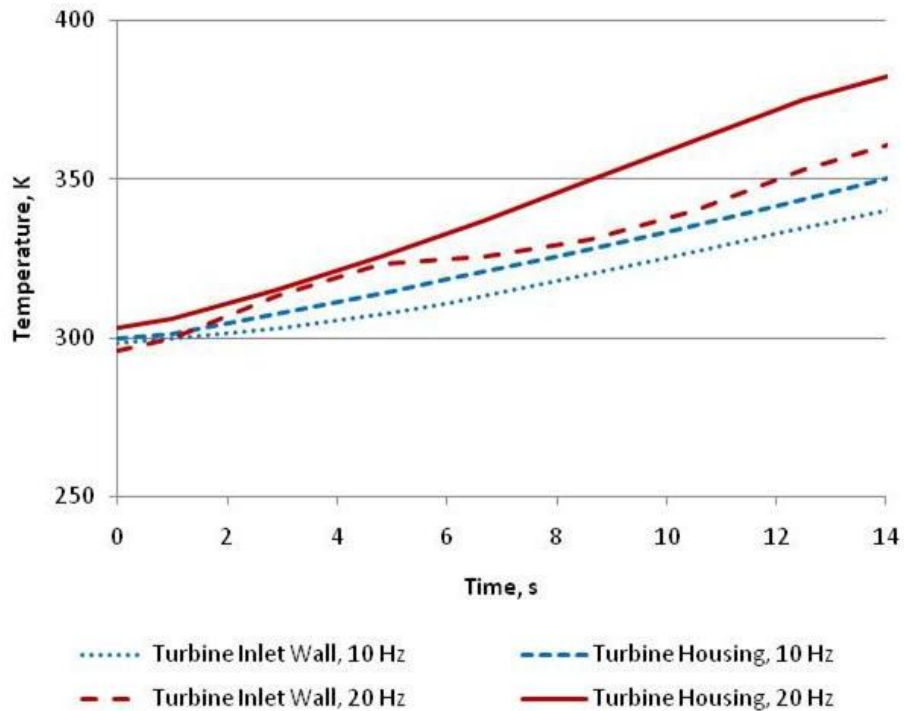


**Figure 17. Turbine housing and inlet wall temperatures with 10 and 20 Hz hydrogen-fueled PDC with 0.75 fueled and purge fractions**

#### IV.D. Turbine Inlet and Exit Flowfield Instrumentation

Turbine inlet and exit flowfield diagnostics included multiple techniques, including laser absorption spectroscopy for inlet and exit static temperature and velocity, optical pyrometry for inlet static temperature, particle streak velocimetry (PSV) for inlet velocity, and inlet and exit wall-mounted static pressure transducers. Two different configurations were used. One configuration employed laser absorption spectroscopy with the static pressure transducers, as shown in Figs. 12 and 13 on page 30, and the other, described below, employed pyrometry and PSV with the transducers. Each configuration sampled data simultaneously, and results from the two configurations allowed for measurement comparison at the same operating conditions. A summary of the flowfield techniques and configurations is included in Tables 2 and 3.

**Table 2. Summary of laser absorption configuration**

<i>Instrumentation Configuration #1</i>			
<b>Flowfield Property</b>	<b>Instrumentation</b>	<b>Location</b>	<b>Sampling Frequency</b>
$T_{in}$	laser absorption spectroscopy	267 mm upstream of turbine inlet flange	50 kHz
$T_{out}$	laser absorption spectroscopy	584 mm downstream of turbine exit flange	50 kHz
$P_{in}$	50 bar static pressure transducer (Kulite)	217 mm upstream of turbine inlet flange	1 MHz
$P_{out}$	50 bar static pressure transducer (Kulite)	634 mm downstream of turbine exit flange	1 MHz
$V_{in}$	laser absorption Doppler shift	267 mm upstream of turbine inlet flange	50 kHz
$V_{out}$	laser absorption Doppler shift	584 mm downstream of turbine exit flange	50 kHz

**Table 3. Summary of pyrometry and PSV configuration**

<i>Instrumentation Configuration #2</i>			
<b>Flowfield Property</b>	<b>Instrumentation</b>	<b>Location</b>	<b>Sampling Frequency</b>
$T_{in}$	two-band optical pyrometry	343 mm upstream of turbine inlet flange	10 kHz
$P_{in}$	50 bar static pressure transducer (Kulite)	343 mm upstream of turbine inlet flange	1 MHz
$P_{out}$	50 bar static pressure transducer (Kulite)	584 mm downstream of turbine exit flange	1 MHz
$v_{in}$	particle streak velocimetry	343 mm upstream of turbine inlet flange	10 kHz

***IV.D.1. Laser Absorption Spectroscopy***

Tunable diode-laser absorption spectroscopy (TDLAS) was employed for flowfield measurements at the turbine inlet and exit diagnostic sections. TDLAS is a well-established method for rapid gas measurements in practical environments. Mattison, et al. (2003) used TDLAS to characterize pulsed detonation engine water temperatures and concentration. Lyle, et al. (2007) used Doppler frequency shift between the absorption features to determine velocity of the flow. In this current study, a single beam was used to determine water temperature, pressure, and molarity from absorption spectroscopy, scanning three wavelength windows centered at 1340 nm, 1358 nm, and 1365 nm every 0.02 ms, as shown in the top view of Fig. 18. Gas velocity was determined from Doppler shift in the water absorption features, using two counter-propagating beams, as shown in the side view of Fig. 18. Temperature and velocity measurements were taken simultaneously and at the same location in the flowfield at 50 kHz, averaged over the beam path. Turbine inlet and exit laser absorption measurements were also simultaneous.

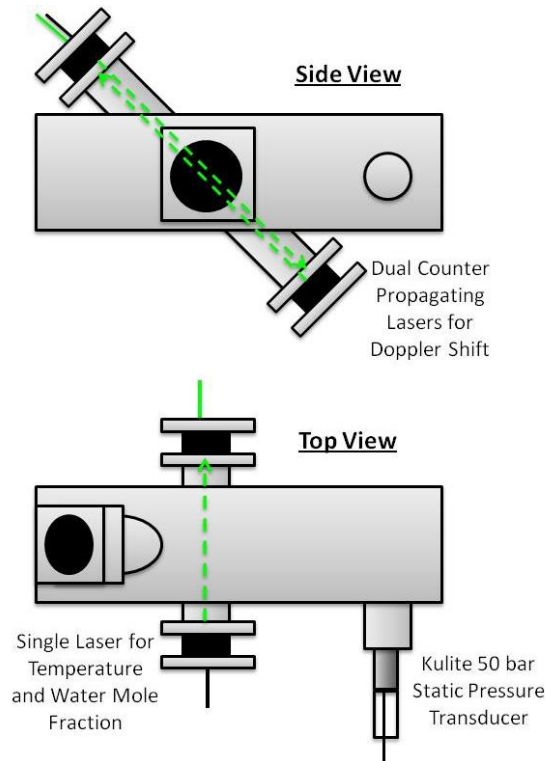


**Figure 18. Top and side view schematics of laser absorption instrumentation**

#### *IV.D.2. Static Pressure Transducers*

An arrangement of 50 bar Kulite static pressure transducers at the turbine inlet and exit, as shown in Fig. 18, were mounted to the tube wall with a 3.2 mm diameter stand-off tube, 76 mm in length, to prevent overheating. The stand-off distance reduced the natural frequency response of the transducer from 750 kHz to an estimated 300 kHz. Pressure measurements from laser absorption were used to synchronize the transducer pressures with the TDLAS temperatures and velocities by aligning the timing of the pressure rise associated with the arrival of the detonation wave. Turbine inlet and exit static pressure transducers were sampled simultaneously at 1 MHz, along with ion probe and dynamometer measurements.

#### IV.D.3. Two-Band Optical Pyrometry

Optical pyrometry instrumentation was used as an alternative method to compare with laser absorption results for turbine inlet static temperature using ethylene soot particles in the optically thin flowfield. A detailed description of the technique is included in Appendix E. The same PDC arrangement was used as with the laser measurements; however, a square pipe section with a 50.8 mm by 50.8 mm cross section, a 457 mm length, and two side-mounted quartz windows was added upstream of the turbocharger in place of the laser diagnostic section, mounted to the detonation tube with a flange as shown in Fig. 19. The measurement location area increased from  $0.00216 \text{ m}^2$  to  $0.00258 \text{ m}^2$ , and the total PDC tube volume increased by 6%; however, the total length remained the same as with the laser diagnostics configuration.

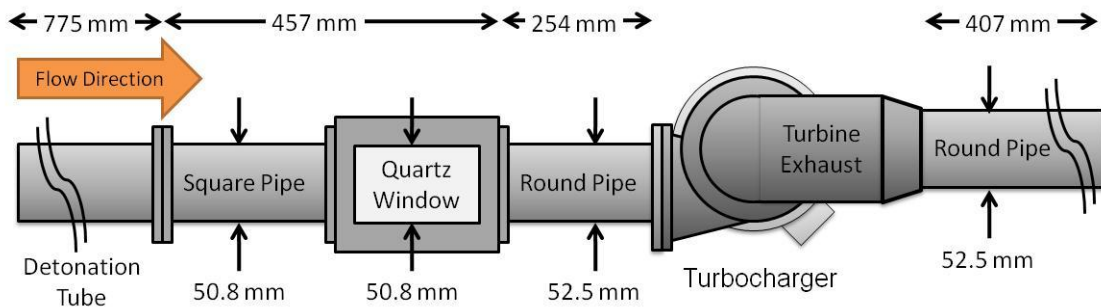


**Figure 19. Side view schematic of optical access arrangement for pyrometry and velocimetry measurements**

A PCO Dimax high-speed color camera with 110.4 micron per pixel was used to detect emission from soot particles to determine static temperature. The emission threshold was 1300 K, below which particle emission was insufficient to detect. Thus, pyrometry temperatures were not available during fill and purge phases. Sampling frequency was determined by frame rate, which was set to 10 kHz to achieve sufficient

time resolution of the fastest transient events in the pulsed detonation flow. The camera was set to a 15  $\mu\text{s}$  exposure, having a 1.5 m focal distance with a 180 mm lens, as shown in Appendix E. Measurements with a tungsten lamp and spectrometer allowed spectral responsivity of the camera red, green and blue channels to be measured. Substituting spectral responses and integrating them with a blackbody function over appropriate wavelengths (350 nm to 750 nm) allowed the ratio to be determined as a function of temperature. Figure 20 shows a single pyrometry frame for a detonation passing into the turbine inlet. Streamwise centerline temperature is plotted alongside the pyrometry frame. Temperature of unburned fuel-air was assumed to be that of the main manifold.

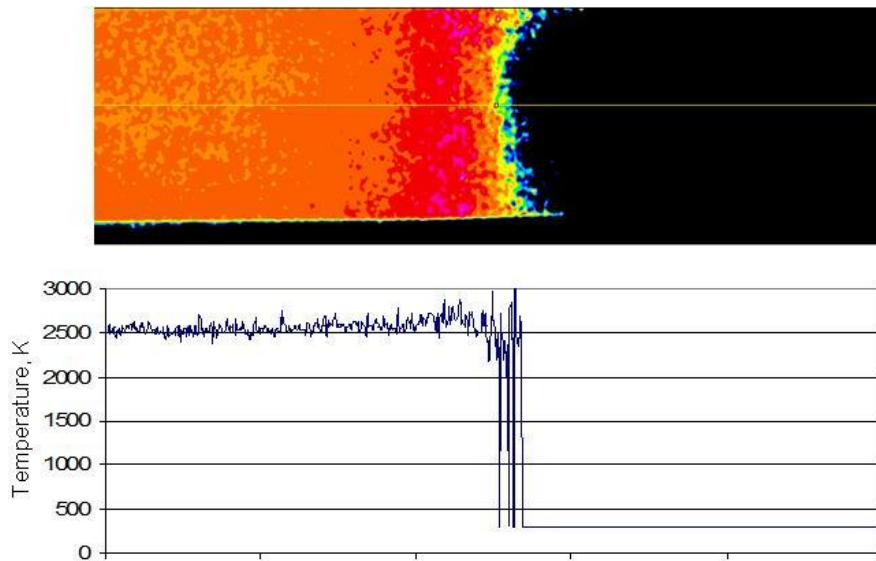


**Figure 20. Single pyrometry frame of a detonation travelling from left to right at the turbine inlet, such that black represents unburned fuel-air**

#### *IV.D.4. Particle Streak Velocimetry*

The ethylene soot particles were also used for particle streak velocimetry (PSV) measurements at the turbine inlet. A detailed description of the technique is included in

Appendix E. Time history of soot particle streaks was traced from frame to frame. The turbine inlet velocity field was determined by dividing the length of particle streaks by the exposure time. To increase the contrast between the soot streaks and the surrounding gas emission, an edge enhancing convolution was applied to images before analysis. Figure 21 shows a single frame of PSV before and after post-processing. During blowdown, the flowfield has a non-axial velocity component due to transverse waves associated with the cellular structure of a confined detonation, as discussed further in Appendix B.

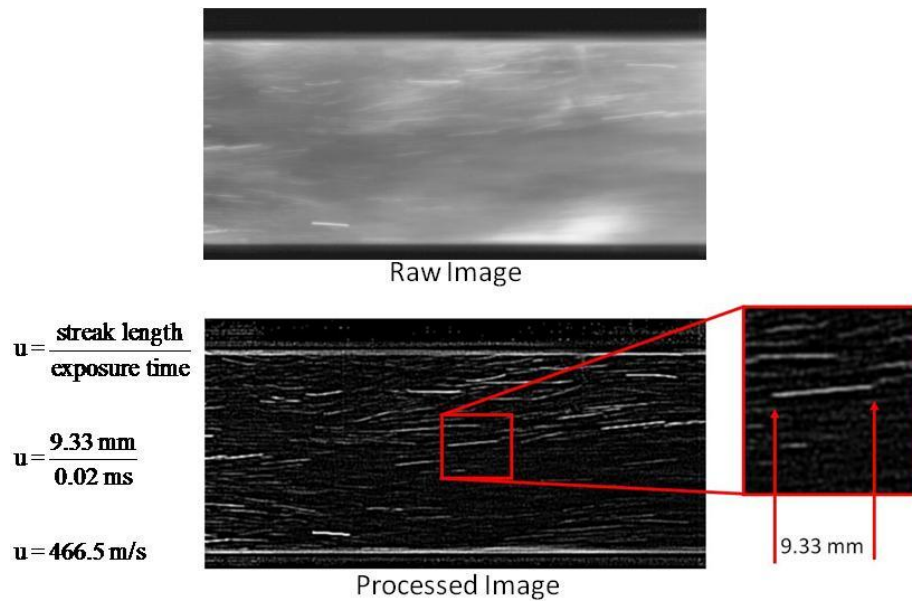


**Figure 21. Single particle streak velocimetry image during blowdown at the turbine inlet**

#### IV.E. Power Instrumentation

The turbocharger compressor was used as a dynamometer to measure turbine power. A mass air flow (MAF) sensor (Professional Flow Technologies Model 92 Special) was mounted to the compressor inlet, as shown in Fig. 22, receiving ambient air. The compressor discharge was instrumented with a wall-mounted Sensotec 3.44 bar static

pressure transducer located 1170 mm downstream of the compressor exit along a 52.5 mm diameter pipe (not shown). A J-type thermocouple was located 152.4 mm downstream of the pressure transducer. A ball valve, located 609 mm downstream of the thermocouple, was used to back-pressure the compressor. The ball valve was set so that the compressor operated toward the center of its operating map. Several different compressor operating conditions were achieved by adjusting the PDC operating frequency and fueled fraction and leaving the ball valve fixed.

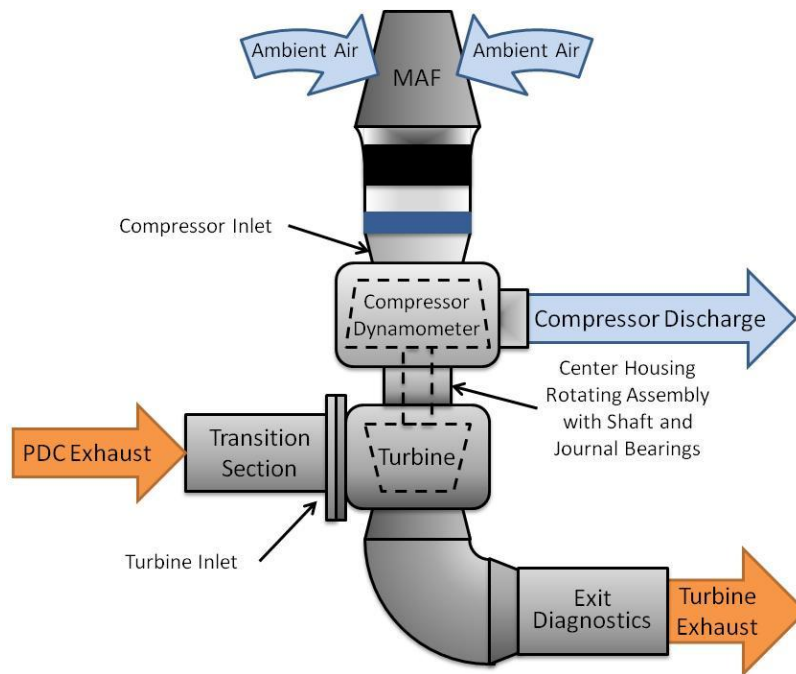


**Figure 22. Top view schematic of test section**

#### IV.F. Rotor Speed Instrumentation

A Garrett speed sensor (part number #781328-0002) was positioned in the compressor housing, as shown in Fig. 23, to detect blades arrival. The sensor emits a magnetic field that is interrupted by passing blades. Rotor speed is determined from the blade passing frequency. The input frequency is one pulse per blade. The internal sensor electronics

divide the input signal by eight (set by the manufacturer), so that the output frequency is a square-wave signal at  $1/8^{\text{th}}$  the actual blade passing frequency. The output frequency is multiplied by eight during post-processing to obtain in the input frequency. The turbocharger compressor has 12 blades; therefore, the rotor speed is equal to  $1/12^{\text{th}}$  the sensor input frequency.

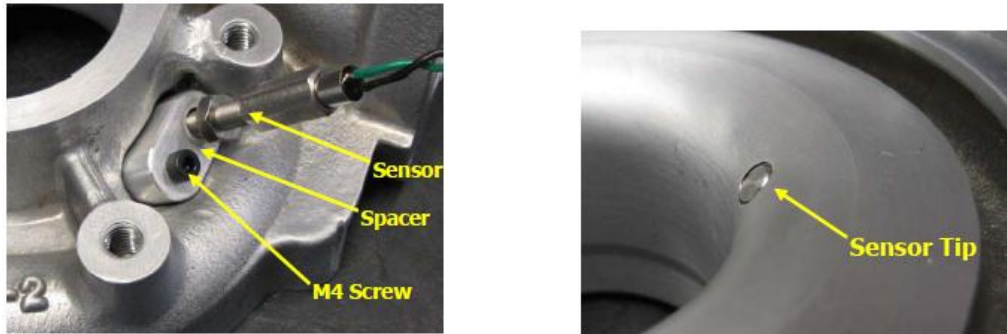


**Figure 23. Garrett speed sensor arrangement (used with permission from Advanced Tuning Products, Inc.)**

## V. Data Reduction and Uncertainty Analysis

There were several data acquisition (DAQ) systems employed in this research, as shown in Fig. 24. The facility system, illustrated in Fig. 25, used to record PDC manifold gage pressures, static temperatures and mass flows, acquired data continuously and simultaneously at 1 Hz, using a *LabVIEW* program. This facility system was also used to record turbocharger housing temperatures and cooling water inlet and exit temperatures, as well as ambient test cell conditions.

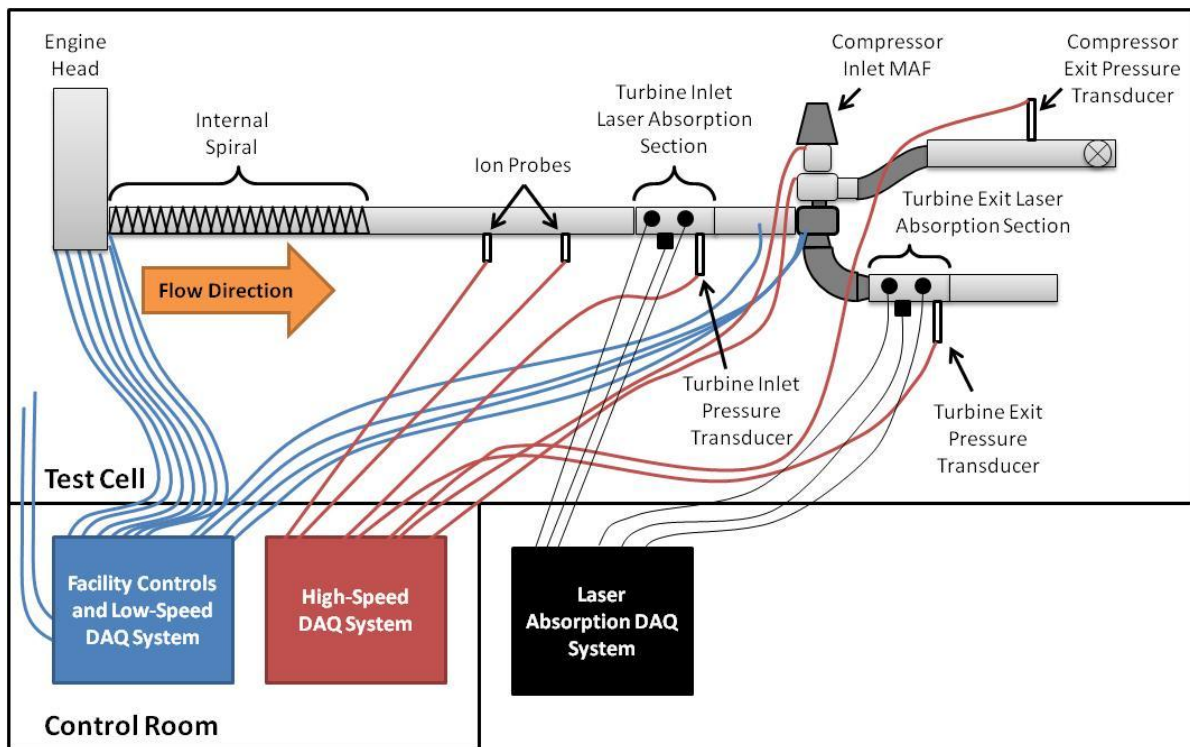
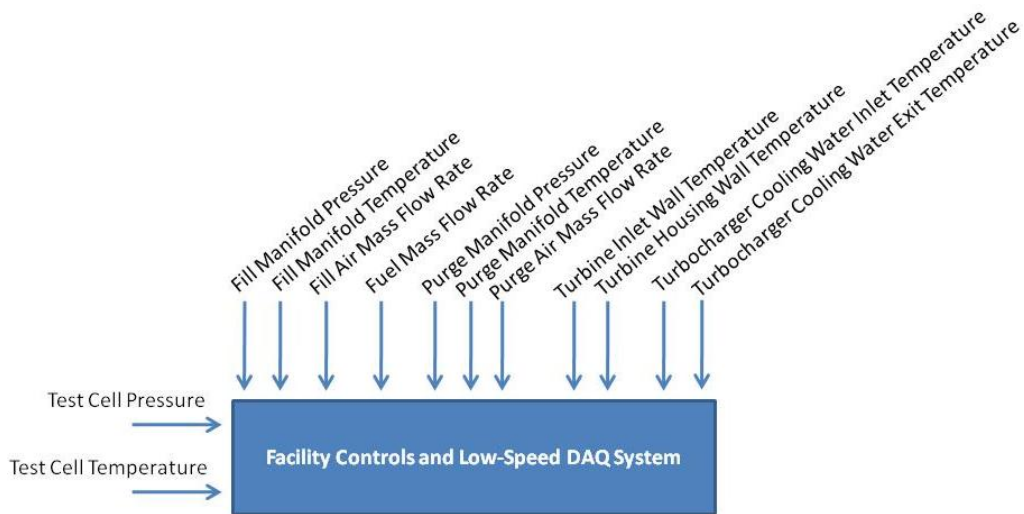
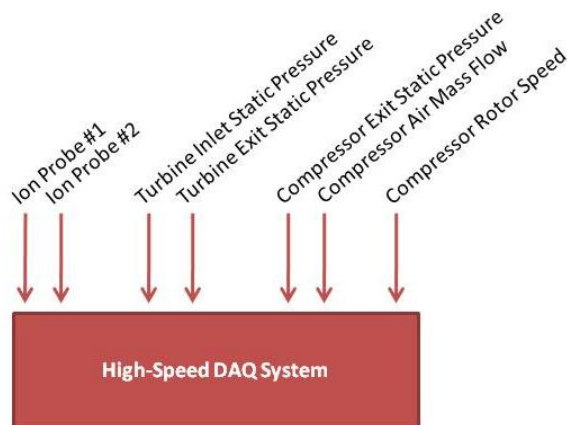


Figure 24. Schematic of data acquisition systems



**Figure 25. Schematic of facility data acquisition system**

A high-speed DAQ system, illustrated in Fig. 26, recorded signals from the turbocharger turbine inlet and exit wall-mounted pressure transducers, compressor inlet MAF and compressor exit wall-mounted pressure transducer, and speed sensor, as well as spark ignition and ion probe signals. The high-speed DAQ system is capable of sampling up to 12 channels simultaneously, using a *LabVIEW* program. The sampling rate used in these experiments was set to 1 MHz with a duration of 0.5 seconds.



**Figure 26. Schematic of high-speed data acquisition system**

Laser absorption signals at the turbine inlet and exit flowfields were recorded simultaneously with a dedicated DAQ system, illustrated in Fig. 27, with a sampling rate of 50 kHz. Laser absorption was synchronized with high-speed DAQ turbine inlet and exit wall-mounted static pressures based on the initial rapid rise associated with the detonation arrival at the turbine inlet. High-speed camera instrumentation for pyrometry and PSV were recorded simultaneously at the turbine inlet at 10 kHz on a separate DAQ system associated with the respective camera.

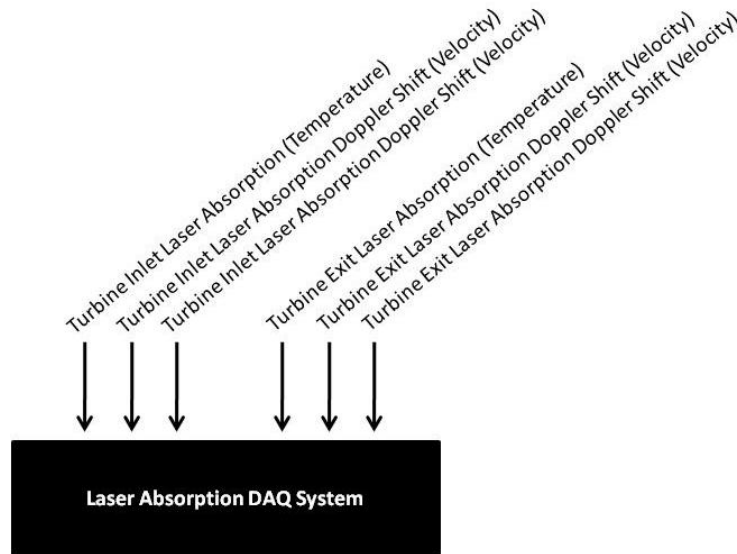


**Figure 27. Schematic of laser absorption data acquisition system**

Data sampled from the high-speed DAQ at 1 MHz was imported into a *LabVIEW* program called *PT Reader*, converted from binary to text format, and parceled by detonation cycle time. During the parcelling process, turbine inlet and exit pressures were reduced to 10 kHz to be consistent with the sampling rate of the optical measurements for pyrometry and PSV. Similar methods were used to convert the laser absorption and high-

speed camera temperatures and velocities into text format so that all turbine inlet and exit flowfields could be assessed at 10 kHz using a simple spreadsheet program.

The following discussion regarding data reduction and uncertainty analysis addresses the properties necessary to determine turbine performance in terms of power, specific work, and turbine isentropic turbine efficiency. Rotor speed is included in the results section; however, it was not used to measure turbine performance. All data reduction was accomplished using *Microsoft Excel* spreadsheet software.

#### **V.A. Turbine Inlet and Exit Flowfields**

Simultaneous temperatures, velocities, and pressures from laser absorption and static pressure transducers at the turbine inlet and exit flowfields were imported in to *Excel* for each detonation cycle. Time-resolved values for total temperature, total pressure, mass flow rate and total enthalpy rate were calculated for each cycle, treating air as an ideal gas and assuming 1-D point properties were representative of the flow field. Values for  $\gamma$  and  $c_p$  were obtained for air as a function of temperature, and cross sectional area was based on the inner diameter of the pipe used in the diagnostic section. Velocities at the inlet were known to have an offset error due to a signal conditioning issue in the TDLAS instrumentation; however, the issue was isolated to the inlet. The magnitude of the offset was determined by matching inlet to exit mass flows and iterating to the applied offset to preserve continuity.

$$T_t(t) = T(t) + \frac{v(t)^2}{2 \cdot c_p} \quad (32)$$

$$P_i(t) = P(t) \left( \frac{T_i(t)}{T(t)} \right)^{\frac{\gamma}{\gamma-1}} \quad (33)$$

$$\dot{m}(t) = \frac{P(t)}{R \cdot T(t)} \cdot A \cdot v(t) \quad (34)$$

$$\dot{H}_i(t) = \dot{m}(t) \cdot c_p \cdot T_i(t) \quad (35)$$

### ***V.A.1. Ensemble Averaging***

Ensemble averages of the raw static temperature, static pressure, and velocity were used to produce time-resolved plots. Peak total enthalpy for each cycle was aligned in time before ensemble averaging. Ensemble-averaged total enthalpy was used to produce time-resolved plots and to calculate cycle-average turbine isentropic efficiency, as described below. The number of cycles included in each ensemble was dependent on the PDC operating frequency due to fixed sampling frequency (1 MHz) and duration (0.5 seconds).

### ***V.A.2. Uncertainty***

There are currently no published time-resolved inlet and exit flowfield properties for a full-admission detonation driven radial turbine that could be used for validation. Therefore, the bias error cannot be quantified for PDC conditions, though the measurement methods are well-established. Cycle-to-cycle variation was characterized using standard deviations from the operating condition at 30 Hz PDC with 0.75 fueled and purge fractions. This condition was chosen due to the largest number of cycles from which a statistical analysis could be performed. Percent standard deviation was

calculated at each point in time over ensemble cycles, and average values are included in Table 4. Variation is larger at the inlet than at the exit, and the biggest contribution is from velocity. Variation in velocity propagates into total temperature and pressure, mass flow, and ultimately into total enthalpy.

**Table 4. Average percent standard deviation of turbine inlet and exit ensemble data**

Property	Average Percent Standard Deviation	
	Inlet	Exit
Static Temperature	9.4%	4.7%
Static Pressure	3.8%	2.7%
Velocity	23.3%	16.6%
Total Enthalpy	9.9%	10.0%

Optical pyrometry and PSV temperatures and velocities were recorded to qualitatively evaluate the uncertainty of the laser absorption method at the 20 Hz operating PDC condition with 0.90 fueled fraction and 0.5 purge fraction, using ethylene fuel. Figure 28 shows good agreement in the inlet static pressures for the two separate runs, demonstrating good test repeatability. The stand-off distance for the wall-mounted transducer was about 38 mm greater in the optical experiment, which limited response time, limiting the pressure slope and peak and obtaining less resolution of the secondary wave-form structures. Peak C-J pressure associated with ethylene-air under this operating condition is expected to be about 20 bar; however, the increase is nearly instantaneous with C-J velocity of about 1800 m/s, and neither experiment captured the expected C-J peak pressure. The plateau condition behind the detonation was expected to have a pressure of between five and six bar, based on ethylene-air detonation properties, and the plateau duration was expected to be between one to two milliseconds, based on shock

travel time through the turbine and exhaust nozzle. The pressure measurements from the laser absorption test case captured the plateau condition, and pressure measurements from both tests captured the remaining expansion portion of the cycle with reasonable agreement in terms of profile and magnitude. Therefore, the operating conditions are assumed to be similar for the two tests for the following comparison of inlet temperature and velocity using the two measurement techniques: optical pyrometry/PSV and laser absorption.

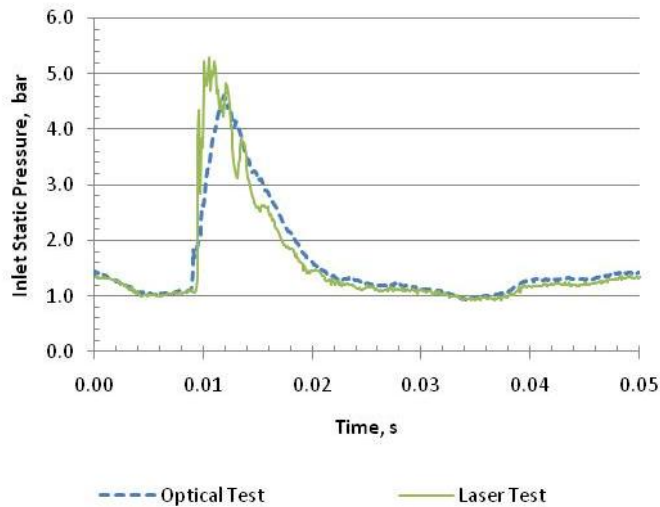


**Figure 28. Comparison of inlet static pressure results for optical pyrometry and laser absorption experiments with 20 Hz ethylene-fueled PDC with 0.9 fueled fraction and 0.5 purge fraction. Transducer stand-off distance was 38 mm greater in the optical experiment.**

Figure 29 shows a comparison of turbine inlet static temperature results from laser absorption and optical pyrometry measurements during 6 ms of blowdown. Peak temperatures, which are associated with detonation arrival, differ by 278 K, and the average difference over the 6 ms duration is 334 K. The expected C-J temperature for ethylene-air at this condition is about 2900 K at detonation, and the expected plateau

condition is expected to be about 2500 K. The peak and plateau temperatures obtained from laser absorption spectroscopy are within 15% of the expected detonation properties. The duration of the plateau condition was about 1.4 ms and occurred between 0.2 ms and 1.6 ms. The measurement differences between 0 and 4.5 ms can be attributed mostly to the estimated emissivity of the ethylene soot particles for pyrometry during the moment associated with the largest excursions in temperature and pressure. Between 4.5 ms and 5.5 ms, the two measurement methods are in reasonable agreement.

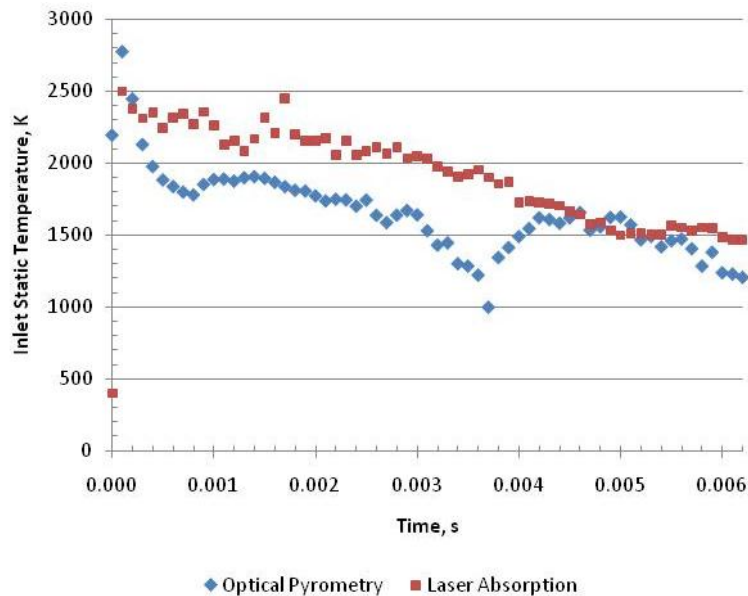


**Figure 29. Comparison of inlet static temperature results from optical pyrometry and laser absorption during 6 ms of blowdown with ethylene-fueled PDC at 20 Hz with 0.9 fueled fraction and 0.5 purge fraction**

Figure 30 shows a comparison of turbine inlet velocity results from laser absorption Doppler shift and PSV measurements during 6 ms of blowdown. The trace from laser measurements was not able to resolve the flow between 0 and 0.4 ms most likely due to beam-steering associated with diffraction through the detonation shock wave

and trailing Taylor wave. The trace from PSV measurements was intermittent after 4 ms due to reduced particle emission. Peak velocities differ by 465 m/s; however, the remaining portion of the blowdown, after the first 0.4 ms, is in good agreement. The C-J speed of sound for ethylene-air at this condition is 1000 m/s detonation, which is expected to occur immediately behind the detonation wave. Whereas the peak velocity from PSV is within 4% of the C-J speed of sound, the peak velocity obtained from laser absorption Doppler shift is 50% of the expected detonation property.

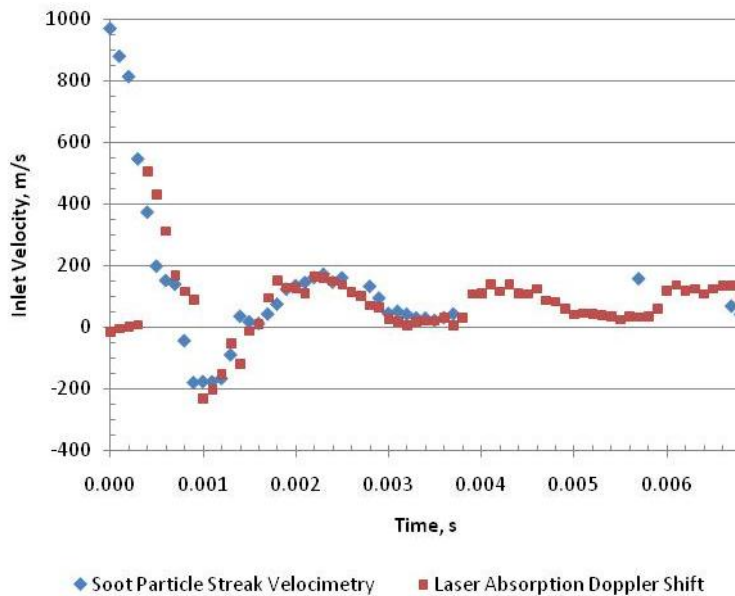


**Figure 30. Comparison of inlet velocity results from soot particle velocimetry and laser absorption Doppler shift during 6 ms of blowdown with ethylene-fueled PDC at 20 Hz with 0.9 fueled fraction and 0.5 purge fraction**

Table 5 includes a summary of the aggregate cycle mass flow uncertainty analysis based on calibrated facility converging-diverging metering nozzles and average mass flow rates. Aggregate mass was calculated using Eq. (36). Error ranges from as low as 5% to 52%, with an average error of 12%. Mass flow rates obtained from laser absorption

experiments were not used to calculate cycle-average specific work, which was computed using the average mass flow rate from the calibrated facility converging-diverging metering nozzles. However, instantaneous mass flow rate was used to calculate instantaneous total enthalpy rate, shown in Eq. (35) on page 49, which was necessary to compute turbine efficiency.

**Table 5. Summary of mass flow uncertainty analysis**

PDC Operating Condition				Aggregate Cycle Mass Flow (kg)		Difference in Aggregate Cycle Mass
Fuel	Frequency	Fueled Fraction	Purge Fraction	Calibrated Facility Nozzle	Turbine Diagnostics	
Hydrogen	10	0.60	0.75	0.00392	0.00438	12%
	10	0.75	0.75	0.00425	0.00536	26%
	10	0.90	0.75	0.00460	0.00701	52%
	20	0.60	0.50	0.00303	0.00393	30%
	20	0.60	0.75	0.00388	0.00422	9%
	20	0.75	0.75	0.00421	0.00458	9%
	20	0.90	0.50	0.00372	0.00249	-33%
	20	0.90	0.75	0.00455	0.00604	33%
	30	0.60	0.75	0.00383	0.00362	-5%
	30	0.75	0.75	0.00414	0.00539	30%
Ethylene	20	0.90	0.50	0.00386	0.00262	-32%

$$m_{agg}(t + \Delta t) = m_{agg}(t) + \frac{\dot{m}(t) + \dot{m}(t + \Delta t)}{2} \Delta t \quad (36)$$

Uncertainty in average total enthalpy rate was estimated by conducting a conservation of energy analysis, accounting for the rate of energy transfer and storage into and out of the PDC-turbine system between inlet and exit measurement locations, as shown in Fig. 31. The cycle average change in total enthalpy rate between inlet and exit measurement locations is equal to average power output, average change in enthalpy rate of the oil and cooling water, and the average rate at which energy is stored in the PDC exit and turbine housing.

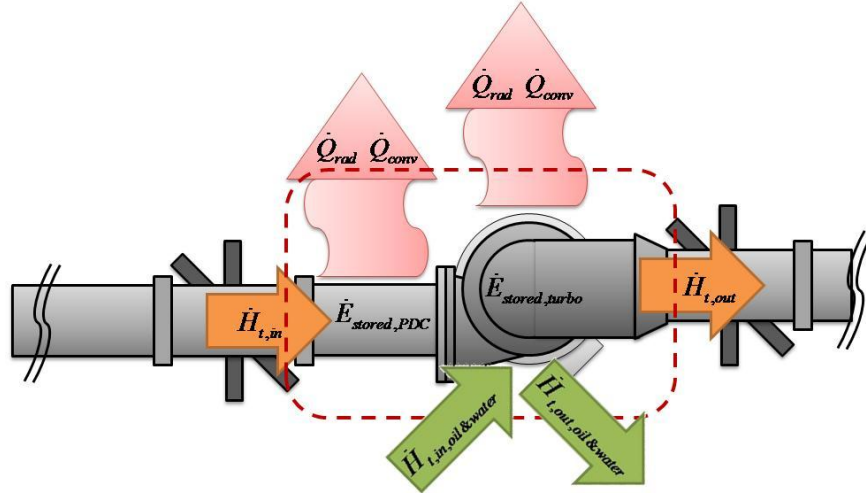


**Figure 31. Schematic of energy conservation analysis for PDC-turbine arrangement**

$$\overline{\dot{H}}_{t,in} = \overline{\dot{H}}_{t,out} + \overline{\dot{W}}_{t,out} + \overline{\dot{Q}}_{out,PDC\&Turbo} + \overline{\dot{E}}_{stored,PDC\&Turbo} \quad (37)$$

The conservation of energy analysis used start-up temperatures acquired from the PDC wall, turbine housing, and cooling water flow. Temperatures for the oil flow were not measured and were assumed to be approximately equal to water flow temperatures. The turbine housing was modeled as a sphere for radiation and free convection estimates. Details of the analysis are included in Appendix G. Table 6 includes a summary of the 1<sup>st</sup> Law analysis for the operating condition with a hydrogen-fueled PDC at 30 Hz with 0.75 fueled and purge fractions, which has an agreement of 1% between estimated and measured change in total enthalpy rate, 24.23 kW and 24.51 kW, respectively. The average heat transfer and storage rate was greater than the cycle-average power from the compressor dynamometer, thus emphasizing the need to account for unsteady heat transfer effects in the turbine efficiency formulation.

**Table 6. Energy conservation analysis with 30 Hz hydrogen-fueled PDC with 0.75 fueled and purge fractions**

Average Energy Storage Rate in PDC Exit Pipe	2.29 kW
Average Heat Transfer Rate from PDC Exit Pipe	0.08 kW
Average Energy Storage Rate in Turbine Housing	9.94 kW
Average Heat Transfer Rate from Turbine Housing	0.12 kW
Average Heat Transfer Rate into Cooling Water	0.83 kW
Average Heat Transfer Rate into Turbocharger Oil	0.25 kW
AVERAGE HEAT TRANSFER & ENERGY STORAGE RATE:	13.51 kW
AVERAGE DYNAMOMETER POWER:	10.72 kW
	24.23 kW
AVERAGE CHANGE IN TOTAL ENTHALPY RATE:	24.51 kW
DIFFERENCE:	1.13%

**V.B. Turbine Power**

Compressor dynamometer power was reduced separately from turbine inlet and exit flowfield properties. Compressor mass flow rates and exit wall-mount static pressures were analyzed at 1 MHz, calculating time-resolved power for 5 cycles using Eq. (27) on page 23 and using test cell static temperature and pressure from the facility DAQ. It was assumed that the test cell ambient conditions were equal to the compressor dynamometer inlet conditions. It was verified that the inlet static temperature and pressure were steady just downstream of the MAF and approximately equal to the test cell ambient conditions.

***V.B.1. Ensemble Averaging***

A cycle-based ensemble average of the power was used to produce smooth time-resolved plots of turbine power. A linear average of the ensemble-averaged power was used in addition to the average total facility mass flow rate from the facility DAQ to calculate the average specific turbine work, as shown in Eq. (28) on page 24. Figure 32

shows time-resolved power for 5 successive detonation cycles at 30 Hz with 0.75 fueled and purge fractions. The profiles and magnitudes are very similar, indicating good repeatability. Figure 33 shows ensemble average power for the same 5 cycles.

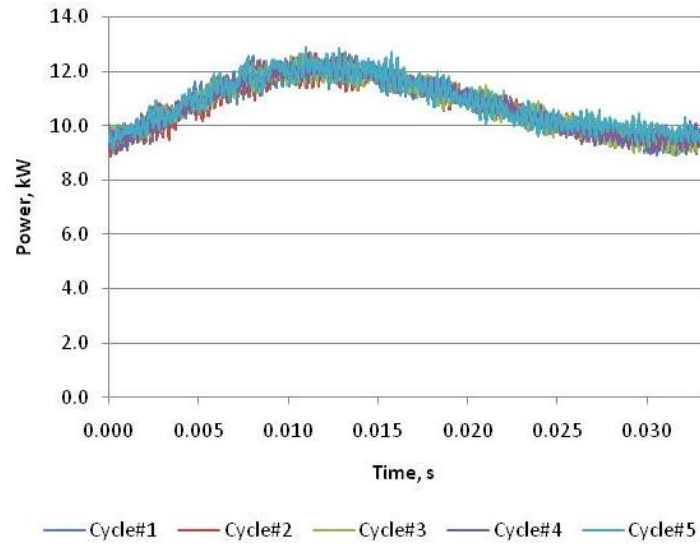


**Figure 32. Time-resolved power over 5 cycles at 30 Hz with 0.75 fueled and purge fractions**

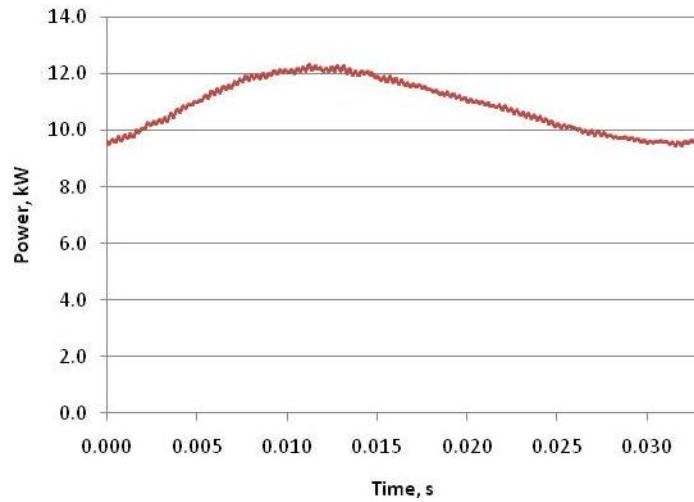


**Figure 33. Ensemble-average power over 5 cycles at 30 Hz with 0.75 fueled and purge fractions**

### ***V.B.2. Uncertainty***

Calibration information was not available for the compressor dynamometer operating in this test configuration; however, cycle-to-cycle variation was estimated using ensemble power from the operating condition at 30 Hz with 0.75 fueled and purge fractions. This condition was chosen due to the largest number of cycles from which a statistical analysis could be performed. Percent standard deviations were calculated at each moment in time across ensemble cycles and the average value was 2.3%, including cycle-to-cycle variability and measurement scatter.

### **V.C. Sources of Error**

A sensitivity study in the results section shows the impact of the measurement error on turbine efficiency. Most of the measurement error was associated with inlet pressure and velocity during the first 0.5 ms after detonation arrival, due to clipped transducer response and beam-steering associated with the laser Doppler measurements. Otherwise, measurements were reasonably close to expected values associated with known fuel-air detonation properties. Cycle-to-cycle variation in temperature, pressure, and velocity measurements, as noted above, also contributed to error in turbine efficiency.

Aside from measurement error, other sources of uncertainty are associated with assumptions in the development of formulations for specific work and turbine efficiency. First, the 1-D analysis assumes that the measured point properties are representative of the 2-D flowfield. The 2-D turbine inlet flowfield is known to be non-uniform, as shown in preliminary experiments detailed in Appendix E. Furthermore, the scroll-type inlet volute associated with the radial turbine “smears” the flow as incoming mass enters the

turbine passages at different moments in time along the length of the volute. The flow at the turbine exit is expected to be mixed, and the 1-D analysis is reasonable. The 1-D assumption was used to evaluate turbine efficiency, as will be discussed in more detail in the next section. The 1-D assumption was also applied to the compressor dynamometer exit, and thus was applied to the evaluation of specific work. The flow at the compressor exit is expected to be mixed, and the 1-D assumption is reasonable.

A linear average was assumed for the ratio of specific heats across the turbine, as well as across the compressor. This assumption is reasonable for the compressor dynamometer, where there was a small change in temperature from the inlet to the exit. Specific heat was calculated as a function of temperature, and it was assumed that the working fluid for both the compressor and turbine was air. A sensitivity study in the results section shows the impact of the specific heat on turbine efficiency.

The specific gas constant for dry air,  $R$ , was assumed to be constant over the detonation cycle, having a value of 287.04 J/kgK; however, the gas constant is expected to be different for detonation products for brief moments in the pulsed detonation cycle. A sensitivity study in the results section shows the impact of the gas constant on turbine efficiency.

The formulation for turbine efficiency in Eq. (29) on page 24 is predicated on instantaneous expansion; however, the time associated with the expansion of a fixed mass through the turbine depends on the gas velocity. The velocity changes over the cycle; therefore, the expansion time also changes over the cycle. A sensitivity study in the results section shows the impact of expansion time on turbine efficiency.

Mechanical efficiency between the turbine and compressor was assumed to be 100%. This assumption was made for both specific work and turbine efficiency formulations. A sensitivity study in the results section shows the impact of mechanical efficiency on specific work and turbine efficiency.

## VI. Results

The following results show that unsteady specific work and isentropic efficiency increase with PDC frequency due to larger duty cycles. The results also show that the proposed formulation for unsteady turbine efficiency in Eq. (29) on page 24 yields reasonable values with the extensive weighting parameter applied to the pressure ratio term. The choice of weighting parameter, inlet heat transfer fraction parameter, and ensemble-averaging technique have a small impact on efficiency results. The next chapter includes a comparison between steady and unsteady turbine models. Appendices I and J include all time-resolved results for turbine power and inlet and exit flowfields, respectively.

### VI.A. Turbine Cycle-Average Specific Work

The following results show the effect of PDC operating parameters on time-resolved turbine power, using Eq. (27) on page 23, and cycle-average specific work, using Eq. (28) on page 24. Table 7 and Fig. 34 include a summary of cycle-average total air flow rate from the facility-calibrated converging-diverging metering nozzles, power output from the dynamometer, and specific work. Average power ranged from 1.07 kW to 12.74 kW. Average specific work ranged from 27 kJ/kg to 111 kJ/kg. At 20 Hz with 0.9 fueled fraction and 0.5 purge fraction, average specific work with ethylene was 7% higher than that with hydrogen. Though hydrogen has a lower heating value (LHV) that is nearly three times greater than ethylene, the fuel mass flow rate of ethylene at the 20 Hz condition was nearly three times higher. Thus, turbine performance was not significantly affected by fuel type.

**Table 7. Summary of turbine cycle-average power and specific work**

Hydrogen ( $\phi = 1.0$ )					
Frequency (Hz)	Fueled Fraction	Purge Fraction	Total Air Flow (kg/min)	Cycle Average Power (Eq. 27) (kW)	Cycle Average Specific Work (Eq. 28) (kJ/kg)
10	0.60	0.75	2.35	1.07	27.37
10	0.75	0.75	2.55	1.50	35.24
10	0.90	0.75	2.76	1.95	42.32
20	0.60	0.50	3.64	3.34	55.04
20	0.60	0.75	4.65	4.01	51.69
20	0.75	0.75	5.05	5.35	63.53
20	0.90	0.50	4.46	6.11	82.16
20	0.90	0.75	5.46	6.94	76.15
30	0.60	0.75	6.89	8.22	71.57
30	0.75	0.75	7.45	10.72	86.39

Ethylene ( $\phi = 1.2$ )					
Frequency (Hz)	Fueled Fraction	Purge Fraction	Total Air Flow (kg/min)	Cycle Average Power (Eq. 27) (kW)	Cycle Average Specific Work (Eq. 28) (kJ/kg)
20	0.90	0.50	4.64	6.81	88.14

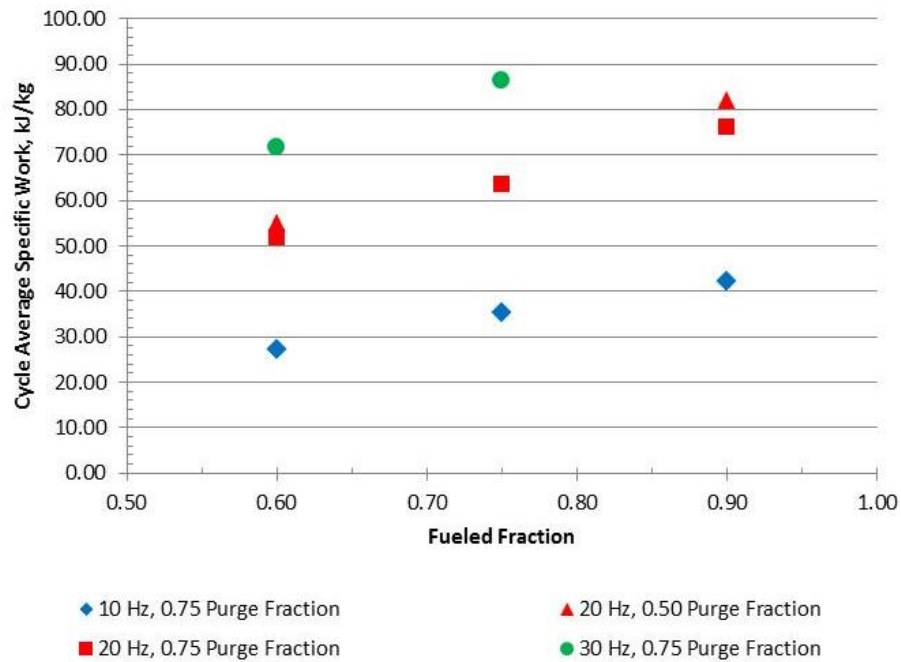


**Figure 34. Summary of turbine cycle-average specific work with hydrogen-fueled PDC**

### VI.A.1. Sensitivity Study

Average specific work increased with increasing fueled fraction and frequency, as shown in Fig. 34. A sensitivity study was conducted with the hydrogen-fueled PDC to show the influence of frequency, fueled fraction and purge fraction on average specific work. The definition of thermal efficiency in Eq. (38), which is typically applied for engine power take-off, is combined with average specific work in Eq. (28) on page 24 to produce the formulation for average specific work in Eq. (39).

$$\eta_{thermal} = \frac{\dot{W}_{out,turb}}{\dot{m}_{in,fuel} LHV_{fuel}} \quad (38)$$

$$\overline{W}_{s,turb} = \frac{\int_{cycle} \dot{W}_{out,turb} dt}{\int_{cycle} \dot{m}_{air,in,turb} dt} = \frac{\eta_{thermal} LHV_{fuel} \int_{cycle} \dot{m}_{in,fuel} dt}{\int_{cycle} (\dot{m}_{in,air,fill} + \dot{m}_{in,air,purge}) dt} \quad (39)$$

Dividing the numerator and denominator in Eq. (39) by the integral of fill air mass flow rate yields the formulation shown in Eq. (40), which includes the fill fuel-air ratio in the numerator and a ratio of purge air to fill air in the denominator. Fuel-air ratio was constant in these experiments. Eq. (40) was rearranged to solve for thermal efficiency so as to show the influence of purge and fueled fraction, as well as frequency.

$$\overline{W}_{s,turb} = \frac{\eta_{thermal} LHV_{fuel} \frac{\int_{cycle} \dot{m}_{in,fuel} dt}{\int_{cycle} \dot{m}_{in,air,fill} dt}}{\left( 1 + \frac{\int_{cycle} \dot{m}_{in,air,purge} dt}{\int_{cycle} \dot{m}_{in,air,fill} dt} \right)} \quad (40)$$

$$\eta_{thermal} = \frac{\overline{W}_{s,turb} LHV_{fuel} \frac{\int_{cycle} \dot{m}_{in,fuel} dt}{\int_{cycle} \dot{m}_{in,air,fill} dt}}{\left( 1 + \frac{\int_{cycle} \dot{m}_{in,air,purge} dt}{\int_{cycle} \dot{m}_{in,air,fill} dt} \right)} \quad (41)$$

Fill and purge air mass flow rates are related to fueled and purge fractions, as show respectively in Eqs. (42) and (43). Formulations for fueled fraction, FF, and purge fraction, PF are shown in Eq. (31) on page 32.

$$\dot{m}_{in,air,fill} = \left( FF \frac{\nabla_{tube}}{t_{fill}} - \dot{V}_{fuel} \right) \rho_{air,fill} \quad (42)$$

$$\dot{m}_{in,air,purge} = \left( PF \frac{\nabla_{tube}}{t_{purge}} \right) \rho_{air,purge} \quad (43)$$

Table 8 includes a summary of the results from the sensitivity study. Cycle-average specific work was calculated from Eq. (28) on page 24, and thermal efficiency was calculated using Eq. (41). As frequency increased and fueled and purge fraction were held constant, the average specific work increase is attributed to increased thermal efficiency, as shown in Eq. (40). Considering the conditions with 0.75 fueled and purge fractions, as frequency changed by 100% from 10 Hz to 20 Hz, thermal efficiency and average specific work increased by 77%. Increasing frequency by 50% from 20 Hz to 30 Hz resulted in a 35% increase in thermal efficiency and average specific work. Thus, the relationship between frequency and average specific work was not linear.

**Table 8. Sensitivity study for cycle-average specific work with hydrogen-fueled PDC**

Hydrogen ( $\phi = 1.0$ )				
Frequency (Hz)	Fueled Fraction	Purge Fraction	Cycle Average Specific Work (Eq. 28) (kJ/kg)	Thermal Efficiency (Eq. 41)
10	0.60	0.75	27.37	2.21%
10	0.75	0.75	35.24	2.48%
10	0.90	0.75	42.32	2.69%
20	0.60	0.50	55.04	3.47%
20	0.60	0.75	51.69	4.17%
20	0.75	0.75	63.53	4.48%
20	0.90	0.50	82.16	4.26%
20	0.90	0.75	76.15	4.83%
30	0.60	0.75	71.57	5.76%
30	0.75	0.75	86.39	6.04%

As fueled fraction increased and fuel-air ratio remained constant, average specific work and thermal efficiency increased with fill air flow rate, as shown in Table 8.

Considering the 20 Hz conditions with 0.75 purge fraction, as fueled fraction increased by 25% from 0.60 to 0.75, average specific work increased by 22%. Using Eq. (41), it was determined that thermal efficiency increased by 12%. Therefore, the increase in average specific work was due to an increase in both fill air flow rate and thermal efficiency.

Increasing fueled fraction by 20% from 0.75 to 0.90 resulted in a 20% increase in average specific work and an 8% increase in thermal efficiency. Average specific work had a nearly linear relationship with fueled fraction. However, there was a non-linear relationship between fueled fraction and thermal efficiency.

As purge fraction decreased, average specific work and thermal efficiency changed with purge air flow rate, as seen in Table 8. Considering the 20 Hz condition

with 0.60 fueled fraction, as purge fraction decreased by 33% from 0.75 to 0.50, average specific work increased by 6.5% and thermal efficiency increased by 3.3%. At the 20 Hz condition with 0.90 fueled fraction, as purge fraction decreased by 33% from 0.75 to 0.50, average specific work increased by 7.9% though thermal efficiency decreased by 27%. Average specific work was relatively insensitive to purge fraction, compared to fueled fraction and frequency. The optimal PDC-turbine arrangement for average specific work occurred with higher frequencies and fueled fraction.

#### ***VI.A.2. Time-Resolved Turbine Power: Effect of PDC Frequency***

Figure 35 shows the effect of increasing frequency on time-resolved power, using Eq. (27) on page 23. Power is shown over a single detonation cycle at three frequencies with 0.75 fueled and purge fractions. Peak power output at 10 Hz was about 2 kW, and peak power at 30 Hz was 12 kW; however, the cycle-integrated mass flow rate was the same. Thus, cycle-average specific work increased with frequency, as seen in Fig. 34 on page 62.

The time from detonation arrival to peak power was nearly equal (about 10 ms) at each frequency, during which time rotor speed increased and rotational energy was stored in the wheel assembly, as discussed in Appendix F. As power drops, rotor speed decreases, and rotational energy dissipates. The rate at which power rose and fell increased with frequency. At 10 Hz, power began to drop midway through the fire phase at 20 ms; however, at 30 Hz, power did not begin to fall until after the fire phase. Power duty cycle was defined in this study as the fraction of cycle time in which power increased. The duty cycle was about 15% at 10 Hz and about 40% at 30 Hz.

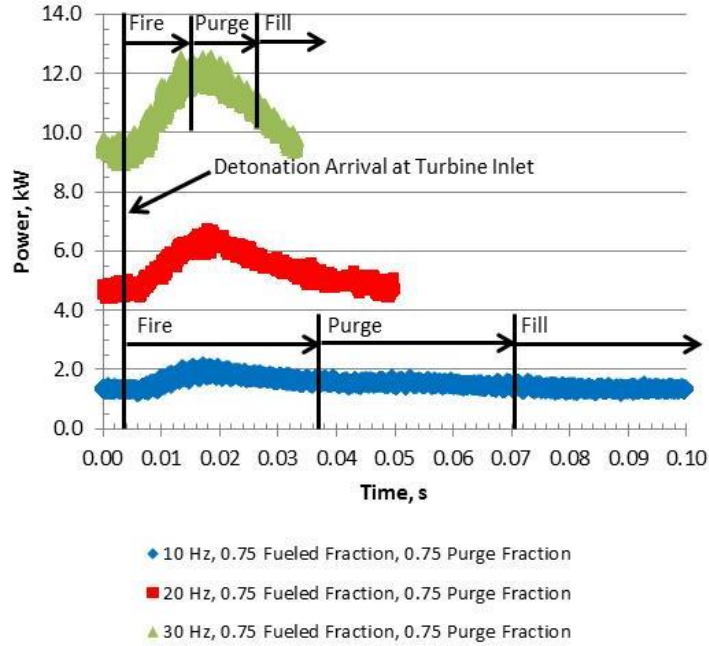


**Figure 35. Time-resolved power with 10, 20, and 30 Hz hydrogen-fueled PDC with 0.75 fueled and purge fractions**

$$Duty\ Cycle_{power} = \frac{t_{rise}}{t_{cycle}} \quad (44)$$

The power duty cycle is illustrated in Fig. 36, which shows time-resolved power from Eq. (27) on page 23 normalized by maximum power and time normalized by total cycle time. At 30 Hz, peak power output occurred near the midpoint of the detonation cycle compared to 10 Hz operation. At 10 Hz, power rose during 15% of the cycle time and fell for the remaining 85%. At 30 Hz, power rose during 40% of the cycle time. The duty cycle became steadier with increased frequency, as seen by a 40% drop from peak power at 10 Hz and 25% drop from peak power 30 Hz. The increase in cycle-average specific work at higher frequencies, as shown in Fig. 34 on page 62, resulted from the

larger and steadier power duty cycle. The optimal frequency for a given PDC-turbine arrangement has a 50% duty cycle.

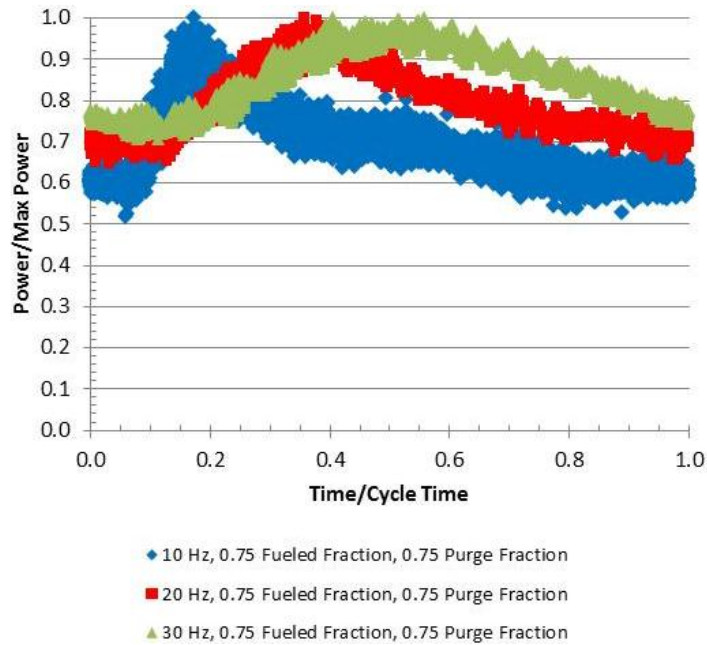


**Figure 36. Normalized time-resolved turbine power with 10, 20, and 30 Hz hydrogen-fueled PDC with 0.75 fueled and purge fractions**

### *VI.A.3. Time-Resolved Turbine Power: Effect of Fueled Fraction*

The power duty cycle did not change significantly with increased fueled fraction, as seen in Fig. 37, which shows time-resolved turbine power over a single 20 Hz detonation cycle at three different fueled fractions. However, power output at each moment in time was higher with increased fueled fraction. At 0.60 fueled fraction, peak power was about 1.5 kW; whereas, peak power at 0.90 fueled fraction was about 2.75 kW. Therefore, instantaneous power and average specific work increased with fueled fraction, as shown respectively in Figs. 37 and 34.

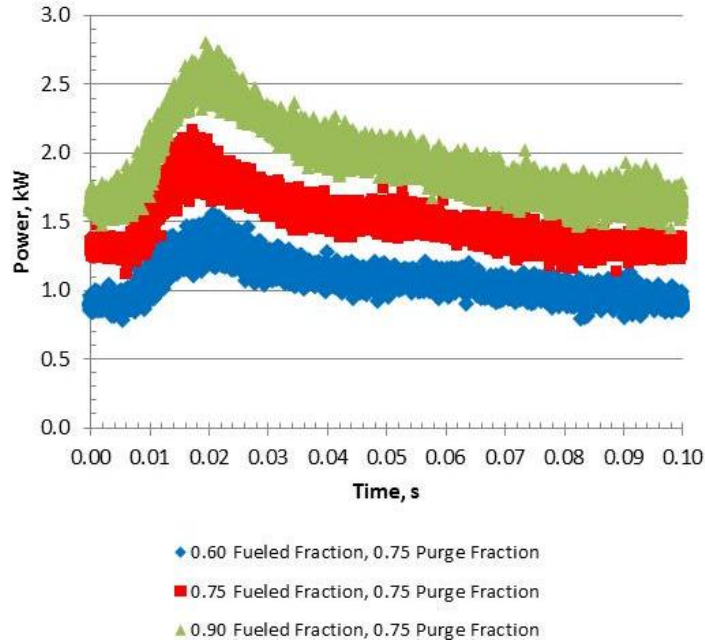


**Figure 37. Time-resolved power with 10 Hz hydrogen-fueled PDC with fueled fractions of 0.60, 0.75, and 0.90 and with 0.75 purge fraction**

#### *VI.A.4. Time-Resolved Turbine Power: Effect of Purge Fraction*

Figure 38 shows the effect of purge fraction on time-resolved turbine power over a single detonation cycle at 20 Hz with 0.90 fueled fraction. There was no significant change in duty cycle, and there was a small increase in instantaneous power with purge fraction, likely due to the increased purge manifold pressure from 1.57 bar to 2.04 bar and increased purge mass flow rate from 1.97 kg/min to 2.98 kg/min. Peak power at 0.50 purge was about 7.5 kW; whereas, peak power at 0.75 purge was about 1.25 kW higher. The percent increase in power was similar to the percent increase in purge air flow rate, and thus there was a small change in average specific work with increasing purge fraction, seen in Fig. 34 on page 62. Purge fraction had less effect on time-resolved turbine power and average specific work, than did fueled fraction or frequency.

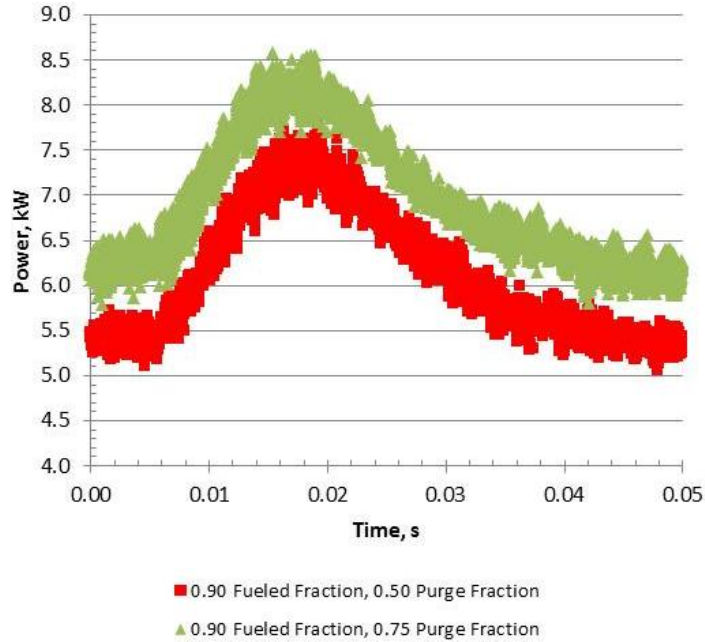


**Figure 38. Time-resolved power with 20 Hz hydrogen-fueled PDC with 0.90 fueled fraction and 0.50 and 0.75 purge fractions**

#### VI.B. Cycle-Average Isentropic Turbine Efficiency

Cycle-average isentropic turbine efficiency was calculated for the hydrogen-fueled operating conditions at 20 Hz and 30 Hz with 0.75 fueled and purge fractions using Eq. (29) on page 24. These frequencies offered larger data sets for ensemble averaging than 10 Hz. The conditions were also chosen because they demonstrated high cycle-average specific work. Appendix K includes results based on the Eq. (4) instantaneous efficiency formulation on page 14, which produced non-physical results with instantaneous efficiencies less than zero and greater than 100%.

Table 9 shows the effect of inlet weighting parameter and inlet heat transfer model on the turbine efficiency formulation in Eq. (29). As expected, the unweighted formulation ( $\xi = 1$ ) yielded unreasonable results with turbine efficiency greater than the

manufacturer reported maximum conventional steady efficiency (61%), indicating that the unsteady efficiency formulation requires the pressure term to be weighted by an extensive property, such as mass flow rate or total enthalpy rate. The difference in efficiency results between the two weighting parameters was about 5% with the constant pressure heat transfer model. Mass flow rate weighting parameter can be helpful when referencing a Mollier diagram, which is based on specific mass; however, total enthalpy rate is physically attractive because it differentiates between hot and cold flows.

**Table 9. Comparison of weighting parameters and inlet heat transfer models for unsteady turbine efficiency with 30 Hz hydrogen-fueled PDC with 0.75 fueled and purge fractions, using Eq. (29) and ensemble-averaged efficiency**

<i>Rayleigh Line Flow at Inlet</i>			
Inlet Weighting Parameter	$\overline{\eta_{turb}}$	Std Dev	$\overline{\Delta\dot{H}_{t,ideal}}$
None ( $WP_{in} = 1$ )	69.5%	1.0%	11.23 kW
Mass Flow Rate	44.9%	6.8%	20.27 kW
Total Enthalpy Flux	42.3%	3.6%	23.22 kW

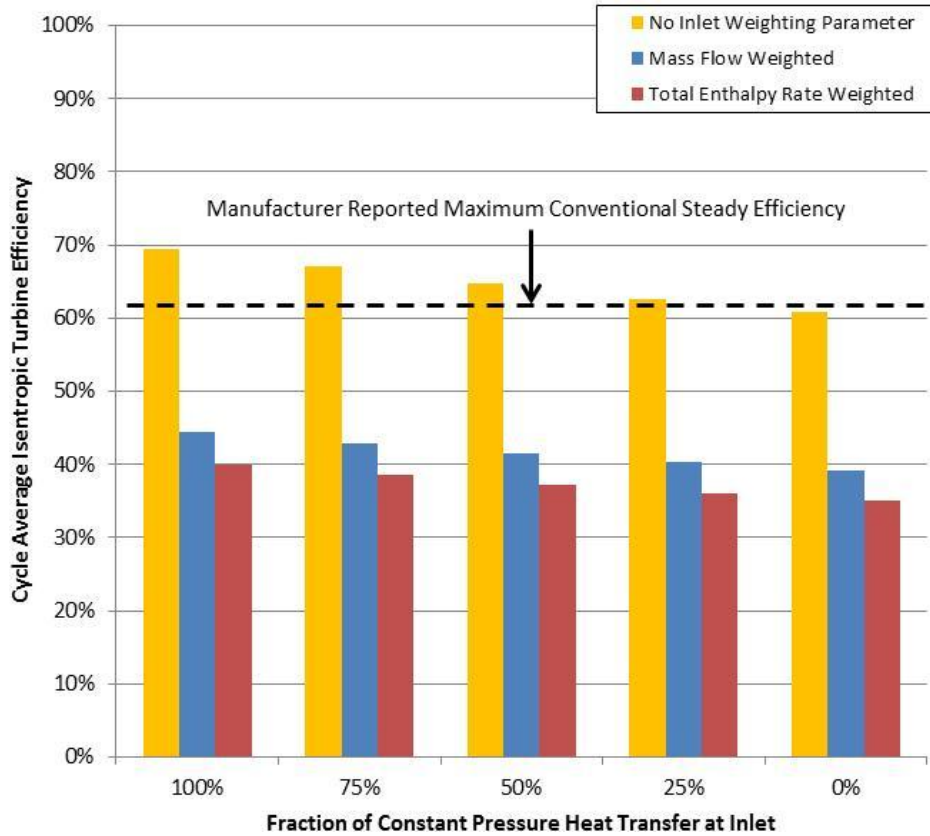
  

<i>Constant Pressure Heat Transfer at Inlet</i>			
Inlet Weighting Parameter	$\overline{\eta_{turb}}$	Std Dev	$\overline{\Delta\dot{H}_{t,ideal}}$
None ( $WP_{in} = 1$ )	69.5%	1.0%	15.65 kW
Mass Flow Rate	44.4%	6.2%	24.47 kW
Total Enthalpy Flux	39.9%	3.4%	27.27 kW

A Rayleigh line flow analysis, detailed in Appendix L, was used to validate the proposed constant pressure heat transfer model. The analysis used Eq. (29) to calculate turbine efficiency, accounting for total pressure change between the inlet measurement location and the turbine. In the Rayleigh model, pressure changes in proportion to momentum changes brought about by heat transfer; however, the model assumes constant area. The turbine inlet and exit are constant area ducts, but the turbine inlet volute is not;

therefore, the Rayleigh model lacks fidelity with test section arrangement. The constant pressure heat transfer model was in reasonable agreement with the Rayleigh model. The change in cycle-average turbine inlet total pressure was 0.4% with the 30 Hz condition.

The effect of the inlet heat transfer fraction parameter,  $\psi$ , is shown in Fig. 39. Turbine efficiency improved as more heat transfer was attributed to the inlet. The potential for heat transfer is expected to decrease from the inlet to the exit, as the flow expands. Therefore, the 75% model is most reasonable.



**Figure 39. Comparison of inlet heat transfer fraction for turbine efficiency with 30 Hz hydrogen-fueled PDC with 0.75 fueled and purge fractions, using Eq. (29) and ensemble-averaged efficiency**

Figures 40 and 41 show a comparison of unsteady turbine efficiency results at the 30 Hz and 20 Hz conditions using Eq. (29) with constant total pressure heat transfer at the inlet only ( $\psi = 1$ ) and using the three different averaging techniques. The first technique used ensemble average pressures, temperatures, and velocities to evaluate cycle-average turbine efficiency. The second technique applied an ensemble average to the total enthalpy rate and total pressure ratio terms before evaluating efficiency. The third technique applied an ensemble average over multiple cycle-averaged turbine efficiencies. The difference between all three techniques is less than 8%. Based on the third averaging method with the total enthalpy rate weighting parameter, the cycle-average turbine efficiency was about 40% at 30 Hz and 36% at 20 Hz.

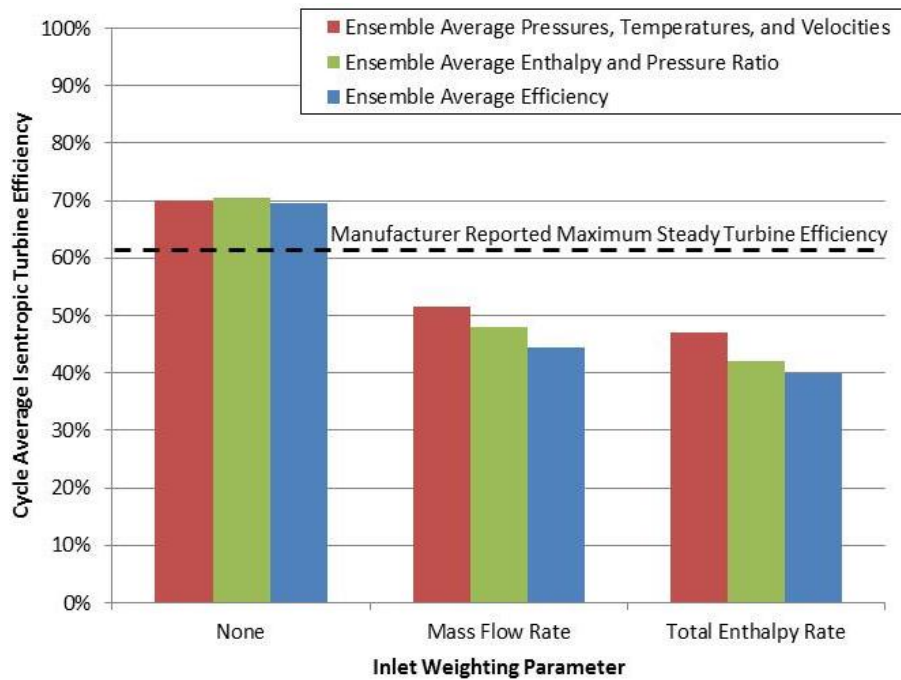


**Figure 40. Comparison of averaging techniques for turbine efficiency with 30 Hz hydrogen-fueled PDC with 0.75 fueled and purge fractions, using Eq. (29) with constant total pressure heat transfer at the inlet only ( $\psi = 1$ )**

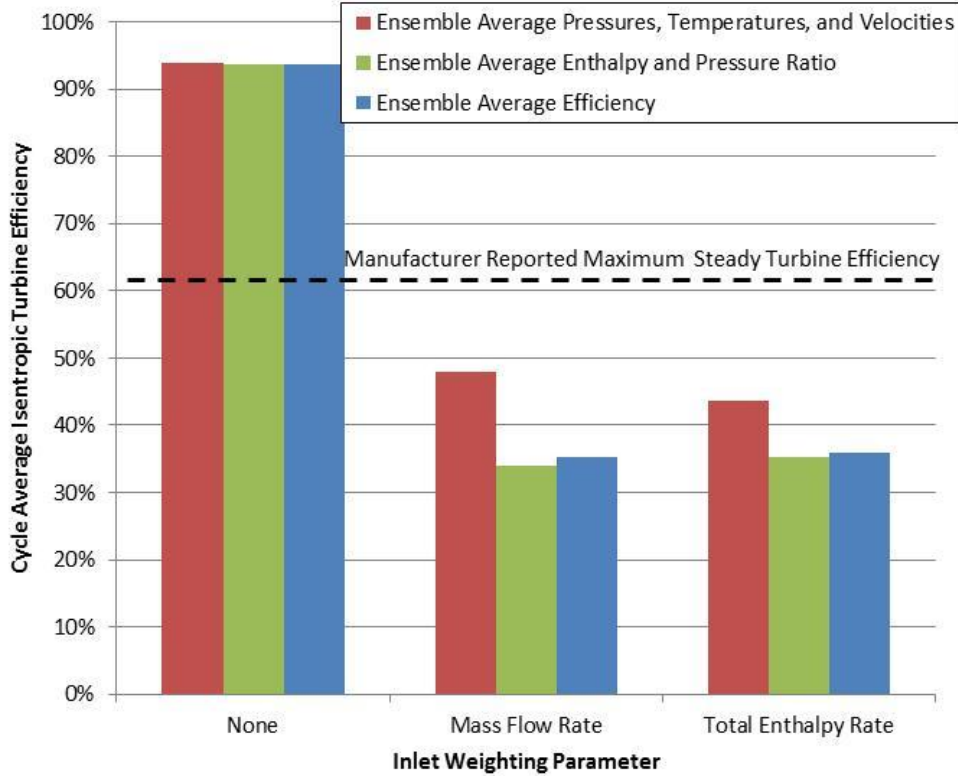


**Figure 41. Comparison of averaging techniques for turbine efficiency with 20 Hz hydrogen-fueled PDC with 0.75 fueled and purge fractions, using Eq. (29) with constant total pressure heat transfer at the inlet only ( $\psi = 1$ )**

### *VI.B.1. Sensitivity Study*

This sensitivity study address the impact of measurement error and uncertainty associated with assumptions used in the development of the unsteady turbine efficiency formulation. Table 10 summarizes the sensitivity of cycle-average turbine efficiency to measurement error associated with turbine inlet and exit pressures, temperatures, and velocities. The baseline case was associated with the 30 Hz hydrogen-fueled PDC with 0.75 fueled and purge fractions, ensemble-averaging efficiency results using Eq. (29) with  $\psi = 1.0$  and weighting the total pressure ratio with inlet total enthalpy rate. A 10% measurement error was independently applied to each flowfield measurement parameter

at each instant in time across the entire PDC cycle, and the difference in turbine efficiency was assessed.

**Table 10. Sensitivity of cycle-average turbine efficiency to measurement error**

Measurement	Cycle-Average Turbine Efficiency		Sensitivity	
	Baseline	with +10% Error	$\Delta\eta$	$\Delta\eta/\eta_{\text{baseline}}$
Inlet Static Pressure	39.9%	36.3%	-3.58%	-8.98%
Exit Static Pressure	39.9%	40.6%	0.78%	1.96%
Inlet Static Temperature	39.9%	40.3%	0.45%	1.13%
Exit Static Temperature	39.9%	39.7%	-0.18%	-0.45%
Inlet Velocity	39.9%	38.8%	-1.08%	-2.71%
Exit Velocity	39.9%	36.8%	-3.06%	-7.68%

Turbine efficiency is most sensitive to inlet static pressure and exit velocity. An inlet static pressure measurement error of 10% resulted in about 9% difference in turbine efficiency, and a 10% exit velocity measurement error resulted in nearly 8% difference in turbine efficiency. As noted in the section on data reduction and uncertainty, average inlet static pressure cycle-to-cycle variation was about 3.8%; however, average exit velocity cycle-to-cycle variation was about 16.6%. Therefore, exit velocity measurements were the largest potential source of error in cycle-average turbine efficiency.

The assumption of average specific heat across the turbine was made for the isentropic pressure ratio term in the Eq. (29) efficiency formulation. Air was assumed to be the working fluid for the calculation of specific heat as a function of temperature. In reality, combustion products for hydrogen-air include air and water; however, purge air comprised a large portion of the total cycle flow used to calculate efficiency. Purge air has less water than the combustion products in the blowdown portion of the cycle. Using the baseline operating condition at 30 Hz with 0.75 fueled and purge fractions,  $\psi = 1.0$ , and inlet total enthalpy rate weighting parameter, a 10% error in the ratio of specific heats

was applied to each moment in time over the entire cycle and resulted in less than a 1% change in cycle-average turbine efficiency. Therefore, the assumption for average specific heat across the turbine had an insignificant effect on cycle-average turbine efficiency

Turbine efficiency was evaluated with the assumption that the specific gas constant for dry air, 287.04 J/kgK, was applicable over the entire PDC cycle. However, the gas constant is expected to about 347.7 J/kgK for detonation products associated C-J conditions during the fire phase. The difference in the gas constant affects calculations for density, which is used in turn for mass flow rate, total enthalpy rate, and turbine efficiency. Furthermore, the gas constant was used to calculate the exponent of the isentropic pressure ratio. Assuming a 10% error in the gas constant at each moment in time over the entire PDC cycle resulted in less than 3% change in cycle-average turbine efficiency, using the 30 Hz hydrogen-fueled PDC baseline condition with 0.75 fueled and purge fractions,  $\psi = 1.0$ , and inlet total enthalpy rate weighting parameter. Because purge air comprised a large portion of the total cycle flow used to calculate efficiency, the assumption for gas constant had an insignificant effect on cycle-average turbine efficiency.

The assumption of instantaneous expansion was made to simplify the analysis for turbine efficiency; however, the actual time associated with expansion across the turbine is dependent on the time required for a particle to travel from the turbine inlet to the exit. The inlet and exit velocities change over the cycle, and the path length of a particle through the radial turbine depends on how far the particle travels through the turbine

volute before entering a turbine blade passage. A sensitivity study was conducted, applying a time shift to the exit temperatures, pressures, and velocities for the operating condition at 30 Hz with 0.75 fueled and purge fractions. Time shifts of one to five milliseconds were applied independently across the entire exit data set, and there was about 1% difference in efficiency results with the one or two millisecond time shift, as seen in Table 11. The results are sensitive to the alignment of the initial inlet and exit pressure peaks, the time between which is about 2 ms. The width of the exit pressure peak is also about 2 ms. Applying a time shift larger than 2 ms aligns the inlet pressure peak with the large flat portion of the exit pressure trace, and results are insensitive to further increases in the time shift.

**Table 11. Sensitivity of cycle-average turbine efficiency to time-shifted turbine exit flowfield pressures, temperatures, and velocities**

Time Shift	Cycle-Average Turbine Efficiency		Sensitivity	
	Baseline	with Time Shift	$\Delta\eta$	$\Delta\eta/\eta_{\text{baseline}}$
1 ms	39.85%	38.64%	-1.21%	-3.04%
2 ms	39.85%	38.62%	-1.23%	3.09%
3 ms	39.85%	39.45%	-0.40%	1.00%
4 ms	39.85%	39.31%	-0.54%	1.36%
5 ms	39.85%	39.49%	-0.36%	0.90%

The mechanical efficiency for the compressor-turbine wheel assembly was assumed to 100% over the entire PDC cycle at each operating condition. Mechanical efficiency for turbochargers operating at high rotor speeds is typically about 95% or greater. A 5% loss in mechanical efficiency directly corresponds to a 5% improvement in cycle-average turbine efficiency, using Eq. (29) and the 30 Hz hydrogen-fueled PDC baseline condition with 0.75 fueled and purge fractions,  $\psi = 1.0$ , and inlet total enthalpy rate weighting parameter.

### ***VI.B.2. Time-Resolved Turbine Inlet and Exit Flowfields: Temperature***

The following figures show time-resolved turbine inlet and exit flowfield properties that were used to calculate turbine efficiency. The time-resolved plots show the interaction between the PDC and turbine. Furthermore, the time-resolved plots aid in the uncertainty analysis, showing repeatability across cycles and peak magnitudes that can be compared with expected detonation properties. Results are shown with the hydrogen-fueled PDC at 0.75 fueled and purge fractions. The 0.75 fueled fraction extends from the engine head to entrance of the inlet diagnostic section. Therefore, the mutually supporting shock-combustion of the detonation front is expected to decouple in the diagnostic section; however, a shock is expected to continue through the diagnostic section, though it is expected to decay without support from combustion.

Figure 42 shows time-resolved inlet and exit static temperatures from laser absorption measurements for five successive detonation cycles at 30 Hz with 0.75 fueled and purge fractions. There is good repeatability between cycles, especially at the turbine exit. The inlet profile and peak magnitudes are very similar, though they indicate a variation in detonation arrival time. Furthermore, there is a small peak in the exit profile at about 11.5 ms which is likely associated with the decaying shock. The variation in exit temperature appears to be damped compared to the inlet, with a peak temperature about one third of that at the turbine inlet. The exit does not experience a long quiescent period like that at inlet, which occurs between 5 ms and 10 ms. The ensemble average static temperature included in Fig. 43 produces a smooth profile, preserving key features, though the peak inlet temperature is reduced from about 2,000 K to about 1,800 K.

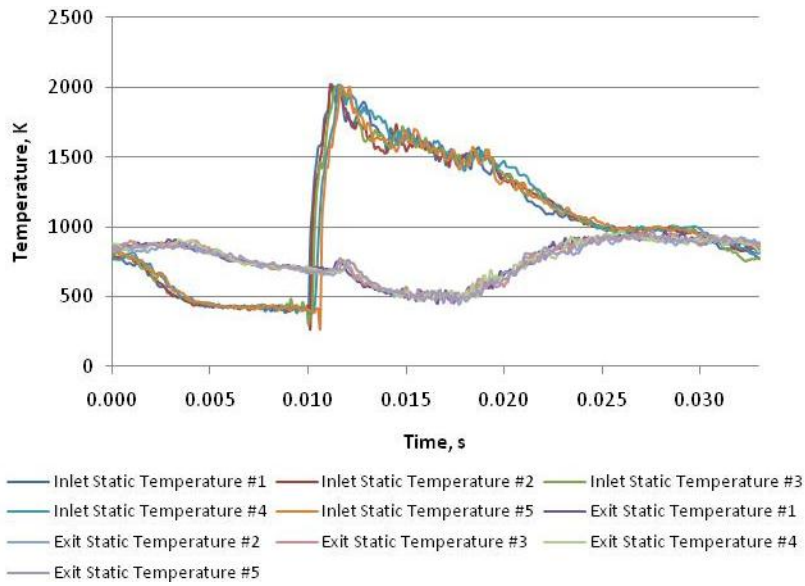


**Figure 42. Turbine inlet and exit static temperature over 5 cycles with 30 Hz hydrogen-fueled PDC with 0.75 fueled and purge fractions**

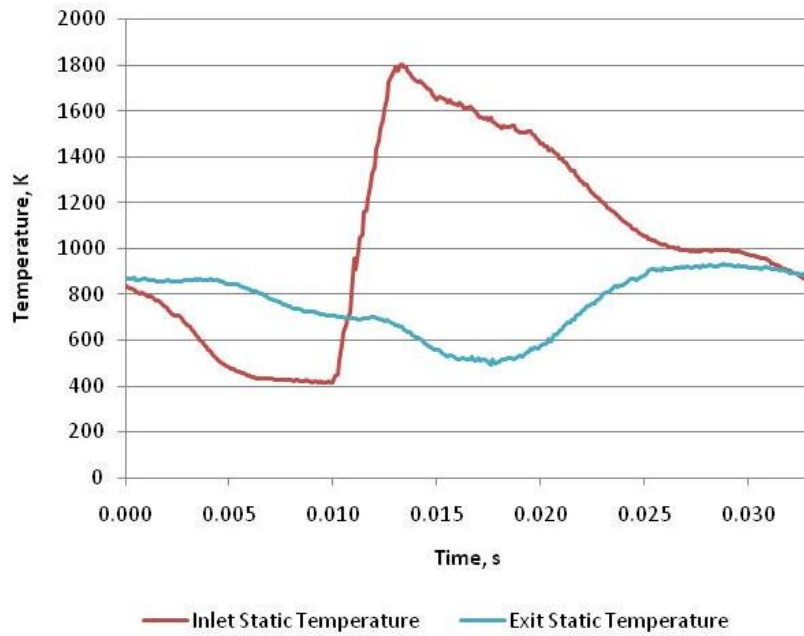


**Figure 43. Ensemble average of turbine inlet and exit static temperature over 13 cycles with 30 Hz hydrogen-fueled PDC with 0.75 fueled and purge fractions**

Figure 44 shows turbine inlet and exit total temperature over two full detonation cycles at 20 and 30 Hz PDC operating frequencies. Total temperature was calculated from laser absorption measurements of static temperature and velocity using Eq. (32) on page 48, assuming specific heat for air as a function of temperature. Peak temperatures were periodic and consistent at the different frequencies. Inlet and exit temperature profiles were very similar at the different frequencies. At 30 Hz the inlet temperature remains above 1000 K for a larger fraction of the cycle time.

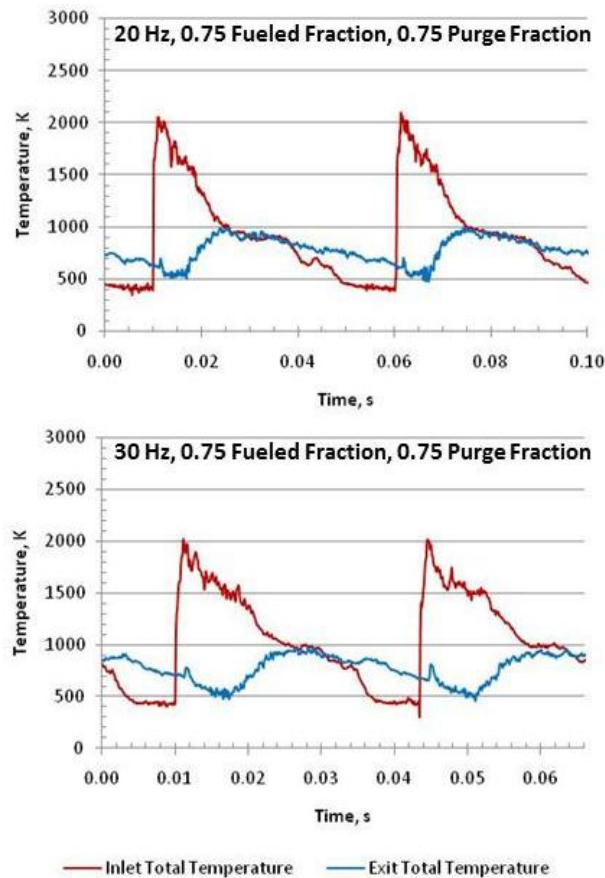


**Figure 44. Turbine inlet and exit total temperature over 2 cycles with 20 and 30 Hz hydrogen-fueled PDC with 0.75 fueled and purge fractions**

### VI.B.3. Time-Resolved Turbine Inlet and Exit Flowfields: Pressure

Figure 45 shows time-resolved inlet and exit static pressures for five successive detonation cycles at 30 Hz with 0.75 fueled and purge fractions. There is good repeatability between cycles with very similar profiles and peak magnitudes. The stand-off distance associated with the wall-mounted pressure transducers limited the response time such that the expected Von Neumann peak pressure (around 40 bar) was not captured at the turbine inlet. The exit peak pressure is attenuated, compared to the turbine inlet peak pressure, and variation in exit pressure magnitude over the cycle time is small compared to the inlet, fluctuating just above the ambient test cell static pressure.

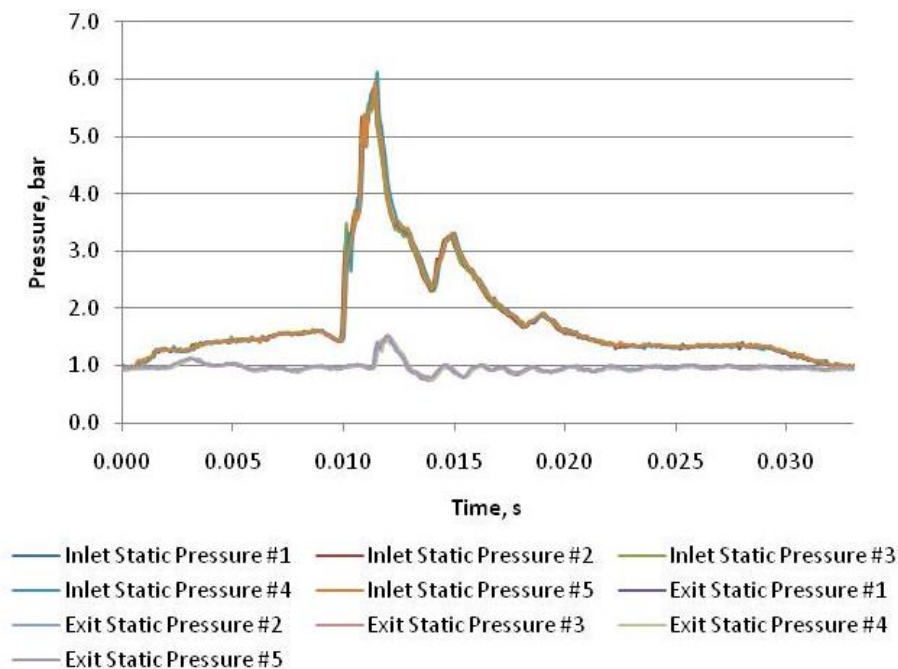


**Figure 45. Turbine inlet and exit static pressure over 5 cycles with 30 Hz hydrogen-fueled PDC with 0.75 fueled and purge fractions**

The time difference between the sharp rise at the inlet (at 10 ms) and at the exit (at 12 ms) indicates the travel time of the detonation pressure wave through the turbine.

Assuming the pressure wave travels at the local speed of sound at the moment it enters and passes through the turbine, the distance associated with transit time between the inlet and exit measurement locations is consistent with the experimental arrangement. The time between the first and second inlet pressure peaks indicates the presence of a reflected wave travelling the length of the PDC tube and back, assuming local speed of sound at the turbine inlet measurement location. Likewise, the time between the second and third inlet pressure peaks indicates the presence of a subsequent reflected pressure wave. The pressure wave travelling upstream likely reflected off the engine head, but it could not be conclusively determined if the subsequent pressure waves travelling downstream reflected off the turbine blades or else where in the turbine volute. Rasheed, et al. (2004) observed shock waves reflecting from blade leading edges. The ensemble average static pressure included in Fig. 46 produces a smooth profile that preserves the key features, though the peak inlet temperature is reduced from about 6 bar to about 5.5 bar.

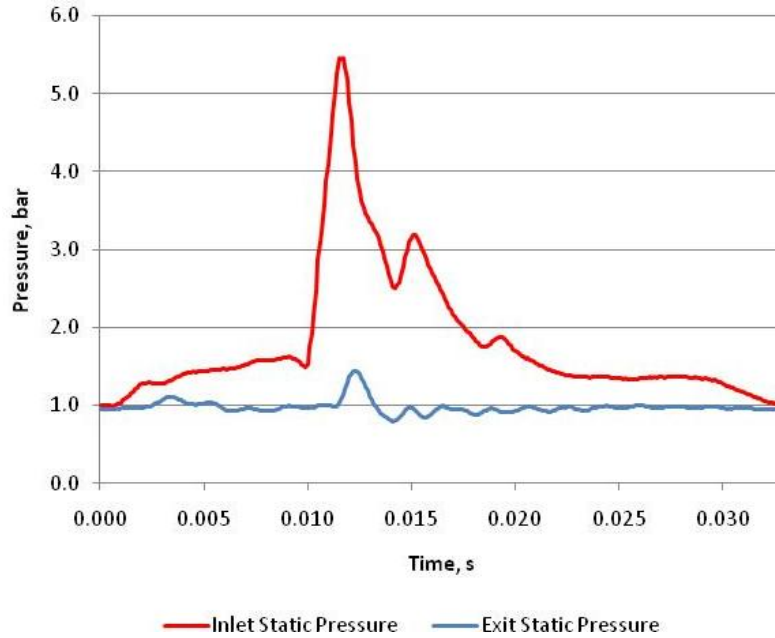


**Figure 46. Turbine inlet and exit static pressure ensemble averaged over 13 cycles with 30 Hz hydrogen-fueled PDC with 0.75 fueled and purge fractions**

Figure 47 shows turbine inlet and exit total pressure over two full detonation cycles at 20 and 30 Hz PDC operating frequencies. Total pressure was calculated from total and static temperature and static pressure using Eq. (33) on page 49, assuming a ratio of specific heat for air as a function of temperature. The peak inlet pressures at 30 Hz were clipped more than at 20 Hz. The trailing portions of the inlet profiles were very similar at both frequencies; however, the quiescent period was smaller at 30 Hz, with the pressure exceeding 2 bar for more than 20% of the cycle time. The manufacturer turbine map indicates choked flow for conventional operation for total pressure ratios greater than 2, which occurs for about 25% of cycle time with the 30 Hz PDC operation.

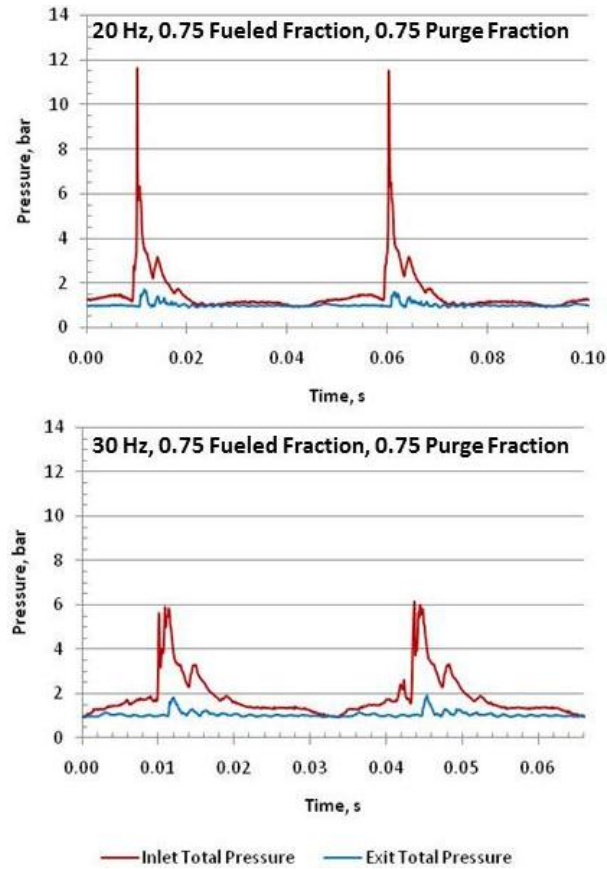


**Figure 47. Turbine inlet and exit total pressure over 2 cycles with 20 and 30 Hz hydrogen-fueled PDC with 0.75 fueled and purge fractions**

#### *VI.B.4. Time-Resolved Turbine Inlet and Exit Flowfields: Velocity*

Figure 48 shows time-resolved laser measurements of inlet and exit velocities for five successive detonation cycles at 30 Hz with 0.75 fueled and purge fractions. There is good repeatability between cycles with similar profiles and peak magnitudes. The peak inlet velocity is near the local speed of sound, which about 1000 m/s. The flow rapidly decelerates after 11 ms during the subsequent expansion, and reverse flow was observed at 12 ms, followed by a quiescent region and then two more velocity peaks, which occur

simultaneously with the reflected pressure waves. Reverse flow was also observed in the high-speed PSV video.

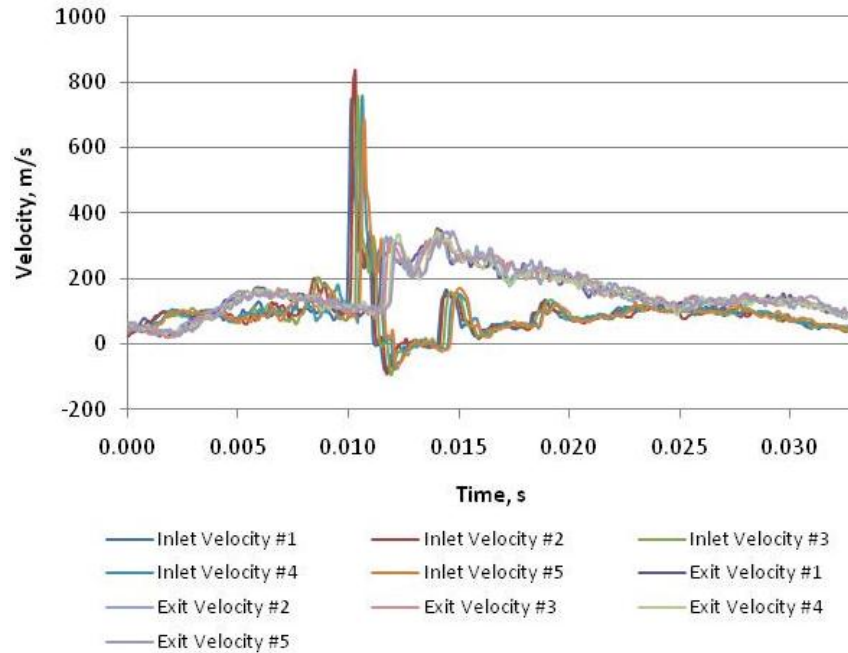


**Figure 48. Turbine inlet and exit velocity over 5 cycles with 30 Hz hydrogen-fueled PDC with 0.75 fueled and purge fractions**

The time between rapid rise in velocity at the turbine inlet and exit is consistent with the time observed in the static pressure plot. The inlet velocity between 10 ms and 12 ms is greater than that of the exit, indicating mass accumulation. Between 12 ms and 24 ms, the exit velocity exceeds that of the inlet, indicating mass expulsion.

Figure 49 shows turbine inlet and exit velocity over two full detonation cycles at 20 and 30 Hz PDC operating frequencies. Reverse flow was observed at the turbine inlet at 10 Hz (not shown), 20 Hz and 30 Hz. Reverse flow was also observed at the turbine exit at 10 Hz, 20 Hz but not at 30 Hz.

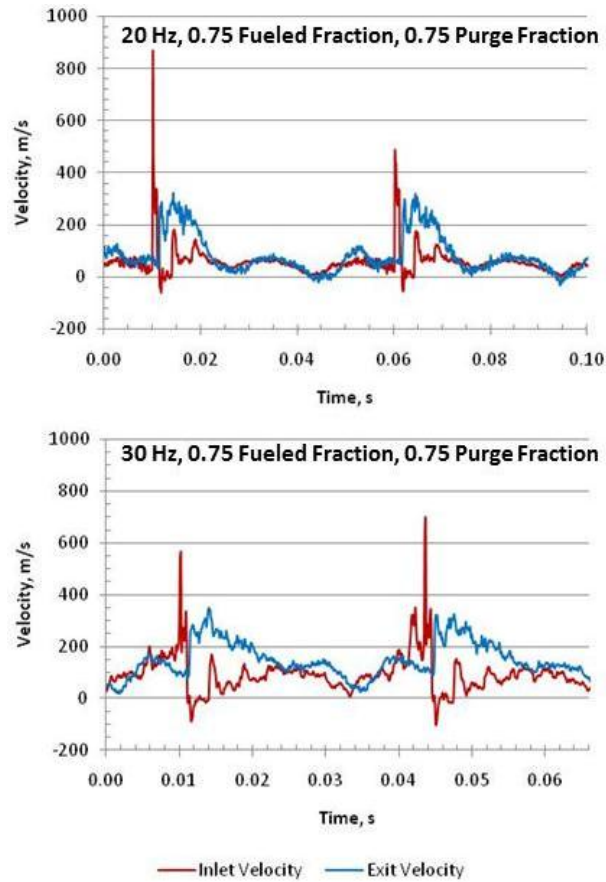
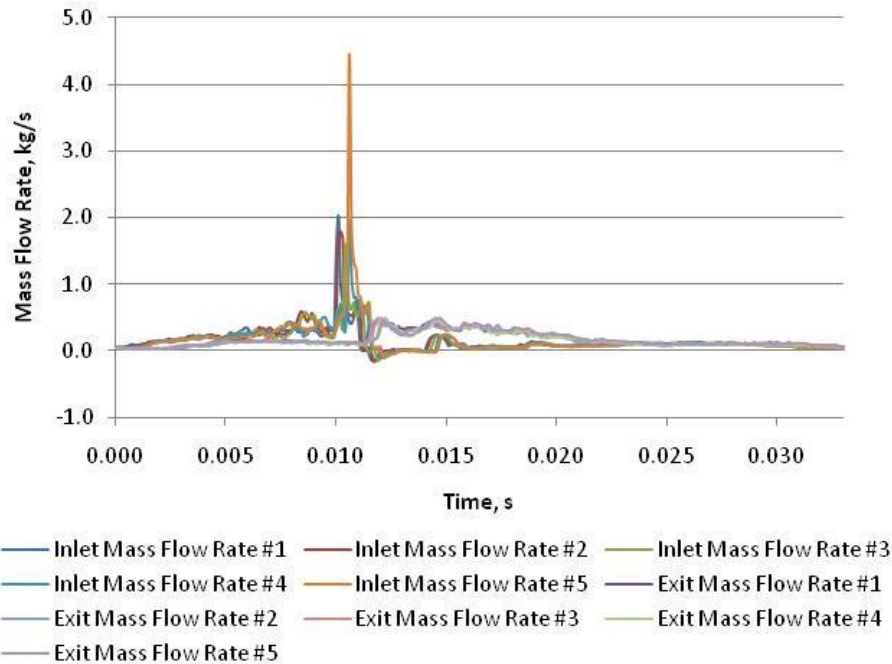


**Figure 49. Turbine inlet and exit velocity over 2 cycles with 20 and 30 Hz hydrogen-fueled PDC with 0.75 fueled and purge fractions**

#### *VI.B.5. Time-Resolved Turbine Inlet and Exit Flowfields: Mass Flow*

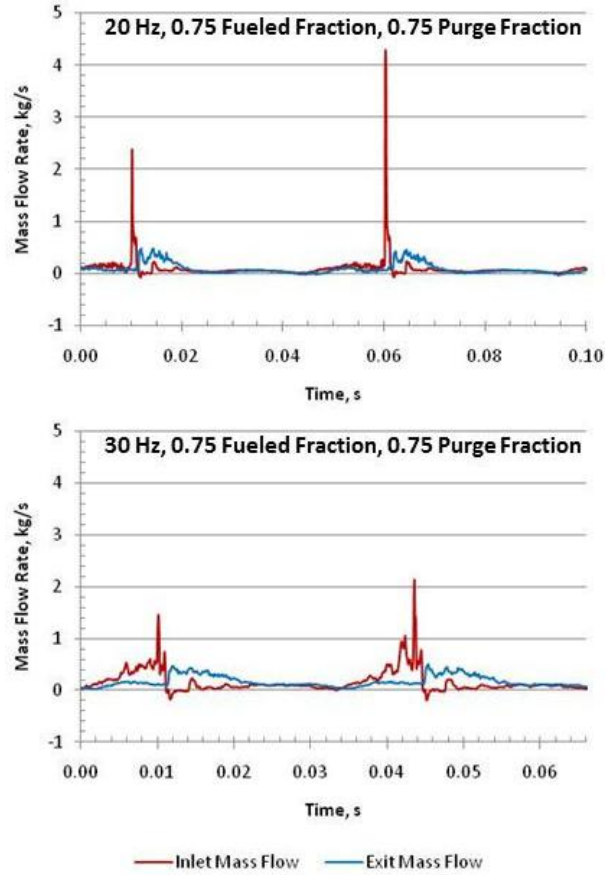
Figure 50 shows time-resolved inlet and exit mass flow rates for five successive detonation cycles at 30 Hz with 0.75 fueled and purge fractions. Mass flow rate is calculated using velocity and static temperature and pressure in the diagnostic section where the cross sectional area is  $0.002 \text{ m}^2$ . There is good repeatability between the first four cycles with similar profiles and peak magnitudes. The peak inlet mass flow during the fifth cycle was significantly greater than the others due to coincidental peak in

pressure and velocity measurements. Otherwise, the mass flow rates indicated the same flow features observed in the velocity results.



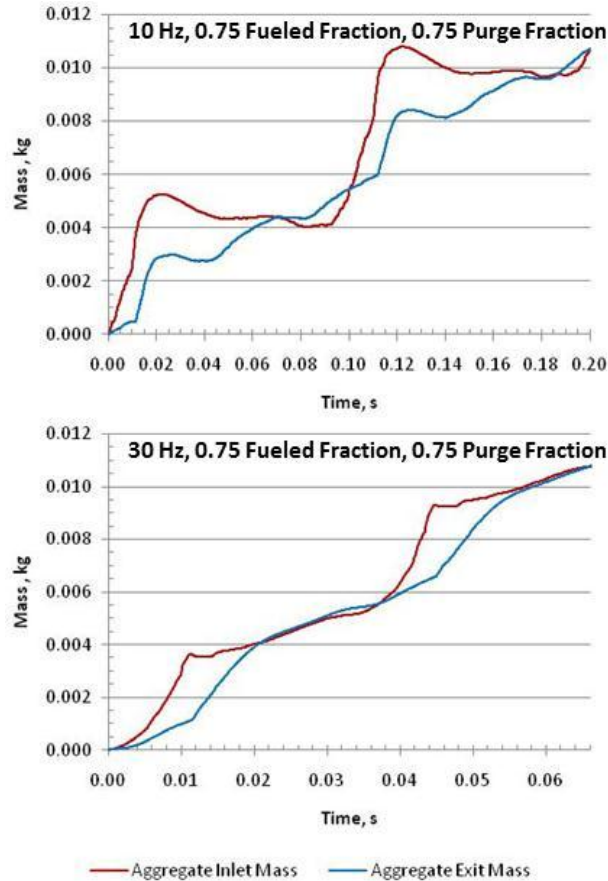
**Figure 50. Turbine inlet and exit mass flow rate over 5 cycles with 30 Hz hydrogen-fueled PDC with 0.75 fueled and purge fractions**

Figure 51 shows turbine inlet and exit mass flow rates over two full detonation cycles at 20 and 30 Hz PDC operating frequencies. Inlet peak mass flow rates are higher at 20 Hz, but the quiescent period is smaller at 30 Hz. As with the velocity profiles, the mass flow rates indicate reverse flow at the turbine inlet just behind the detonation wave. A secondary inlet peak mass flow rate is also apparent about 4 to 5 ms after the reverse flow event, coinciding with the trailing pressure peaks. The exit mass flow rate is relatively steady compared to the inlet mass flow rates. As noted with the velocities, momentary mass accumulation and expulsion is observed.



**Figure 51. Turbine inlet and exit mass flow rate over 2 cycles with 20 and 30 Hz hydrogen-fueled PDC with 0.75 fueled and purge fractions**

Figure 52 shows turbine inlet and exit aggregate mass over two full detonation cycles at 10 and 30 Hz PDC operating frequencies. Aggregate mass was calculated to show the accumulation and expulsion of mass in the system, using an average of mass flow rate over a sampling time interval, as shown in Eq. (36) on page 54.



**Figure 52. Turbine inlet and exit aggregate mass over 2 cycles with 10 and 30 Hz hydrogen-fueled PDC with 0.75 fueled and purge fractions**

Figure 52 shows storage in the system as the difference between the inlet and exit aggregate mass at a moment in time. Initially, aggregate mass is zero at time zero. As the detonation arrives at the turbine inlet, mass storage increases between the inlet and exit measurement locations, while the exit mass flow rate remains relatively low. Subsequently, the inlet mass flow rate decreases while the exit mass flow rate increases and remains higher than the inlet, depleting the mass storage. By the end of the detonation cycle, mass accumulation returns to returns to zero. The unsteady mass storage behavior is more pronounced at 10 Hz; however, the same amount of mass flows

through the system at both frequencies over each complete detonation cycle because the fueled and purge fractions were the same at both frequencies.

Figure 53 shows time-varying mass storage in the system over 14 full cycles at the 30 Hz PDC operating frequency with 0.75 fueled and purge fractions. Variation in mass storage and depletion results from cycle-to-cycle variation in pulsed detonation arrival time and flowfield pressures, temperatures, and velocities.

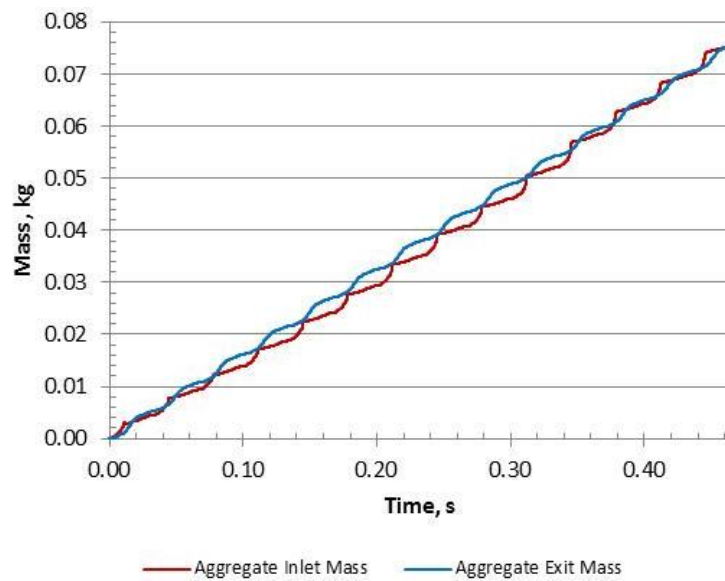
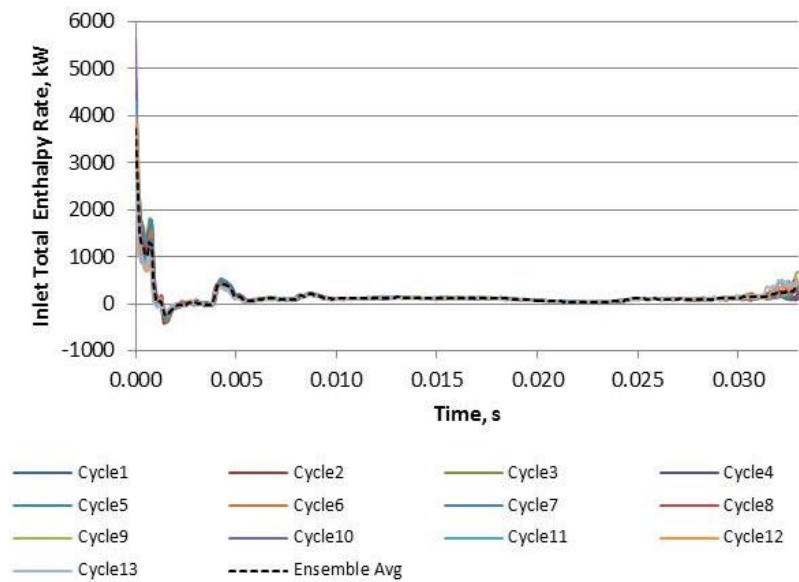


**Figure 53. Turbine inlet and exit aggregate mass over 14 cycles with 30 Hz hydrogen-fueled PDC with 0.75 fueled and purge fractions**

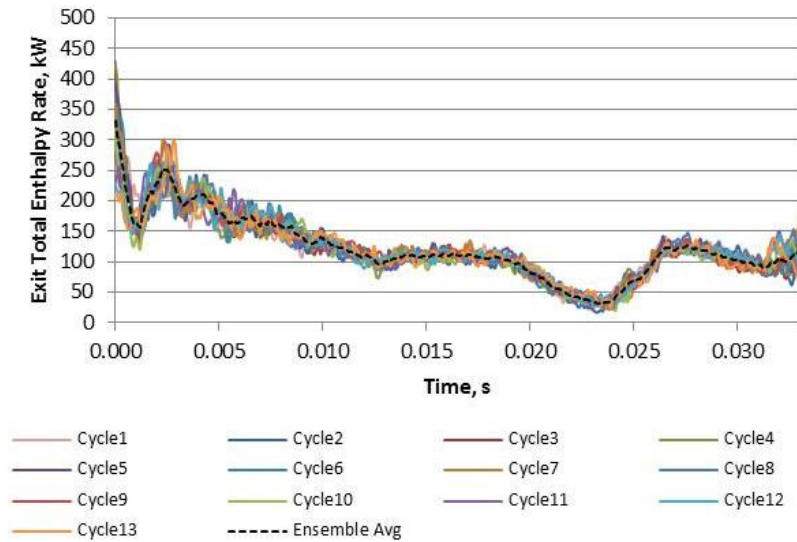
#### ***VI.B.6. Time-Resolved Turbine Inlet and Exit Flowfields: Total Enthalpy Rate***

Figure 54 shows time-resolved inlet total enthalpy rate for 13 successive detonation cycles at 30 Hz with 0.75 fueled and purge fractions. Total enthalpy rate was calculated using Eq. (35) on page 49. The profiles were shifted to align peak magnitudes. The profiles are very similar in shape except for a small portion of the cycle time after 30 ms during the fill phase and during the detonation expansion in the first 2 ms. The

ensemble average is indicated by the dashed line. Figure 55 shows time-resolved exit total enthalpy rate for 13 successive detonation cycles at 30 Hz with 0.75 fueled and purge fractions. The scale of the vertical axis is much smaller than for the inlet figure, amplifying the variation between cycles. As observed at the inlet, the exit total enthalpy rate profiles are very similar in shape except in the last 30 ms. The variation during the fill phase is likely due to the relatively low water content in the air, compared to that of the combustion products which are expelled during blowdown and purge. The laser absorption measurements were based on water molecules and relies on sufficient water content to resolve absorption features.

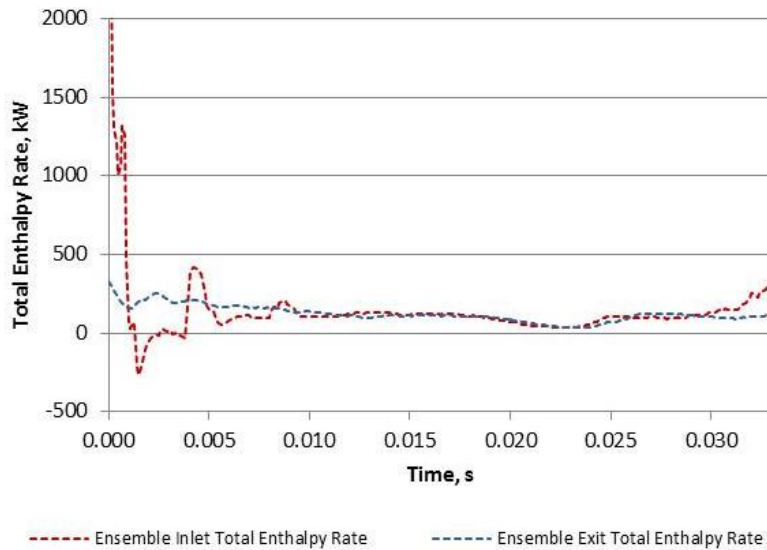


**Figure 54. Turbine inlet total enthalpy rate over 13 cycles with 30 Hz hydrogen-fueled PDC with 0.75 fueled and purge fractions**



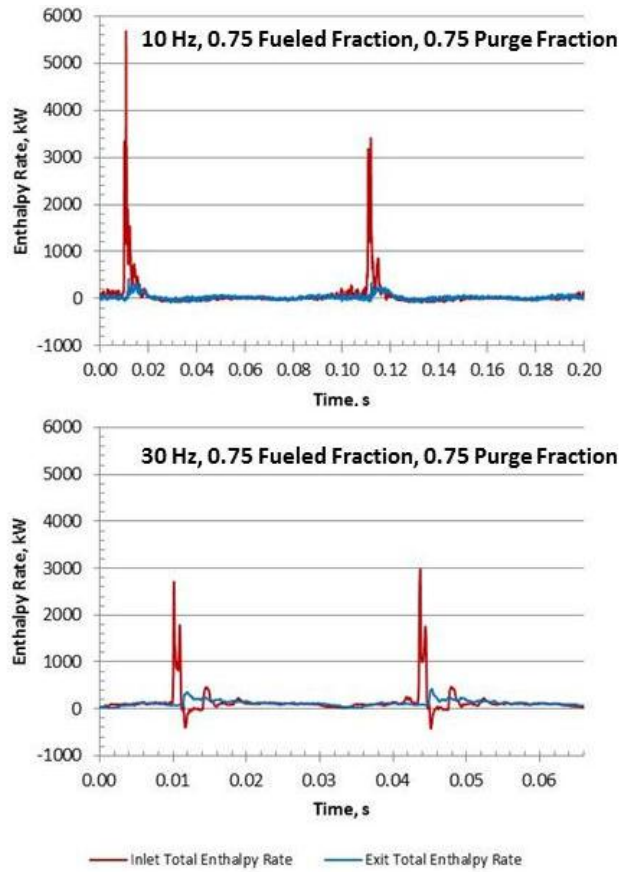
**Figure 55. Turbine exit total enthalpy rate over 13 cycles with 30 Hz hydrogen-fueled PDC with 0.75 fueled and purge fractions**

Figure 56 compares the ensemble-averaged inlet and exit total enthalpy rate at 30 Hz with 0.75 fueled and purge fractions. The peak ensemble-average inlet enthalpy rate is reduced from about 5 MW to about 2 MW. Reverse flow at the turbine inlet results in negative total enthalpy rate at about 2 ms; however, the subsequent peak is associated with the reflected pressure wave that likely returns from the engine head at about 5 ms. There is another peak at the inlet which occurs around 8 ms and is associated with the second reflected pressure wave returning from the engine head. The exit total enthalpy rate appears to be relatively steady, compared to that of the inlet.



**Figure 56. Turbine inlet and exit total enthalpy rate ensemble-averaged over 13 cycles with 30 Hz hydrogen-fueled PDC with 0.75 fueled and purge fractions**

Figure 57 shows turbine inlet and exit total enthalpy rate over two full detonation cycles at 10 and 30 Hz PDC operating frequencies. Inlet peak enthalpy rate is higher at 10 Hz, but the quiescent period is smaller at 30 Hz. The peak inlet enthalpy rate at 10 Hz exceeded 5 MW; whereas, peak inlet enthalpy rate at 30 Hz did not exceed 2.5 MW. During the quiescent region of the 10 Hz enthalpy profile, there is little enthalpy available for turbine power. The turbine spins down during the quiescent region, depleting stored rotational energy, as discussed in Appendix F. The duration of the quiescent region at 30 Hz is shorter; therefore, there is less turbine spin down.



**Figure 57. Turbine inlet and exit total enthalpy rate over 2 cycles with 10 and 30 Hz hydrogen-fueled PDC with 0.75 fueled and purge fractions**

## VII. Discussion

The following discussion addresses the broader application of this research: applying the unsteady turbine efficiency formulation to steady turbine turbines, comparing unsteady to steady turbine operation, and comparing radial to axial turbines.

### VII.A. General Application of the Unsteady Turbine Efficiency Formulation

A simulated steady test case was created to determine if the proposed unsteady turbine efficiency formulation would function with a steady operation. The test case included single step transient conditions, which were related to a nominal, near adiabatic, steady turbine with 86% isentropic efficiency. A profile of the periodic run conditions is shown in Fig. 58, including initial transients at the turbine exit with increasing velocity and decreasing static temperature and static pressure. Subsequently, there was a sudden inlet static pressure drop followed immediately by a rise in turbine exit static temperature and static pressure and drop in turbine exit velocity. Inlet static temperature and velocity were steady over the cycle. Continuity was maintained over the period. The run profile was that of a step change in turbine inlet pressure, affecting inlet density, mass flow and total enthalpy rate. The turbine inlet pressure change was attenuated at the exit, such that the changes in density and mass flow rate at the turbine exit were realized in terms of changes in velocity and temperature. Applying Eq. (29) on page 24, with the inlet enthalpy total rate weighting parameter and the constant pressure heat transfer model with  $\psi = 0.75$  yielded a result of 86.34% turbine efficiency. Therefore, the formulation shows good potential for general application across unsteady and steady turbine operation.

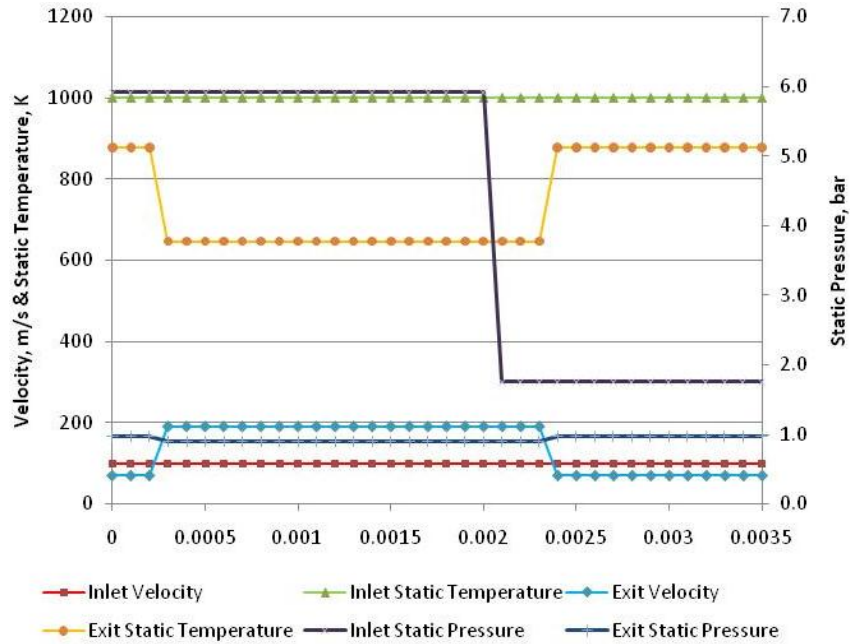


**Figure 58. Simulated test case for evaluating the proposed unsteady turbine efficiency formulation with a steady operation including a single transient condition**

A separate study was conducted to determine the effect of unsteady turbine efficiency on apparent average efficiency. Figure 59 shows an analytical model for time-varying turbine efficiency, with equal steps in time, turbine efficiency drop, and total specific enthalpy expansion. Change in total pressure for each expansion step was calculated based on the initial total specific enthalpy and the turbine efficiency associate with the expansion. The first total specific enthalpy expansion step occurred with 60% turbine efficiency and final expansion step occurred with 48% efficiency. Thus, the average efficiency is 54%; however, the apparent efficiency from the initial total specific enthalpy and total pressure condition to the final state is 40%. Apparent average turbine efficiency was skewed toward a lower efficiency over the full expansion. Therefore, average turbine efficiency results in this study were likely skewed in a similar fashion.

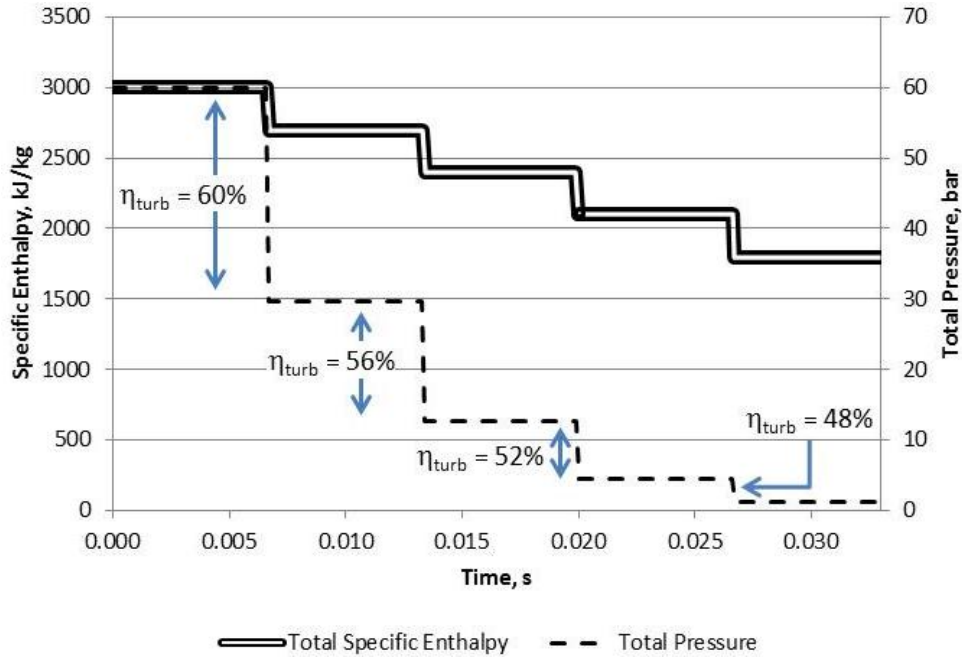


**Figure 59. Simulated test case for time-varying turbine efficiency, with equal steps in time, turbine efficiency drop, and total specific enthalpy expansion**

### VII.B. Steady and Unsteady Turbine Operation

Instantaneous and cycle-average operating points indicated on the steady dynamometer map shown in Fig. 60 show that the coupled compressor experienced nearly steady operation. The instantaneous dynamometer operating points are indicated for the 30 Hz operation with 0.75 fueled and purge fractions, showing that compressor conditions through-out the cycle remained within the 77% efficiency island, which was used to calculate power with Eq. (27) on page 23. The instantaneous behavior was similar at the other PDC driven conditions, in that operation was confined to cyclic pattern at about the same pressure ratio and ranging by about 15,000 RPM across speed lines. Furthermore, the time-average operating points from the all the operating PDC

driven conditions fell on the dashed dynamometer operating line connecting the center of the efficiency islands.

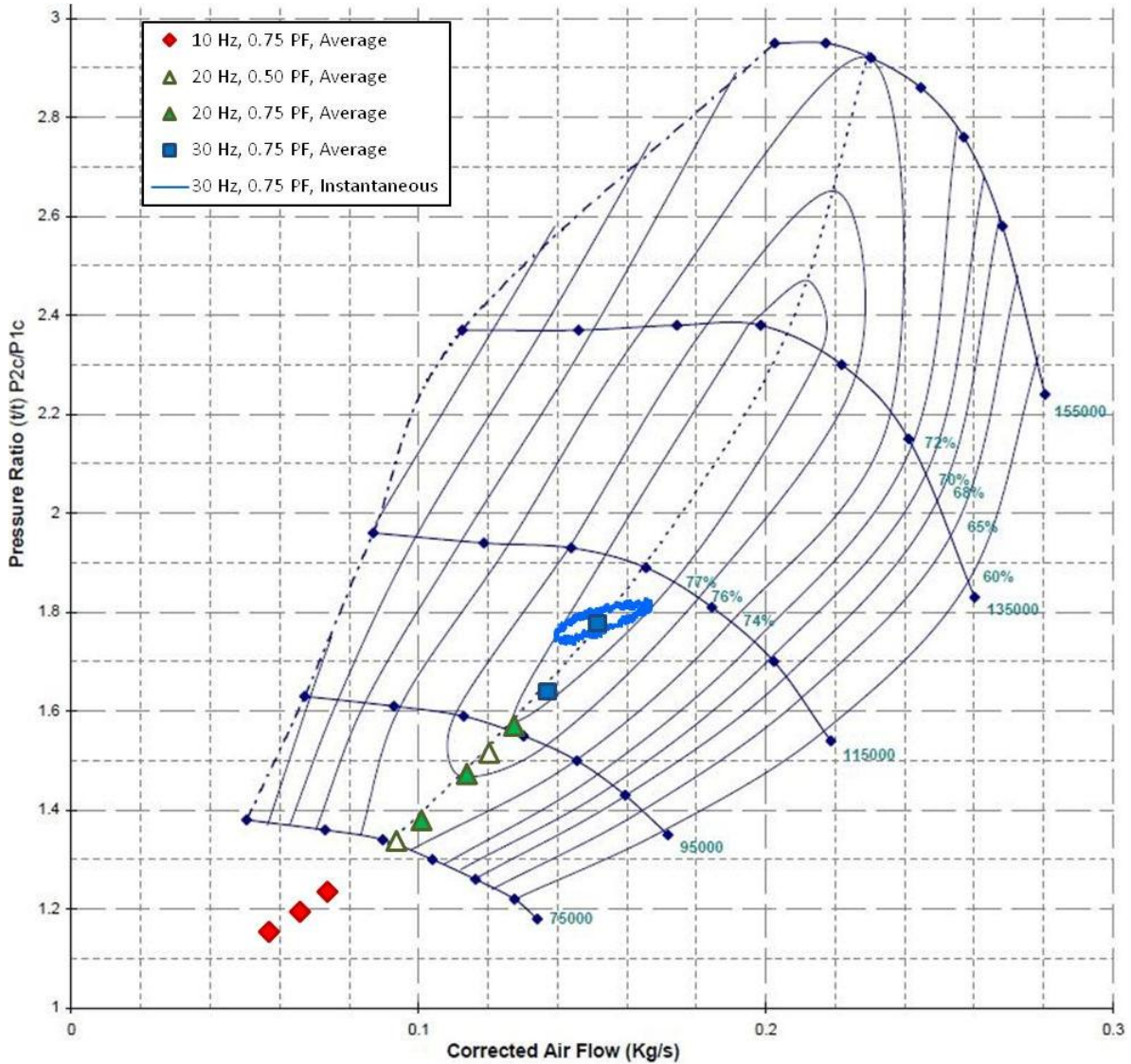


**Figure 60. Compressor dynamometer map with instantaneous and average operating points with 30 Hz hydrogen-fueled PDC with 0.75 fueled and purge fractions and with average operating points for other frequencies, fueled fractions, and purge fractions**

The cycle-average dynamometer operating condition for the hydrogen-fuel PDC at 30 Hz with 0.75 fueled and purge fractions was used to model an equivalent steady

deflagration driven turbine, using a formulation for corrected compressor mass flow,  $\dot{m}_{c,compr}$ , shown in Eq. (45) that was developed from compressor-turbine work and mass balanced relations presented by Mattingly (1996).

$$\dot{m}_{c,compr} = \frac{\pi_{compr}}{\sqrt{\pi_{compr}^{\frac{\gamma-1}{\gamma}} - 1}} \left( \frac{\dot{m}_{c,turb} \pi_{burner}}{1+f} \right) \sqrt{\eta_{compr} \eta_{turb} \eta_{mech} \left( 1 - \pi_{turb}^{\frac{\gamma-1}{\gamma}} \right) \frac{c_{p,turb}}{c_{p,compr}} (1+f)} \quad (45)$$

Compressor pressure ratio,  $\pi_{compr}$ , and efficiency,  $\eta_{compr}$  were obtained from the cycle-average condition on the dynamometer map. Turbine efficiency was assumed to be the manufacturer reported maximum 61%, which is expected for the high-power condition. Combustor pressure ratio,  $\pi_{burner}$ , was assumed to be unity. Fuel-air ratio,  $f$ , was assumed to be stoichiometric. Constant pressure specific heat for the compressor,  $c_{p,compr}$ , was assumed for ambient air (1.005 kJ/kg K). Constant pressure specific heat for the turbine,  $c_{p,turb}$ , was assumed to be 1.143 kJ/kg K, which was based on an average turbine inlet temperature of 1100 K. Iterations on corrected turbine mass flow,  $\dot{m}_{c,turb}$ , and expansion ratio,  $\pi_{turb}$ , were made until the point was converged on the manufacturer steady turbine operating map, as shown by point A<sub>2</sub> in Fig. 61 with a pressure ratio of 2.20. At this operating point, steady turbine operation would normally be choked, as indicated by the plateau in turbine efficiency at point A<sub>1</sub>. Point B<sub>2</sub> on the operating map represents the equivalent steady operating point for the cycle-average turbine expansion ratio of 1.72 experienced with the actual PDC-driven operation; however, the cycle-average corrected turbine mass flow was above the steady operating line, as denoted by

point B<sub>3</sub>. Thus, the cycle-average turbine operating condition does not fall on the steady turbine operating map. The PDC-driven turbine produces equal power to the compressor as a steady turbine, while at an operating condition with a lower average turbine efficiency. Therefore, the potential exists for design improvements to the sub-optimal PDC-driven turbine used in this study, thereby producing greater power than a similar steady deflagration driven turbine.

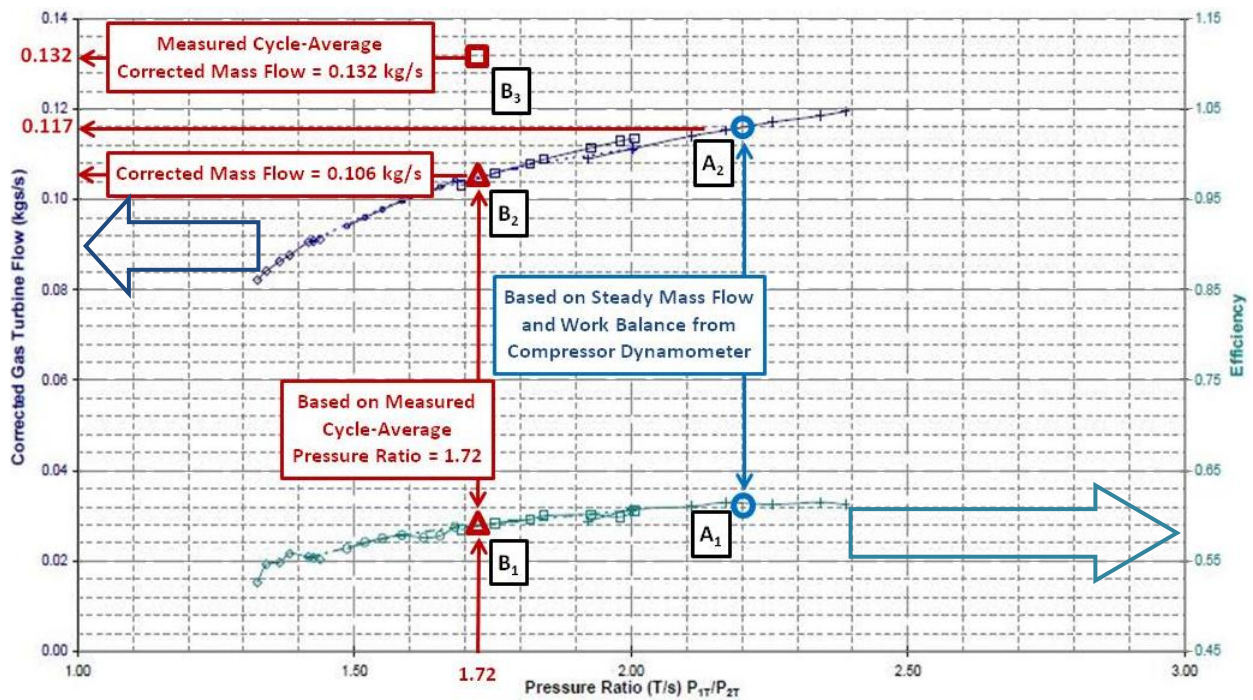


**Figure 61. Steady turbine model operating points for the condition equivalent to the steady compressor dynamometer map with 30 Hz hydrogen-fueled PDC with 0.75 fueled and purge fractions**

Whereas the instantaneous dynamometer operating points did not fluctuate significantly from the cycle-average operating condition, the instantaneous turbine operating points fluctuate beyond the scale of the manufacturer turbine operating map, as shown in Fig. 62, and do not collapse to a single operating line. The instantaneous points

indicate that the majority of time is spent on the left side of the map with a pressure ratio less than 2.0; however, nearly half of the turbine mass flow, associated with blowdown, occurs on the right side, where the turbine is choked under steady operating conditions.

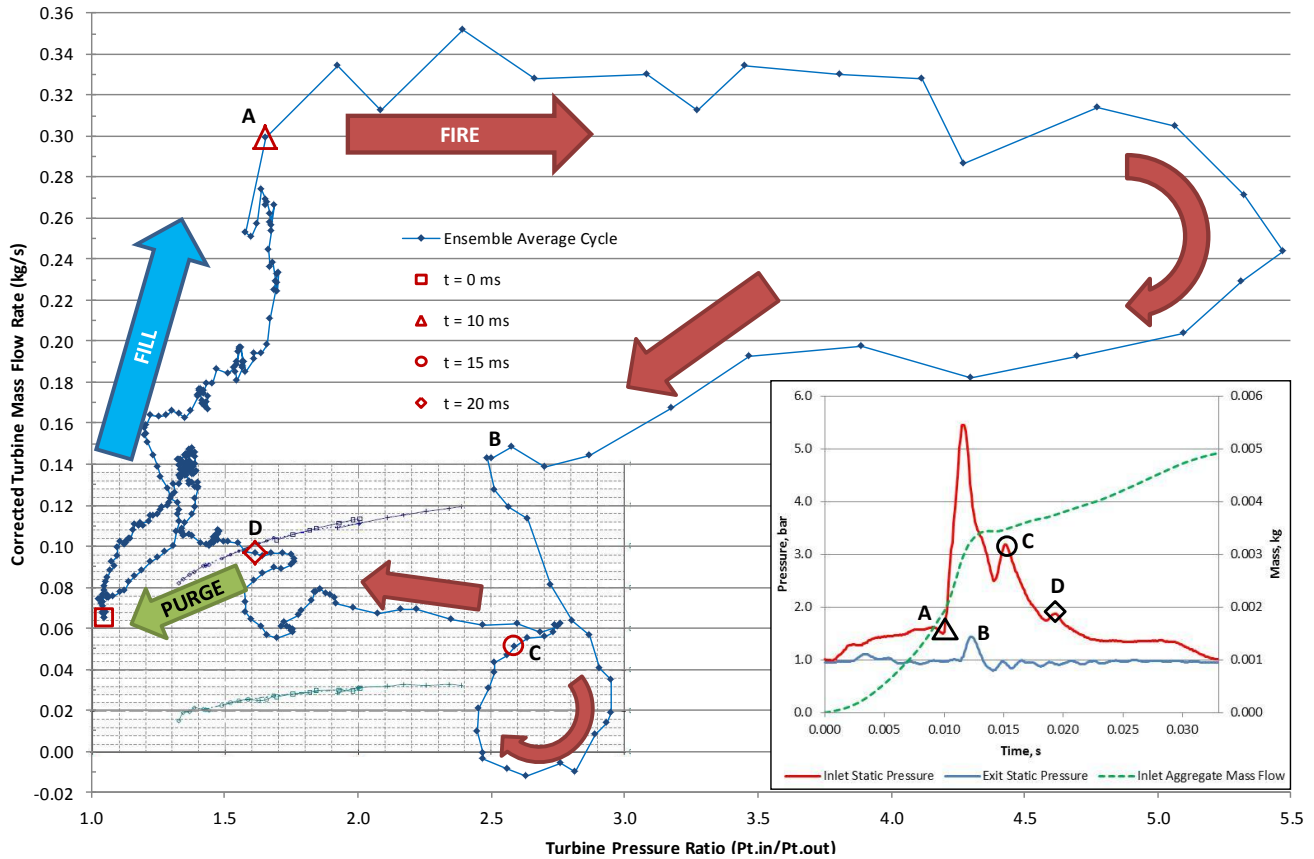


**Figure 62. Instantaneous turbine model operating points with 30 Hz hydrogen-fueled PDC with 0.75 fueled and purge fractions**

The instantaneous turbine operating points in Fig. 62 show that the turbine responded to the reflected pressure waves at the turbine inlet that were observed during blowdown at about 15 ms and 20 ms. The time-resolved power shown in Fig. 36 on page 68 did not show the fluctuation in turbine response. Therefore, the instantaneous unsteady forcing function imparted to the turbine was damped in the power output. It is

not apparent from this study whether or not an axial turbine would also have a damped power response.

### **VII.C. Radial and Axial Turbines**

The following discussion distinguishes the operational differences between radial and axial turbines and addressed the potential general application of this research for both types of turbines. Both turbine types serve the same basic purpose to extract mechanical work from the kinetic energy of exhaust gas. Wilson (1993) provides a detailed discussion of the design and operational differences between axial and radial flow turbines. Radial-inflow turbines typically have lower efficiencies than axial turbines due to more flow turning, higher aerodynamic loading, and larger surface area. Due to the lower efficiency, radial turbines are typically run as a single stage; whereas, axial turbines are often multi-stage with a lower exit velocity.

Radial turbines usually have a higher rotor speed than axial turbines and higher rotating inertia than axial turbines, a potential advantage in a pulsed detonation operation. However, the longer hub of a radial turbine with more wetted surface area has high thermal stresses, which is a potential disadvantage in detonation driven operation. On the other hand, axial turbines are more susceptible to stresses from bending moments, torsion, buffeting, flutter, and/or vibration. Both types of turbines would experience significant axial loads from pulsed detonations; however, the manner in which they handle the load is different. The axial turbine is more likely to experience blade bending, and the radial turbine is more likely to transmit the axial load to the bearings, as was observed with preliminary tests in this research.

The design method for axial and radial turbines is similar, usually based on Euler's equation and involving velocity triangles; however, traditional design methodologies for both turbine types do not account for such unsteady flow as experienced with pulsed detonation operation. In general, radial turbines are more stall tolerant due to longer blade passages. Therefore, the reverse flow observed at the turbine inlet is more likely to stall an axial turbine, reducing performance in terms of power output and isentropic efficiency.

The thermodynamic analysis and modeling in this research was not predicated on either type of turbine, and the formulation for unsteady turbine efficiency has good potential to treat radial and axial turbines impartially. Average specific power will likely increase with frequency, regardless of the turbine type, due to larger duty cycles; however, it is unknown how significant the inherent differences in operability will effect isentropic efficiency.

## VIII. Conclusions

Previous work demonstrated the capability of a PDC to drive a radial turbine. The practicality of that arrangement was examined in this current study, identifying relationships between turbine inlet and exit flowfield properties, time-resolved turbine power and cycle-averaged specific work and isentropic turbine efficiency. Experiments were conducted with the radial turbine of Garrett GT28R journal bearing turbocharger driven by a pulsed detonation combustor fueled by hydrogen or ethylene.

The results in this study show that cycle-average specific work and isentropic efficiency of pulsed detonation driven radial turbine increase with increasing frequency. The increase in specific work was related to increased power duty cycle increased, as shown by time-resolved turbine power. The increase in efficiency was related to shorter quiescent periods at the turbine inlet, as shown by the time-resolved flowfield. Time-resolved fluctuations were attenuated at the turbine exit. The optimal PDC frequency was found to have a 50% duty cycle, minimizing the quiescent periods at the turbine inlet. Practical integration of a PDC in a gas turbine engine will require the ability to throttle power while maintaining high operating frequency.

Mass accumulation and expulsion was observed during the cycle, requiring cycle-averaged formulations for specific work and turbine efficiency. The formulation for turbine efficiency requires an inlet weighting parameter for the total pressure ratio term. Inlet total enthalpy rate is the preferred weighting parameter because it differentiates between hot and cold gases. The proposed formulation for average unsteady turbine efficiency produced sound results for steady and unsteady operation, using a constant

pressure heat transfer model with a 75% inlet heat transfer fraction parameter. Ensemble averaging turbine efficiency showed that standard deviation across multiple cycles was low.

Preliminary results showed a 41.3% improvement in cycle-average specific work over conventional steady deflagration driven operation; however, the current study showed that cycle-average turbine efficiency was about 30% less than the manufacturer reported maximum turbine efficiency. Therefore, performance improvements from the combustor were marginally greater than performance deterioration in the turbine. Comparison of steady and unsteady turbine operation showed that the unsteady turbine was less efficient than the steady turbine while producing equivalent power. Significant potential was demonstrated for future PDC-turbine design improvements to produce more power than a steady deflagration driven turbine.

## **IX. Recommendations**

This current work evaluated turbine performance during short duration test runs. Longer duration runs were performed but did not include flowfield instrumentation. In the future, actively cooled flowfield instrumentation should be used to run experiments to thermal equilibrium, reducing the effects of heat transfer into the turbine housing.

The experiments conducted in this study included a radial turbine; however, an axial turbine is more likely for future applications in which a pulsed detonation combustor would be embedded into conventional Brayton cycle gas turbine engines. Potential applications include large engines, in which radial turbines are unusual. Further research should consider an arrangement with full admission pulsed detonation driven axial turbines in order to determine if the results and conclusions from this research apply in a broad sense across both radial and axial turbines.

Topics for future research with axial turbines should include performance, durability, and operability. Generally, radial turbine blades are more durable and more stall tolerant than axial turbines. Thus, future experiments with axial turbines should include studies to determine if similar time-resolved turbine power and inlet and exit flowfield characteristics are present as those observed in this study with a radial turbine, including reverse flow at the turbine inlet. The laser absorption instrumentation approach used in this research should be used in future experiments for time-resolved flowfield measurement, in order to acquire full-cycle temperatures, pressures and velocities. High speed cameras should also be used for flow visualization at the turbine inlet and for

optical pyrometry and particle streak velocimetry during blowdown, in order to increase confidence in laser absorption measurements at the same conditions.

Further research should be conducted to determine how axial turbines respond to the reflected inlet pressure waves observed in this study with a radial turbine. Axial turbines are more generally more susceptible to fatigue stresses from blade bending, flutter, and vibration, which are more likely to occur in the pulsed detonation driven operation with reflected pressure waves at the turbine inlet. Future experiments should include blade stress measurements for bending and twist. Once the blade stresses are characterized, turbine design improvements should be made and tested.

Operability experiments should be conducted with pulsed detonation driven axial turbines to study the relationship between PDC operating parameters and separated flow on the blade surface. Specifically, surface pressure taps should be placed along blade suction and pressure surfaces to characterize unsteady pressure coefficients and determine regions of separated flow. Several passive and active flow control schemes exist for conventional axial turbines that offer the potential to improve operability and performance in a PDC arrangement.

Finally, the formulation for unsteady turbine efficiency proposed in this study should be used as the standard when comparing steady and unsteady turbine performance. There is currently a need for an industry standard, and the formulation proposed here is based on sound thermodynamic principles. In particular, the unsteady formulation must be integrated over at least one full cycle and apply an extensive property as a weighting parameter for the pressure ratio term.

## Appendix A: Development History of Pressure-Gain Combustion and Gas Turbine

### Integration

A brief summary of previous research is provided here to explain how the current research fits into the development history of pressure-gain combustion and gas turbine integration. A general timeline is provided in Fig. 63, including significant milestones which are discussed in further detail below. The term “pressure-gain combustion” is intended to include the broad class of combustion processes that experience a pressure rise, including constant volume and near constant volume combustion with subsonic and supersonic combustion fronts. Subsonic pressure-gain combustors are also referred to as pulsejet combustors. The theory and operation of pulsed detonation combustors is contained in Appendices B and C. There are three general classifications for arrangements that have been studied for extracting power from confined detonations in an aircraft propulsion system: a multi-tube PDC array and mixed-flow axial turbine, a detonation wave rotor and axial turbine, and an integrated PDC and radial turbine.

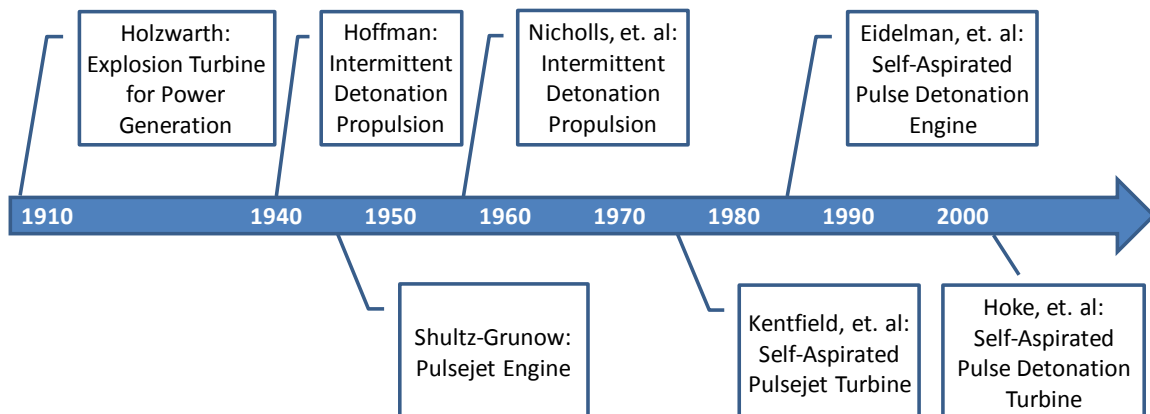


**Figure 63. Development timeline of pressure-gain combustion driven turbines**

## Early Developments with Pressure Gain Combustion

One of the earliest gas turbines utilized pressure-gain combustion and is attributed to German engineer Hans Holzwarth (Holzwarth 1912). In 1908, Holzwarth ran experiments with a turbine driven by a confined explosion, and ultimately achieved a 1 Hz operating frequency and 13% overall efficiency while producing over 4,474 kW (6,000 hp). His powerplants ran successfully on a variety of coal gas and liquid fuels, including benzene and tar oil. A cross section of the arrangement is shown in Fig. 63. The powerplant installed in Mannheim in 1910 used ten combustion chambers with mechanical valves for fuel and air, and the cycle included fill, fire and purge phases. Peak chamber pressure was 11.7 to 13.8 bar (170 to 200 psia) with 2.3 to 3.0 bar (33 to 43 psia) pre-compression. The turbine may not have been driven by detonations, but it demonstrated practical application of unsteady, pressure-gain combustion driven operation.

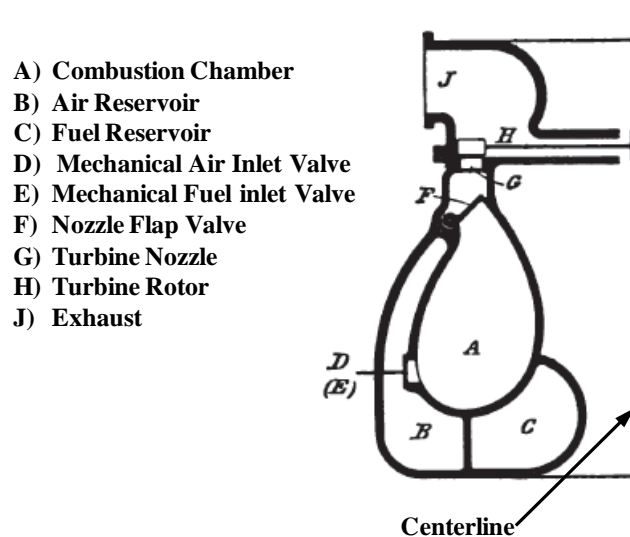


**Figure 64. Cross section of the Holzwarth pressure-gain combustion gas turbine (Holzwarth 1912)**

As German research in pressure gain combustion progressed, Hoffman (1940) explored intermittent detonations for propulsion without turbomachinery, using acetylene/oxygen and benzene/oxygen mixtures. He attempted to determine an optimum cycle frequency; however, the injection flow rate and ignition were out of phase, leading to the conclusion that intermittent detonations could only occur at low frequencies. Subsequent work (Shultz-Grunow 1947) continued through World War II, and the German pulsejet powered V-1 Buzz Bomb was an offshoot. Shortly after the war, U.S. researchers Zipkin and Lewis (1948), achieved a 2.9 maximum pressure ratio with an explosion cycle engine and reported specific thrust as high as  $35 \text{ s}^{-1}$ .

#### **Developments in the 1950's and 1960's with Pulsed Detonations**

In the span of 1950-1970, several other research efforts continued to explore the practicality of pressure-gain combustion for thrust applications, using detonations without turbomachinery. In 1952, detonations were studied with a Schlieren system (Nicolls and Morrison 1952), and subsequent experimental investigations studied the feasibility of a thrust producing device using intermittent gaseous detonation waves (Nicholls, et al. 1955; Dunlap, et al. 1957). Operating frequencies peaked at 35 Hz, using hydrogen and acetylene fuels. Krzycki (1962) conducted similar analytical and experimental investigations with propane/air, demonstrating operating frequencies of 25 and 50 Hz.

#### **Developments in the 1970's with Pressure-Gain Combustion Driven Turbines**

In the 1970's, there was a resurgence in coupling turbines with pressure-gain combustion (Kentfield 1971; Marzouk and Kentfield 1974; Catchpole and Runacres 1974; Kentfield, et al. 1977; Kentfield, et al. 1979). Kentfield, et al. (1979) postulated

that for simple cycles, specific power output and specific fuel consumption improved one to two percent for every percent pressure gain in the combustor as illustrated in Fig. 65. They studied the effect of combustor geometry and operating conditions on the performance of a valveless pulsejet combustor with an ejector at the exit, achieving an operating frequency of 190 Hz. They achieved a combustor total pressure gain of 6% at a combustor total temperature ratio of 2.5. Kentfield, et al. (1979) also concluded that pressure-gain combustors could have very beneficial effects on overall gas turbine performance. Ultimately, a second version of their pulsejet combustor demonstrated the capability to maintain a small pressure gain of up to 1.6% while driving Cussons P9000 gas-generator turbine, concluding that a 40% potential net power improvement was achievable with a low pressure ratio engine (Kentfield and O'Blenes 1990). Whereas this conclusion was promising, it did not offer the advantages of detonation combustion.

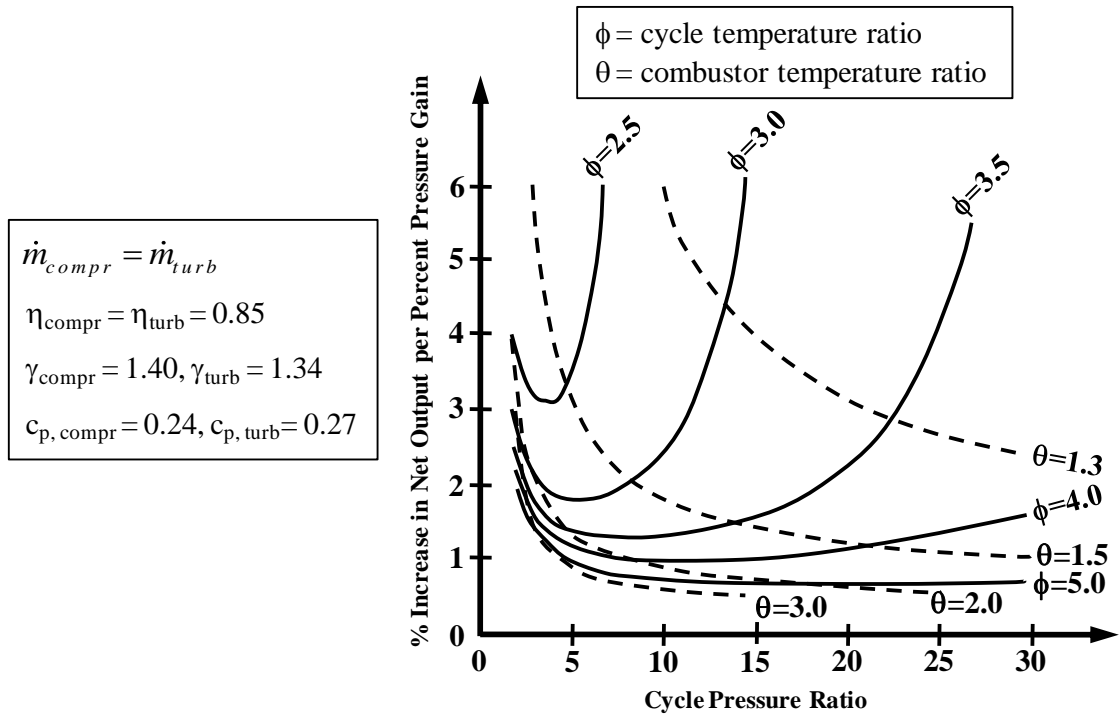


**Figure 65. Relative improvement in net power output per percent pressure gain in the combustor, varying with of cycle pressure ratio, cycle temperature ratio, and combustor temperature ratio (Kentfield, et al. 1979).**

### Developments in the 1980's with Detonation Engines

In the mid 1980's, detonation engine concepts were revisited (Helman, et al. 1986), and a self-aspirated PDE system demonstrated operation at 25 Hz without a turbine. Early versions of these engines used an oxygen rich pre-detonator to initiate the cycle. Subsequently, much focus was given to improvements in detonation initiation, as well as PDE thrust production (Dean 2003). This continued through the 1990's, and is still the subject of much PDE research.

### Developments in the 1990's with Wave Rotors

In the 1990's, a renewed interest in wave rotors was targetted toward jet engine application, as shown in Fig. 66 (Wilson and Fronek 1993). Wave rotors use axially

aligned passages and unsteady waves to produce streams of gas at either higher or lower total pressure than the input stream. As the rotor spins, the passages are exposed to ports at different pressures. As a passage containing high pressure gases is exposed to a low pressure exhaust port, an expansion wave propagates into the passage. As the rotor continues to spin, the passage achieves a lower pressure until it reaches the next inlet port which is at a higher pressure, which results in propagation of a shock wave, increasing the passage back to its initial condition. Early NASA research determined that leakage losses were very significant (Wilson and Fronek 1993). Later NASA work (Welch, et al. 1999) predicted a 300% increase in peak engine temperature and 25 to 30% increase in engine overall pressure, coupling a self-cooled, four-port wave rotor (shown in Fig. 67) to a Rolls-Royce Allison model 250 turboshaft engine. Recent studies have proposed a new wave rotor concept that integrates a PDC, as shown in Fig. 68 (Snyder, et al. 2002; Akbari, et al. 2007).

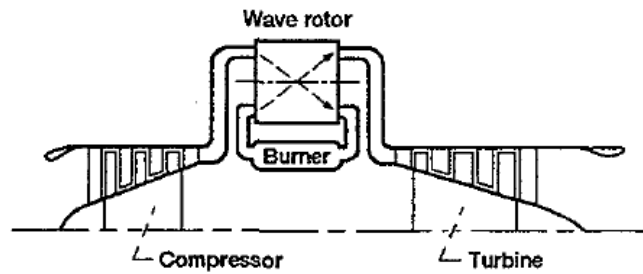


**Figure 66. Schematic of a wave rotor used as a topping cycle for jet engines (Wilson and Fronek 1993)**

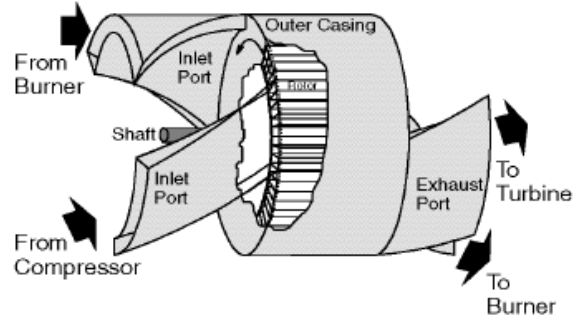


**Figure 67. Schematic of NASA self-cooled, four-port wave rotor (Welch, et al. 1999)**

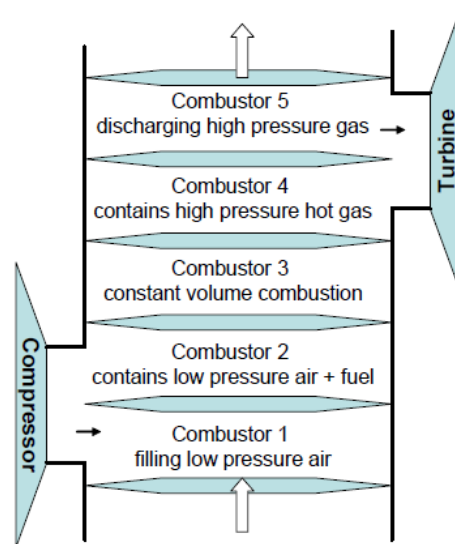


**Figure 68. Schematic of constant volume combustion wave rotor (Akbari, Szynda and Nalim 2007)**

### **Developments in the 21<sup>st</sup> Century with Pulsed Detonation Driven Turbines**

A gas turbine driven by pulsed detonation combustion was first realized by the Air Force Research Laboratory (AFRL) with a self-aspirated PDE and Garrett T3 turbocharger (Hoke, et al. 2002). Two simultaneously firing PDE tubes drove the turbine, and the capability demonstration included a 25 minute continuous run time. Subsequent work (Schauer, et al. 2003) reported average cycle thermal efficiencies up to 6.8%.

Operating frequencies ranged from 20 to 40 Hz with stoichiometric hydrogen-air mixtures. Peak pressure attenuated through the turbine from over 27.6 bar (400 psi) to less than 6.9 bar (100 psi).

Sakurai, et al. (2005) also experimented with PDC driven turbocharger with a single detonation tube, showing that power extraction improved with increasing operating frequency. They reported thermal efficiencies as high as 2.2%. Later work by Tsuji, et al. (2008) explored higher frequencies up to 40 Hz, using two alternately firing PDC tubes for an overall operating frequency as high as 80 Hz. Turbine inlet pressure diminished with increasing frequency and thermal efficiency did not exceed 1%. Tsuji, et al. (2008) concluded that the alternating fire pattern caused interference between detonation tubes, so that the exit shock from one tube affected the fill phase of the other tube.

Deng, et al. (2009) experimented with a turbocharger, comparing cold flow driven operation with detonation driven operation. Results showed the impact of equivalence ratio on peak turbine inlet pressure and pressure attenuation through the turbine. Peak pressure occurred at an equivalence ratio of 1.15; however, this condition also experienced the least attenuation.

Tsukui, et al. (2009) investigated turbocharger performance with non-reacting high pressure flow, simulating PDC operation. The parametric study considered the effect of operating frequency, duty cycle, and mass flow on rotor speed. The test facility used a pressure tank and rotary valve. Results indicated that higher tank pressure and longer duty cycles resulted in higher rotor speeds. Rotor speed also increased with mass flow and remained independent of frequency.

### *Two-Dimensional Detonation-Turbine Interaction Studies*

Rasheed, et al. (2004) performed experimental and numerical investigations of a 2-D turbine cascade, using high-speed flow visualization and unsteady computation fluid dynamics. In both sets of results, strong shocks were observed to reflect off the turbine cascade and proceed upstream. A weaker shock passed through the turbine cascade. Furthermore, there was significant time variation in turbine performance from one cycle to the next. The cycle-to-cycle variation diminished over time, reaching a quasi-steady state. The study included a cold-flow starting arrangement in which the first pressure pulse impacted the turbine cascade without a combustion reaction. Peak turbine pressure ratio dropped by 20% from the first to sixth cycles, and the temperature ratio became quasi-steady within the first three cycles. Nango, et al. (2007) also observed a strong reflected shock in a 2-D finite difference method study of a turbine cascade. Additionally, time integration of total enthalpy revealed an 81.8% isentropic turbine efficiency and 18.9% thermal efficiency. Isentropic efficiency improved at higher rotor speeds. Nango, et al. (2008) defined thermal efficiency as:

$$\eta_{th} = \frac{\dot{W}_s}{LHV} \quad (46)$$

where  $\dot{W}_s$  is specific turbine power, and LHV is the lower heating value of the fuel: hydrogen. Specific power, as defined by Nango, et al. (2008), is the time integrated power (i.e., work) divided by total mass flow per cycle and fuel-air ratio as shown in Eq. (47).

$$\dot{W}_s = \frac{W_{cycle}}{m_{cycle} \cdot \phi_{fuel/air}} \quad (47)$$

Nango, et al. (2008) defined turbine work as total mass flow per cycle multiplied by the difference in time-averaged enthalpy across the turbine as shown in Eq. (48).

$$W_{cycle} = m_{cycle} \cdot (\bar{h}_{in} - \bar{h}_{out}) \quad (48)$$

Kojima, et al. (2007) performed a design study for integrating a turbine and PDC, assuming a general single stage axial turbine without mixed flow. The 2-D numerical study modeled a detonation tube with converging nozzle that simulated a turbine. Three different nozzle shapes were considered with converging angles ranging from 0 to 10 degrees.

#### ***Mixed-Flow, Detonation-Driven Axial Turbine Studies***

Axial turbines have been experimentally studied with a multi-tube, can-annular PDC arrangement (Caldwell and Gutmark 2008; Glaser, et al. 2007; Van Zante, et al. 2007; Baptista, et al. 2006). Rasheed, et al. (2005) experimented with an arrangement consisting of eight, 52.5 mm (2 inch) diameter PDC tubes driving a single axial turbine stage designed for 3.6 kg/s (8 lbm/s), 25000 RPM, and 746 kW (1000 hp). The rig operated up to 30 Hz (per tube) with stoichiometric ethylene-air, achieving a rotor speed as high as 18,500 RPM and extracting as much as 261 kW (350 hp). Secondary air, referred to as “bypass” air, mixed with PDC exhaust before entering the turbine. The steady stream of bypass air was used to cool the PDC tubes and also served as a means to dampen the pressure pulses of detonation waves. Secondary flow rates were equal to or

greater than primary air flow into the PDC. The turbine stator and rotor were from a locomotive scale turbocharger, and the coupled compressor was used as a dynamometer to apply a load to the turbine and measure power. Work extraction was determined from measurements of the compressor mass flow, pressures, and temperatures. Turbine pressure measurements indicated that peak pressure was attenuated across the turbine from 18.0 bar (260 psi) at the inlet to 2.1 bar (30 psi) at the exit.

Subsequent work performed by Baptista, et al. (2006) used the same test rig and reported mechanical blade response with strain gages placed on six turbine stator vanes. Tests were conducted at 2 kg/s (4.4 lbm/s) air flow, split evenly between primary and secondary flow paths, achieving 11000 RPM rotor speed. Tests were conducted for both sequential PDC tube operation and simultaneous operation. The staggered firing pattern spread the resonance response over a wider frequencies and reduced the maximum resonance amplitude.

Van Zante, et al. (2007) conducted numerical studies with a PDC and axial turbine arrangement, including a single stage stator and rotor. A 3-D, viscous, time-accurate Reynolds-average Navier-Stokes solver was used in a rotating cartesian coordinate system. The PDC arrangement was such that secondary air passed around the detonation tubes with a volumetric flow rate similar to that of the primary air flow, mixing just before entering the turbine. The initial condition was set with unreacting primary and secondary flow, then the solver proceeds with three PDC cycles. Van Zante, et al. (2007) observed pressure attenuation with shock reflection off turbine leading edges. They also reported regions of reverse flow in the reflected shock, such that the

flow proceeded upstream through the secondary flow duct. This indicates that the turbine is not able to process all the energy immediately available from the PDC exhaust.

Glaser, et al. (2006 and 2007) and Caldwell, et al. (2006 and 2008) conducted experiments with an array of six, 25.4 mm (1 in) diameter PDC tubes feeding an axial turbine designed for 0.72 kg/s (1.6 lbm/s), 60,400 RPM, and 67.1 kW (90 hp). Maximum operating frequency was 20 Hz for each tube. Secondary air flow mixed with the primary flow before entering the turbine. Parametric studies investigated the effects of fueled-fraction, equivalence ratio, operating frequency, bypass ratio, and firing patterns. Glaser, et al (2007) conducted a side-by-side study of steady cold flow, steady deflagrative and unsteady detonation combustion driven turbine performance. The turbine was couple to a torque cell and water dynamometer to obtain power measurements. Specific power was defined as:

$$\dot{W}_s = \frac{\dot{W}}{\dot{m} T_{t,in}} \quad (49)$$

where  $T_{t,in}$  is stagnation temperature entering the turbine. PDC driven turbine performance was very similar to performance when driven by steady deflagration combustion. Also, PDC driven turbine performance decreased with increasing fueled fraction. A subsequent study performed by Caldwell and Gutmark (2008) using high speed shadowgraph images revealed a shock-jet interaction between the PDC exhaust and secondary flow that attenuated the shock and induced a vortex that propagated into the turbine passage. Some of the energy from the shock is presumed to create the secondary flow effect and is therefore not available to the turbine for power extraction.

## **Thermodynamic Analysis of a Pulsed Detonation Driven Cycle**

Traditional approaches to thermodynamic cycle analysis based on steady flow may not be adequate for a pulsed detonation driven turbine engine, and there have been several proposed methods to model unsteady behavior. Heiser and Pratt (2002) published a thermodynamic cycle analysis comparing an ideal PDE cycle with classical ideal Brayton (constant pressure combustion) and Humphrey (constant volume combustion) cycles. A temperature-entropy (T-s) diagram for these cycles is shown in Fig. 69. The process between point 3 and 3a is associated with part of the detonation wave heat addition process and is the entropy sum of an adiabatic normal shock wave. The entropy generated from point 3a to 4 is a constant-area heat addition process (i.e., Rayleigh flow). Heiser and Pratt (2002) concluded that the ideal PDE cycle has a higher efficiency at all conditions, but the difference diminishes with increasing compressor temperature ratio.

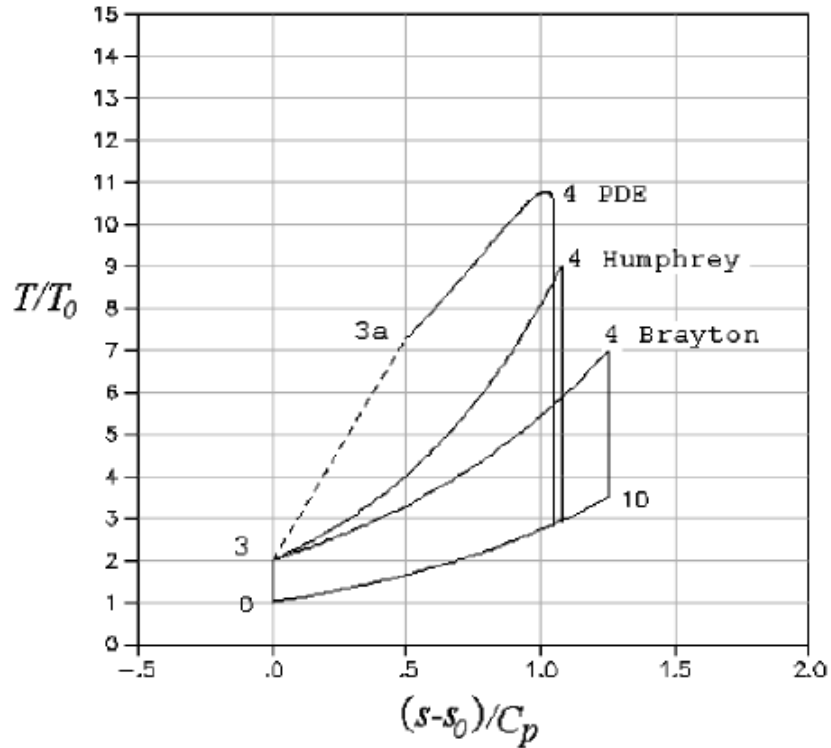


**Figure 69. Heiser and Pratt comparison of ideal PDE, Humphrey, and Brayton cycles on a temperature-entropy diagram (Heiser and Pratt 2002)**

Dyer and Kaemming (2002) proposed a thermodynamic model similar to that of Heiser and Pratt (2002), including perfect gas assumptions and treatment of fuel-air ratios. When comparing the ideal PDE to an ideal ramjet in Fig. 70, Dyer and Kaemming (2002) noted that the leading shock wave of the detonation does work on the fluid element, raising its pressure and energy state (point 3 to 3'). At this point, the total enthalpy includes the kinetic energy associated with detonation velocity. The heat of combustion is released at this elevated energy state (point 3' to 4), such that the static enthalpy of the fluid element is higher than the combined entrance total enthalpy and heat release (state 4 on the dashed line).

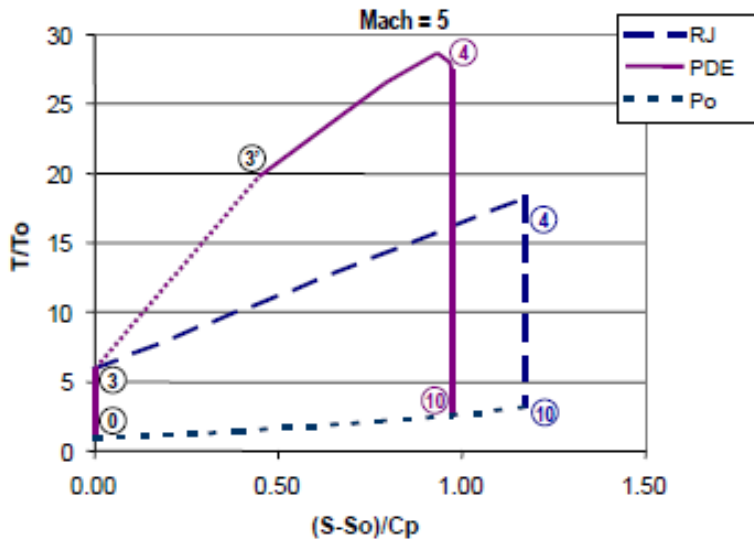


**Figure 70. Comparison of ideal PDE and ramjet cycles on a temperature-entropy diagram (Dyer and Kaemming 2002)**

Cycle thermal efficiency, as defined by Dyer and Kaemming (2002), is:

$$\eta_{th} \equiv \frac{q_{added} - q_{rejected}}{q_{supplied}} \quad (50)$$

where  $q_{added}$  is the heat of combustion,  $q_{rejected}$  is the thermal energy rejected in the exhaust, and  $q_{supplied}$  is the energy available from the fuel. A comparison of ideal PDE, ramjet, and Brayton cycle thermal efficiencies is shown in Fig. 71 (Dyer and Kaemming 2002), in which heat addition losses are the only difference between the Brayton and ramjet cycles. Higher inlet compression experienced by Brayton and ramjet cycles diminishes the thermal efficiency advantage of the ideal PDE.

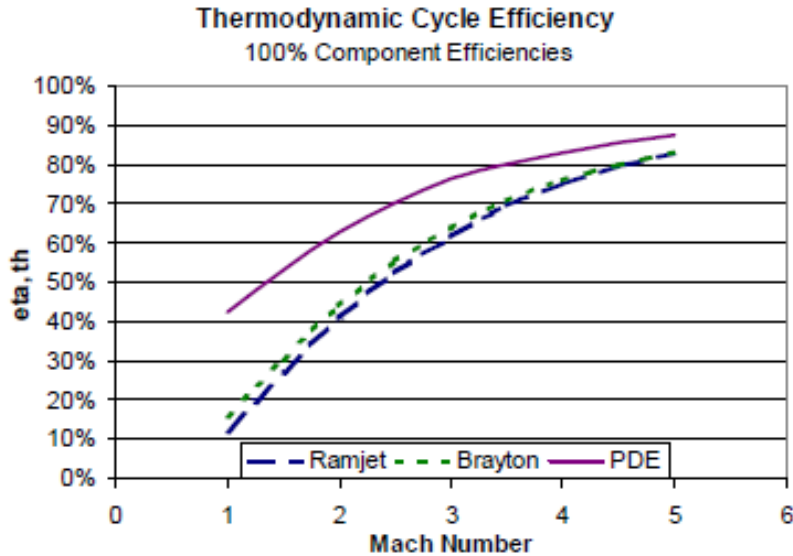


**Figure 71. Comparison of ideal PDE, ramjet and Brayton cycle thermal efficiencies (Dyer and Kaemming 2002)**

Petters and Felder (2002) used an on-design thermodynamic cycle analysis of a hybrid PDC high-bypass turbofan in the Numerical Propulsion Systems Simulation (NPSS) program, simulating the PDC as a conventional steady ramjet. The model predicted an improvement in thrust and fuel consumption over the baseline conventional high bypass turbofan. Andrus and King (2007) used an on-design cycle deck study of a high-bypass turbofan with an embedded PDC, comparing results from the NPSS program to results from Mattingly's AEDsys program (Mattingly 2006). The model assumed an ideal transition from unsteady PDC exhaust to steady mixed turbine inlet flow. Unlike Petters and Felder (2002) who treated the PDC as a ramjet, the study incorporated Heiser and Pratt (2002) equations for an ideal PDE. NPSS and AEDsys results showed good agreement and a potential 8% decrease in thrust specific fuel consumption.

Wintenberger and Shepherd (2004) offered a control mass approach to compute unsteady ideal PDE performance. The analysis incorporates time-averaged flow properties and the Fickett-Jacobs (FJ) cycle; a closed system. A comparison of cycle thermal efficiencies is shown Fig. 72. Thermal efficiency of the FJ cycle as defined by Wintenberger and Shepherd (2004) is:

$$\eta_{FJ} = \frac{W_{net}}{q_{combustion}} = \frac{h_{exit} - h_{in}}{q_{combustion}} \quad (51)$$

Whereas the FJ cycle has a higher thermal efficiency than the Brayton cycle, it is also better than the Humphrey cycle. This is consistent with the Heiser and Pratt (2002) T-s diagram, which indicates that the ideal PDE has less heat addition losses than the Humphrey cycle. Also, the thermal efficiency improvement of the FJ cycle over the Brayton cycle diminishes with increasing pressure ratio, which is consistent with Dyer and Kaemming (2002).

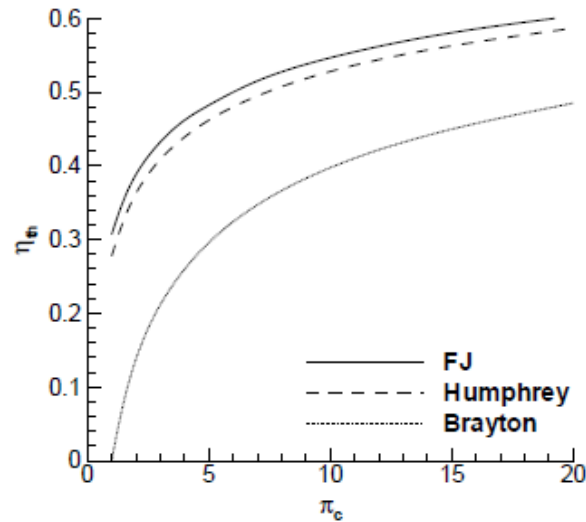


**Figure 72. Comparison of ideal Fickett-Jacobs, Humphrey and Brayton cycle thermal efficiencies (Wintenberger and Shepherd 2004)**

Hofer, et al. (2009) developed a performance metric for pulsed detonation turbine engines, treating the combustor and turbine as a single component. This approach avoids the complexity of unsteady turbine inlet conditions, making use of steady compressor exit conditions. The formulation for isentropic efficiency includes a ratio of actual pulsed detonation driven turbine work to ideal Brayton turbine work.

$$\eta^* = \frac{W_t}{W_{t,Bi}} \quad (52)$$

$$W_{t,Bi} = c_p \cdot T_{4,Bi} \cdot \left[ 1 - \left( \frac{P_8}{P_3} \right)^{\frac{\gamma-1}{\gamma}} \right] \quad (53)$$

Station 3 is the combustor inlet, station 4 is the turbine inlet, and station 8 is the turbine exit. Hofer, et al. (2009) presume to measure turbine work directly with torque and speed sensors. An energy balance around the combustor is used to obtain an ideal turbine inlet temperature:

$$T_{4,Bi} = \frac{\dot{m}_{fuel} c_{p,fuel} T_{fuel} + \dot{m}_3 c_{p,3} T_3 + \dot{m}_{fuel} \eta_{combustor} LHV - Q_{lost}}{c_{p,4} \cdot (\dot{m}_{fuel} + \dot{m}_3)} \quad (54)$$

where ideal combustor efficiency is 100%, and there is no heat loss. The approach proposed by Hofer, et al. (2009) allows for a more direct comparison of turbine performance with pulsed detonation combustors and conventional steady combustors.

## Appendix B: Theory of Confined Detonations

The following discussion of detonation theory is intended to orient the reader's understanding of PDC operation and its advantages. A one-dimensional (1-D) Rayleigh flow analysis leads to the Rayleigh line relation and one of the Rankine-Hugoniot relations. Development of the Hugoniot curve illustrates the significance of the Chapman-Jouguet conditions. Introduction of a 1-D model explains the coupled and mutually supporting nature of the detonation shock wave and combustion reaction. The ensuing discussion of three-dimensional (3-D) detonation wave structure highlights length scales and unsteady behavior of confined detonations.

### Rayleigh Line and Rankine-Hugoniot Relations

A simplified 1-D thermodynamic model of a generalized combustor is shown in Fig. 73 with constant area duct flow and a stationary combustion wave, either deflagration or detonation. In reality, the combustion wave would move from right to left, but for convenience, the frame of reference is such that the wave is considered fixed. Pre-mixed reactants enter from the left toward the combustion wave front, and products exit to right.

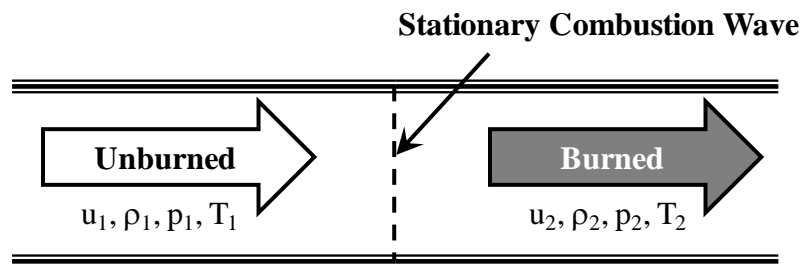


**Figure 73. Schematic of stationary, one-dimensional, confined combustion wave model**

Assuming steady, 1-D flow with no body forces and no external heat addition or rejection, the equations for continuity, momentum and energy conservation are, respectively (Kuo 1986):

$$\frac{d(\rho u)}{dx} = 0 \quad (55)$$

$$\rho u \frac{du}{dx} = -\frac{dp}{dx} + \frac{d}{dx} \left[ \left( \frac{4}{3} \mu + \mu' \right) \frac{du}{dx} \right] \quad (56)$$

$$\rho u \left[ \frac{d}{dx} \left( h + \frac{u^2}{2} \right) \right] = -\frac{d}{dx} q_{cond} + \frac{d}{dx} \left[ u \left( \frac{4}{3} \mu + \mu' \right) \frac{du}{dx} \right] \quad (57)$$

where  $\mu$  is the dynamic viscosity,  $\mu'$  is the bulk viscosity and  $q_{cond}$  is the conduction heat transfer per unit mass associated with the combustion reaction as described in Eq. (58),

$$q_{cond} = -\lambda \frac{dT}{dx} \quad (58)$$

where  $\lambda$  is thermal conductivity.

The velocity gradient ( $du/dx$ ) and thermal gradient ( $dT/dx$ ) are both zero on either side of the combustion wave. Assuming  $\mu'$  is very small and can be neglected, the integration from state one to state two yields:

$$\rho_1 u_1 = \rho_2 u_2 \quad (59)$$

$$p_1 + \rho_1 u_1^2 = p_2 + \rho_2 u_2^2 \quad (60)$$

$$c_p T_1 + \frac{1}{2} u_1^2 + q = c_p T_2 + \frac{1}{2} u_2^2 \quad (61)$$

The Rayleigh line relation follows from the combination of Eq. (59) for mass and Eq. (60) for momentum, as shown in Eq. (62).

$$\rho_1^2 u_1^2 = \frac{p_2 - p_1}{\frac{1}{\rho_1} - \frac{1}{\rho_2}} \quad (62)$$

The Rankine-Hugoniot relation in Eq. (63) is derived from a combination of mass Eq. (59), momentum Eq. (60), energy Eq. (61), and ideal gas equation of state.

$$\frac{\gamma}{\gamma - 1} \left( \frac{p_2}{\rho_2} - \frac{p_1}{\rho_1} \right) - \frac{1}{2} (p_2 - p_1) \left( \frac{1}{\rho_1} + \frac{1}{\rho_2} \right) = q \quad (63)$$

The Hugoniot curve in Fig. 74 is for a fixed heat release per unit mass ( $q$ ). Rayleigh lines, which are tangent to the Hugoniot curve at U and L, emanate from the initial pressure and specific volume ( $1/\rho_1$ ) (point A in Fig. 74). The distance between point A and the Hugoniot curve is proportional to  $q$ . The points of tangency are the upper and lower Chapman-Jouguet (C-J) points. The Hugoniot curve is divided into five regions, I through V, as demarcated by the C-J points and the intersections of constant pressure and constant specific volume lines through with the initial conditions. These regions contain all of the possible solutions to Eq. (63). Domain V is a region of imaginary solutions to the Rayleigh line relation, Eq. (62), and is consequently not relevant. Region IV would require gases to accelerate from subsonic to supersonic speeds across a deflagration wave, and this is not physical. Region III contains solutions corresponding to subsonic deflagration. The upper branches of the curve, regions I and II, include detonation solutions to the Rankine-Hugoniot equation, Eq. (63).

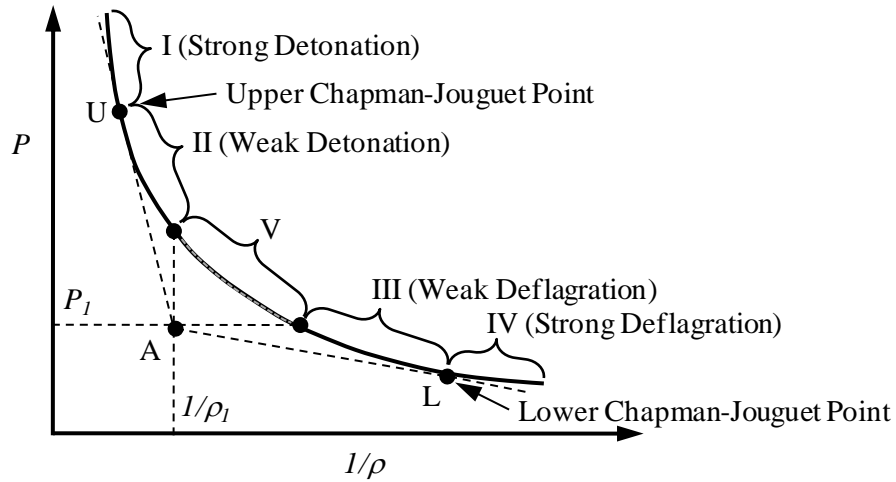


**Figure 74. Hugoniot curve with solution domains of different combustion conditions**

Table 12 contains a comparison of typical detonation and deflagration combustion properties. Station numbering is consistent with Fig. 73, where  $c_1$  is the speed of sound in the unburned, pre-mixed reactants. Detonation waves can propagate at five times the speed of sound, whereas deflagration occurs at low subsonic speeds. Furthermore, there is significant pressure gain from detonation, with pressure ratios greater than ten. Conversely, deflagration results in a slight expansion of gases.

**Table 12. Comparison of detonation and deflagration (Kuo, 1986:234)**

	<i>Detonation</i>	<i>Deflagration</i>
$u_1/c_1$	5-10	0.0001-0.03
$u_2/u_1$	0.4-0.7 (deceleration)	4-6 (acceleration)
$p_2/p_1$	13-55 (compression)	~0.98 (slight expansion)
$T_2/T_1$	8-21	4-16
$\rho_2/\rho_1$	1.7-2.6	0.06-0.25

### **Chapman-Jouguet Conditions**

The upper and lower C-J points correspond to unique velocities associated with the set of simultaneous solutions to Eq. (62), the Rayleigh line relation, and Eq. (63), the Hugoniot equation. The velocity at the upper C-J point (called the Chapman-Jouguet velocity,  $V_{C-J}$ ) is usually five times or more the speed of sound (Friedman 1953). The magnitude of  $V_{C-J}$  can be calculated using a Newton-Raphson iterative method (Kuo 1986) and has been determined experimentally (Dean 2007).  $V_{C-J}$  varies as a function of fuel and oxidizer, equivalence ratio, and pressure (Dean 2007). For an ethylene-air mixture at 25 deg C and 1.013 bar,  $V_{C-J}$  is approximately 1822 m/s, and the corresponding C-J pressure is 18.6 bar (Baker, et al. 1983).

### **Zeldovich, von Neumann and Döring One-Dimensional Model**

A detonation front consists of a closely coupled shock wave followed by a combustion reaction. The shock raises temperature and pressure of the reactants, initiating a fast reaction, and the resulting combustion energy sustains the shock wave. A model for a 1-D planar detonation wave was independently contrived by Zeldovich, von Neumann and Döring (ZND) (Kuo, 1986; Glassman 1996). The ZND model assumes 1-D, steady flow, with respect to the detonation front and is depicted in Fig. 75. A narrow induction zone separates the shock wave from the trailing rapid reaction zone. During the induction period, the reaction rate is assumed to follow the Arrhenius law and increases slowly, resulting in nearly constant pressure, temperature, and density. The reaction rate spikes in the reaction zone, rapidly releasing the energy required to sustain the strength and speed of the shock wave. Concurrently, the shock wave pre-heats and pressurizes

reactants prior to combustion. The reaction zone and shock wave decouple if the space between them becomes so great that they can no longer support each other.

Consequently, the shock loses strength, the reaction rate slows and the detonation fails.

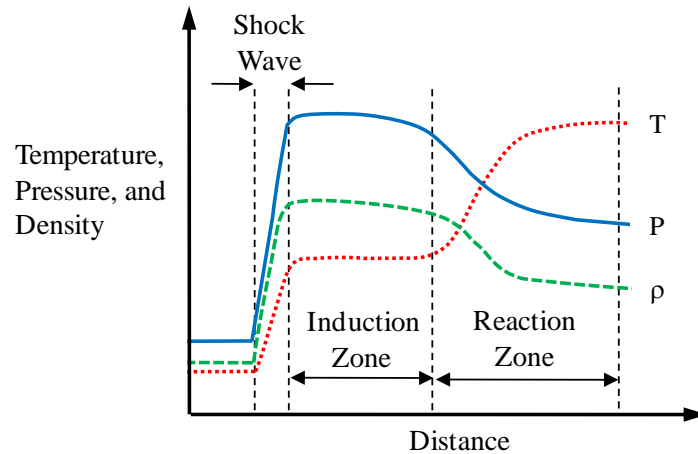


**Figure 75. Notional variation of temperature, pressure, and density through a ZND 1-D detonation wave model (not to scale)**

### Three-Dimensional Structure of Confined Detonations

The ZND model is useful for revealing general characteristics of a steady detonation; however, it has inconsistencies with experimental observations (Glassman 1996), revealing that it has limited ability to completely characterize the nature of a real detonation (Coleman 2001). A fish-scale pattern was observed in a detonation channel that was lined with a soot-covered foil (Coleman 2001; Guirao, et al. 1982). The pattern was etched into the soot as shown in the sketch of Fig. 76, indicating that the planar detonation front is actually multi-dimensional, consisting of incident shocks and Mach stems that intersect at a triple point with a transverse-moving shock wave (Kuo 1986). The cellular pattern results from the transverse motion of these triple points associated

with the propagating detonation wave. The lines composing the diamond shapes are the trajectories traced by the triple points. The resulting characteristic dimension is the cell width,  $\lambda$ .

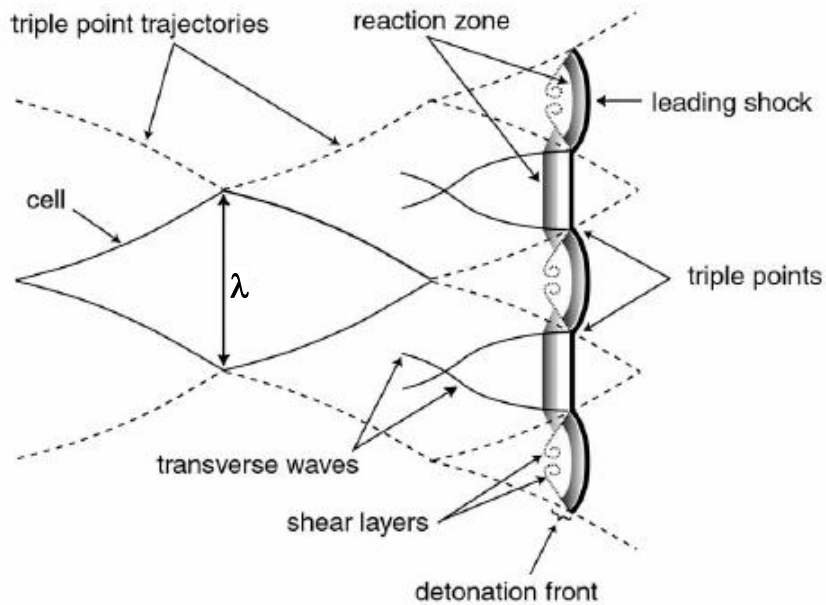


**Figure 76. Components of detonation wave cell structure (Porowski and Teodorczyk 2009)**

The magnitude of  $\lambda$  depends on various reactant properties, such as equivalence ratio ( $\phi$ ) as shown in Fig. 77. Experimentally measured cell widths are plotted for four different fuel-air mixtures over a range of equivalence ratios (Guirao, et al. 1982; Knystautas, et al. 1984). The minimum  $\lambda$  occurs near stoichiometric conditions ( $\phi = 1.0$ ) and increases for either lean or rich mixtures. Hydrogen ( $H_2$ ) and short-chain hydrocarbons such as acetylene ( $C_2H_2$ ) and ethylene ( $C_2H_4$ ) have relatively lower minima. In general,  $\lambda$  increases with the length of the hydrocarbon chain; however, some hydrocarbon chains longer than propane ( $C_3H_8$ ) have been measured with approximately

the same cell size as propane (Austin and Shepherd 2003). Initial pressure of the mixture also has a strong inverse relationship with  $\lambda$ , in which higher pressures result in small  $\lambda$  (Bauer, et al. 1984; Bauer, et al. 1986).

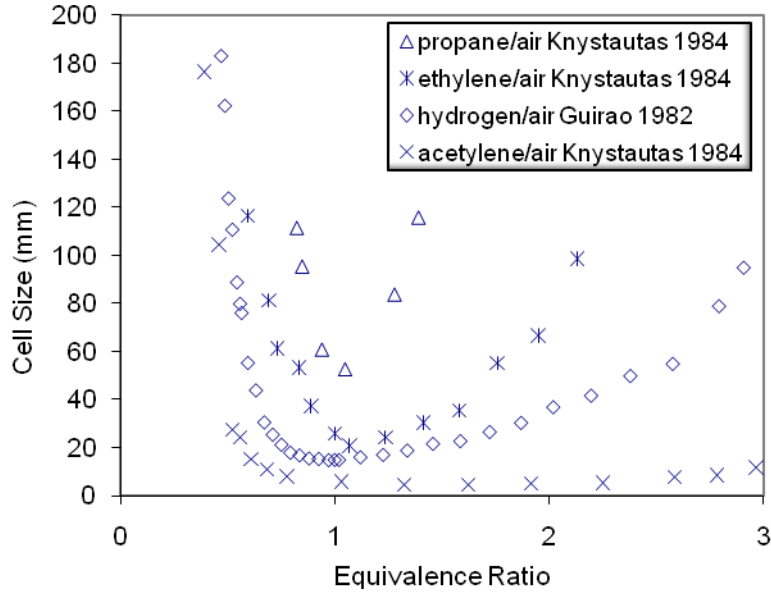


**Figure 77. Measured cell sizes of different fuels (Guirao, et al. 1982:583-590; Knystautas 1984:23-37)**

Experimental Schlieren and computational images have more accurately depicted the 3-D cellular structure (Austin and Shepherd 2003; Pintgen, et al. 2003a; 2003b; Austin, et al. 2005a; 2005b; Pintgen and Shepherd 2005). These images reveal periodic weakening and strengthening of the leading shock wave, as well as oscillating shock velocities between  $0.8 V_{C-J}$  and  $1.5 V_{C-J}$  (Austin, et al. 2005b). Furthermore, a keystone shaped pocket of reactants is seen to form behind the leading shock just prior to the collision of transverse waves (Pintgen, et al. 2003a; 2003b; Austin, et al. 2005b; Oran, et al. 1982; Mikutsu, et al. 1999). The shock front and combustion wave continually decouple and the detonation wave begins to fail; however, the transverse waves prevent

the detonation from failing completely (Oran, et al. 1982). The reaction quickens whenever transverse waves collide, bringing the reaction zone closer to the shock wave, accelerating the detonation wave, and strengthening the shock front. Therefore, the 1-D, steady planar detonation wave in the ZND model cannot really exist without the 3-D, unsteady interaction of transverse waves necessary for the continually coupled and mutually supporting shock wave and reaction zone. Furthermore, the transverse waves are integral to creating the cellular structure, and PDC diameter limits are a function of the cell width. If the PDC diameter is too large, transverse waves are not able to sustain the necessary cell width for successful detonation operation.

## Appendix C: Pulsed Detonation Combustor Operation

The PDC operates in a periodic fashion with three phases as illustrated in Fig. 78. The cycle begins with the fill phase, in which premixed fuel and oxidizer are introduced into the PDC tube. The second phase is composed of four parts and is referred to as the fire phase. During this phase, the reactants are ignited, combustion then transitions from a subsonic deflagration to supersonic detonation, the detonation wave completes the combustion process, and finally the exhaust products expand out of the tube. The third phase is a buffer between cycles, in which a charge of non-reacting gas purges any remaining exhaust products from the tube. This so called purge phase separates hot exhaust products and fresh reactants. Cycle frequency is a direct function of the total time duration consumed of the three phases as shown in Eq. (64).

$$f = \frac{1}{t_{fill} + t_{fire} + t_{purge}} \quad (64)$$

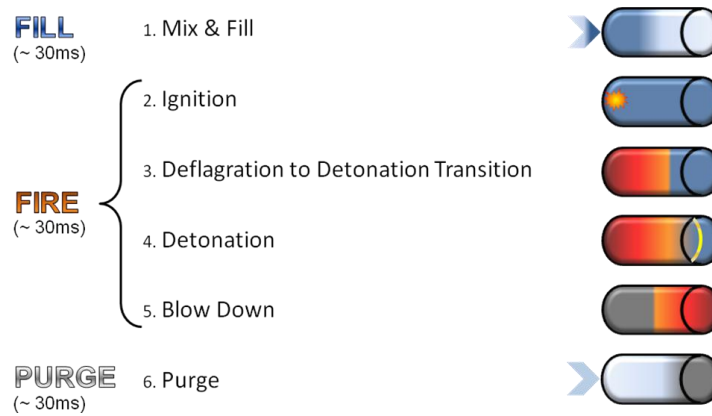


**Figure 78. Pulsed detonation combustor cycle with timing for 11 Hz operation with equal phase times**

## Fire Phase

The fire phase begins when the fill valve is closed and ends when the purge valve opens. An example timeline of the intermediate processes in the fire phase is shown in Fig. 79. After a deliberate delay, a spark is deposited, igniting the fuel/oxidizer mixture. Combustion involves a deflagration to detonation transition (DDT), after which the detonation wave proceeds down the remaining length of the tube, raising the chamber pressure. The ensuing blowdown process reduces pressure through a series of expansion waves that propagate upstream from the combustor exit. Minimizing or eliminating as many of these events as possible will enable increased PDC operating frequency.

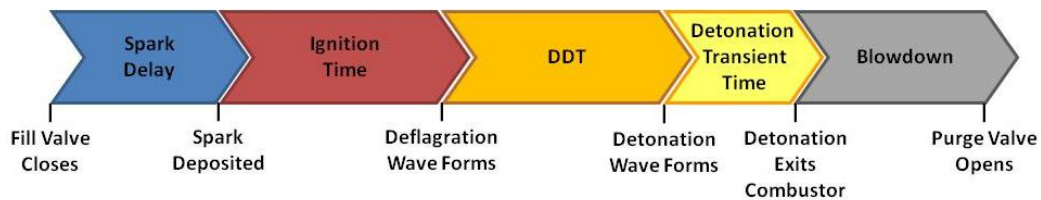


**Figure 79. Notional timeline of events in fire phase (adapted from Hopper 2008)**

Hoke, et al. (2002) showed that ignition and DDT times for a PDE increased as a consequence of expansion waves resulting from valve closure, which decreased tube pressure. Tube pressure followed a cyclical pattern, oscillating between maxima and minima. This behavior suggested that optimal spark timing coincided with pressure rise, potentially improving ignition and DDT and reducing overall fire phase time.

Helfrich (Helfrich 2006; Helfrich, et al. 2006) found that increasing the spark delay from 2 ms to 4 ms decreased ignition time by more than 2 ms when operating at 15 Hz with JP-8/air and using a test setup similar to that of Hoke, et al. (2002).

Additionally, Helfrich (Helfrich 2006; Helfrich, et al. 2006) found that delays of 6, 8 and

10 ms decreased ignition and DDT time as much or even further than with a 4 ms delay. Furthermore, he determined that the minimum overall time to detonation (i.e., spark delay, ignition time, and DDT) was achieved with a 4 ms spark delay.

Some PDE researchers (Glaser, et al. 2005; Glaser, et al. 2007) may have avoided the need for a spark delay because they were using highly detonable gaseous mixtures such as ethylene/oxygen, diminishing the effects of pressure fluctuations. The large pressure fluctuations experienced by Helfrich, Hoke, Bradley and Schauer may also be associated with the automotive valves used in their research. Werner (2002) avoided these pressure fluctuations using a “valveless” PDE design, flowing a continuous stream of inlet air.

The formation of a deflagration wave has been determined experimentally with an optical sensor detecting increased luminescence and with a pressure transducer indicating pressure rise at the PDE head (Tucker 2005; Helfrich 2006; Slack 2007). DDT has been characterized by measuring wave transient times in the detonation tube with ion probes and pressure transducers, determining when the velocity reaches  $V_{C-J}$  (Tucker 2005; Austin and Shepherd 2003; Helfrich 2006; Werner 2002; Rolling 2002; Panzenhagen 2004; Miser 2005). The DDT process starts with a laminar deflagration that propagates compression waves. Shock formation results from these coalescing compression waves, disturbing the flow and causing turbulence (Kuo, 1986). The resulting turbulent flame propagates at much higher speeds than the laminar flame, on the order of  $0.5 V_{C-J}$  (Zhu, et al. 2007). A localized explosion occurs within the turbulent region (Oran and Khokhlov 1999; Gamezo, et al. 2007), creating transverse waves that quickly accelerate the shock

front into a bona fide detonation and simultaneously forming a detonation wave; a shock wave that travels upstream through the combustion products (Kuo, 1986). DDT can occur unaided in a confined tube as transverse waves reflect off side walls; however, obstacles have been inserted into the tube accelerate the process (Schauer, et al. 2001; Meyer, et al. 2002; Sinibaldi, et al. 2001). Schauer, et al. (2002) used high speed imaging in a polycarbonate PDE tube to show that a spiral obstacle increases flame turbulence and encourages hot spot formation, promoting DDT.

During blowdown, mass exits the combustor and tube head pressure is higher than atmospheric, adding a component of thrust. As the exhaust mass exits, chamber pressure and thrust diminishes. Opening the purge valve too early at the head of the tube reduces the thrust benefit, and if the tube pressure is higher than the purge manifold pressure, hot reactants may flow into the purge manifold. When a turbine is coupled to the PDC, chamber pressure will remain higher than atmospheric pressure. It is prudent to allow blowdown to proceed long enough for chamber pressure to fall below purge manifold pressure.

### **Fill and Purge Phases**

Fill and purge phases operate in similar fashions. The duration is a function of the convection time associated with a gaseous mixture in the detonation tube. The only difference is the mixture of fuel and oxidizer in the fill phase, and the non-reactive mixture in the purge phase. Fueled fraction is the fill mixture volumetric flow rate (governed by manifold pressures and temperatures), multiplied by fill time, and divided by detonation tube volume. A fueled fraction equal to unity implies that the tube is

completely filled with a reactive mixture; whereas, a partially filled tube has a fueled fraction less than 1.0. Similarly, purge fraction is the volumetric ratio of inert mixture to tube volume.

The duration of these two phases is a function of the fill and purge manifold pressure differentials, flow coefficients, and the volume of the detonation tube, itself. Increasing supply pressure reduces fill/purge time up to a choked-flow condition limited by the supply system. Reducing the time further requires either lower fueled/purge fractions, a shorter tube, and/or a smaller tube diameter. Changing the tube volume also has effects on the timing of the fire phase. If the tube is too short, DDT may not occur and detonations may not be produced. Therefore, all three phases must be considered when specifying the detonation tube geometries.

### **Rotating Detonation Configuration**

A continuous, rotating detonation engine (RDE) configuration, illustrated in Fig. 80, has been proposed as an alternative to the axial pulsed detonation tube arrangement (Bykovskii, et al. 2006; Daniau, et al. 2005; Hayashi, et al. 2009). The RDE contains an annular duct with one open end for exhausting detonation products. Fuel and oxidizer are injected at the upstream head and ignited by one or more continuously running detonation waves that traverse the circumference of the chamber. The expanding detonation products travel downstream with a radial component of velocity, tracing out a helical trajectory. Therefore, the RDE operates with only the fill and fire phases, like a PDE, and omits the purge phase.

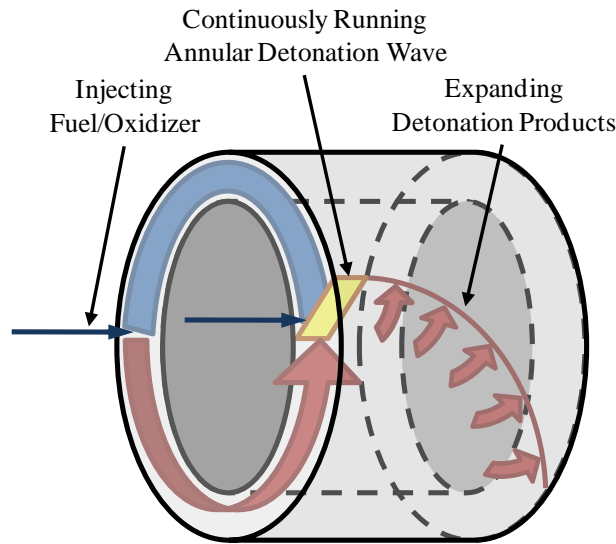


**Figure 80. Notional diagram of a rotating detonation combustor (adapted from Daniau, Falempin and Zhdan 2005)**

When coupled to a turbine the RDE is called a rotating detonation combustor (RDC). The potential benefit of this arrangement includes an annular exhaust flow that may be more easily integrated with an axial turbine flow. Furthermore, the exhaust is potentially steadier without oscillating between such disparate pressures as an axial detonation tube. Whereas the flow field at the RDC head is very heterogeneous, the expanding exhaust at the exit is expected to be more uniform in terms of pressure and temperature. Using a two-wave numerical model with one-step chemical kinetics of hydrogen/air, Yi, et al. (2010) reported inlet chamber pressures oscillating between 2 bar to 39 bar at a fixed circumferential location, while exit pressures only oscillated between 0.5 bar and 2.2 bar. As RDE technology capabilities mature, the potential for experimental studies of RDC-turbine configurations increases.

## **Key Operating Parameters**

There are many parameters to consider when implementing a PDC, and they are often interrelated. Fuel selection influences detonation tube diameter and length. The cell width associated with the fuel determines the range of tube diameters, and DDT length relates to fuel detonability, which is also related to cell width (Hopper 2008). DDT length is also influenced by the type of obstacles in the tube. Tube length is generally a little longer than the DDT length (e.g., a 305 mm or more longer). Tube length and diameter are used to determine tube volume. Fueled and purge fractions are a function of tube volume, as well as fill/purge volumetric flow rates (governed by manifold pressures and temperatures) and fill/purge time. Frequency is determined by the time associated with fueled and purge fractions, ignition time, DDT time, detonation wave travel time, and blowdown time, which are also functions of fuel selection. Therefore, adjusting one parameter has broad implications on PDC operation.

**Appendix D: Comparison of Pulsed Detonation and Steady Deflagration Turbine,  
Presented at the 2010 AIAA Aerospace Sciences Meeting (AIAA-2010-1116)**

Experimental turbine performance driven by an unsteady PDC is compared directly to turbine performance driven by a near constant pressure, steady deflagration combustor (SDC). Additionally, time-dependent turbine response is correlated to the unsteady forcing function imposed by the PDC. The turbine used in this study has nine blades and is part of a Garrett GT2860RS automotive turbocharger, pictured in Fig. 81. The turbine wastegate (as seen in Fig. 82) is disabled so that all combustor exhaust passes through the turbine. The GT2860RS is equipped with a radial compressor having six primary impeller blades and six splitter blades. The water-cooled, center housing contains the shaft and dual ball bearing assembly.

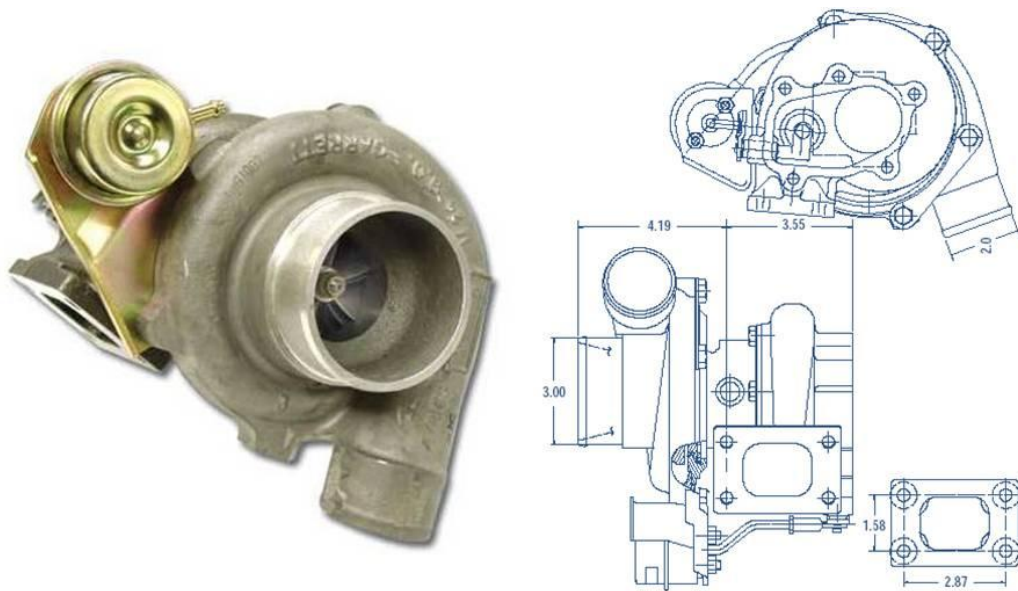


**Figure 81. Garrett GT2860RS automotive turbocharger (used with permission)**

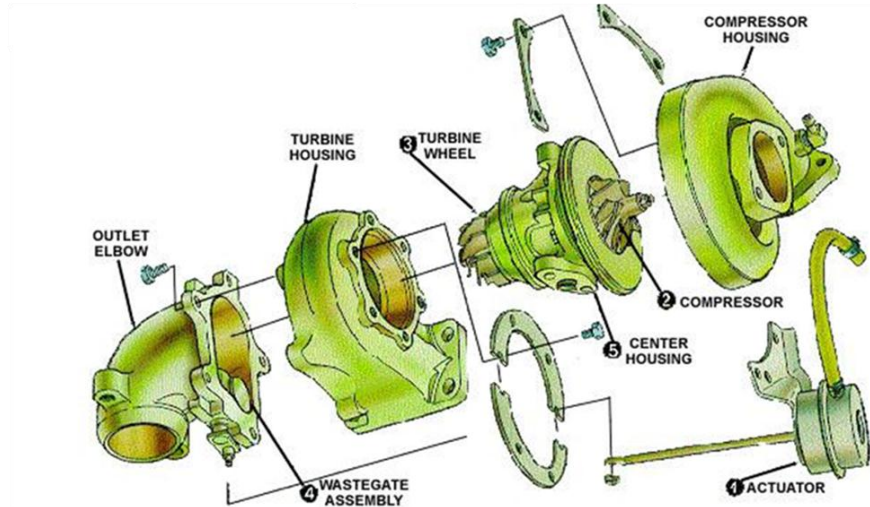


**Figure 82. Turbocharger components (used with permission)**

### Performance Figures of Merit

Two measures of merit are considered for turbine performance: specific work and brake specific fuel consumption (BSFC). An expression for turbine shaft power output is obtained in Eq. (65) from a one-dimensional, adiabatic thermodynamic analysis, as seen in Fig. 83. The development of this expression assumes steady flow and an average specific heat and includes a mechanical efficiency term. To compare turbine performance at different operating conditions, power is considered per unit of turbine mass flow (i.e., specific power), as shown in Eq. (66). Dimensional analysis shows this expression to be specific work because mass flow rate is used.

$$\dot{W}_{turb} = \eta_{mech} \cdot \dot{m} (h_{in} - h_{out}) = \eta_{mech} \cdot \dot{m}_{turb} \cdot c_{p,avg} (T_{t,3} - T_{t,3.5}) \quad (65)$$

$$W_{s,turb} = \frac{\dot{W}_{turb}}{\dot{m}_{turb}} \quad (66)$$

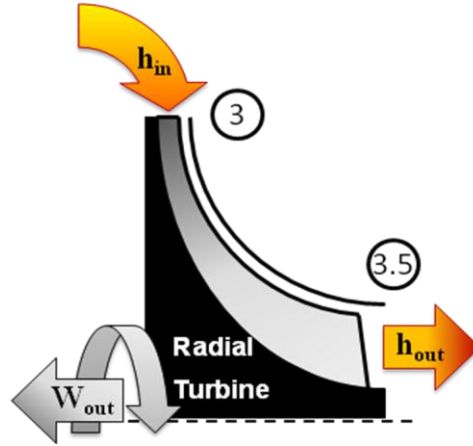


**Figure 83. Schematic of one-dimensional, adiabatic thermodynamic analysis of a radial turbine**

Direct measurement of time-resolved PDC and turbine exhaust temperatures is problematic; therefore, the compressor side of the turbocharger is treated as a dynamometer for measuring turbine power. Turbine power is equal to compressor power (assuming 100% mechanical efficiency), because the two components are coupled to the same shaft. An expression for compressor power, shown in Eq. (68), is developed using the same assumptions and similar one-dimensional, adiabatic thermodynamic analysis as used for turbine power. For the turbocharger, the mechanical efficiency term for the compressor and turbine are equal because they share a common bearing assembly.

$$\dot{W}_{turb} = \dot{W}_{compr} \quad (67)$$

$$\dot{W}_{compr} = \dot{m}_{compr} \cdot c_{p,avg} (T_{t,2} - T_{t,1}) \quad (68)$$

Equation (68) requires steady-state compressor inlet and exit temperatures; however, exit temperature measurements did not reach steady-state due to short run times. Duration of combustor run times was restricted by combustor wall temperature

limits, which were reached less than a minute after ignition with the SDC configuration. Therefore, an expression for exit temperature is developed in Eqs. (69) and (70), using isentropic relations and the definition of compressor efficiency. These equations assume constant specific heat. Compressor efficiency can be obtained from the manufacturer's compressor map, shown in Fig. 84.

$$\eta_{compr} = \frac{\dot{m}(h_{out} - h_{in})_{isentropic}}{\dot{m}(h_{out} - h_{in})_{actual}} = \frac{\left(\frac{P_{t,2}}{P_{t,1}}\right)^{\frac{\gamma-1}{\gamma}} - 1}{\frac{T_{t,2}}{T_{t,1}} - 1} \quad (69)$$

$$T_{t,2} = T_{t,1} \left( \frac{1}{\eta_{compr}} \left( \left(\frac{P_{t,2}}{P_{t,1}}\right)^{\frac{\gamma-1}{\gamma}} - 1 \right) + 1 \right) \quad (70)$$

The temperature obtained from Eq. (70) is then used in Eq. (68) for compressor power, resulting in Eq. (71). Equation (71) is combined with Eqs. (66) and (67) to produce an expression for specific turbine work, shown in Eq. (72).

$$\dot{W}_{compr} = \dot{m}_{compr} \cdot c_{p,avg} \cdot \left( \frac{T_{t,1}}{\eta_{compr}} \left( \left(\frac{P_{t,2}}{P_{t,1}}\right)^{\frac{\gamma-1}{\gamma}} - 1 \right) \right) \quad (71)$$

$$W_{s,turb} = \frac{\dot{m}_{compr} \cdot c_{p,avg} \cdot T_{t,1} \left( \left(\frac{P_{t,2}}{P_{t,1}}\right)^{\frac{\gamma-1}{\gamma}} - 1 \right)}{\dot{m}_{turb}} \quad (72)$$

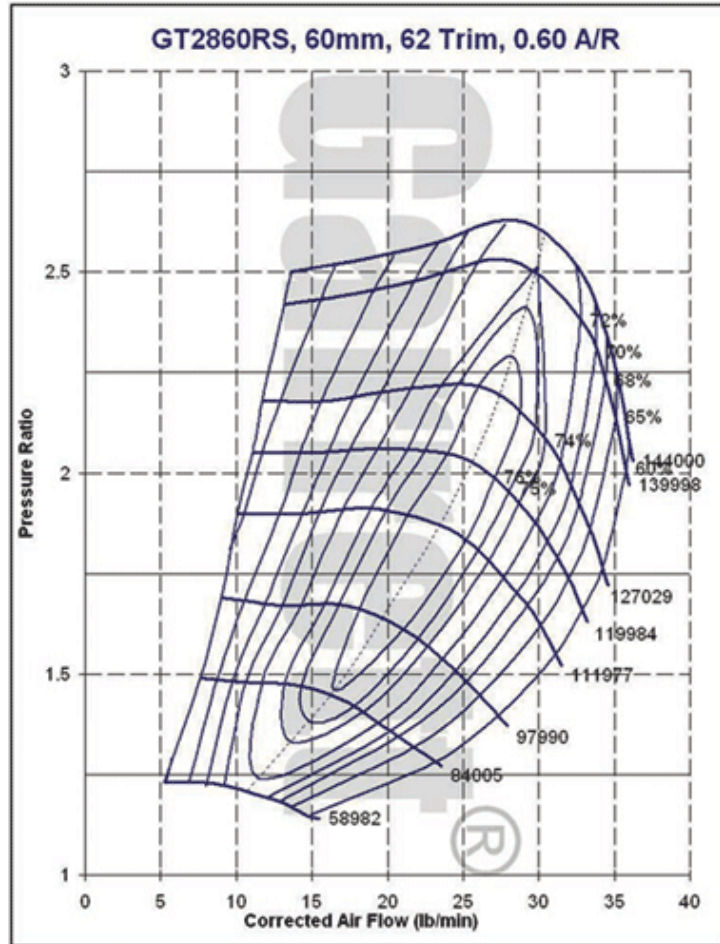


**Figure 84. Compressor map for GT2860RS (used with permission)**

To compare specific turbine work between SDC and PDC configurations using Eq. (72), similar compressor operating conditions must be matched to reduce influence from variations in compressor efficiency. Furthermore, the same mechanical and compressor efficiencies must be assumed for steady and unsteady operation (i.e., SDC and PDC configurations). Using the SDC driven turbine configuration as a baseline, Eq. (73) quantifies relative improvements.

$$\Delta W_{s,turb} = \frac{(W_{s,turb})_{PDC} - (W_{s,turb})_{SDC}}{(W_{s,turb})_{SDC}} \quad (73)$$

Another figure of merit for turbine performance is BSFC, which is simply fuel flow rate divided by power. An equation for BSFC is derived from Eqs. (67) and (71), and relative improvements are reported using Eq. (75).

$$BSFC = \frac{\dot{m}_{fuel}}{\dot{W}_{turb}} = \frac{\dot{m}_{fuel}}{\frac{\dot{m}_{compr} \cdot c_{p,avg} \cdot T_{t,1}}{\eta_{mech} \eta_{compr}} \left( \left( \frac{P_{t,2}}{P_{t,1}} \right)^{\frac{\gamma-1}{\gamma}} - 1 \right)} \quad (74)$$

$$\Delta BSFC = \frac{(BSFC)_{SDC} - (BSFC)_{PDC}}{(BSFC)_{SDC}} \quad (75)$$

Time-dependent compressor power and turbocharger rotor speed are correlated to the three-phase PDC cycle. For this study, the duration of each phase is about equal and depends on the operating frequency.

### Experimental Arrangement and Methodology

Experiments were carried out in the AFRL Detonation Engine Research Facility, using an ethylene-air mixture. For PDC operation, fill distribution and ignition takes place using an automotive engine head and cam to operate intake and exhaust valves for a desired operating frequency. The intake valves are used for the main fill fuel-air mixture, and the exhaust valves are used to inject purge air. During the fire phase, intake and exhaust valves are closed. For SDC operation, the intake valves remain fixed in the full-open position, exhaust valves remain closed, and fuel is injected and mixed downstream

of the intake valves to prevent backfire into the main manifold. For both PDC and SDC configurations, combustion products expand through the turbocharger turbine and then exit through a 77.9 mm (3 inch) diameter elbow. A temperature-entropy (T-s) diagram in Fig. 85 illustrates the notional ideal cycle for these two configurations.

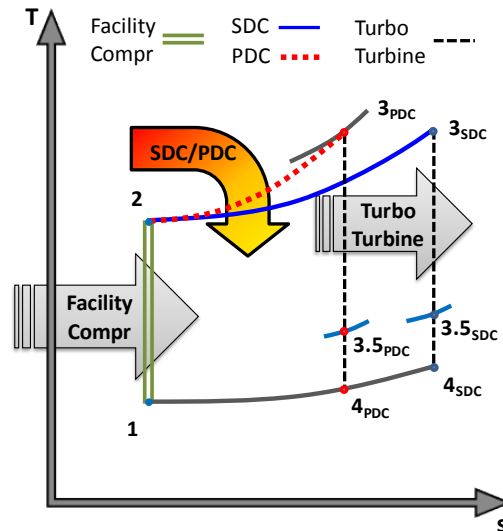


**Figure 85. Notional ideal temperature-entropy diagram of PDC and SDC configurations**

The general approach to this experiment study consisted of three phases. First, the PDC configuration was operated without fuel, such that the equivalence ratio is zero, and fueled fraction is unity. The objective was to observe the turbine response to pressure pulses, as well as to confirm instrumentation operability. The second phase was the SDC configuration. The objective was to set a performance baseline for comparison with the PDC configuration and to determine the range of operating conditions for which a continuous flame may be established. The final phase of testing was in the PDC configuration, and the primary objective was to assess turbine performance at a matching SDC inlet operating condition.

### ***Turbocharger Instrumentation***

The compressor side of the turbocharger received ambient air through a mass air flow (MAF) sensor. A 3.45 bar (50 psi) static pressure transducer and J-type thermocouple were just downstream of the MAF on a 77.9 mm (3 inch) diameter elbow, as seen in Fig. 86. The compressor exhaust contained a 3.45 bar (50 psi) static pressure transducer and J-type thermocouple along a 52.5 mm (2 inch) diameter pipe and a ball valve to back-pressure the compressor, as seen in Fig. 87. The ball valve is set such that the compressor is on its design operating map. Several different compressor operating conditions are considered by adjusting the PDC operating frequency. J-type thermocouples are attached to the turbine and compressor housings. Turbocharger temperature measurements also include center housing cooling water inflow and outflow. All temperatures were sampled once per second, separately from the other turbocharger measurements.

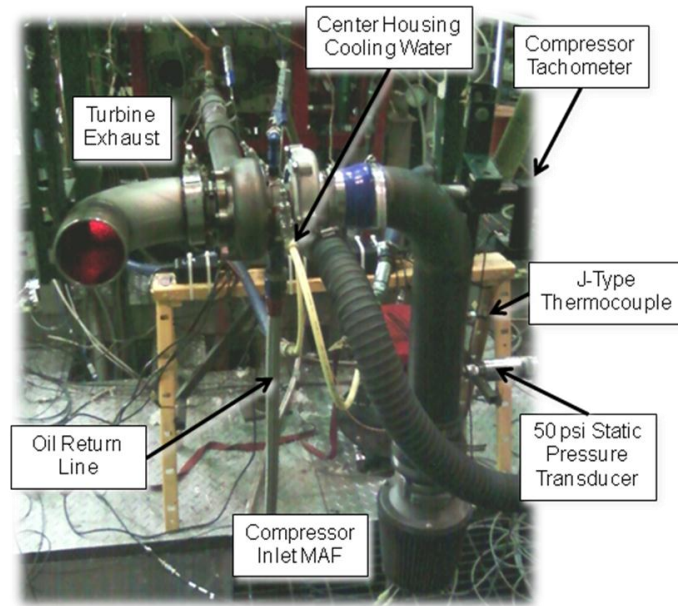


**Figure 86. Turbocharger experimental arrangement**

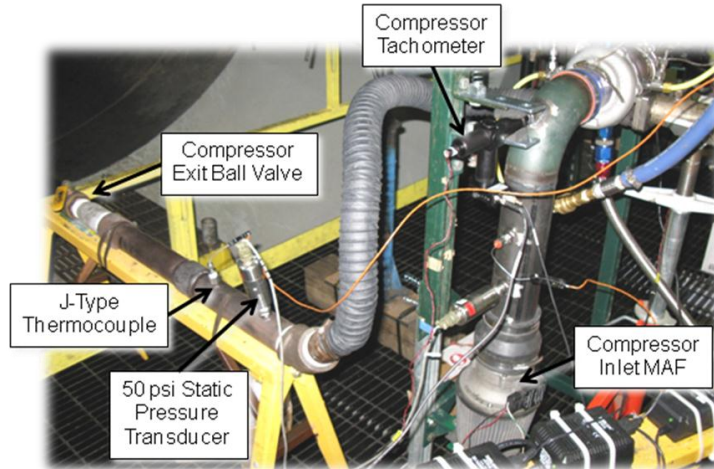


**Figure 87. Turbocharger compressor instrumentation and control valve**

Laser tachometers positioned at the compressor inlet and turbine exhaust, as shown in Fig. 88, determined turbocharger rotor speed. Each tachometer was constructed with a 4 mW, 670 nm diode laser with a collimating lens that focused a beam on blade leading/trailing edges, as shown in Fig. 89. The return deflected off an internal mirror toward a photodiode with a switchable-gain, amplified silicon detector. Blade arrival was indicated by a peak signal from the photodiode. Rotor speed was determined by the difference in blade arrival times. Pressure, mass flow rate, and rotor speed were sampled simultaneously at 5 MHz.

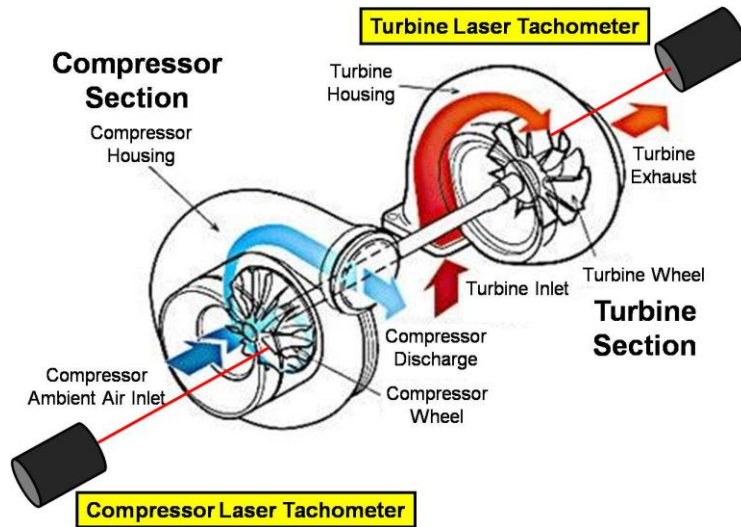


**Figure 88. Schematic of turbocharger tachometer arrangement**

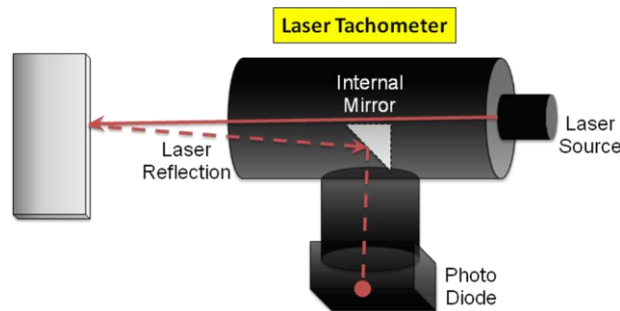


**Figure 89. Schematic of laser tachometer**

***Phase One: Cold Flow Driven Turbine***

For the first phase of testing, the turbocharger was mounted to a 152.4 mm (6 inch) long, 52.5 mm (2 inch) diameter steel pipe nipple that extends from the engine head. A quartz crystal, piezoelectric, dynamic pressure sensor was placed on the nipple at the turbine entrance. This pressure measurement was used to determine arrival of pressure pulses at the turbine inlet. Testing was conducted at a 10 Hz operating

frequency with 5.16 kg/min (11.35 lb/min) total turbine inlet air flow. As the equivalence ratio was zero, the fire phase only consisted of blow down from fill-air momentum.

***Phase Two: Steady Deflagration-Driven Turbine***

The second phase involved a modification to the normal PDE configuration for near constant pressure, steady deflagration combustion (shown in Fig. 90), by holding the main fill valves open and purge valves closed. The turbocharger was mounted to the end of the PDE tube such that the total length of 52.5 mm (2 inch) diameter steel pipe was 1219 mm (48 inches).

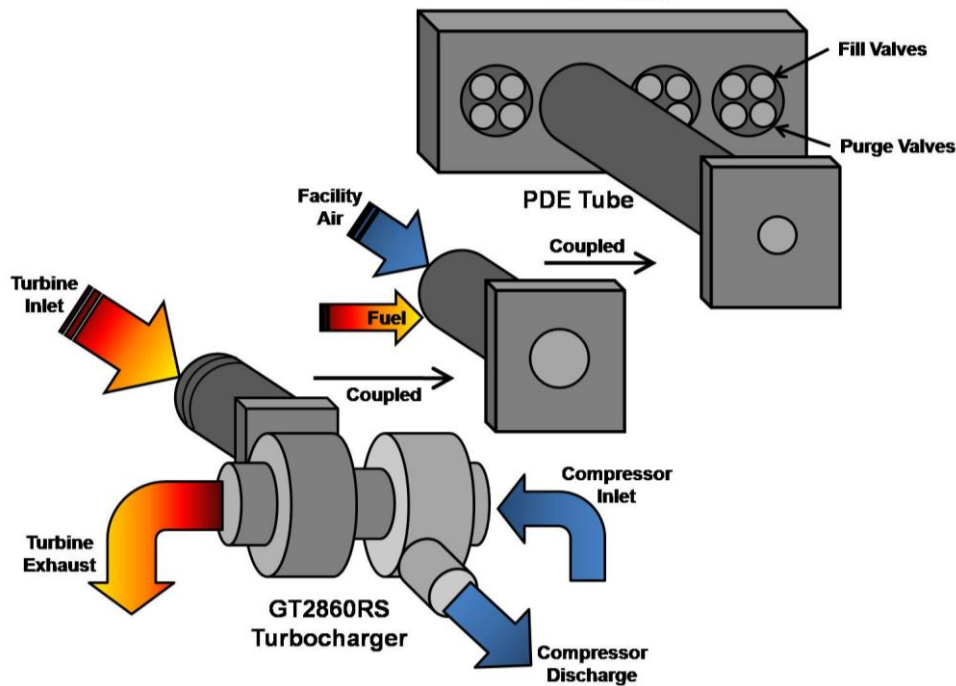


**Figure 90. Schematic of steady deflagration turbine experimental arrangement with GT2860RS turbocharger**

All internal DDT obstacles were removed that are normally used for PDE operation. An orifice plate with a 19 mm (0.75 inch) diameter hole was added 152.4 mm (6 inches) downstream of the fill valve to aid combustion. Fuel was injected just

downstream of this orifice plate at three equally spaced circumferential locations. A second orifice plate with a 31.75 mm (1.25 inch) diameter hole was added 304.8 mm (12 inches) downstream of the first orifice plate to assist with mixing and flame holding. An automotive spark plug was used for ignition just upstream of the second orifice plate. It was mounted flush to the tube wall and discontinued sparking once a flame was established. The remaining 762 mm (30 inches) of tube length was sufficient to ensure complete combustion before exhausting through the turbine. A J-type thermocouple was attached to the tube wall 304.8 mm (12 inches) downstream of the second orifice. After ignition, tube wall temperatures reached 644 K (700 deg F) in less than one minute, at which time data was sampled. The flame length was estimated to extend 152.4 mm (6 inches) downstream of the second orifice based on visible tube temperature discoloration.

SDC operation was attained by first setting desired air flow and then increasing fuel flow to a 0.75 equivalence ratio, at which point the spark plug operated at 100 Hz until a flame was achieved. The spark was then discontinued and tube temperature was observed to confirm that a continuous flame had been established. If tube temperature did not rise, spark ignition was repeated. Data was sampled as soon as the flame was established and before tube wall temperatures exceeded 644 K (700 deg F). Flames were established with up to 4.1 kg/min (9 lb/min) inlet air flow, bounding the range of operating conditions to be used for turbine performance comparisons.

### ***Phase Three: Pulsed Detonation-Driven Turbine***

The PDC in this experiment was a 52.5 mm (2 inch) diameter steel pipe. It was 1219 mm (48 inches) long, and used a 914.4 mm (36 inches) long, internal spiral to assist

with DDT. Equivalence ratio was set to 0.75 and is computed with both fill and purge air, as shown in Eq. (76). Fueled fraction was set to unity, and purge fraction was 0.31.

$$\phi = \frac{\left( \frac{\dot{m}_{fuel}}{\dot{m}_{air, fill} + \dot{m}_{air, purge}} \right)}{\left( \frac{\dot{m}_{fuel}}{\dot{m}_{air}} \right)_{stoich}} \quad (76)$$

Two ion probes were installed downstream of the spiral to verify Chapman-Jouget velocities. The probes short-circuit when the flame front arrives, and velocity is determined from the transition time between probes. The turbocharger turbine inlet was coupled to the PDC exhaust nozzle, as shown in Fig. 91. Data was sampled when tube wall temperatures reach 644 K (700 deg F).

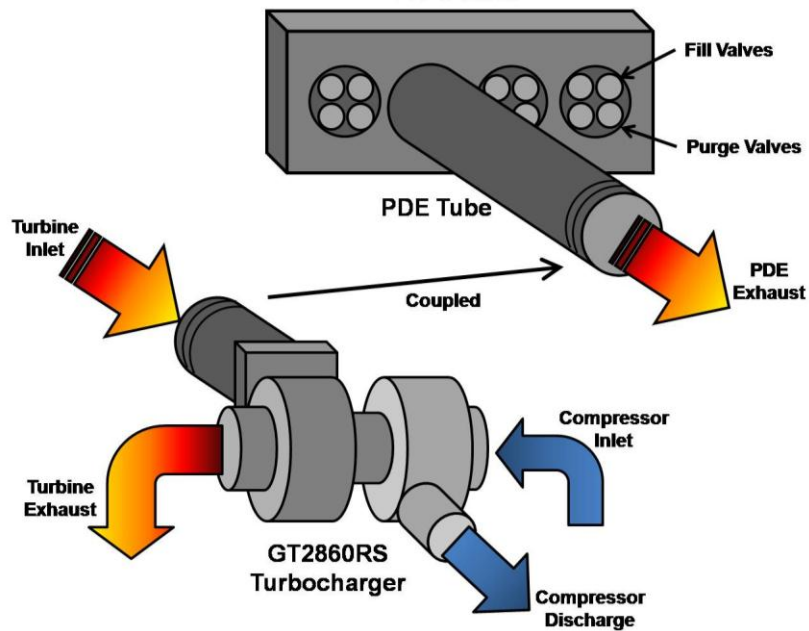


**Figure 91. Schematic of PDC-turbine experimental arrangement with GT2860RS turbocharger**

PDC operation was attained by first setting desired air flow and operating frequency. Then fuel was added until a 0.75 equivalence ratio is achieved, at which point spark ignition of the first detonation cycle occurred. Before the first detonation was achieved, the turbocharger turbine was driven by the fill and purge phases associated with the start-up sequence.

### ***Operating Conditions***

Combustor inlet operating conditions are tabulated below in Table 13. The range of conditions evaluated was constrained by SDC blow-out limits. Turbine rotor speed response was evaluated with the 10 Hz cold flow and 10 Hz PDC conditions. Total air flow for the PDC 11 Hz operating condition was matched to the SDC main air flow at approximately 3.63 kg/min (8 lb/min). The results from these two matching conditions were used for performance comparisons. Manifold pressures were higher for the SDC configuration because of the additional blockage from the orifice plate; however, there was also a greater associated total pressure loss with this configuration, such that initial combustor pressures were about the same, approximately 1.65 bar (24 psia), for both SDC and PDC operation.

**Table 13. Summary of SDC and PDC operating conditions**

Test Configuration	Operating Frequency (Hz)	Main Manifold Pressure (psia)	Main Manifold Temperature (deg F)	Purge Manifold Pressure (psia)	Purge Manifold Temperature (deg F)	Main Air Flow (lb/min)	Purge Air Flow (lb/min)	Fuel Flow (lb/min)
SDC	-	29.76	69.16	-	-	7.51	-	0.380
SDC	-	31.76	69.57	-	-	8.04	-	0.405
SDC	-	33.16	70.15	-	-	8.49	-	0.427
PDC	10	22.42	78.24	16.67	72.73	5.53	1.83	0.373
PDC	11	23.83	79.96	16.89	73.13	6.05	2.01	0.410
PDC	12	25.53	79.14	17.01	73.40	6.63	2.20	0.448

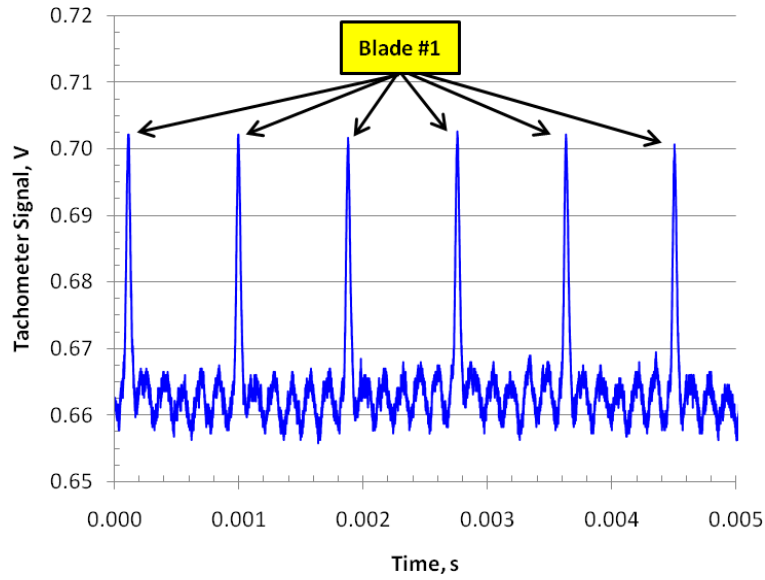
## Results

Turbine performance was assessed in terms of specific work and BSFC using Eqs. (72) through (75). PDC results are normalized by cycle time to compare average performance. Additionally, PDC driven turbine power and rotor transients are presented to assess unsteady turbine response.

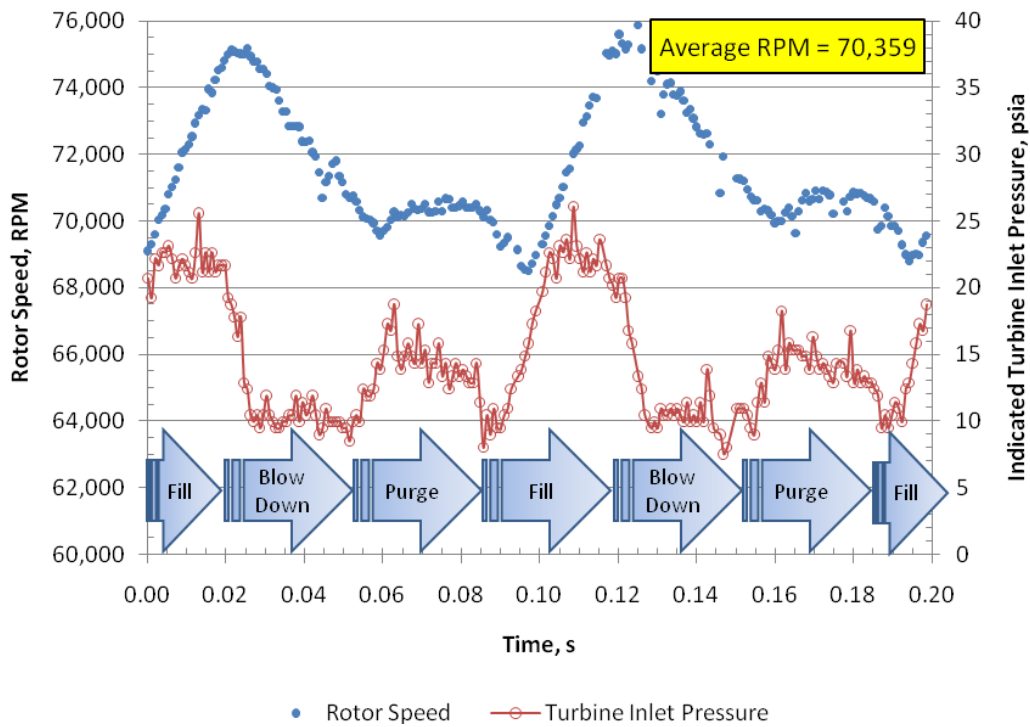
### *Cold Flow Driven Turbine*

Figure 92 includes a trace from the compressor laser tachometer at an average compressor operating condition of 5.05 kg/min (11.11 lb/min) corrected mass flow and an average pressure ratio of 1.29. One of the blade leading edges is painted white, rendering a stronger return than the others. This blade is arbitrarily called, “Blade #1.”

Instantaneous rotor speed is computed from Blade #1 arrival time subtracted from the previous Blade #1 arrival time (i.e., transient time for one revolution). The average rotor speed over the two cycles is about 70,359 RPM, which is consistent with the compressor operating map in Fig. 84 on page 146. Time history of rotor speed response and turbine inlet pressure is shown in Fig. 93. Transients in rotor speed correspond to transients in turbine inlet pressure, rising and falling with a lag of about 10 milliseconds. The first rise in rotor speed corresponds to the fill phase pressure, then decays during blow down, levels off momentarily at start of the purge phase, and then decays again until the start of the next fill phase.



**Figure 92. Compressor tachometer signal with 10 Hz cold flow operation**



**Figure 93. Rotor speed response over 2 cycles with 10 Hz cold flow operation**

### *Steady Deflagration Combustor Driven Turbine*

Results for the SDC driven turbine are tabulated below in Table 14. Compressor exit temperature was computed using Eq. (70) and 72% isentropic compressor efficiency. Specific turbine work was computed with Eq. (72), assuming 100% mechanical efficiency. In general, specific power increases with increasing inlet air flow, indicating an increase in either combustor, compressor or turbine efficiency, or a combination thereof. The second operating condition with 3.65 kg/min (8.02 lb/min) inlet air flow was selected as the baseline condition for comparing SDC and PDC driven turbine performance, minimizing the potential effects of variations in compressor efficiency.

**Table 14. Results from steady deflagration operation**

<b>Combustor</b>		<b>Compressor</b>					<b>Turbine</b>	
Inlet Air Flow Rate (kg/min)	Inlet Fuel Flow Rate (kg/min)	Corrected Mass Flow (kg/min)	Pressure Ratio	Average Rotor Speed (RPM)	Average Corrected Rotor Speed (RPM)	Average Exit Static Temp (K)	Average Power (Eq. 70) (kW)	Average Specific Work (Eq. 72) (kJ/kg)
3.40	0.17	4.68	1.19	60981	61722	316	1.61	28.41
3.65	0.18	4.98	1.22	62241	62997	319	2.00	32.94
3.86	0.19	5.29	1.24	65847	66647	321	2.33	36.30

### *Pulse Detonation Combustor Driven Turbine*

Results for the PDC driven turbine are tabulated below in Table 15. As with the SDC configuration, compressor exit temperature was computed using Eq. (70) and 72% isentropic compressor efficiency. Specific turbine work was computed with Eq. (72), assuming 100% mechanical efficiency. Specific work increases more significantly from the 10 Hz to 11 Hz operating conditions, than from the 11 Hz to 12 Hz, indicating a possible gradient in rising compressor/turbine efficiency.

**Table 15. Results from pulsed detonation operation**

<b>Combustor</b>			<b>Compressor</b>				<b>Turbine</b>		
PDC Frequency (Hz)	Inlet Air Flow Rate (kg/min)	Inlet Fuel Flow Rate (kg/min)	Corrected Mass Flow (kg/min)	Pressure Ratio	Average Rotor Speed (RPM)	Average Corrected Rotor Speed (RPM)	Average Exit Static Temp (K)	Average Power (Eq. 70) (kW)	Average Specific Work (Eq. 72) (kJ/kg)
10	3.35	0.17	5.20	1.23	66716	67526	321	2.21	39.85
11	3.66	0.19	5.67	1.28	70873	71734	325	2.84	46.66
12	4.01	0.20	5.94	1.30	74793	75701	328	3.21	48.04

Figure 94 includes a trace of rotor speed at the 10 Hz PDC operating condition. Scatter in the rotor speed is attributed to the vibration induced by the PDC. Therefore, a moving average of five data points was applied. The average rotor speed is 66,716 RPM with one major peak corresponding to the fire phase. Other signal traces included in Fig. 94 indicate the start of the fire phase and presence of the detonation wave. Spark ignition occurs at 30 milliseconds, followed by a drop in the ion probe signal 10 milliseconds later, indicating the detonation wave arrival. The photodiode in the turbine tachometer indicates the detonation wave exiting the turbine. The rotor speed rises just after the detonation wave exits the turbine, and peak rotor speed occurs less than 10 milliseconds later. Turbine rotor speed increases faster with the PDC at 10 Hz than with the cold flow driven turbine at 10 Hz. Rotor speed drops off during blow down and purge and settles during the fill phase.

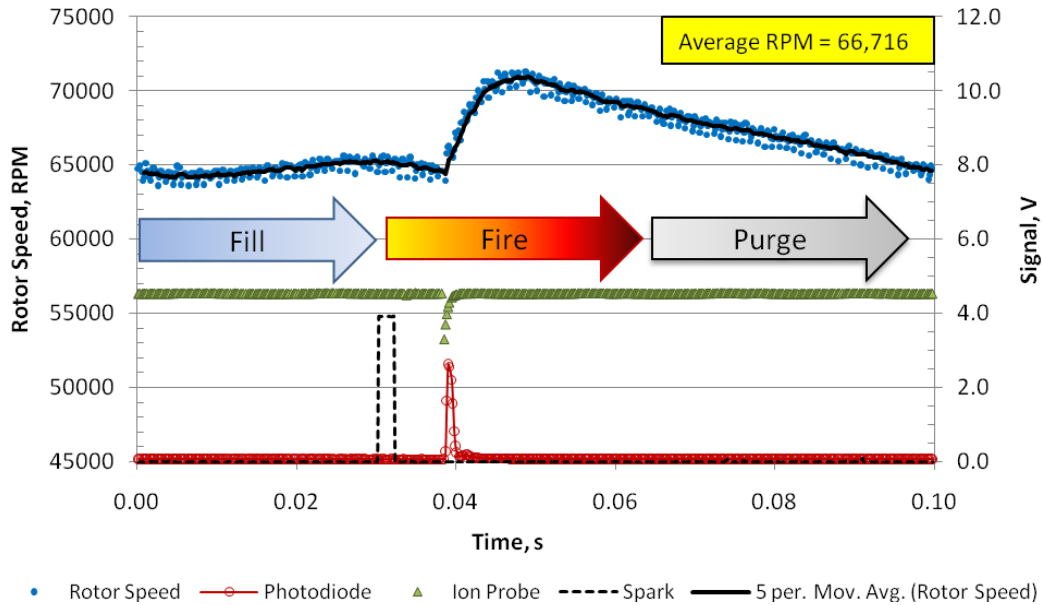


**Figure 94. Rotor speed response with 10 Hz PDC**

***Comparison of SDC and PDC Driven Turbine Performance***

Relative improvements are considered at a baseline operating condition in which combustor inlet air flow was about eight pounds per minute. Using Eq. (73) on page 147 for SDC and PDC results at this operating condition, there is a 41.3% relative improvement in specific work. This relative improvement is consistent with the 30% to 50% potential improvement reported by Bussing and Pappas (1994), using stoichiometric hydrogen-air at a compressor ratio of six. The ratio of inlet manifold pressure to ambient pressure in this study is about two. Using Eq. (75) on page 147, there is also a 28.7% relative improvement in BSFC at this baseline operating condition. Specific work is plotted in Fig. 95 for all inlet air flow operating conditions, and the PDC results are all higher than for the SDC driven turbine.

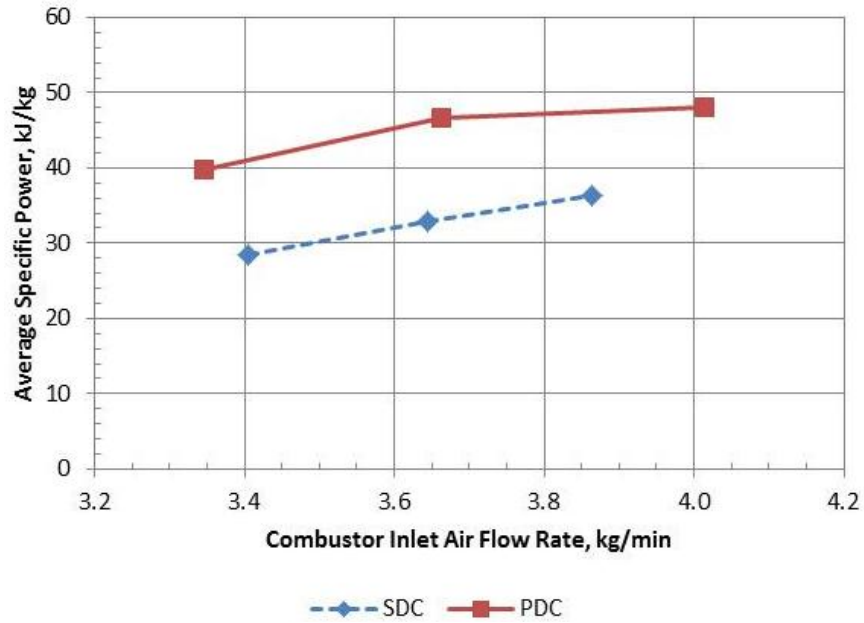


**Figure 95. Comparison of specific work for SDC and PDC configurations**

Figure 96 includes traces for two PDC cycles at 11 Hz, indicating the time dependent relationship between rotor speed and power. Peaks in compressor power correspond to peaks in rotor speed. Furthermore, there is a quasi-steady performance trend, in which power remains higher than the steady 2.0 kW (2.68 hp) achieved with the SDC configuration.

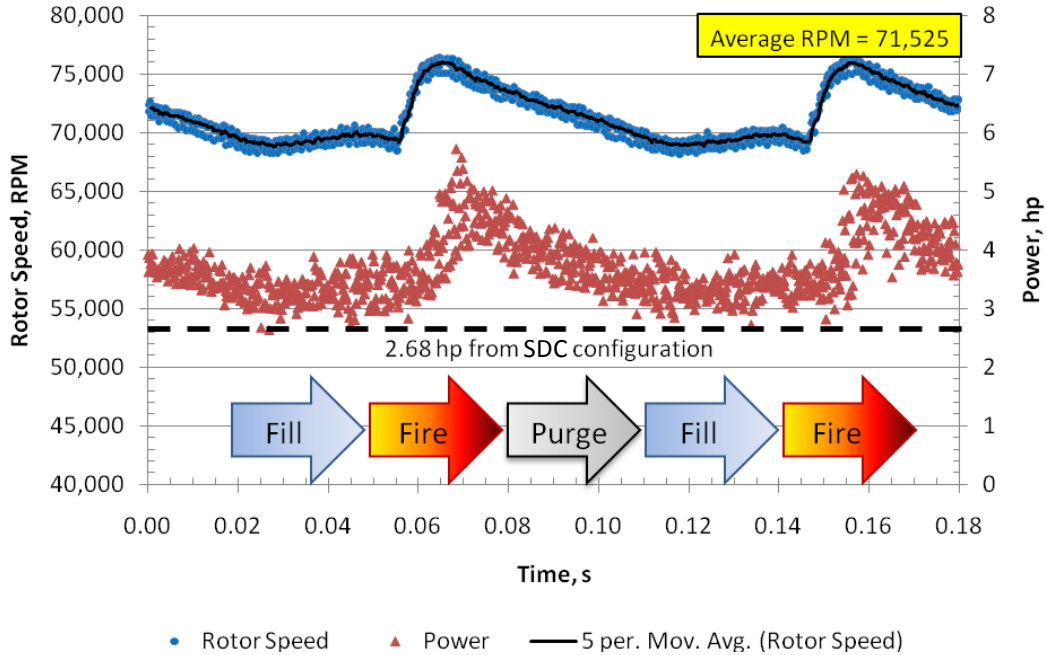


**Figure 96. Compressor power response over 2 cycles driven by PDC at 11 Hz with cycle turbine air flow of 3.65 kg/min**

**Summary**

At approximately the same combustor inlet conditions, there is a 41.3% relative improvement in specific power with the PDC driven turbine driven and a 28.7% relative improvement in BSFC, indicating that the turbine is able to extract the unsteady power in an effective manner. Turbine rotor speed reached peak RPM in less than 10 milliseconds after a detonation wave exited the turbine.

**Appendix E: Preliminary Parametric Study of PDC Operating Parameters,  
Presented at the 2010 AIAA Joint Propulsion Conference (AIAA-2010-6536)**

This experiment is an extension of previous work described in Appendix C; however, there are three distinct differences in the experimental configuration: use of hydrogen fuel, a GT28 journal bearing turbocharger, and a PDC with two orifice plate DDT obstacles that match the SDC arrangement. The first objective is to assess the current PDC-turbine arrangement by comparing PDC and SDC operation at conditions similar to the previous work. The primary objective is a parametric study of PDC overall equivalence ratio and operating frequency, assessing average specific work and rotor speed response. As equivalence ratio approaches unity, specific work is expected to increase. As operating frequency increases, specific work is expected to increase and rotor speed response is expected to approach a quasi-steady behavior with less variation between maximum and minimum rotor speed over a cycle.

The nine-blade, radial turbine used in this study is part of a Garrett GT28 automotive turbocharger, pictured in Fig. 15 on page 35. The turbine wastegate is capped so that all combustor exhaust passes through the turbine. The water-cooled, center housing contains the shaft and journal bearing assemblies. A journal bearing was chosen for durability with respect to thrust loads. The GT28 has a T04B class .60 A/R compressor housing and T3 5-Bolt, .63 A/R turbine housing.

**PDC-Turbine Arrangement with Orifice Plates for DDT**

The PDC in this experiment is a 52.5 mm (2 inch) diameter steel pipe with an overall length of 1.7 m. Two orifice plates assist with DDT. The first orifice is 31.75

mm in diameter and is located 355.6 mm from the head. The second orifice is 25.4 mm in diameter as is located 673.1 mm from the head. The blockage ratio is 0.6 for the upstream orifice and 0.75 for the downstream orifice. Blockage ratio is defined as the duct area blocked by orifice plates divided by total duct area. Two ion probes are installed downstream of the orifice plates to verify Chapman-Jouguet velocities. The probes indicate arrival of the flame front, and flame speed is determined from the transition time between probes.

PDC operation is attained by first setting desired air flow and operating frequency. Fuel is then added until a stoichiometric fill ( $\phi_{\text{fill}} = 1.0$ ) is achieved, at which point spark ignition of the first detonation cycle occurs. The turbocharger turbine inlet is coupled to the PDC exit as shown in Fig. 97 so that all of the mass flow from the PDC enters the turbocharger. Before the first detonation, the turbine is driven by fill and purge phases associated with the start-up sequence. The same configuration is used for SDC operation; however, fuel is mixed and ignited just downstream of the first orifice. During SDC operation, fill valves remain open and purge valves remain closed.

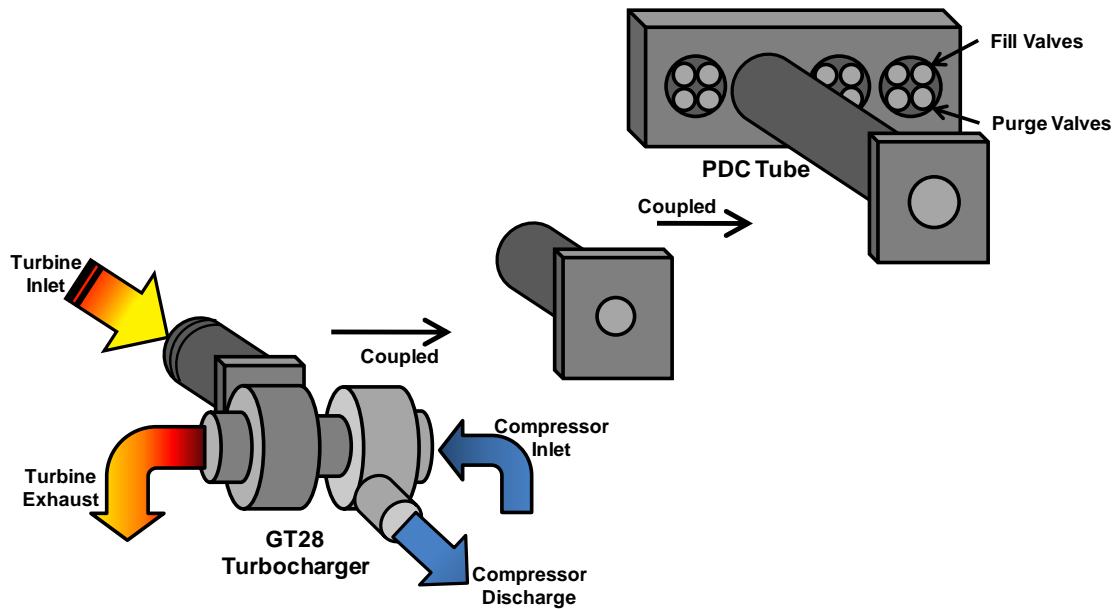


**Figure 97. Schematic of PDC-turbine rig with orifice plate DDT obstacles**

PDC operating frequency ranges from 10 Hz to 20 Hz while fueled fraction is held at unity. At each frequency tested, purge fraction ranges from 0.5 to 0.2. Overall equivalence ratio is defined in Eq. (76) on page 154. Test conditions are included in Table 16. Detonations were not observed at overall equivalence ratios of 0.58 and 0.64 while running at 20 Hz operating frequency.

**Table 16. Summary of PDC operating conditions with orifice plate DDT obstacles**

PDC Frequency (Hz)	Fueled Fraction	Purge Fraction	Overall Equivalence Ratio (Eq. 76)	Total Air Flow Rate (kg/min)
10	1.0	0.5	0.58	3.18
10	1.0	0.4	0.64	2.92
10	1.0	0.3	0.70	2.67
10	1.0	0.2	0.78	2.35
15	1.0	0.5	0.58	4.76
15	1.0	0.4	0.64	4.37
15	1.0	0.3	0.70	3.98
15	1.0	0.2	0.78	3.37
20	1.0	0.3	0.70	5.09
20	1.0	0.2	0.78	4.42

## **Power and Rotor Speed Instrumentation**

The compressor side of the turbocharger was used as a dynamometer, receiving ambient air through a mass air flow (MAF) sensor. A 3.45 bar (50 psi) static pressure transducer and J-type thermocouple are just downstream of the MAF on a 77.9 (3 inch) diameter elbow. The compressor exhaust contains a 3.45 bar (50 psi) static pressure transducer and J-type thermocouple along a 52.5 mm (2 inch) diameter pipe and a ball valve to back-pressure the compressor, as shown in Fig. 87 on page 150. The ball valve is set such that the compressor is on its design operating map. Several different compressor operating conditions are considered by adjusting the PDC operating frequency and equivalence ratio.

A Garrett speed sensor is positioned in the compressor housing, as shown in Fig. 23 on page 44. The sensor emits an electromagnetic field that is interrupted by passing blades. Rotor speed is determined by the difference in blade arrival times. Pressure, mass flow rate, and rotor speed were sampled simultaneously at 1 MHz.

## **Results**

A summary of PDC-turbine results are included in Table 17. At an overall equivalence ratio of 0.7, there is almost twice as much average specific work at 20 Hz than at 10 Hz. Variation in average rotor speed is shown in Fig. 98. At each frequency, average rotor speed varied less than 10% while overall equivalence ratio varied 34%. At an equivalence ratio of 0.70, average rotor speed increased 66% from 10 Hz to 20 Hz operation.

**Table 17. Summary of results with PDC having orifice plate DDT obstacles**

<b>Combustor</b>					<b>Turbine</b>		
PDC Frequency (Hz)	Fueled Fraction	Purge Fraction	Overall Equivalence Ratio (Eq. 76)	Total Air Flow Rate (kg/min)	Average Rotor Speed (RPM)	Average Power (Eq. 70) (kW)	Average Specific Work (Eq. 72) (kJ/kg)
10	1.0	0.5	0.58	3.18	75,356	1.80	33.93
10	1.0	0.4	0.64	2.92	77,960	2.01	41.13
10	1.0	0.3	0.70	2.67	75,356	1.92	43.20
10	1.0	0.2	0.78	2.35	74,764	1.77	45.27
15	1.0	0.5	0.58	4.76	105,426	4.41	55.63
15	1.0	0.4	0.64	4.37	104,471	4.35	59.68
15	1.0	0.3	0.70	3.98	102,796	4.12	62.14
15	1.0	0.2	0.78	3.37	100,971	3.99	71.12
20	1.0	0.3	0.70	5.09	124,924	7.04	82.95
20	1.0	0.2	0.78	4.42	114,360	5.53	75.06

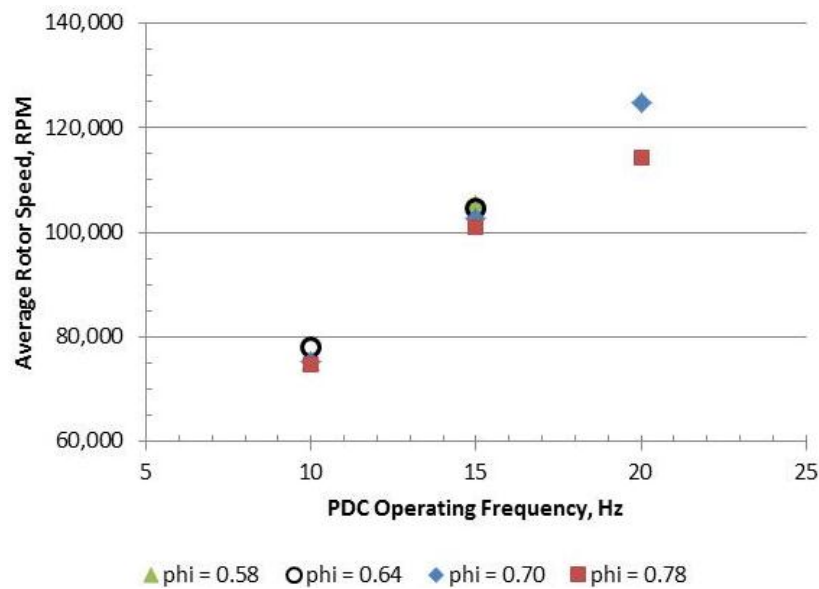


**Figure 98. Variation in average rotor speed with increasing PDC frequency**

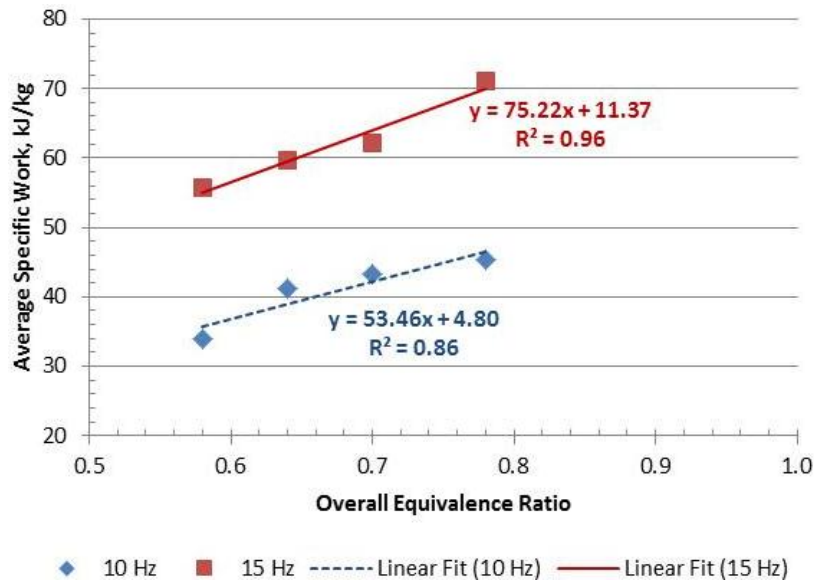
*Comparison of SDC and PDC Turbine Performance*

There was a 74% improvement in average specific work at 10 Hz operating frequency with purge fraction of 0.4, compared to SDC operation at the same airflow and fuel flow conditions. Main manifold pressure for the SDC was 0.2 bar (3 psi) greater

than for the PDC arrangement; however, a 0.2 bar (3 psi) drop was measured across the two orifice plates while running in the SDC mode. Airflow in SDC operation was 3.0 kg/min (6.6 lb/min), which was within 2% of the matching PDC operation. The large improvement in average specific work is comparable to previous work described in Appendix C.

### *Average Specific Work*

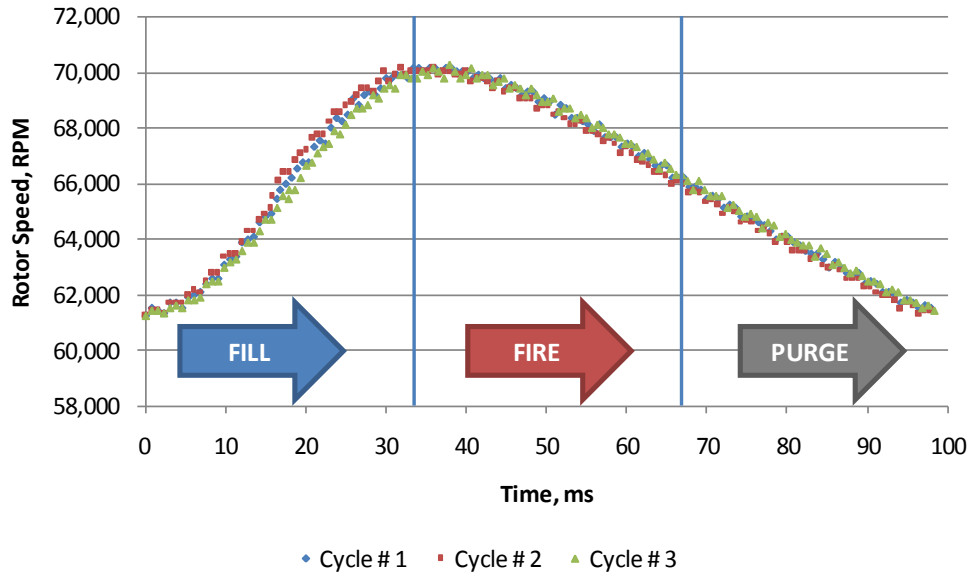
Figure 99 shows a linear relationship between overall equivalence ratio and specific work, such that average specific work increases with increasing equivalence ratio. At 20 Hz operating frequency, average specific work decreases with increasing equivalence ratio possibly due to sub-optimal PDC operation. Specific work increases significantly with operating frequency and is more sensitive to changes in operating frequency than overall equivalence ratio. In this study, equivalence ratio increased by reducing purge fraction. Therefore, the relative insensitivity of specific work to equivalence ratio indicates relative insensitivity of specific work to purge fraction. Increasing purge flow does not have a significant effect on specific work because of the relatively low energy content compared to the fueled flow. However, specific work does not distinguish between performance contributions from the combustor and the turbine. Rotor speed response must be considered to describe the turbine contribution.



**Figure 99. Comparison of average specific work at four equivalence ratios and two operating frequencies**

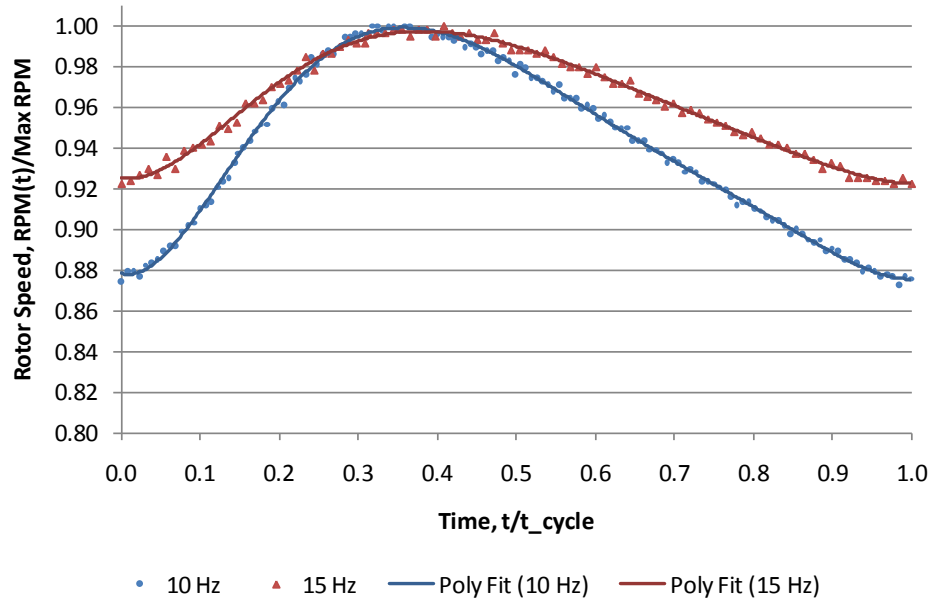
***Rotor Speed Response to Pulsed Cold Flow ( $\phi = 0.0$ )***

Figure 100 includes a time history of rotor speed while operating the combustor without fuel (i.e., equivalence ratio of zero) at 10 Hz with a fueled fraction of one and purge fraction of zero. During the fire phase, valves are closed and tube pressure drops as the fill charge evacuates. Mass flow during the fill phase was 6.12 kg/min (13.5 lb/min). Main manifold pressure was 1.86 bar (27 psi), and there was about a 0.69 bar (10 psi) pressure drop across the orifice plates. Three cycles are overlaid from a single run, synchronized by minimum RPM. Figure 100 indicates good periodicity. During the fill phase, rotor speed climbs more than 8,000 RPM. Rotor deceleration was constant during fire and purge phases due to the absence of combustion and purge flow.



**Figure 100. Rotor speed periodicity for 10 Hz cold flow operation ( $\phi = 0.0$ ) with 1.0 fueled fraction and zero purge fraction**

Figure 101 shows rotor speed time history for two cold flow operating frequencies, normalized by total cycle time and max RPM. Rotor speed drops 8% during 15 Hz operation and 12% during 10 Hz operation. As frequency increases, rotor response approaches quasi-steady behavior. A polynomial fit was applied to the data to help visualize the turbine behavior.



**Figure 101. Normalized rotor speed time history with 10 and 15 Hz cold flow operation ( $\phi = 0.0$ ) with 1.0 fueled fraction and zero purge fraction**

### *Rotor Speed Response to Pulsed Detonations*

Figure 102 includes rotor speed history for three PDC cycles at 10 Hz operating frequency with a fueled fraction of one and purge fraction of 0.4. Good periodicity is indicated in Fig. 103, where the three cycles are overlaid and synchronized by minimum RPM. During the fire phase, rotor speed climbs more than 15,000 RPM in about 15 ms. As with cold flow operation, rotor deceleration is constant, indicating that purge flow does not contribute significantly rotor speed response. The turbine unwinds during blowdown, purge and fill over the course of 85 ms.

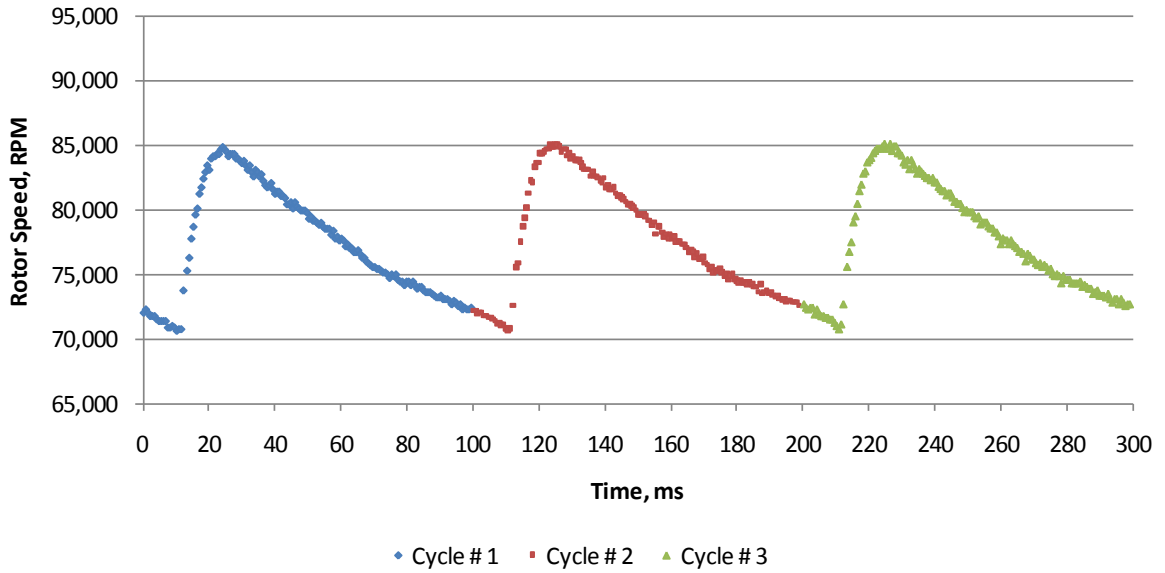


**Figure 102. Rotor speed time history with 10 Hz PDC with 1.0 fueled fraction and 0.40 purge fraction**

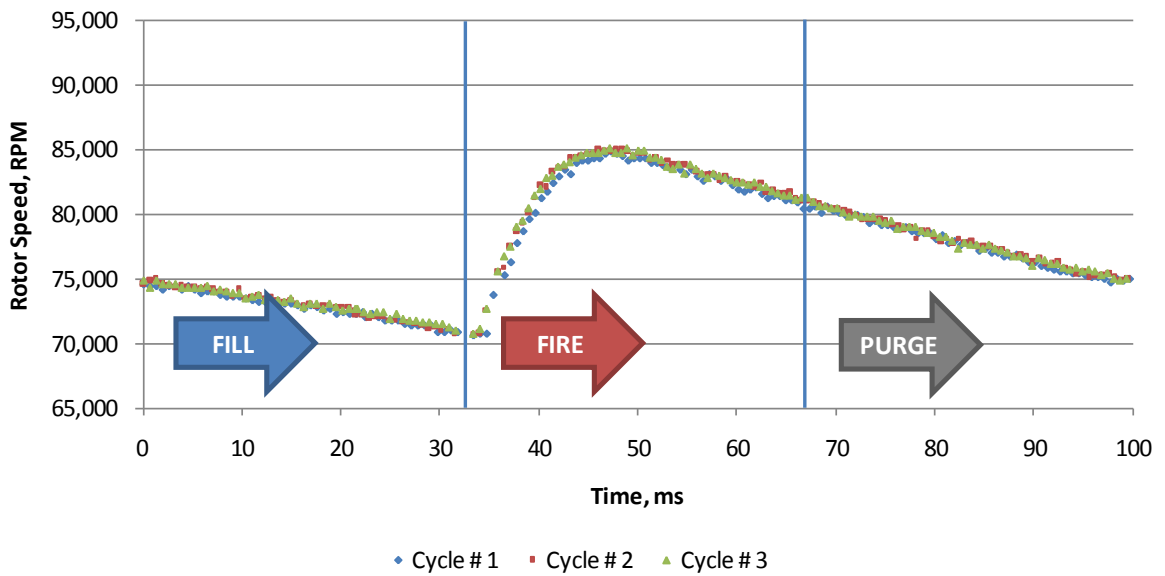


**Figure 103. Rotor speed periodicity with 10 Hz PDC with 1.0 fueled fraction and 0.40 purge fraction**

Figure 104 shows rotor speed time history for three PDC operating frequencies normalized by cycle time and max RPM. Purge fraction is 0.3 for an overall equivalence

ratio of 0.70. Rotor speed drops 10% during 20 Hz operation, 13% during 15 Hz operation, and about 17% during 10 Hz operation. As with cold flow operation, rotor response approaches quasi-steady behavior with increasing operating frequency. Peaks level-off and slide to the right as frequency increases. There is 4 times more rotational energy stored during the fire phase at 20 Hz than 10 Hz. A polynomial fit was applied to the data to help visualize the turbine behavior.

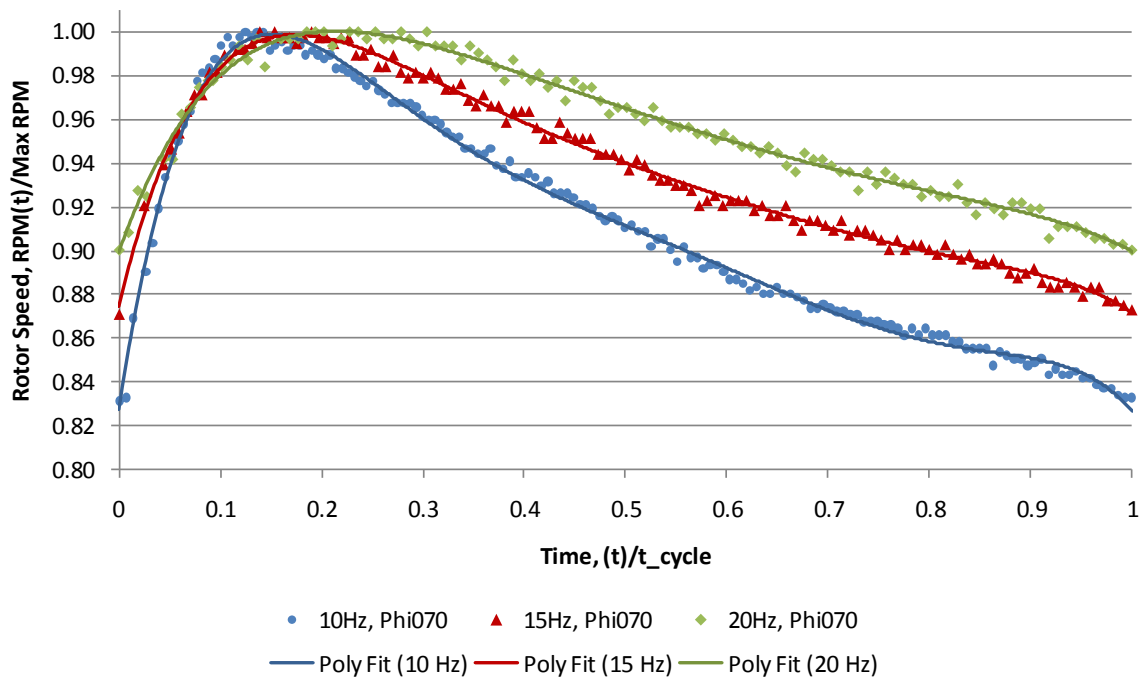


**Figure 104. Normalized rotor speed time history with 10, 15, and 20 Hz PDC with overall equivalence ratio of 0.70**

Figure 105 overlays rotor speed history for four overall equivalence ratios at 15 Hz PDC operating frequency, synchronized by minimum rotor speed. The shapes of the curves are not sensitive to changes in equivalence ratio; however, the magnitudes increase slightly with decreasing equivalence ratio due to additional purge mass flow. Whereas purge mass flow increased by 259% from equivalence ratio of 0.78 to 0.58, peak rotor

speed increased by 3.61%. Peak rotor speed occurs around 12 ms for each curve, and the difference between minimum and maximum rotor speed is about 15,000 at each equivalence ratio. A polynomial fit was applied to the data to help visualize the turbine behavior.

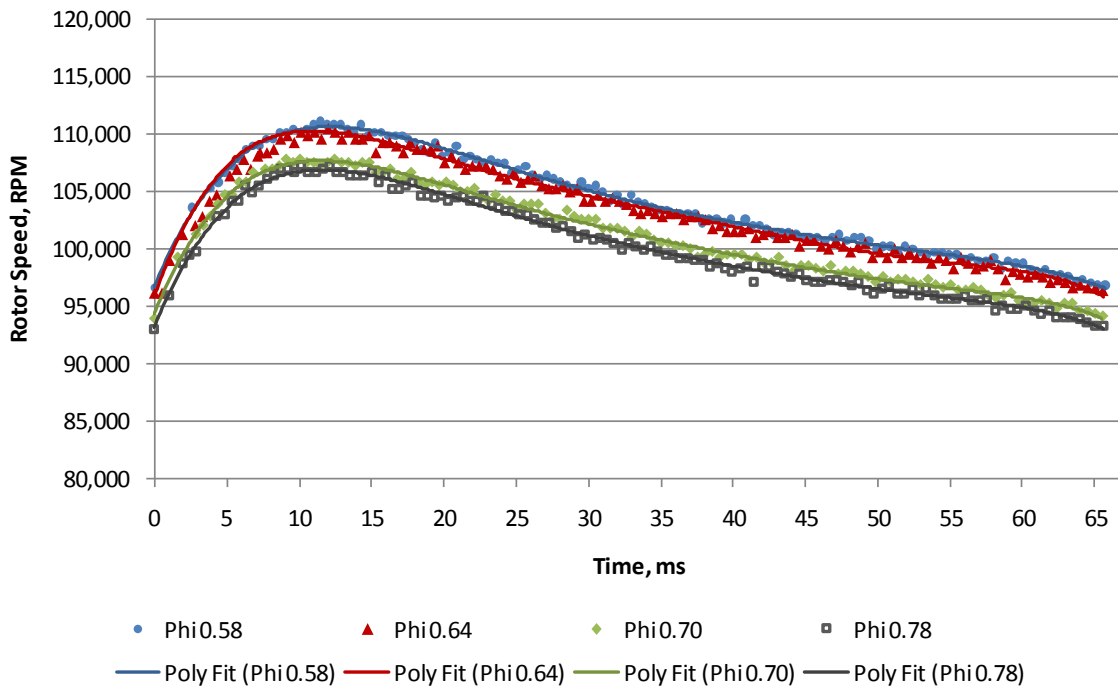


**Figure 105. Rotor speed history with 15 Hz PDC with overall equivalence ratios of 0.58, 0.64, 0.70, and 0.78**

### Summary

The current study investigated the effect of PDC operating parameters on turbine performance. Higher operating frequencies increased average specific work and resulted in rotor speed response approaching quasi-steady behavior. Average specific work was not as sensitive to equivalence ratio as it was to operating frequency. Rotor speed response was not sensitive to overall equivalence ratio, increasing slightly in magnitude as purge mass flow increased.

**Appendix F: Preliminary PDC-Turbine Flowfield and Rotor Speed Measurements,  
Presented at the 2011 AIAA Aerospace Sciences Meeting (AIAA-2011-0577)**

The primary motivation of this experiment is to evaluate instrumentation methods with sampling frequencies greater than 10 kHz, acquiring data required for future unsteady turbine performance assessments. Time-resolved temperature, pressure, and velocity are required to calculate unsteady turbine efficiency, and time-resolved rotor speed is essential for describing turbine response to detonations. Additionally, a comparison of rotor speed instrumentation techniques is made with measurements of compressor blade passing frequencies. High frequency events in the pulsed detonation cycle, such as the von Neumann spike, size the time scale and determine the minimum sampling rate for adequate wave-form resolution.

**PDC-Turbine Arrangement with Internal Spiral for DDT**

The nine-blade, radial turbine used in this initial configuration was part of a Garrett GT28 automotive turbocharger, pictured in Fig. 15 on page 35. The turbine wastegate was capped so that all combustor exhaust passes through the turbine. Experiments were carried out in the AFRL Detonation Engine Research Facility, using configurations similar to previous work described in Appendix C and Appendix D. The PDC in this configuration was a 52.5 mm (2 inch) diameter steel pipe that is 914.4 mm (36 inches) in length. An internal spiral 457.2 mm (18 inches) in length assisted DDT.

PDC start-up operation was attained by first setting desired air flow and operating frequency. Then, start-up spark ignition occurred as hydrogen fuel was added until a desired equivalence ratio ( $\phi = 1.0$ ) was achieved, by which time the detonation cycle was

established. The turbine inlet of the turbocharger was coupled to the PDC exit as shown in Fig. 106. All of the mass flow from the PDC entered the turbocharger. Before the first detonation, the turbocharger turbine was driven by the fill and purge phases associated with the start-up sequence. The compressor side of the turbocharger was used as a dynamometer, as described in Appendix C and shown in Fig. 87 on page 150.

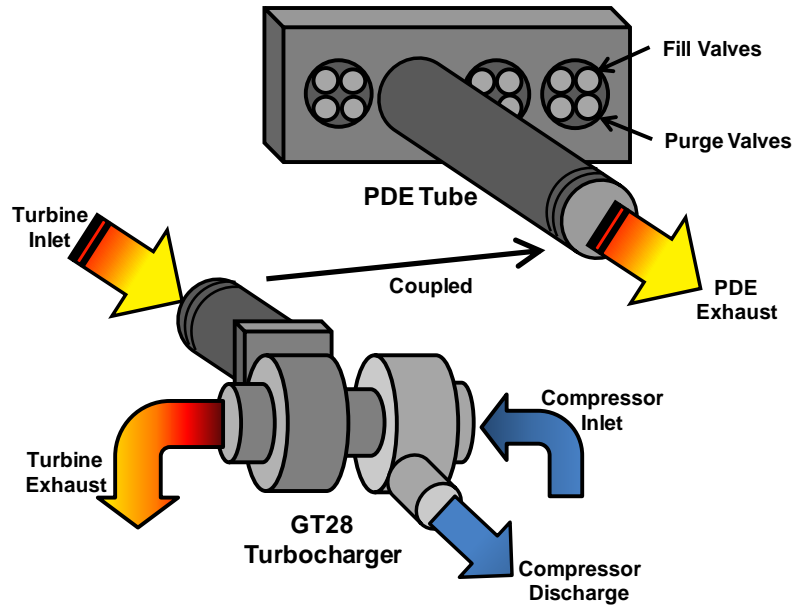


**Figure 106. Schematic of PDC-turbine test rig arrangement for preliminary high-speed flowfield measurements**

### **Rotor Speed Measurement Techniques**

Two different rotor speed instrumentation packages were used during testing. A Garrett speed sensor (part number #781328-0002) was positioned in the compressor housing, as shown in Fig. 23 on page 44, to detect blades arrival. The sensor emits a magnetic field that is interrupted by passing blades. Rotor speed is determined from the blade passing frequency. The input frequency is one pulse per blade. The internal sensor electronics divide the input signal by eight, so that the output frequency is a square-wave

signal at  $1/8^{\text{th}}$  the actual blade passing frequency. The output frequency is multiplied by eight during post-processing to obtain the input frequency. The turbocharger compressor has 12 blades.

The second rotor speed measurement was made with laser tachometers positioned at the compressor inlet and turbine exhaust, as described in Appendix C and shown in Figs. 86 and 87 on pages 149 and 150, respectively. Each tachometer was comprised of a 4 mW, 670 nm diode laser with a collimating lens that focused a beam on compressor blade leading edges and turbine blade trailing edges. The return beam deflected off an internal mirror toward a photodiode with a switchable-gain, amplified silicon detector. Blade arrival was indicated by a peak signal from the photodiode. As with the Garrett sensor, rotor speed was determined by the difference in blade arrival times. The photodiode output frequency matched the blade passing frequency. The compressor tachometer does not detect the six secondary splitter blade leading edges, which are concealed by the six primary blades. In hot flow (with detonations) the turbine laser tachometer photodiode was saturated by the flame illumination, preventing the detection of blade trailing edges. Though this effect was limited to a brief period, the timing coincides with the rapid acceleration in rotor speed. Therefore, the compressor tachometer results are used for rotor speed in this study, not the turbine tachometer.

#### **Turbine Inlet and Exit Flowfield High-Speed Measurement Techniques**

Table 18 includes a summary of the flow field instrumentation techniques employed in this experiment. A combination of these techniques will be used to collect the necessary flow field properties to calculate unsteady turbine efficiency. Static

pressure transducers were flush mounted on the inlet and exhaust tube walls. The inlet transducer was located 25.4 mm (1 inch) upstream of the turbocharger turbine inlet flange. The exit transducer was located 152 mm (6 inches) downstream of the turbine.

**Table 18. Preliminary turbine inlet and exit flowfield measurement techniques**

Technique	T_in	T_exit	P_in	P_exit	u_in	u_exit
Wall-Mounted Static Pressure Transducer			X	X		
Two Color Band Optical Pyrometry	X	X				
Particle Streak Velocimetry (PSV)					X	
Background Oriented Schlieren (BOS)				X*		X
*Note: The BOS technique provides density, which will ultimately produce pressure data when combined with temperature data from optical pyrometry						

Turbine inlet and exit pressures, temperatures, and velocities were measured on different test runs, under the same test set-up and operating conditions. Kulite static pressure transducers were mounted to the inlet and exhaust walls with a 14 mm stand-off for cooling. The inlet transducer was located 25.4 mm upstream of the T3 flange. The exit transducer was located 152 mm downstream of the turbine. The sampling frequency for pressures was 1 MHz. Inlet and exit pressure measurements were made simultaneously; however, they were made apart from velocity and temperature measurements.

For velocity and temperature optical instrumentation, a square pipe section with a 50.8 mm by 50.8 mm cross section, a 610 mm length, and two side-mounted quartz windows was added upstream of the turbocharger, coupled between the second and third combustor sections, as shown in Fig. 107. A similar arrangement with a polycarbonate

window was mounted downstream of the turbo, coupled to the exhaust elbow with a pipe reducer.

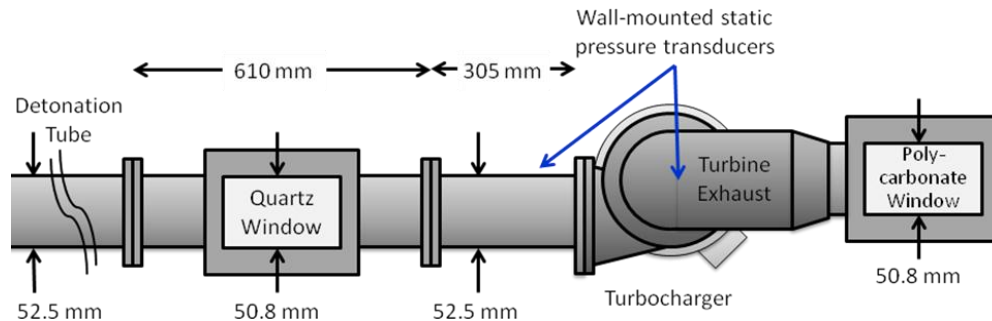


**Figure 107. Schematic of optical access for preliminary high-speed measurements**

### *Optical Pyrometry*

For optical pyrometry temperature and PSV velocity measurements, a square pipe section with a 50.8 mm x 50.8 mm (2 in x 2in) cross section, 305 mm (1 ft) in length, and two side-mounted quartz windows was mounted upstream of the turbocharger turbine, as shown in Fig. 108. A square pipe section with a 50.8 mm x 50.8 mm (2 in x 2in) cross section, 915 mm (3 ft) in length, and with two side-mounted plexiglass windows was mounted downstream of the turbine, coupled to the turbine exhaust elbow with a pipe reducer. To demonstrate the capability of a high speed color camera to capture temperature fields in combustion systems, a PCO Dimax high-speed color camera was used. Measurements with a tungsten lamp and spectrometer allowed the spectral responsivity of the red, green and blue channels of this camera to be measured (see Fig. 109 left graph). Substituting the spectral responses and integrating them with a blackbody function over the appropriate wavelengths allows the ratio to be determined as a function of temperature (see Fig. 109 right graph).

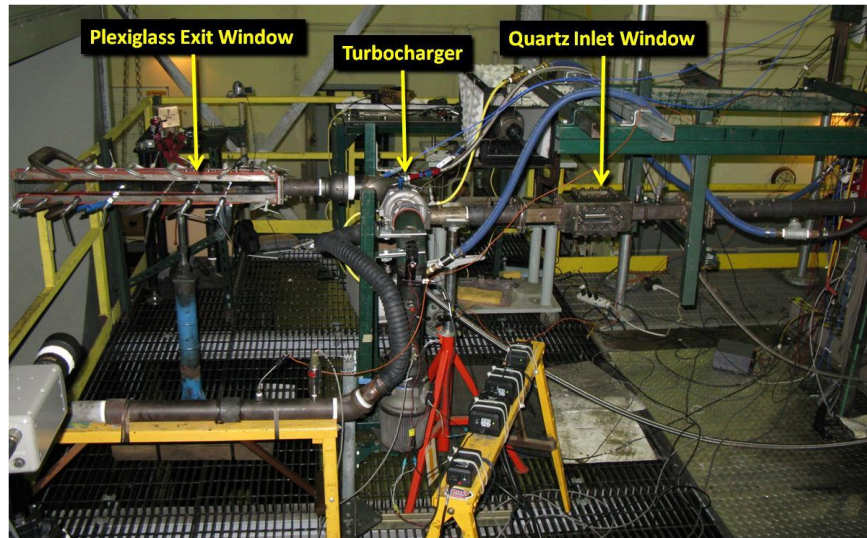


**Figure 108. Preliminary arrangement of turbine inlet and exit optical access high-speed flowfield measurements**

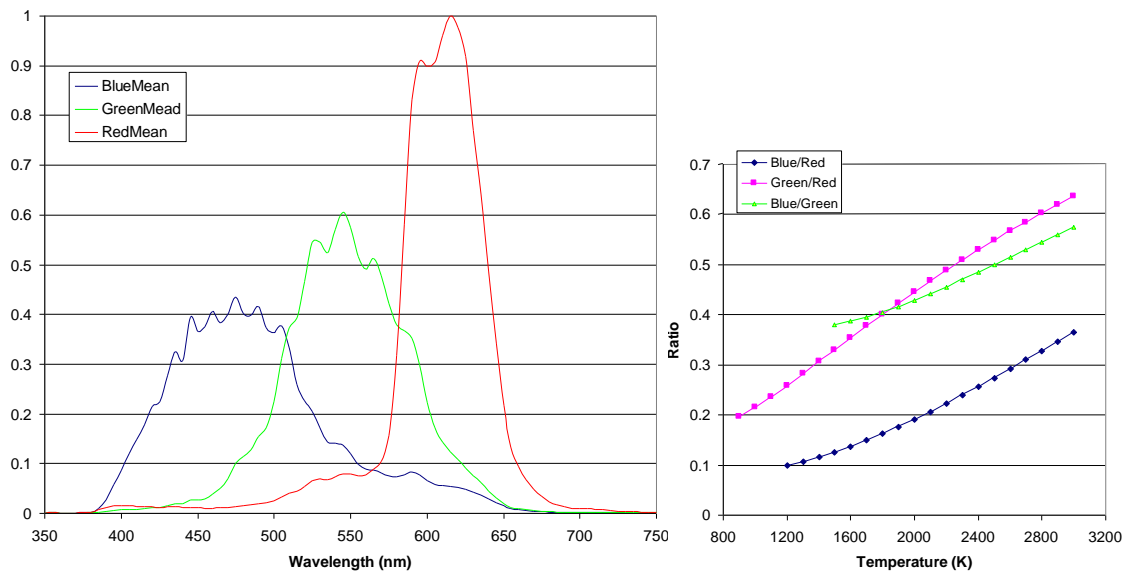


**Figure 109. Left graph: PCO Dimax camera relative responsivity for the blue, green and red channels as a function of wavelength. Right graph: ratio of the various color channels for a PCO Dimax camera as a function of temperature for a black or gray body emitter**

Soot is only formed in the fuel rich areas of flames and may not be present in a combustion region of interest. Therefore, silicon carbide (SiC) seed particles (1-2  $\mu\text{m}$  in size) have been used for seeding combustion flow fields. SiC filaments have been used for thermometry for many years. The technique termed Thin Filament Pyrometry (TFP) has been used in a variety of laboratory flame systems (Vilimpoc, et al. 1988). Graybody emission from the filament is recorded and used to determine flame temperature. Because the filament is small, the temporal response of the filament to temperature changes is high ( $>1,000$  Hz). The technique is somewhat limited, however, by the fragility of the small  $10 \mu\text{m}$  filaments. To overcome this limitation, SiC particles are used to seed combustion flow, rather than filaments. The SiC particles, 2400 grit size, were injected into the PDC fuel line with a standard dry cyclone seeder. The PCO Dimax camera was operating with a  $1.5 \mu\text{s}$  exposure and  $87 \mu\text{s}$  inter-frame time to achieve a frame rate of 11,484 frames/s. Pyrometry was only valid when particles were at high enough temperatures to produce sufficient emission. Thus, pyrometry temperatures were not available during fill and purge phases.

### ***Particle Streak Velocimetry***

PSV measurements were taken through the quartz window at the turbine inlet to determine the velocity of the PDC gases after the detonation front. When using ethylene fuel, a significant amount of soot was formed in exhaust gases at stoichiometric conditions. By increasing exposure time of the PCO Dimax high-speed camera from 1 to  $10 \mu\text{s}$ , time history of the soot particle streaks were traced from frame to frame. The turbine inlet velocity field was determined by dividing the length of a particle streaks by

the exposure time. To increase the contrast between the soot streaks and the surrounding gas emission, an edge enhancing convolution was applied to the image before analysis.

### ***Background Oriented Schlieren***

BOS is an optical measurement technique that has the ability to visualize density gradients. Meier (1998) first proposed BOS, which can be described as a simple Schlieren technique based on image displacements of a background caused by density gradients in the optical path. A major advantage of the technique is that it requires only a digital camera of sufficient resolution to allow background displacements to be accurately captured. The background displacements are typically determined using particle image velocimetry (PIV) based correlation methods which are well established. Early studies (Richard, et al. 2000; Raffel, et al. 2000) demonstrated several possible applications of BOS for determining density fields of helicopter-generated vortices and supersonic jets. Recent work has demonstrated quantitative visualization of density flow in an axisymmetric cone-cylinder in a Mach 2,0 flow. Venkatakrisnan and Meier (2004) successfully validated the BOS technique by comparing the cone cylinder results with data from cone tables and isentropic solutions. The kilohertz capability of the BOS technique was demonstrated in 2009 when it was successfully used to capture transient igniter temperatures at rates in excess of 24,000 frames per second (Blunck, et al. 2010).

The BOS technique was chosen for this study because of its ability to function with high speed cameras, which allow density field images of pulsed detonation exhaust to be captured at a very high rate. To achieve these high rates, a Phantom v7 was utilized in conjunction with an over-driven pulsed LED array. High framing rates required that

the BOS background be setup in a transmission mode with the LED array arranged as a back light. This ensured that the maximum amount of light was available to the Phantom camera, which helped to minimize the pulse width of the LED array ( $\sim 1\mu\text{s}$ ) and allowed the use of a large  $f\#$  (22) needed for increased sensitivity and measurement resolution.

The experimental arrangement used to capture the BOS data is shown in Fig. 110. The output of the pulsed LED array was directed through a series of scattering glass plates that formed the random background needed for the BOS experiment. The background image from the scattering plate was recorded with a high speed cine Phantom v7 camera with a 500 ns exposure and 122  $\mu\text{s}$  inter-frame time. Transient density gradients caused by the PDC-turbine exhaust pulse distorted the background image and were recorded by the Phantom camera. The displacement of the background due to the density field was determined by conducting a correlation analysis between the non-disturbed image (no flow) and the gradient disturbed images (flow). This is an established approach used in PIV analysis where particle movement between successive images is correlated to yield the velocity field. If the temperature field or pressure field is known from an independent measurement, then either the transient-temperature or transient-pressure can be determined from the density field.

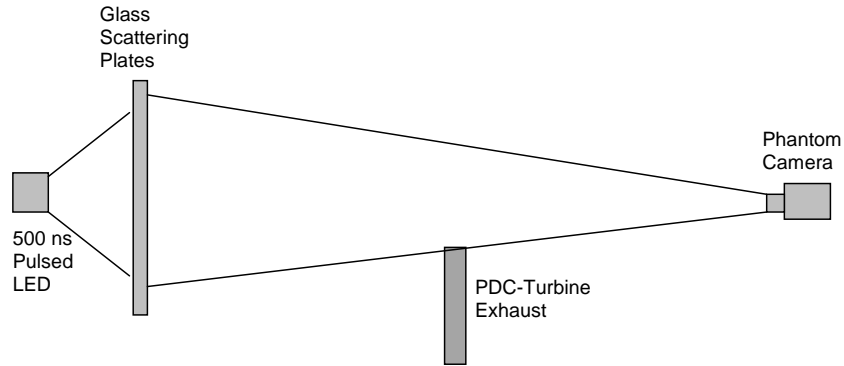


**Figure 110. Schematic of background oriented Schlieren arrangement utilized for high-speed visualization, density and velocity measurements at the PDC-turbine exit**

Figure 111 shows the BOS displacement vector magnitudes in the flow field of the pulsed detonation driven turbine exit. Not only was the BOS technique used to determine density, it was also used to measure the velocity of the density structures. To accomplish this task, the displacement magnitude images were correlated (using PIV analysis software) to yield the gradient density velocity.

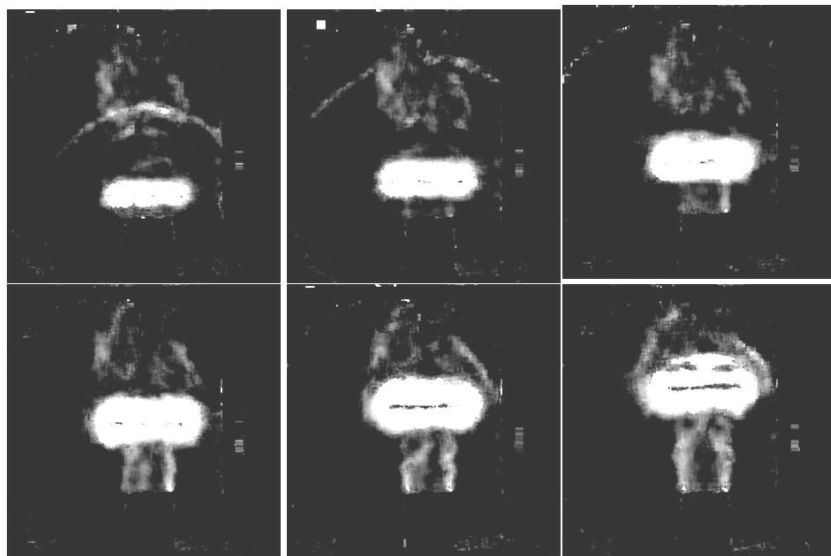


**Figure 111. Six sequential frames of BOS vector magnitude plots for a pulsed detonation turbine exhaust flow field. Flow in each image is from bottom to top, and the sequence proceeds from left to right with 0.12 ms time step.**

### Comparison of Rotor Speed Results

Figure 112 shows a sample trace of rotor speed history from the compressor laser tachometer for a 10 Hz PDC with a fueled fraction of 1.0 and a purge fraction of 0.3. Scatter in rotor speed is attributed to vibration induced by the PDC. A simple arithmetic average of rotor speed was 66,716 RPM with the major peak corresponding to the effects of fire phase. The spark signal trace included in Fig. 112 indicates the start of the fire phase at about 30 ms, and the signal peak from the turbine laser tachometer photodiode indicates the detonation wave exits the turbine at about 40 ms. The rotor speed rises just after the detonation wave exits the turbine, and peak rotor speed occurs about 10 ms later.

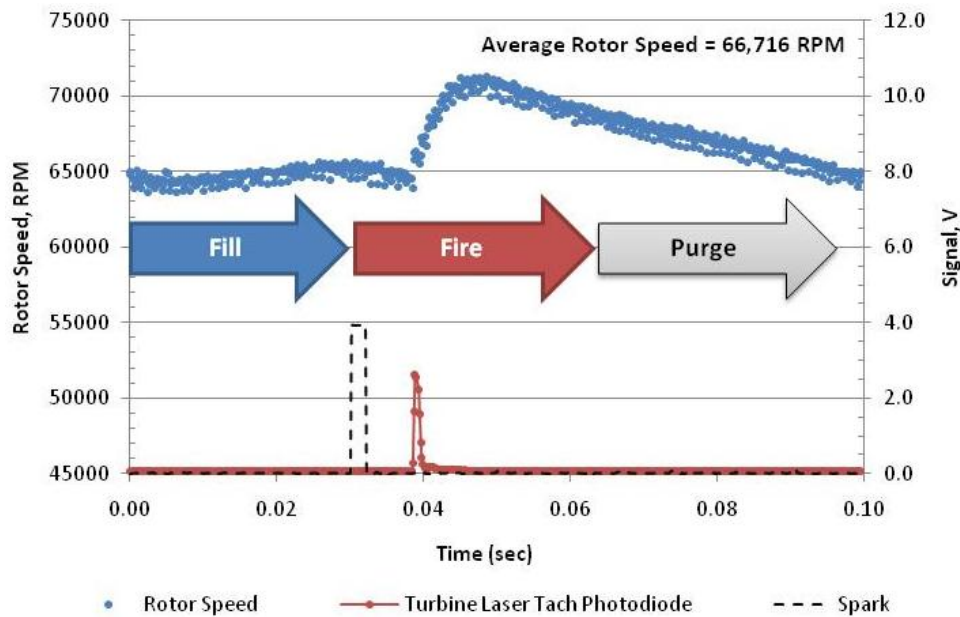


**Figure 112. Rotor speed history using the compressor laser tachometer with 10 Hz PDC with 1.0 fueled fraction and 0.3 purge fraction**

Figure 113 shows compressor rotor speed history from the Garrett speed sensor over three detonation cycles for a 15 Hz PDC with a fueled fraction of 1.0 and a purge fraction of 0.5. There is less scattered than with the laser tachometer, due to the 1/8<sup>th</sup>

frequency filter; however, there is also less resolution around the time that the detonation arrives at the turbine (about 0.06 ms). There is good periodicity between detonation events, and the rotor speed climbs about 15,000 RPM. Peak rotor speed occurs in less than 10 milliseconds, as was observed with the laser tachometer.

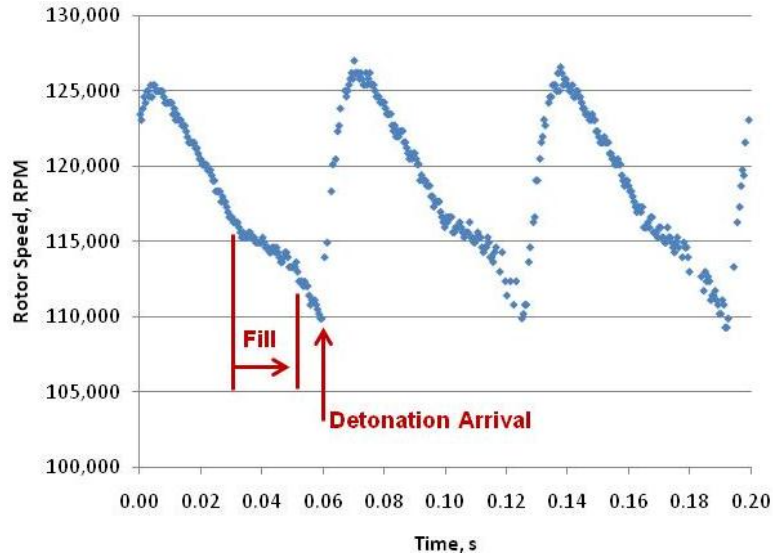


**Figure 113. Compressor rotor speed history using a Garrett speed sensor with 15 Hz PDC with 1.0 fueled fraction and 0.5 purge fraction**

Time-resolved net shaft torque,  $\tau_{shaft,net}$ , was calculated using Eq. (77), and rotational energy was calculated using Eq. (78), using data from the Garrett speed sensor. The manufacturer’s reported moment of inertia for the wheel assembly is  $3.2E-5 \text{ kg m}^2$ .

$$\tau_{shaft,net}(t) = I \left( \frac{\omega(t + \Delta t) - \omega(t)}{\Delta t} \right) \quad (77)$$

$$KE_{rot}(t) = \frac{1}{2} I (\omega(t))^2 \quad (78)$$

Figure 114 shows time history of rotational energy and net shaft torque for one complete detonation cycle. From minimum rotor speed at the detonation arrival time to the time at peak rotor speed (about 11 ms), the average rate at which rotational energy was stored was 59.34 kW (from the slope of the curve), and the average rate at which rotational energy was depleted over the remaining 55 ms was 11.57 kW, from the time at peak rotor speed until the next detonation arrived. Torque response was dynamic, with a sharp increase that coincided with the rise in rotor speed with the detonation arrival at the turbine inlet. The ensuing large peaks and valleys in torque indicate possible winding and unwinding in the shaft. This ringing in the shaft was most pronounced during the rise in rotor speed but quickly settled as rotor speed began to fall.

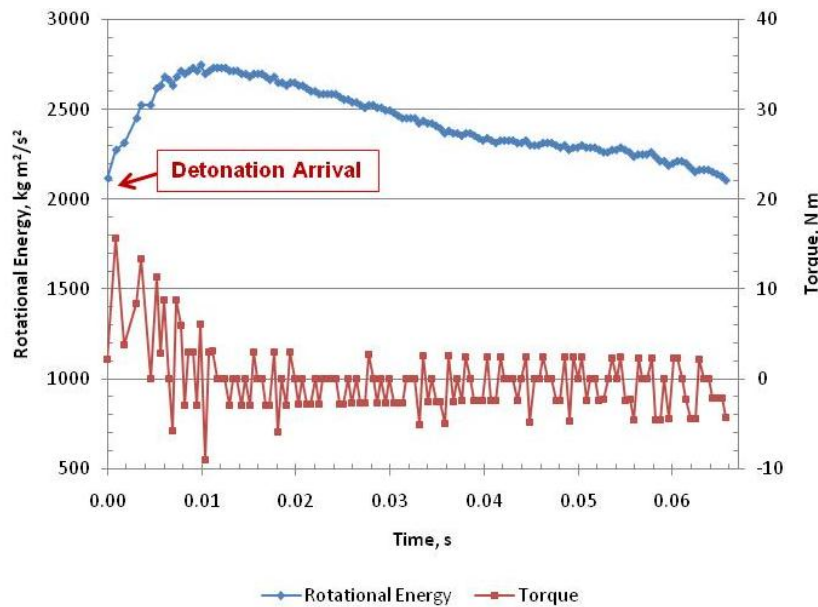


**Figure 114. Time history of rotational energy and net shaft torque with 15 Hz PDC with 1.0 fueled fraction and 0.5 purge fraction**

Figure 115 shows time history of turbine power from compressor dynamometer measurements, and rotational energy stored in the rotating assembly. The peak power

lagged the peak rotational energy because the response of the compressor dynamometer is slower than that of the speed sensor. Peak power and peak rotational energy were both attained about 11 ms after their initial rise. Evaluations of time-averaged performance circumvent the phase shift between measurements.

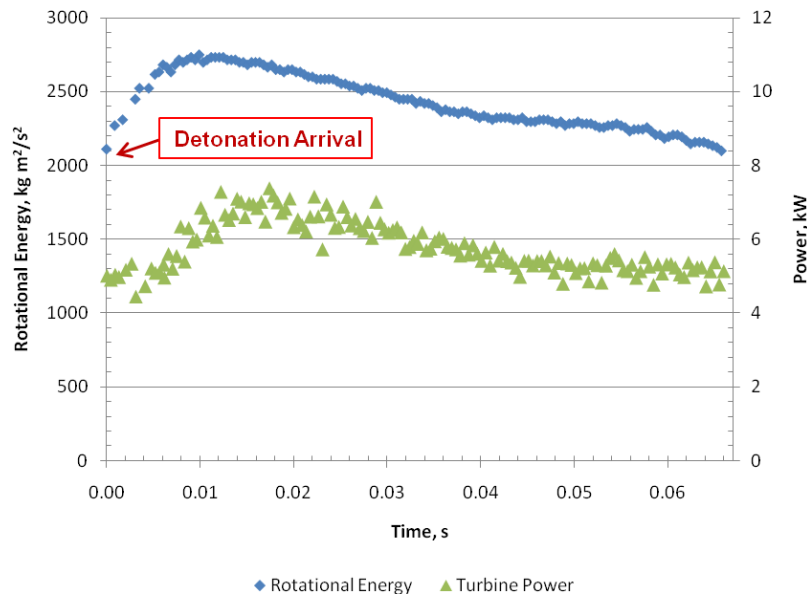


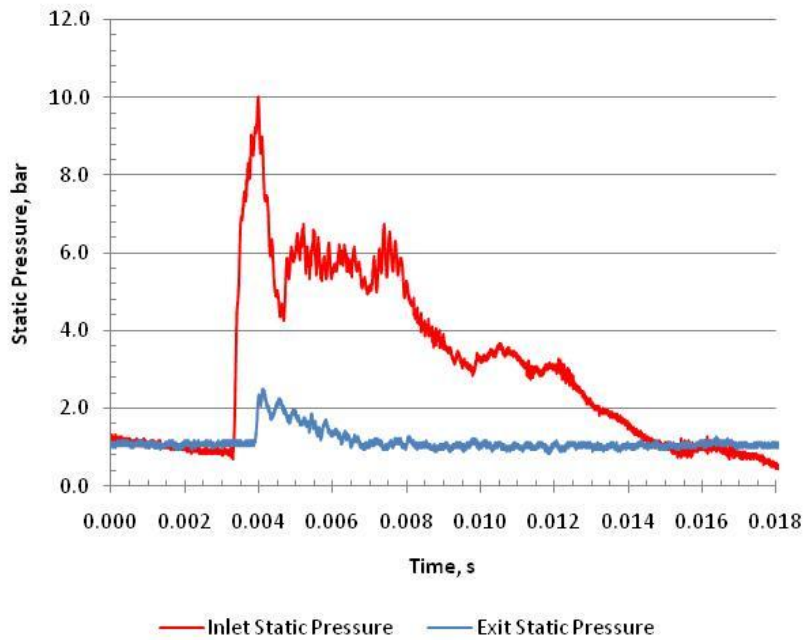
**Figure 115. Time history of rotational energy and power with 15 Hz PDC with 1.0 fueled fraction and 0.5 purge fraction**

Both compressor rotor speed measurement techniques capture the magnitudes and transients associated with the turbine response to detonations. The sharp acceleration that occurs with the detonation arrival indicates a large shaft torque. Whereas the Garrett sensor produces a rotor speed trace with less scatter, it is also less resolved around the detonation arrival time at the turbine.

### Initial High-Speed Flowfield Results

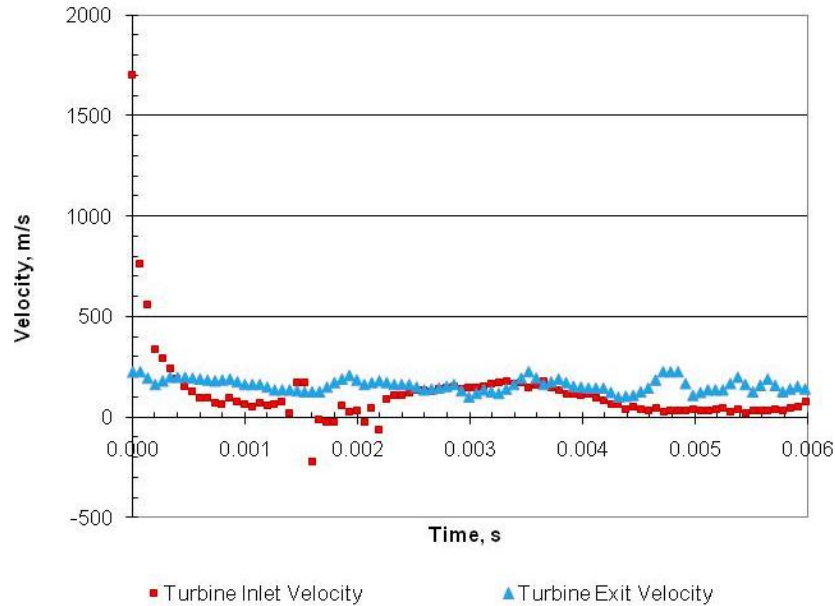
Figure 116 shows time history of static pressure at the turbine inlet and exit during the fire phase for a 15 Hz PDC with a fueled fraction of 1.0 and a purge fraction of 0.5.

Peak inlet pressure is about 10 bar (150 psia), which is less than the expected 60 bar magnitude of the von Neumann pressure spike associated with a detonation wave. This single point measurement technique to obtain pressures may not necessarily be representative of the average 2-D pressure field.



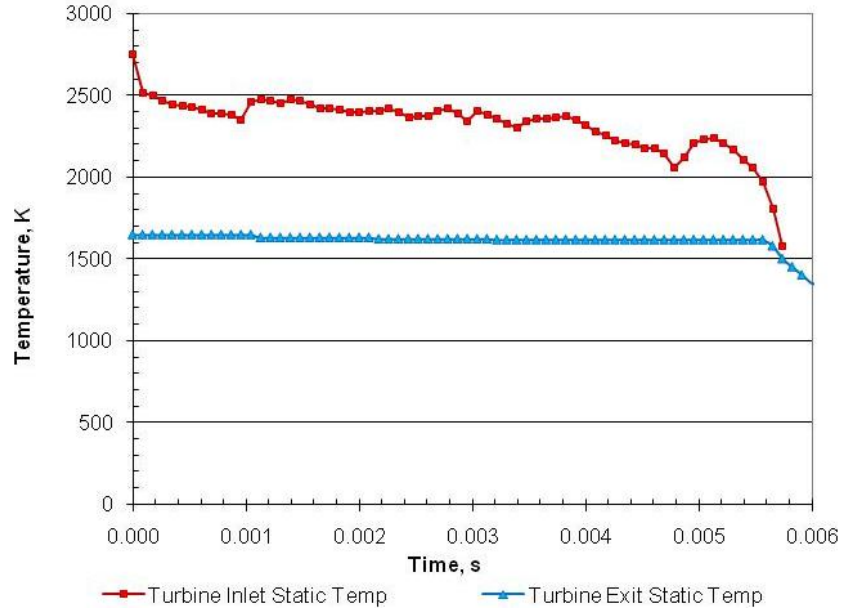
**Figure 116. Turbine inlet and exit wall static pressures with 15 Hz PDC with 1.0 fueled fraction and 0.5 purge fraction**

Figure 117 shows turbine inlet and exit flow field velocity results from PSV and BOS 1-D point measurements, respectively, for a 15 Hz PDC with a fueled fraction of 1.0 and a purge fraction of 0.5. The velocity is shown over the blowdown portion of the PDC fire phase. The initial inlet gas velocity appears high, possibly due to an expected Taylor wave following the detonation front. The large inlet velocity fluctuations are damped by the turbine, such that the exit velocity is more linear. The turbine inlet velocity excursions include momentary reverse flow.



**Figure 117. Turbine inlet and exit velocities from PSV and BOS measurements, respectively, with 15 Hz PDC with 1.0 fueled fraction and 0.5 purge fraction**

Figure 118 shows pyrometry turbine inlet and exit static temperatures for a blowdown event at 15 Hz PDC operation with a fueled fraction of 1.0 and a purge fraction of 0.5. Temperatures were obtained at a single centerline point. The initial inlet gas temperature exceeds the adiabatic flame temperature for hydrogen because of the elevated combustion pressure. The exit temperature is nearly constant, but drops quickly at the end of the blowdown. The difference between the inlet and exit temperatures indicates a drop in enthalpy across the turbine.



**Figure 118. Turbine inlet and exit static temperatures from pyrometry measurements with 15 Hz PDC with 1.0 fueled fraction and 0.5 purge fraction**

**Turbine Inlet Temperature and Pressure Spatial Variation**

For this work, 1-D temperatures and velocities are measured at a single x-location, midway along the flowfield streamwise centerline. Only the x-component of velocity magnitude is reported. Figure 119 shows variation of turbine inlet velocity along the centerline at two moments in time: 0.174 ms after the detonation arrival and 3.306 ms after detonation arrival, respectively. Velocity varied by 200 m/s at 0.174 ms and by about 100 m/s at 3.306 ms.

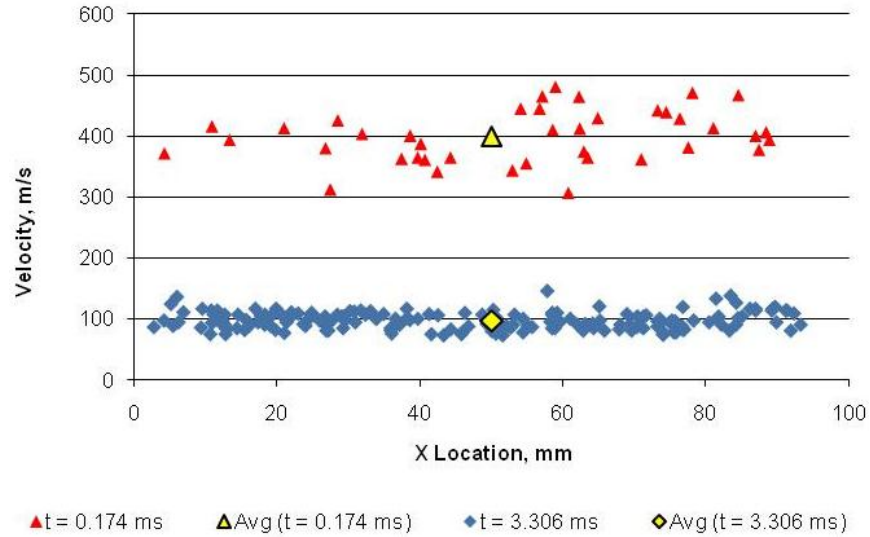


**Figure 119. Axial turbine inlet velocity variation in the x-direction along the centerline at two moments during blowdown**

Figure 120 shows turbine inlet static temperature variation in the y-direction at the streamwise mid x-location, approximately 610 mm upstream of the T3 turbine inlet flange. Temperature varied by 80 K at 0.174 ms and by nearly 300 K at 3.306 ms.

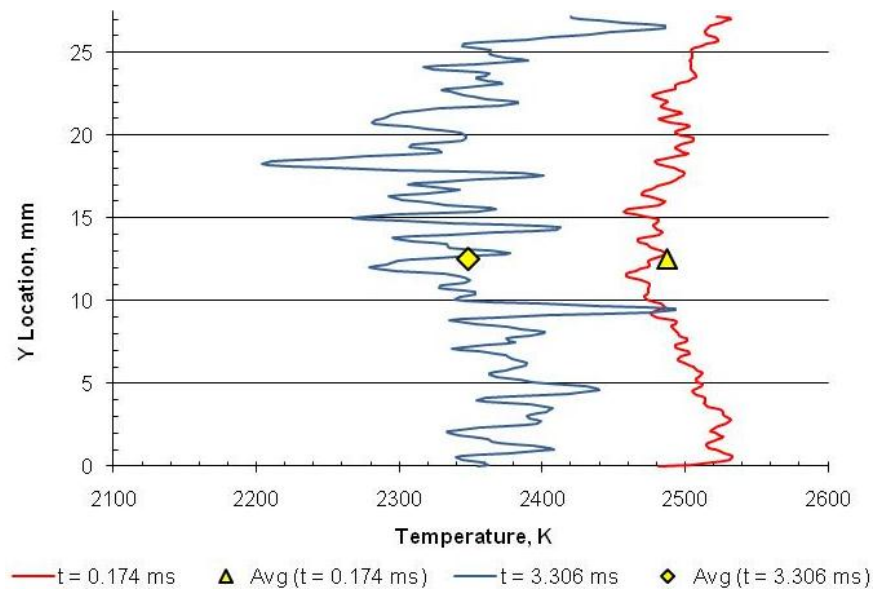


**Figure 120. Turbine inlet temperature variation in the y-direction at two moments during blowdown**

### **Summary of Initial High-Speed Measurements and Rotor Speed Results**

This current work evaluated various instrumentation techniques to acquire the flowfield properties of a PDC driven turbine, which are necessary to calculate turbine efficiency. Furthermore, this study compared instrumentation techniques to measure rotor speed, which is essential to characterizing the turbine response to detonations. Static pressure transducers adequately captured 1-D magnitudes of gas pressures and pressure ratio across the turbine. Use of SiC particles made it possible to use a combination of optical pyrometry and particle streak velocimetry to obtain temperature and velocity. The results included expected magnitudes and flow field transients. The background oriented Schlieren (BOS) technique was able to provide velocity and density flow field. Turbine exit velocities obtained from the BOS measurements did not fluctuate as much as the inlet velocities obtained from PSV. The BOS density results showed good potential for obtaining 2-D flow field pressures by combining results from optical pyrometry. Rotor speed from compressor blade passing frequencies obtained with a laser tachometer and a Garrett speed sensor were also similar. Laser tachometer results had better resolution of the rotor acceleration; however, there was some scatter.

**Appendix G: Performance of a PDC-Turbine with a Pre-Detonator Configuration,  
Presented at the 2011 ASME Turbo Expo (GT2011-45396)**

The purpose of this experiment was to evaluate an alternate PDC-turbine arrangement using a pre-detonator and a transition from small to large diameter tubes in the PDC. The motivation to study this arrangement was to reduce total pressure loss associated with DDT obstacles. Experiments are carried out in the AFRL Detonation Engine Research Facility. The radial turbine used in this subsequent configuration was part of a Garrett T3/T4E turbocharger, pictured in Fig. 121. The turbine wastegate was capped so that all combustor exhaust passed through the turbine. As with the previous experiment described in Appendix E, a 77 mm diameter steel pipe elbow was attached to the turbine exhaust flange.

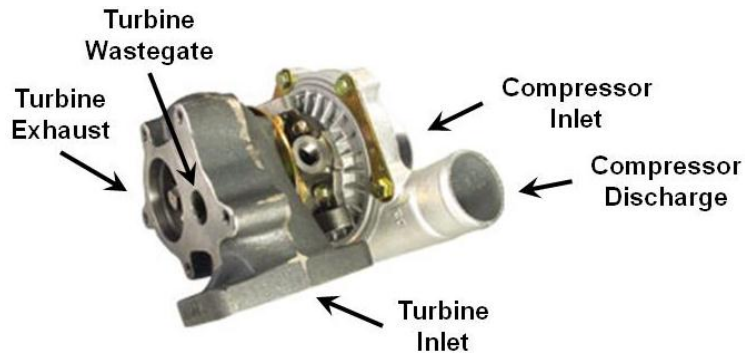


**Figure 121. Garrett T3/T4E Turbocharger (used with permission from Advanced Tuning Products, Inc.)**

The T3/T4E turbocharger is equipped with an 11-blade, radial turbine and a 45-trim radial compressor having six primary impeller blades and six splitter blades. A water-cooled center housing contains the shaft and journal bearing assembly. The compressor was used as dynamometer as previously described Appendix C.

### PDC Arrangement with a Pre-detonator

As with the initial experiments, testing was carried out in the AFRL Detonation Engine Research Facility, using a different configuration, as shown in Fig. 122. The pulsed detonation combustor consisted of three sections of schedule-40 steel pipe. The first section was a 26.6 mm diameter pipe, 305 mm in length, and coupled to the engine head. The second section was a 40.8 mm diameter pipe, 915 mm in length, and coupled to the first pipe with a reducer. The final section was a 52.5 mm diameter pipe, 152 mm in length, and coupled to the second pipe with a reducer. The exit of the final pipe section transitioned from round to rectangular and was welded to a T3 turbocharger flange. The total combustor length was 1.4 m, and the volume was 0.0019 m<sup>3</sup>. There were no internal DDT obstacles or devices. Such devices would reduce the amount of pressure gain from combustion. Ignition was accomplished with a pre-detonator.

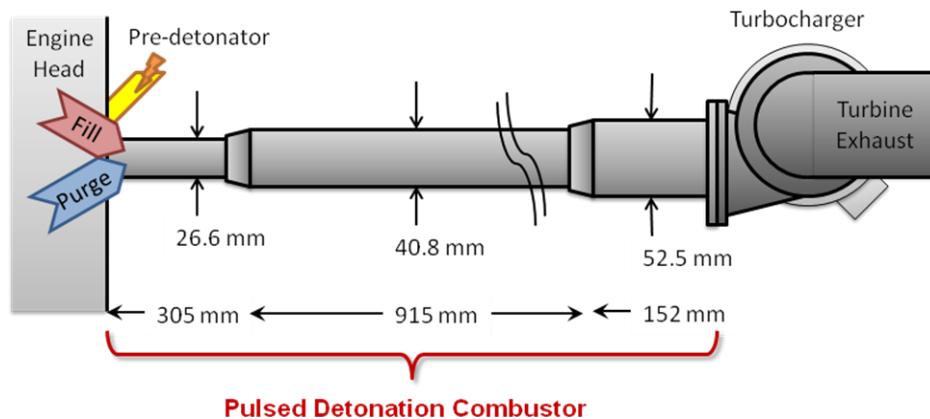


**Figure 122. Schematic of PDC-turbine arrangement using a pre-detonator and small to large diameter pipe transition**

The diameter of the first combustor section was chosen to ensure that the detonation from the pre-detonator was re-established. The diameter of the third

combustor section was chosen to match the T3 inlet circumference. The diameter of the second combustor section was chosen to ensure a smooth transition between the first and third sections.

The pre-detonator, pictured in Fig. 123, consisted of a 14 mm tube with an internal spiral for DDT. The tube was contained in a water jacket for cooling. Propane and nitrous oxide were the pre-detonator fuel and oxidizer, respectively, and an automotive spark plug was the ignition source. A detonation was established in the pre-detonator tube and then passed into the pulsed detonation combustor.

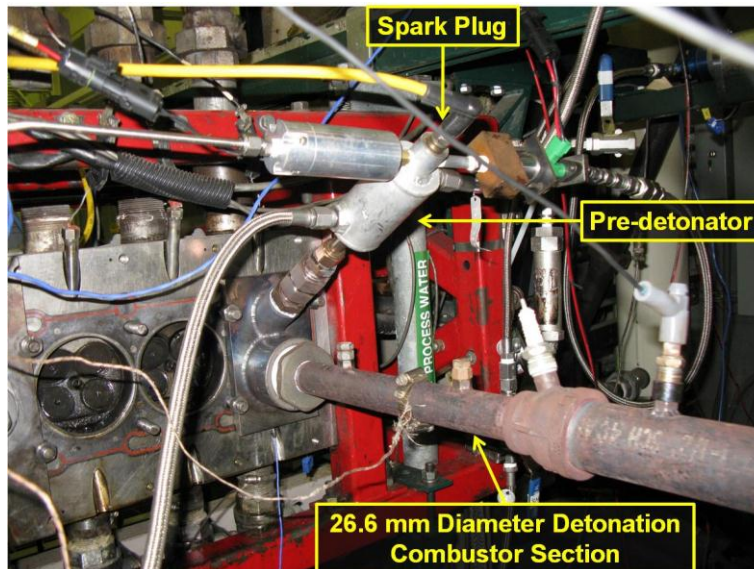


**Figure 123. Pre-detonator and PDC arrangement at the engine head**

PDC operation was attained by first setting fill and purge air flow at a desired operating frequency via cam speed. At that point, pre-detonator operation was started, and hydrogen was added to the main fill manifold to achieve a stoichiometric fuel-air ratio. Typically, the desired fuel-air ratio was achieved within five seconds, during which

time intermittent detonations occurred. Once the start-up sequence was complete and stoichiometric operation was achieved, data was taken and then fuel was shut-off. Most run times were less than 30 seconds.

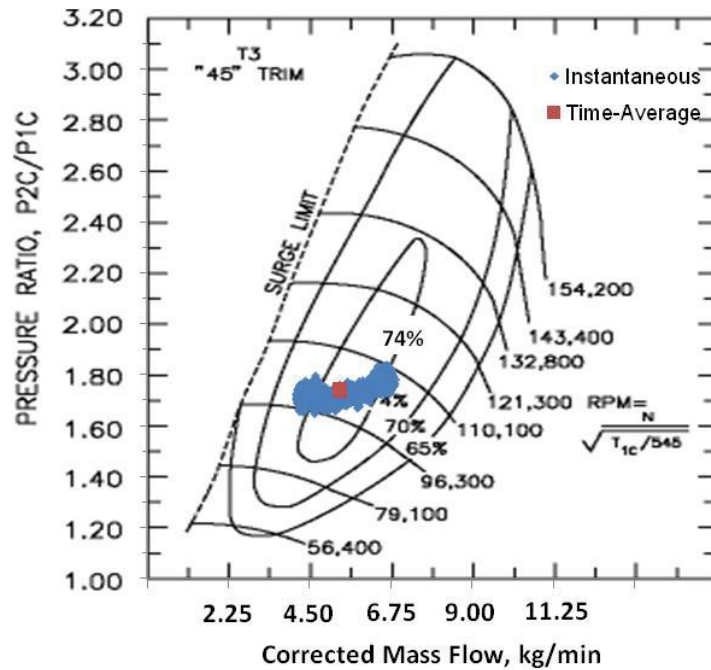
Table 19 includes the range of operating conditions explored in this study. Total turbine airflow ranged from 1.6 kg/min to 5.1 kg/min as frequency increased from 10 Hz to 25 Hz and fueled fraction increased from 0.5 to 1.0.

**Table 19. Summary of PDC operating conditions using a pre-detonator**

PDC Frequency (Hz)	Fueled Fraction	Purge Fraction	Fill Air Flow Rate (kg/min)	Purge Air Flow Rate (kg/min)	Fill Pressure (kPa)	Purge Pressure (kPa)	Manifold Temp (K)
10	0.5	0.5	0.65	0.93	113.5	115.8	296.6
10	0.6	0.5	0.78	0.94	117.2	116.7	296.6
10	0.7	0.5	0.91	0.94	121.4	117.8	296.6
10	0.8	0.5	1.06	0.94	126.3	118.0	296.6
15	0.5	0.5	0.99	1.41	131.6	223.3	296.6
15	0.6	0.5	1.19	1.41	138.2	233.6	296.6
15	0.7	0.5	1.39	1.41	145.1	234.1	296.6
15	0.8	0.5	1.58	1.41	152.1	241.3	296.6
15	1.0	0.5	2.96	2.11	82.7	103.9	301.9
20	0.5	0.5	1.33	1.88	139.9	147.4	293.7
20	0.6	0.5	1.59	1.88	149.9	148.9	293.7
20	0.7	0.5	1.86	1.88	159.5	149.9	293.7
20	0.8	0.5	2.11	1.88	167.4	150.9	293.7
25	0.5	0.5	1.68	2.36	162.9	200.3	294.0
25	0.6	0.5	2.01	2.36	162.9	200.3	294.0
25	0.7	0.5	2.33	2.36	172.5	203.4	294.0
25	0.8	0.5	2.66	2.35	184.7	203.1	294.0

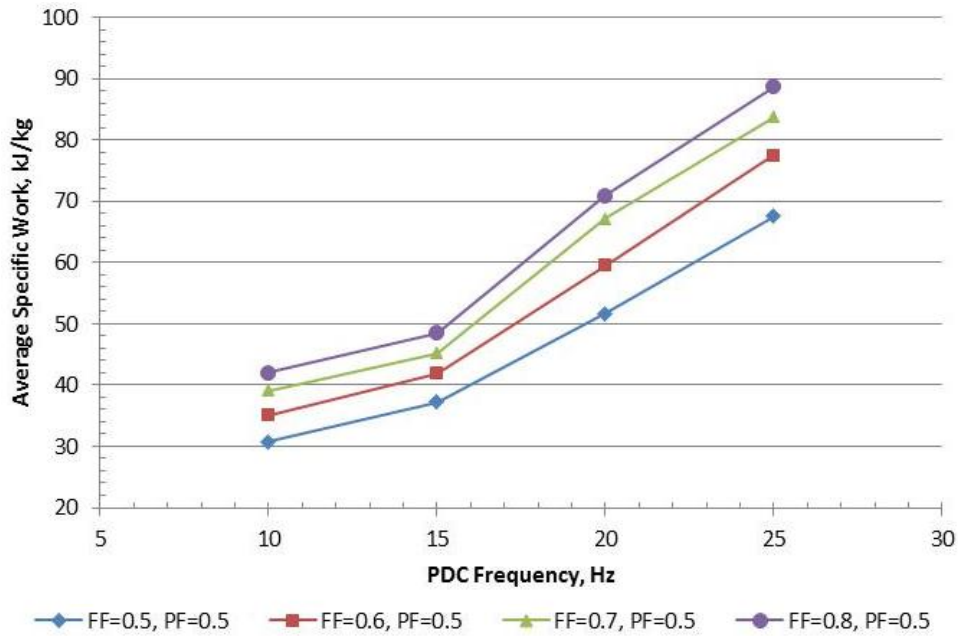
**Results for PDC-Turbine with a Pre-Detonator**

Figure 124 includes instantaneous compressor dynamometer operating points overlaid on the manufacturer’s map. The compressor dynamometer varied 15,000 RPM in corrected rotor speed. The red square represents the time-average point over a complete cycle, and most of the operation occurred within the 74% efficiency island.



**Figure 124. Variation in corrected rotor speed with 25 Hz PDC with 0.8 fueled fraction and 0.5 purge fraction**

Figure 125 shows a consistent trend in average specific work as shown previous experiments described in Appendix D. Average specific work increases both with fueled fraction and frequency. As shown in Table 19, main and purge manifold pressures also increases with fueled fraction and frequency, as does average rotor speed. At 25 Hz, there is a 22% increase in main fill pressure from a fueled fraction of 0.5 to 0.8, as shown in Table 19, and a 30% increase in average specific work. At a fueled fraction of 0.8, there is a 21% increase in main fill pressure from 15 Hz to 25 Hz and an 80% increase in average specific work. Thus, specific work gains appear more sensitive to frequency than to main fill pressure (combustor inlet pressure).



**Figure 125. Time-average specific work with 10 to 25 Hz operation with 0.5 to 0.8 fueled fractions and 0.5 purge fraction**

### Summary and Conclusions

This experiment evaluated an alternate PDC-turbine arrangement using a pre-detonator and a transition from small to large diameter tubes in the PDC. Average specific work followed the same trend as noted in previous experiments described in Appendix D, increasing with PDC frequency. Average specific power also increased with fueled fraction but was more sensitive to frequency. Though this arrangement is a viable alternative, it is not be the preferred option for experiments that rely on a trigger for instrumentation, such as high-speed video measurements. The inherent “soft start” nature of the pre-detonator arrangement did not consistently establish PDC operation with the first spark.

## Appendix H: PDC-Turbine Energy Conservation Analysis

Heat Transfer from Turbine Housing	(treating housing as a sphere)						
<b>PROPERTIES:</b>							
	EE	SI					
T <sub>housing</sub> (deg F, deg C, K)	329	165.00	438.15				
T <sub>amb</sub> (deg F, deg C, K)	65	18.33	291.48				
T <sub>delta</sub> (deg F, deg C, K)	264	146.67	146.67				
T <sub>avg</sub> (deg F, deg C, K)	197.00	91.67	364.82				
Density, ρ (kg/m <sup>3</sup> )		0.96610					
Dynamic Viscosity, μ (N s/m <sup>2</sup> )		2.14E-05					
Kinematic Viscosity, ν (m <sup>2</sup> /s)		2.22E-05					
β (K <sup>-1</sup> )		0.00273					
Pr		0.70260					
Gr <sub>D</sub>		1.64E+07					
Ra <sub>D</sub>		1.15E+07					
Nu <sub>D</sub>		27.03835					
Thermal Conductivity, k (W/m K)		0.03085					
Convective Coefficient, h (W/m <sup>2</sup> K)		6.56897					
D (in, m)	5	0.127					
Emissivity of Steel, ε		0.8					
q' <sub>free_conv</sub> (W, kW)		48.819	0.0488				
q' <sub>rad</sub> (W, kW)		68.12	0.0681				
q' <sub>total</sub> (W, kW)		116.935	0.1169				

**EQUATIONS:**

*Coefficient of Volumetric Expansion :*

$$\beta = \frac{1}{T} \text{ (ideal\_gas)}$$

*Prandlt Number :*

$$Pr = \frac{c_p \mu}{k}$$

*Grashof Number :*

$$Gr_D = \frac{D^3 \cdot \rho^2 \cdot g \cdot \beta \cdot \Delta T}{\mu^2}$$

*Rayleigh Number :*

$$Ra_D = Gr_D \cdot Pr$$

*Nusselt Number :*

$$Nu_D = 2 + 0.43(Ra_D)^{1/4}$$

*Convective Heat Transfer Coefficient :*

$$h = \frac{k}{D} Nu_D$$

*Heat Transfer Rate :*

$$q'_{free\_conv} = h A_{sphere} (T_s - T_\infty)$$

$$q'_{rad} = \varepsilon A_{sphere} \sigma (T_s^4 - T_\infty^4)$$

$$q'_{total} = q'_{free\_conv} + q'_{rad}$$

Heat Transfer into Housing Cooling Water			(30 Sep 10 Data)		
<b>PROPERTIES:</b>			EE	SI	
T <sub>in</sub> (deg F, deg C, K)	82.5	28.06	301.21		
T <sub>out</sub> (deg F, deg C, K)	86.3	30.17	303.32		
T <sub>delta</sub> (deg F, deg C, K)	3.8	2.11	2.11		
T <sub>avg</sub> (deg F, deg C, K)	84.40	29.11	302.26		
Specific Heat, c <sub>p</sub> , Water, (kJ/kg K)		4.179			
Mass Flow, Water (gal/min, kg/s)	1.5	0.095			
PDC Frequency (Hz)		30			
Cycle Time, t <sub>cycle</sub> (sec)		0.0333			
ΔH <sub>flux</sub> (W, kW)	834.8	0.83			

**EQUATIONS:**

$$\Delta H_{flux} = \dot{m} \cdot c_p \cdot (T_{out} - T_{in})$$

$$\sum_{cycle} \Delta H_{flux} \cdot t_{cycle}$$

Heat Transfer into Energy Storage in Turbine Housing			(30 Sep 10 Data)		
<b>PROPERTIES:</b>					
T <sub>amb</sub> (deg F, deg C, K)	81.9	27.72	300.87		
T <sub>final</sub> (deg F, deg C, K)	329	165.00	438.15		
T <sub>delta</sub> (deg F, deg C, K)	247.1	137.28	137.28		
Run Time (s)			20		
dT/dt (K/s)			6.86		
Housing Mass (lbm, kg)	6.5		2.955		
Specific Heat, c <sub>p</sub> , Steel (kJ/kg K)			0.49		
ΔE <sub>stored</sub> (W, kW)		9937.0	9.94		

**EQUATIONS:**

$$\Delta \dot{E}_{stored} = m_{steel} \cdot c_{p,steel} \cdot (T_{final} - T_{initial})$$

$$\sum_{cycle} \Delta \dot{E}_{stored} \cdot t_{cycle}$$

Heat Transfer Estimate into Turbocharger Oil					
<b>PROPERTIES:</b>			EE	SI	
T <sub>in</sub> (deg F, deg C, K)	72	22.22	295.37		
T <sub>out</sub> (deg F, deg C, K)	75	23.89	297.04		
T <sub>delta</sub> (deg F, deg C, K)	3	1.67	1.67		
Specific Heat, c <sub>p</sub> , Oil (kJ/kg K)		2			
Mass Flow, Oil (gal/min, kg/s)	1.5	0.076			
ΔH <sub>flux</sub> (W, kW)	252.3	0.25			

**EQUATIONS:**

$$\Delta H_{flux} = \dot{m} \cdot c_p \cdot (T_{out} - T_{in})$$

$$\sum_{cycle} \Delta H_{flux} \cdot t_{cycle}$$

Heat Transfer into PDC Exit Pipe (between Diagnostic Section and Turbine Inlet)			
	Imp	SI	
	F	K	
T <sub>tube,avg</sub> (conservative)	314.33	430	
T <sub>amb</sub>	72	295.3722	
T <sub>delta</sub>	242.33	134.6278	
T <sub>avg</sub>		362.6861	
Beta (K <sup>-1</sup> )		0.002757	
D (in, m)	2.375	0.060325	
L <sub>tube</sub> (in, m)	6	0.1524	
Visc (N s/m <sup>2</sup> )		2.11E-05	
rho (kg/m <sup>3</sup> )		0.961255	
nu,avg (m <sup>2</sup> /s)		2.19E-05	
alpha,avg (m <sup>2</sup> /s)		3.16E-05	
Pr,avg		0.691125	
k,avg (W/mK)		0.0469	
emiss,Steel		0.8	
Ra,D		1150295	
Nu,D		15.06775	
h (W/m <sup>2</sup> K)		11.7145	
q',nat.conv. (W/m) (W) (kW)		298.8862	45.55025
q',rad. (W/m) (W) (kW)		228.463	34.81776
q,total (Hp, W, kW)	0.107693	80.36801	0.08

$$Gr_L = \frac{g\beta(T_s - T_\infty)L^3}{\nu^2} - \beta = \frac{1}{T} (ideal\_gas)$$

$$Ra_D = \frac{g\beta(T_s - T_\infty)D^3}{\nu\alpha}$$

$$\overline{Nu}_D = \left[ 0.60 + \frac{0.387Ra_D^{1/6}}{\left[ 1 + (.559/Pr)^{9/16} \right]^{8/27}} \right]^2$$

$$\overline{h} = \frac{k}{D} \overline{Nu}_D$$

$$q' = q'_{conv} + q'_{rad} = \overline{h}\pi D(T_s - T_\infty) + \varepsilon\pi D\sigma(T_s^4 - T_\infty^4)$$

Heat Transfer into Energy Storage in PDC Exit Pipe			(30 Sep 10 Data)
<b>PROPERTIES:</b>			
T <sub>amb</sub> (deg F, deg C, K)	81.9	27.72	300.87
T <sub>final</sub> (deg F, deg C, K)	329	165.00	438.15
T <sub>delta</sub> (deg F, deg C, K)	247.1	137.28	137.28
Run Time (s)			20
dT/dt (K/s)			6.86
Housing Mass (lbm, kg)	1.5		0.682
Specific Heat, c <sub>p</sub> , Steel (kJ/kg K)			0.49
ΔE <sub>stored</sub> (W, kW)		2293.2	2.29

**EQUATIONS:**  

$$\Delta \dot{E}_{stored} = m_{steel} \cdot c_{p,steel} \cdot (T_{final} - T_{initial})$$

$$\sum_{cycle} \Delta \dot{E}_{stored} \cdot t_{cycle}$$

### Appendix I: Time-Resolved PDC-Turbine Power Results

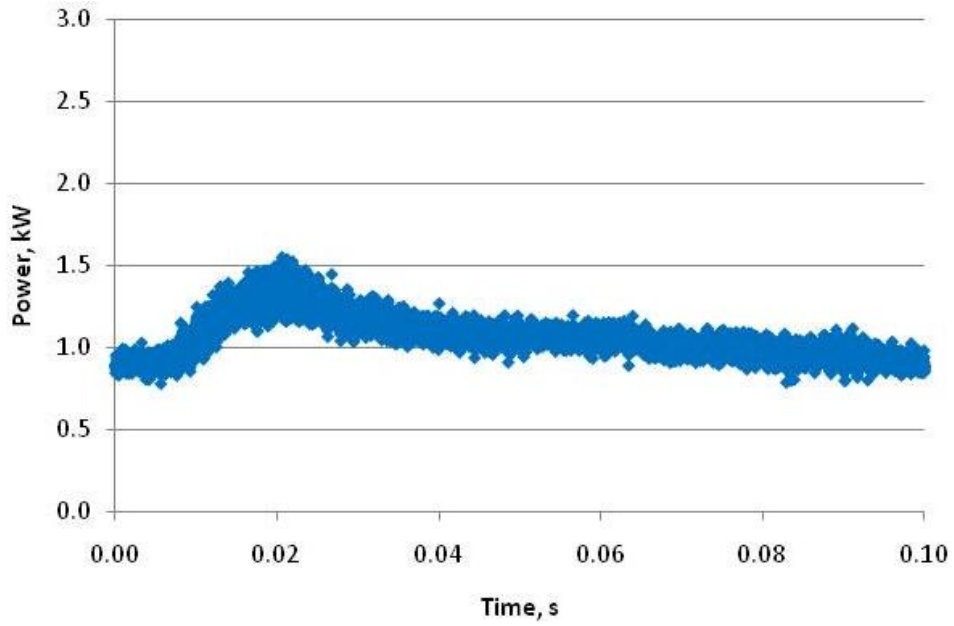


**Figure 126. Time-resolved power with 10 Hz hydrogen-fueled PDC with 0.60 fueled fraction and 0.75 purge fraction**

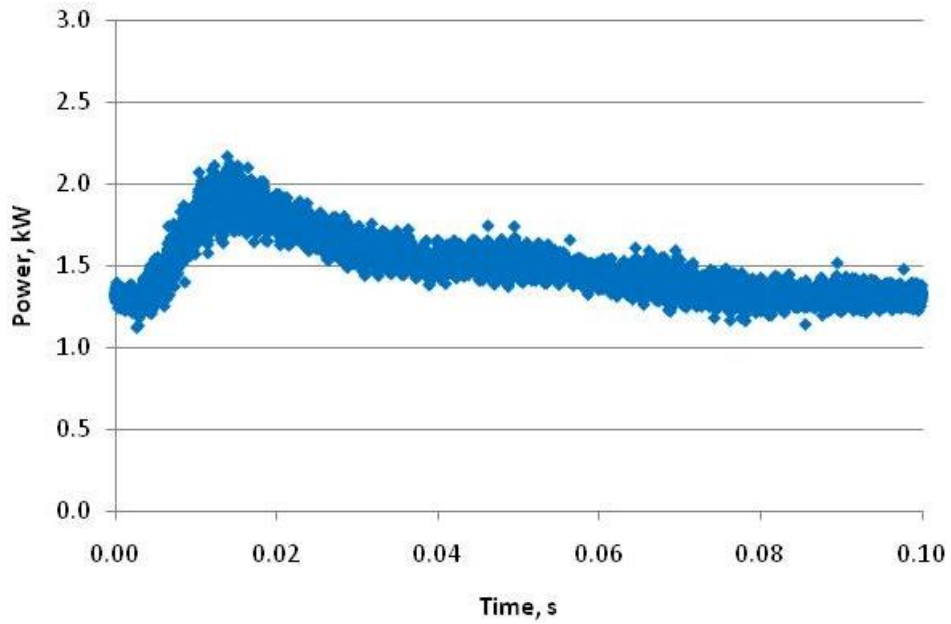


**Figure 127. Time-resolved power with 10 Hz hydrogen-fueled PDC with 0.75 fueled fraction and 0.75 purge fraction**

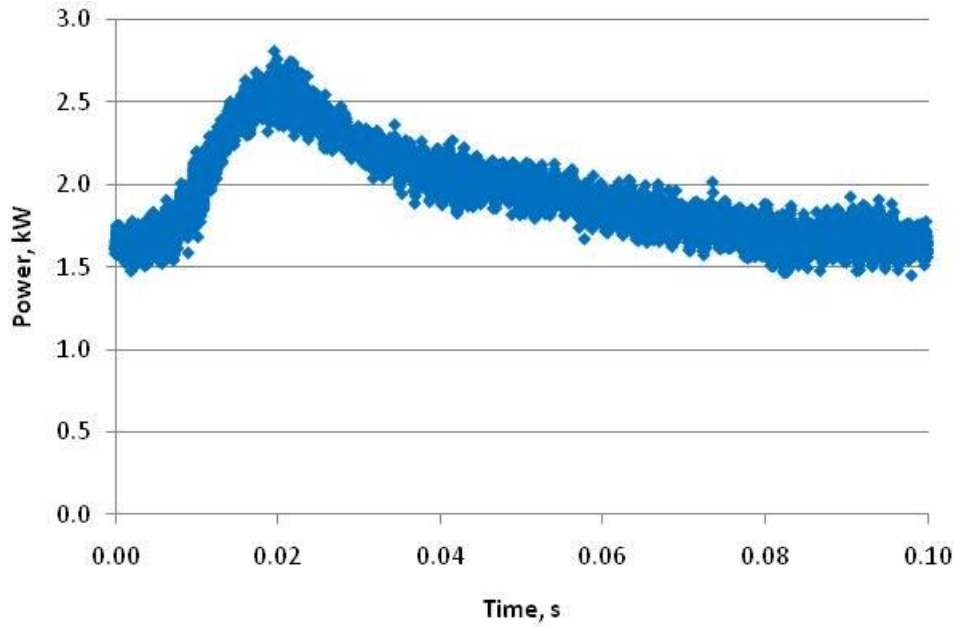


**Figure 128. Time-resolved power with 10 Hz hydrogen-fueled PDC with 0.90 fueled fraction and 0.75 purge fraction**

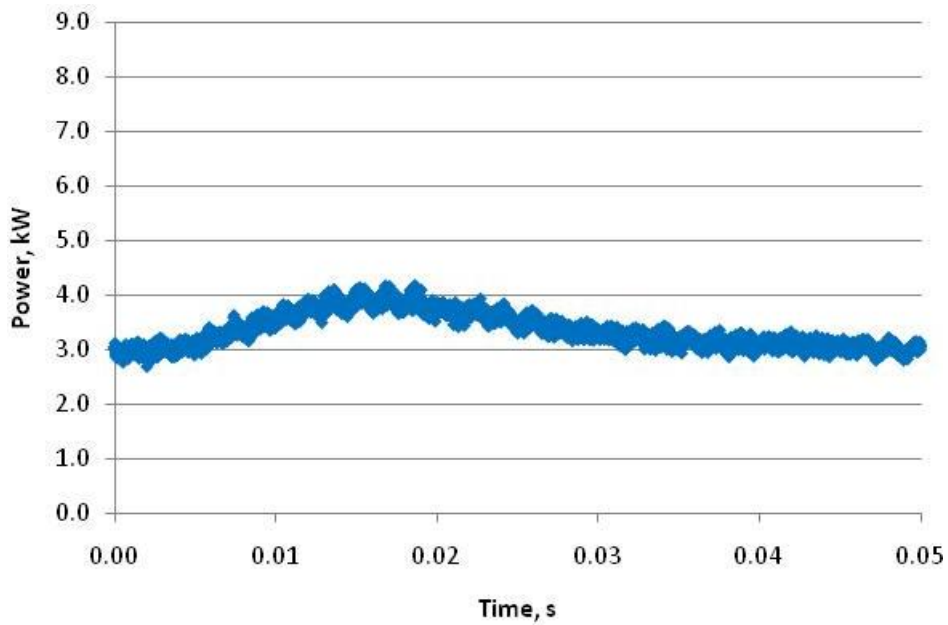


**Figure 129. Time-resolved power with 20 Hz hydrogen-fueled PDC with 0.60 fueled fraction and 0.50 purge fraction**

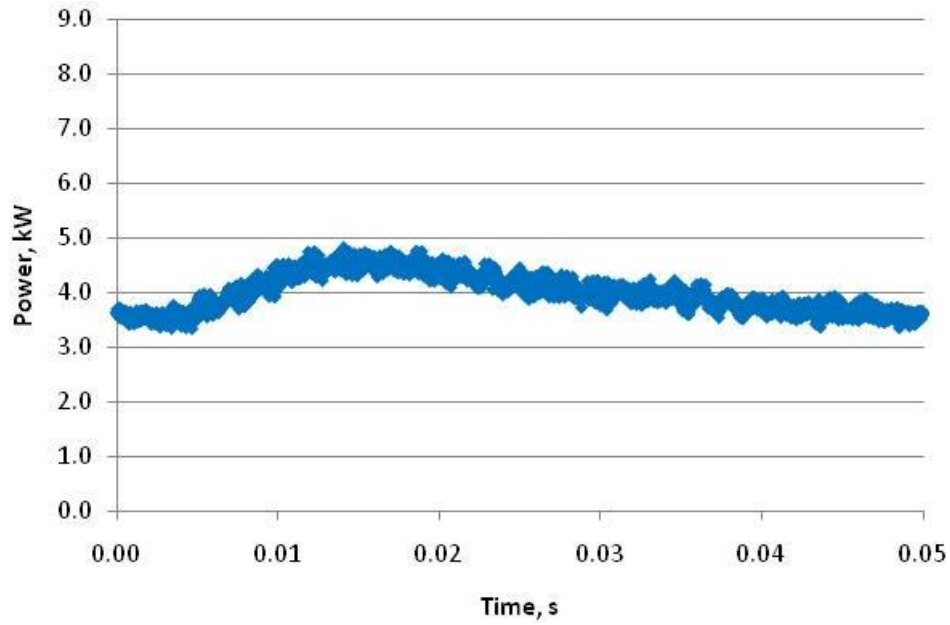


**Figure 130. Time-resolved power with 20 Hz hydrogen-fueled PDC with 0.60 fueled fraction and 0.75 purge fraction**

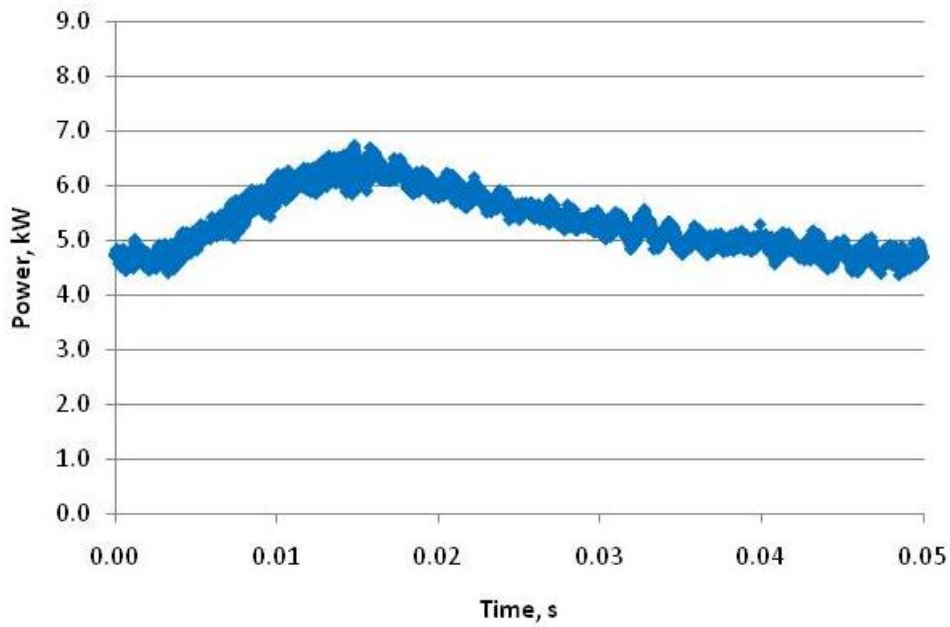


**Figure 131. Time-resolved power with 20 Hz hydrogen-fueled PDC with 0.75 fueled fraction and 0.75 purge fraction**

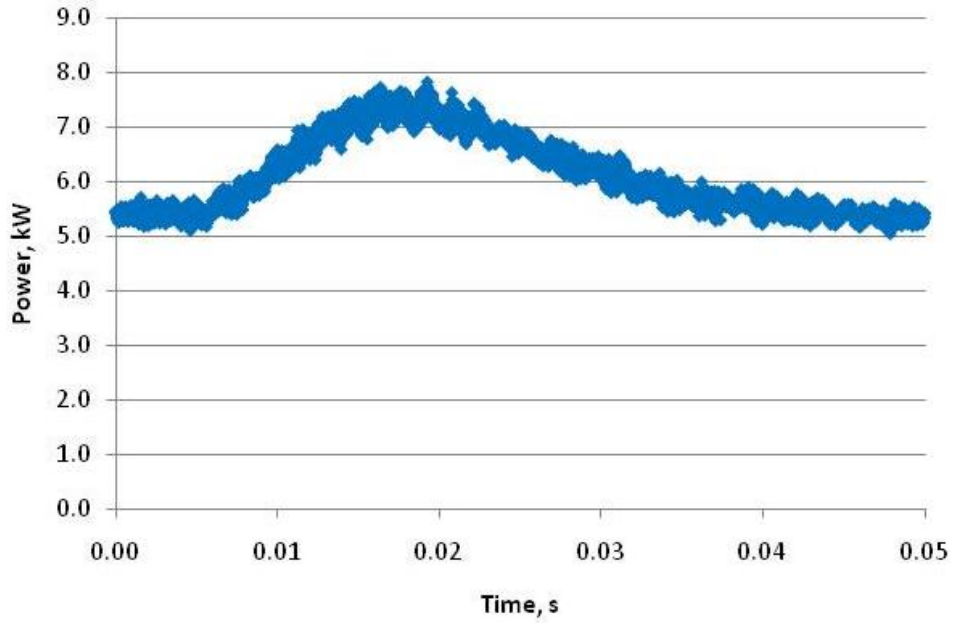


**Figure 132. Time-resolved power with 20 Hz hydrogen-fueled PDC with 0.90 fueled fraction and 0.50 purge fraction**

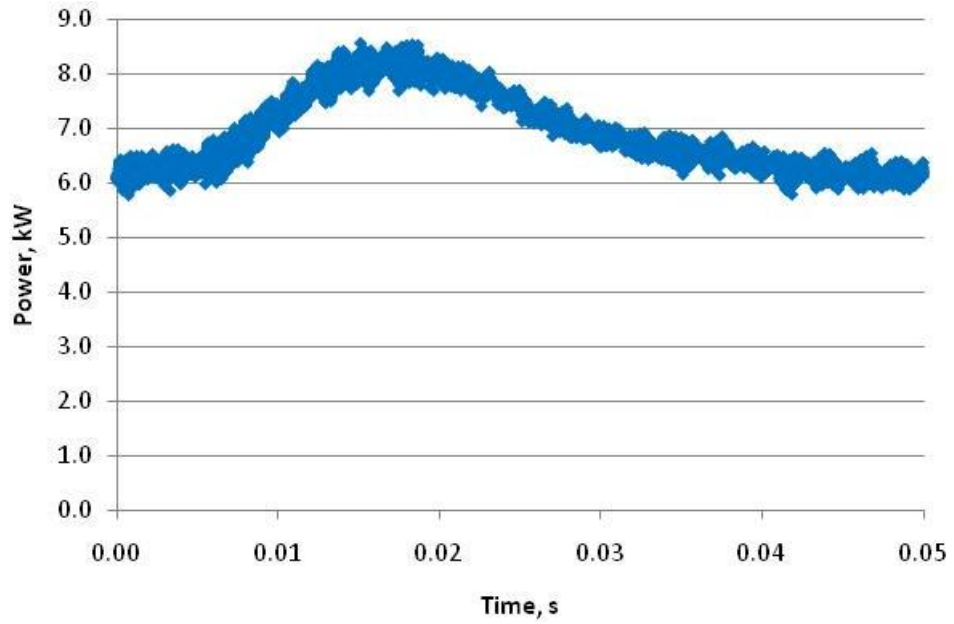


**Figure 133. Time-resolved power with 20 Hz hydrogen-fueled PDC with 0.90 fueled fraction and 0.75 purge fraction**

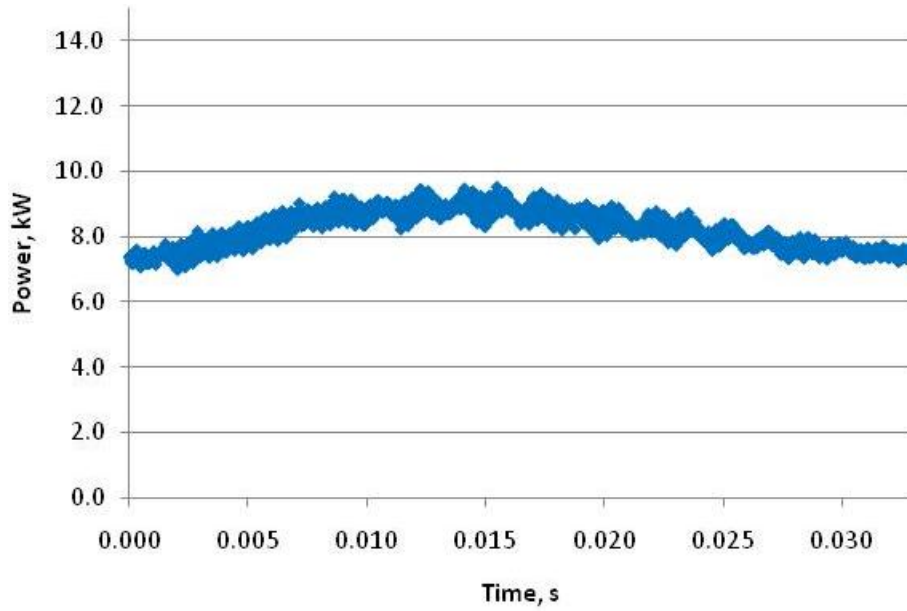


**Figure 134. Time-resolved power with 30 Hz hydrogen-fueled PDC with 0.60 fueled fraction and 0.75 purge fraction**

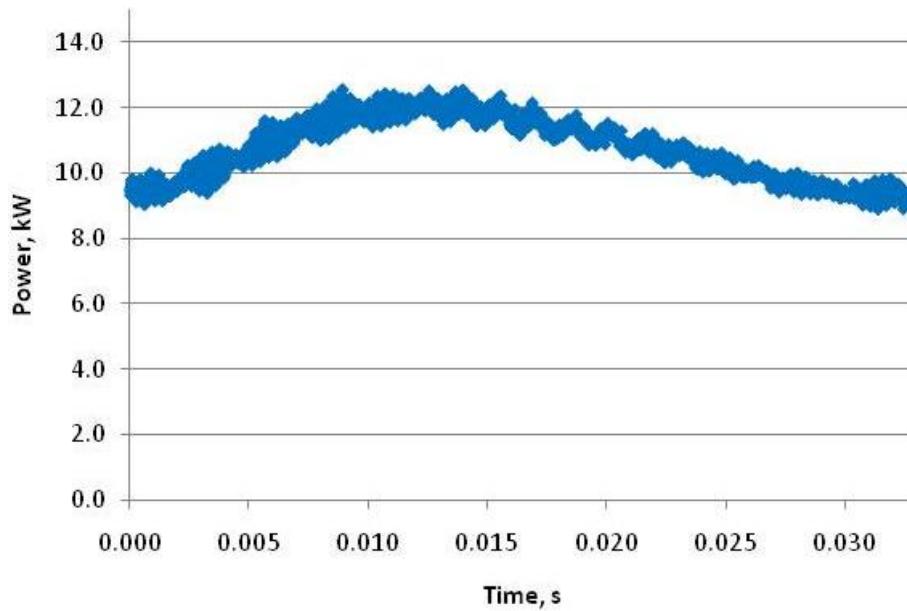


**Figure 135. Time-resolved power with 30 Hz hydrogen-fueled PDC with 0.75 fueled fraction and 0.75 purge fraction**

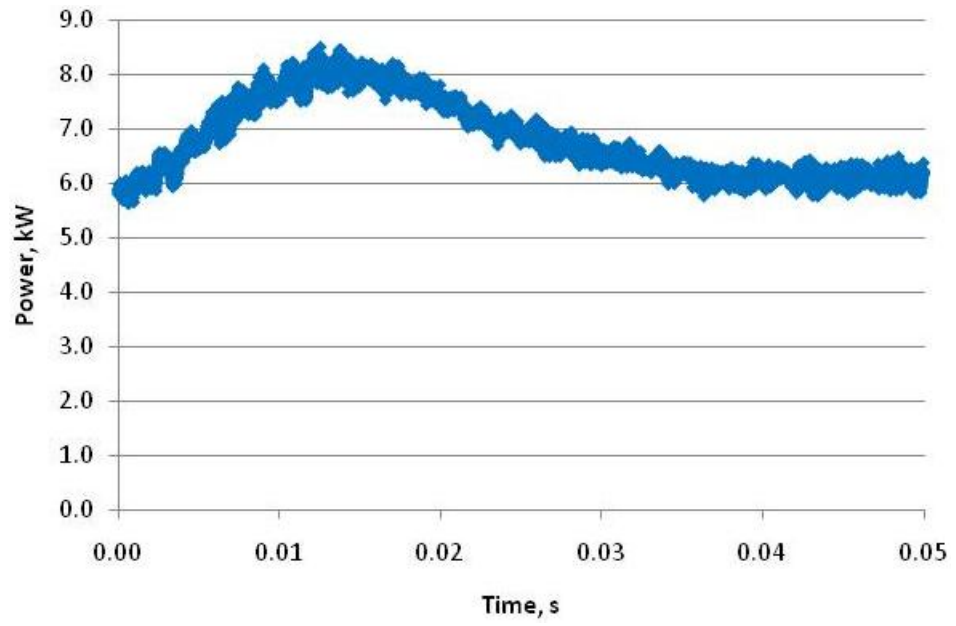


**Figure 136. Time-resolved power with 20 Hz ethylene-fueled PDC with 0.90 fueled fraction and 0.50 purge fraction**

## Appendix J: Time-Resolved PDC-Turbine Inlet and Exit Flowfield Results

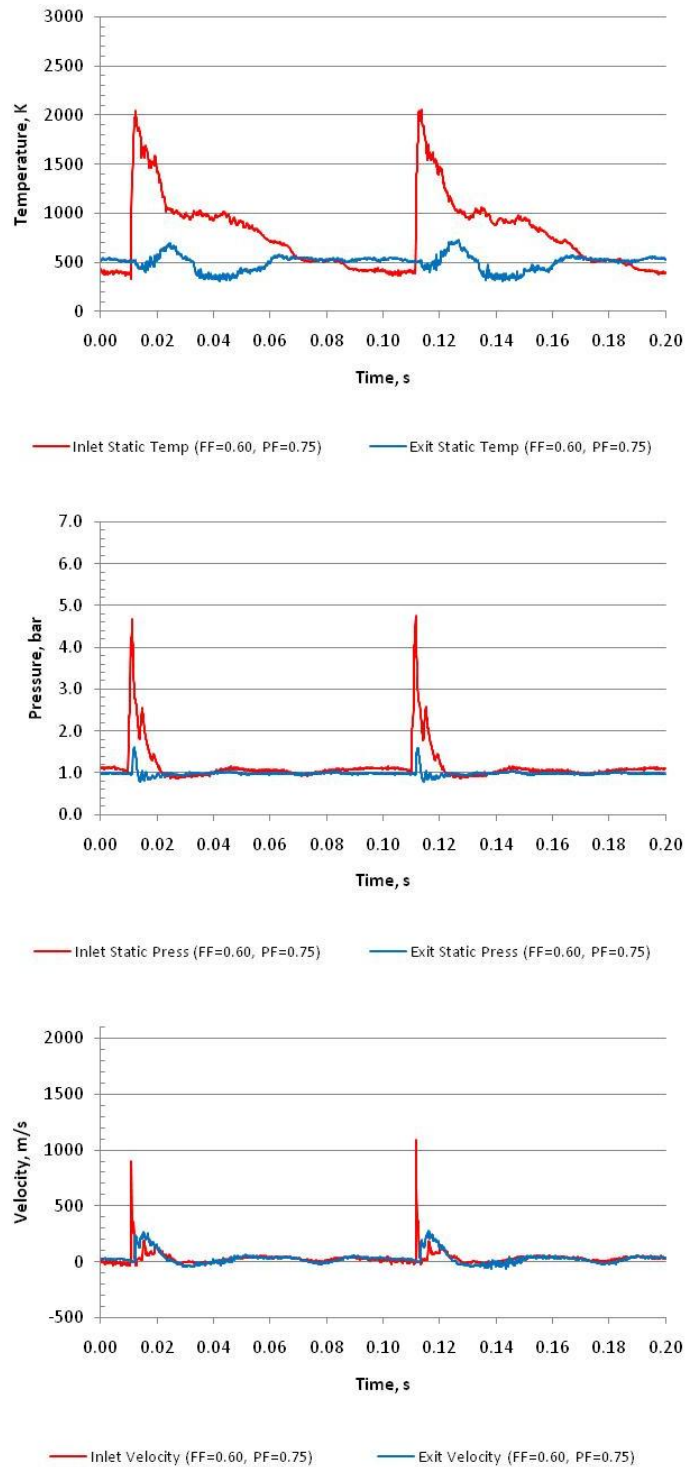


**Figure 137. Time-resolved turbine inlet and exit flowfield properties with 10 Hz hydrogen-fueled PDC with 0.60 fueled fraction and 0.75 purge fraction**

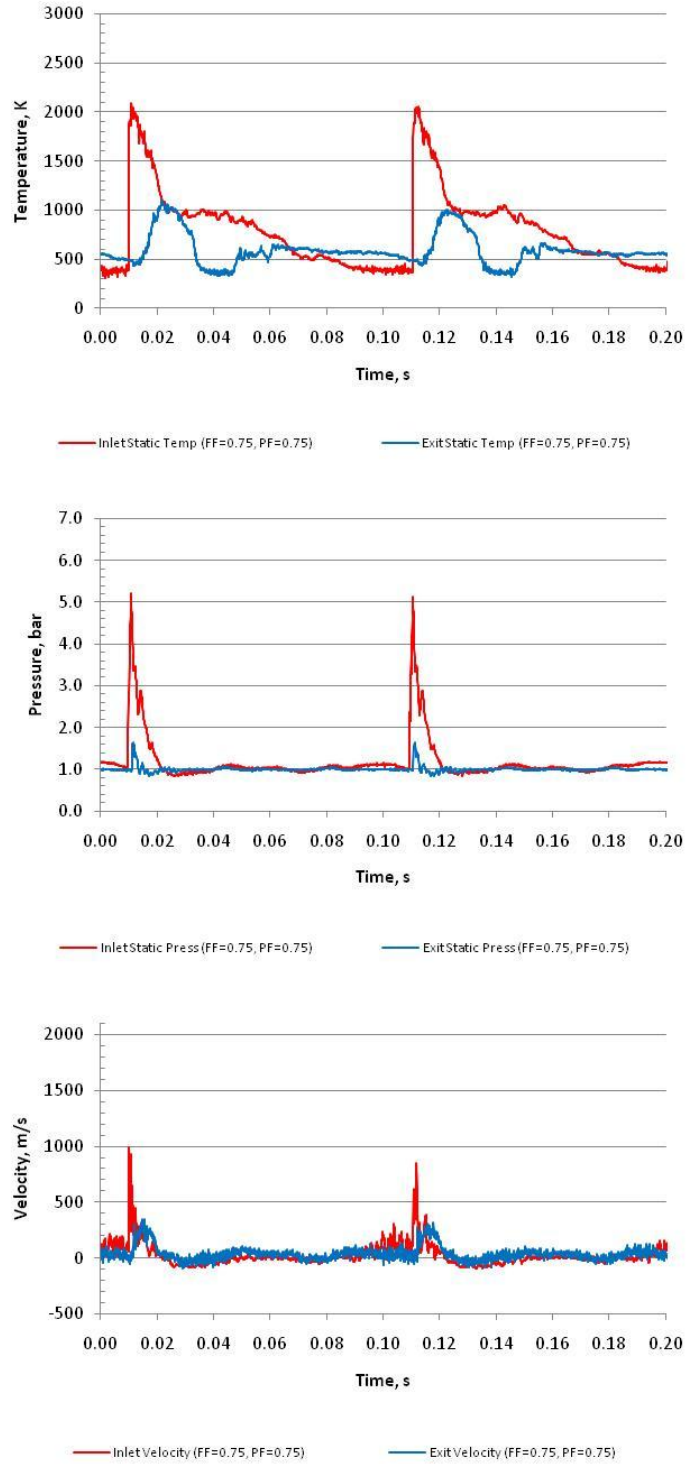


**Figure 138. Time-resolved turbine inlet and exit flowfield properties with 10 Hz hydrogen-fueled PDC with 0.75 fueled fraction and 0.75 purge fraction**

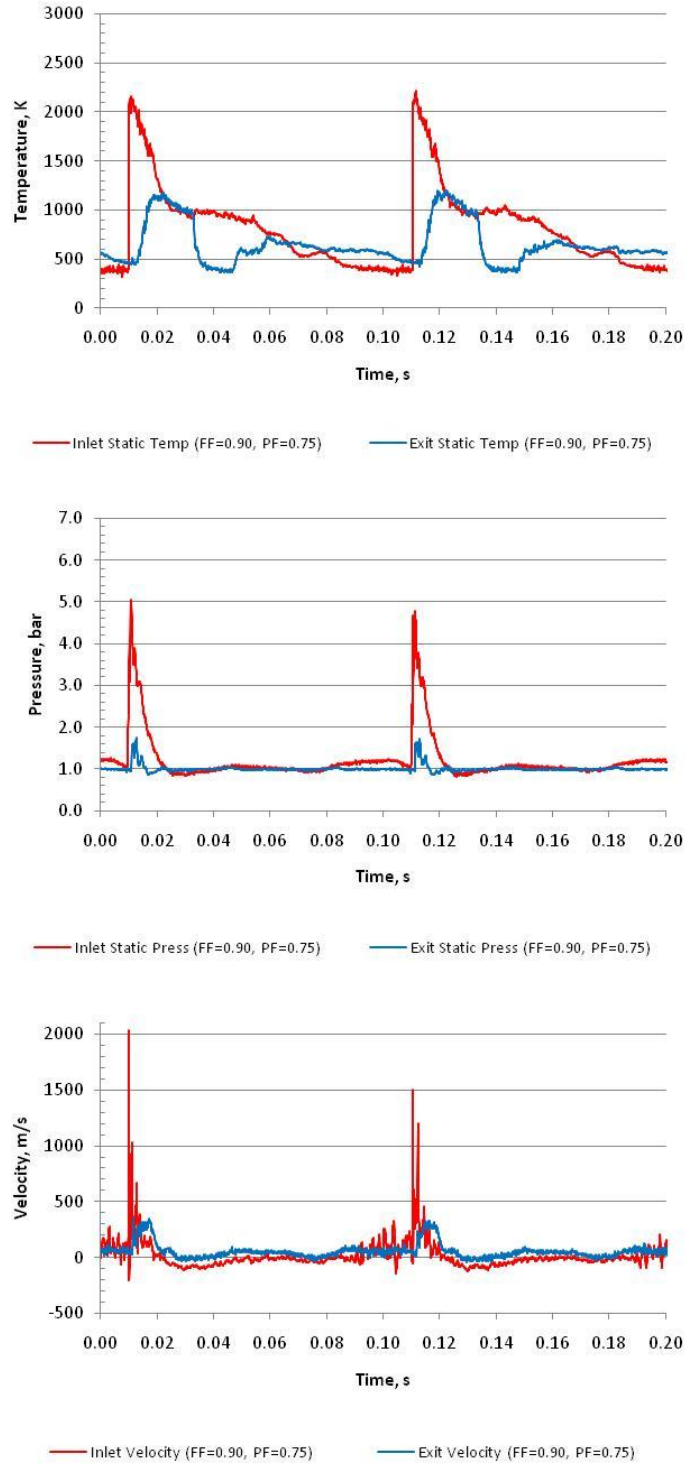


**Figure 139. Time-resolved turbine inlet and exit flowfield properties with 10 Hz hydrogen-fueled PDC with 0.90 fueled fraction and 0.75 purge fraction**

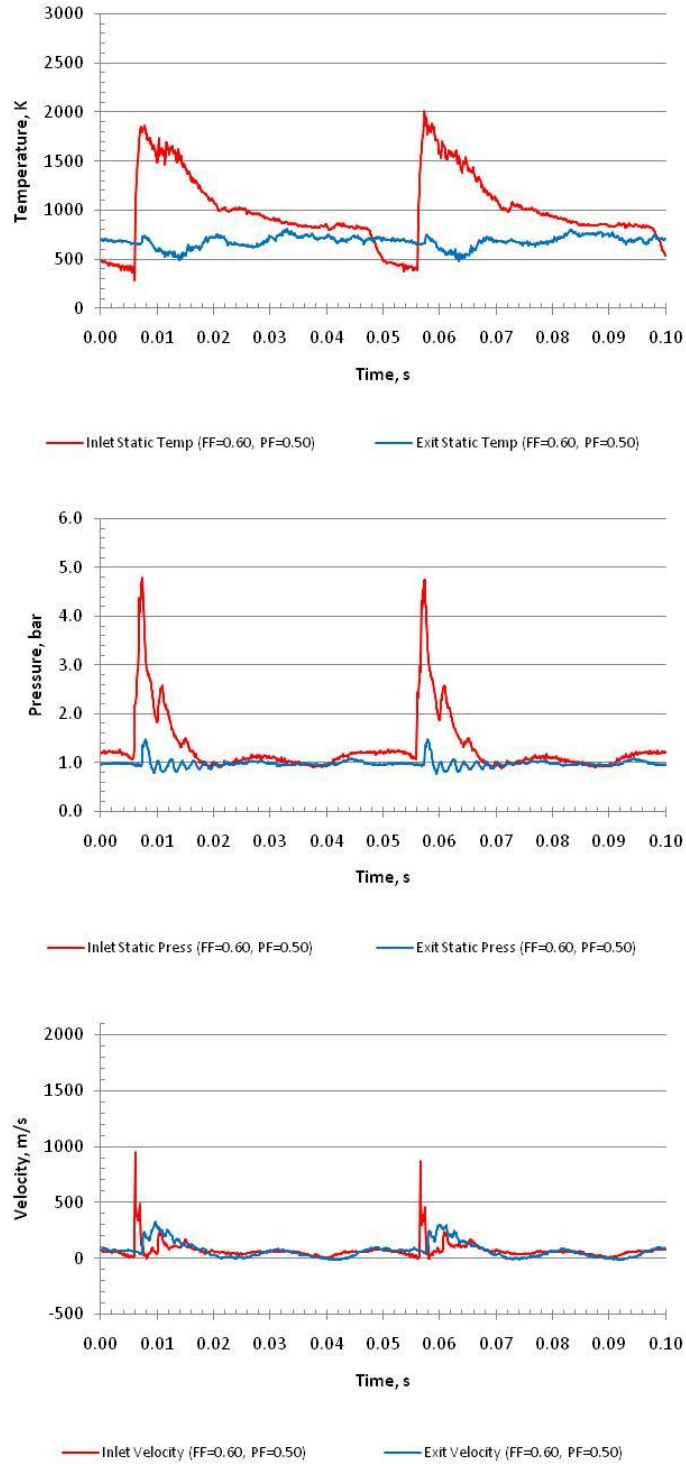


**Figure 140. Time-resolved turbine inlet and exit flowfield properties with 20 Hz hydrogen-fueled PDC with 0.60 fueled fraction and 0.50 purge fraction**

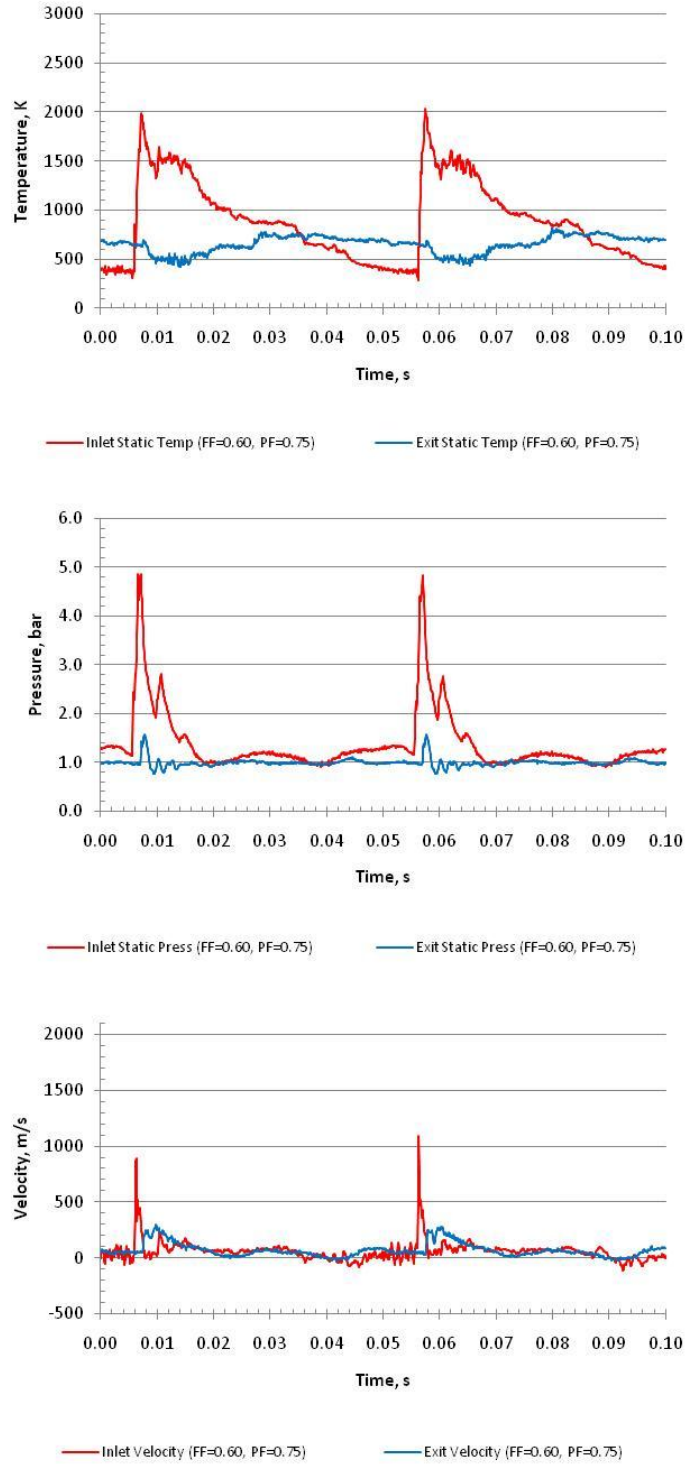


**Figure 141. Time-resolved turbine inlet and exit flowfield properties with 20 Hz hydrogen-fueled PDC with 0.60 fueled fraction and 0.75 purge fraction**

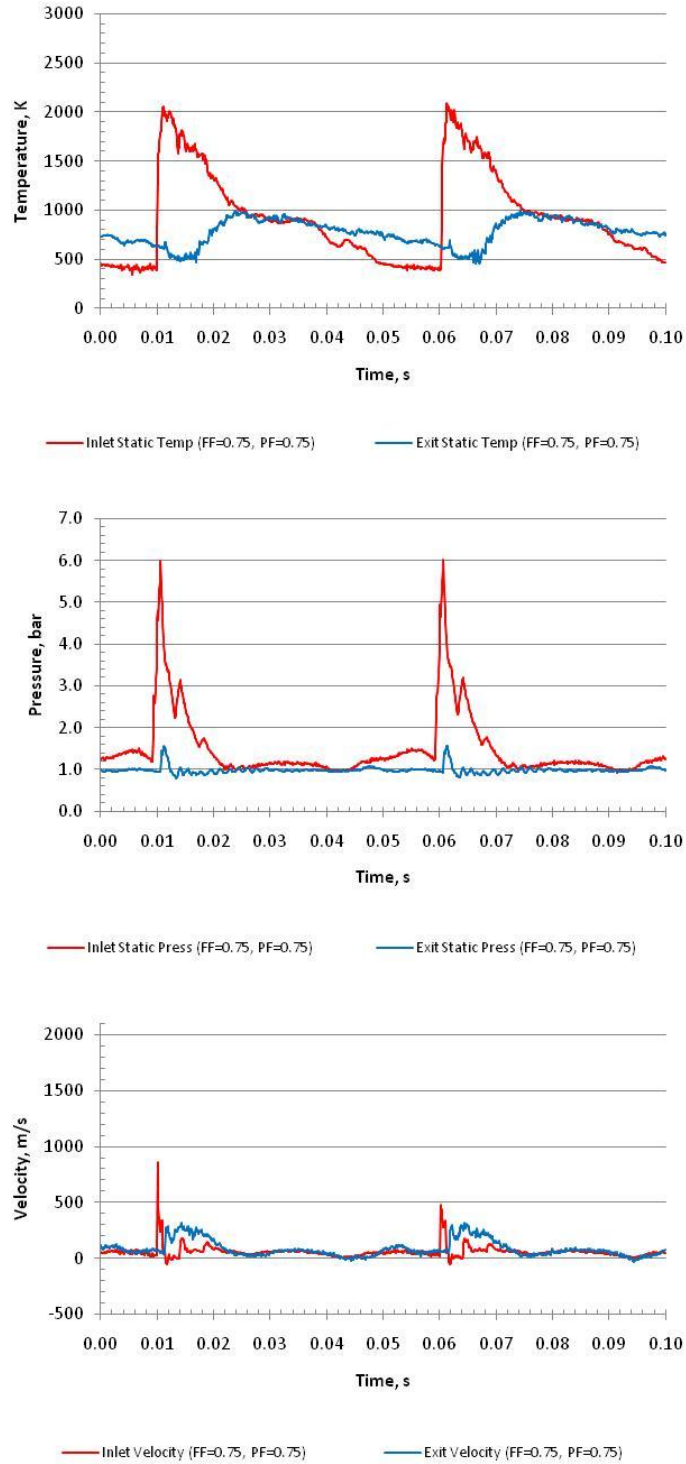


**Figure 142. Time-resolved turbine inlet and exit flowfield properties with 20 Hz hydrogen-fueled PDC with 0.75 fueled fraction and 0.75 purge fraction**

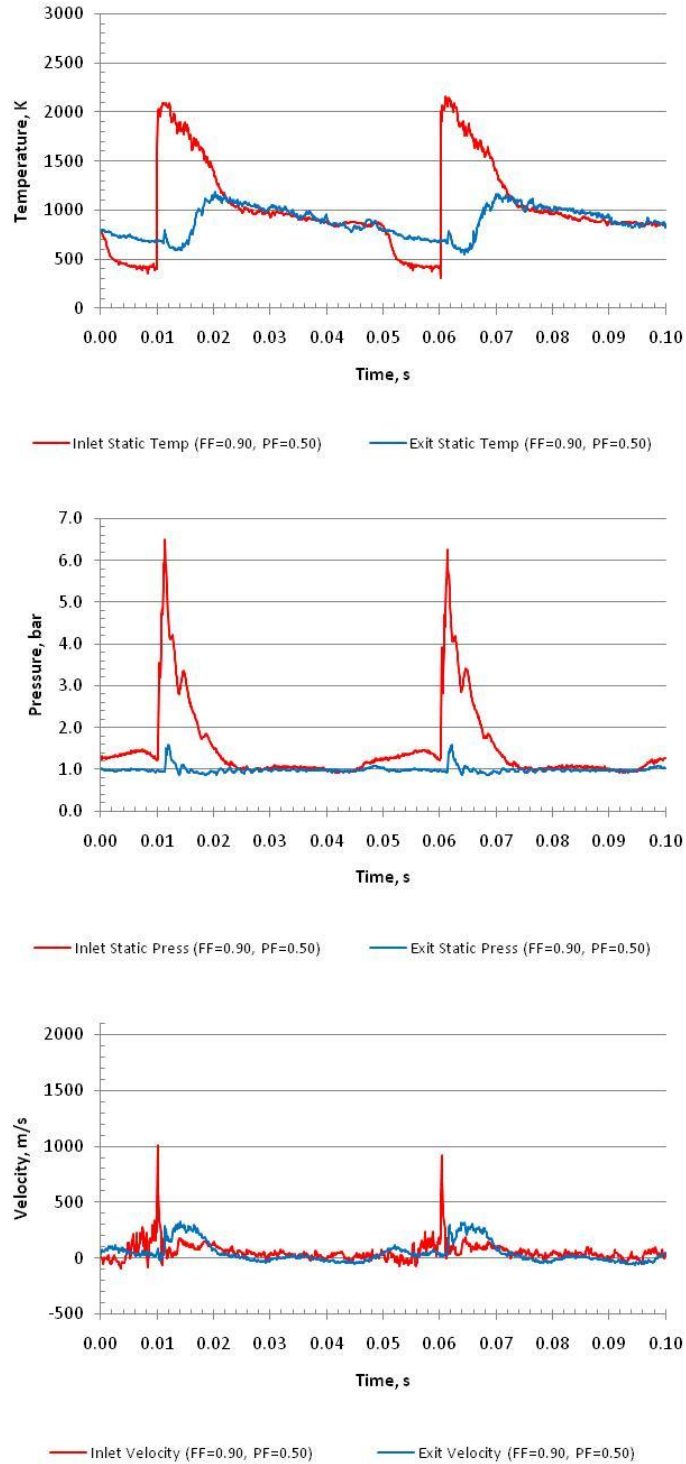


**Figure 143. Time-resolved turbine inlet and exit flowfield properties with 20 Hz hydrogen-fueled PDC with 0.90 fueled fraction and 0.50 purge fraction**

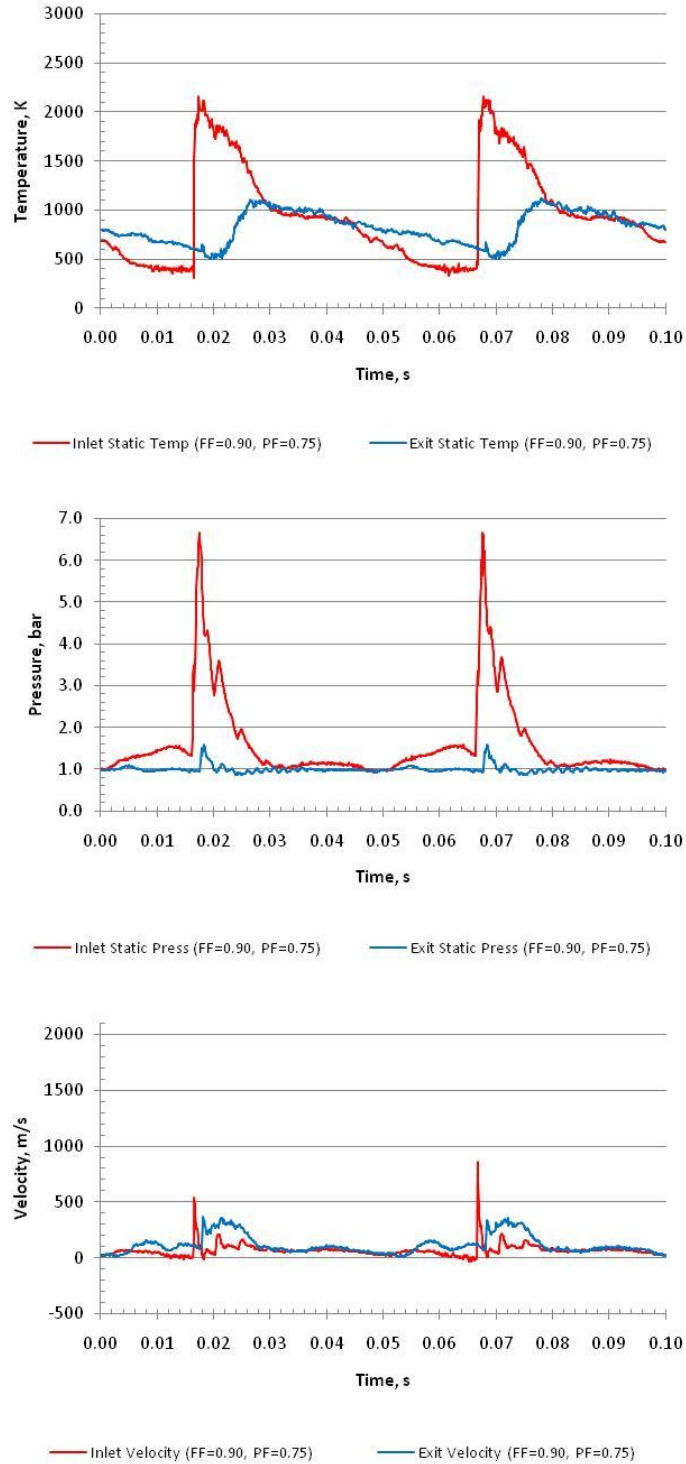


**Figure 144. Time-resolved turbine inlet and exit flowfield properties with 20 Hz hydrogen-fueled PDC with 0.90 fueled fraction and 0.75 purge fraction**

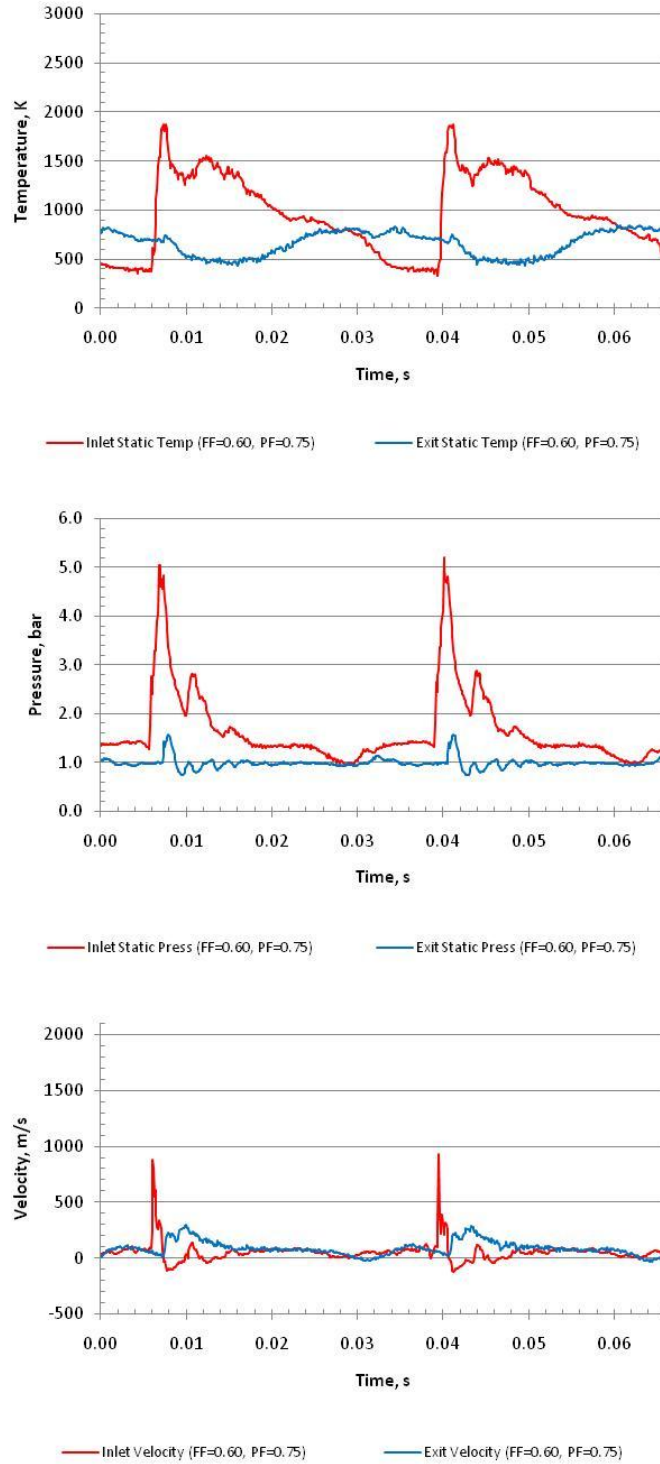


**Figure 145. Time-resolved turbine inlet and exit flowfield properties with 30 Hz hydrogen-fueled PDC with 0.60 fueled fraction and 0.75 purge fraction**

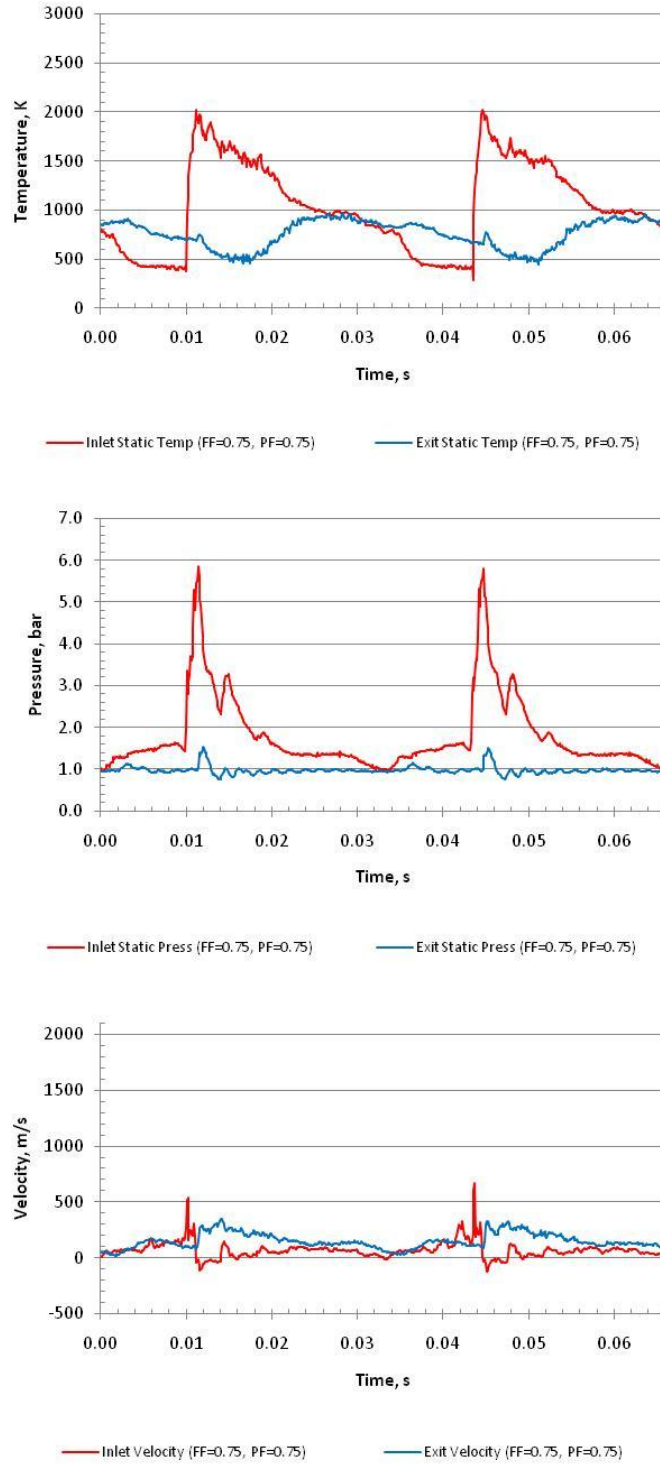


**Figure 146. Time-resolved turbine inlet and exit flowfield properties with 30 Hz hydrogen-fueled PDC with 0.75 fueled fraction and 0.75 purge fraction**

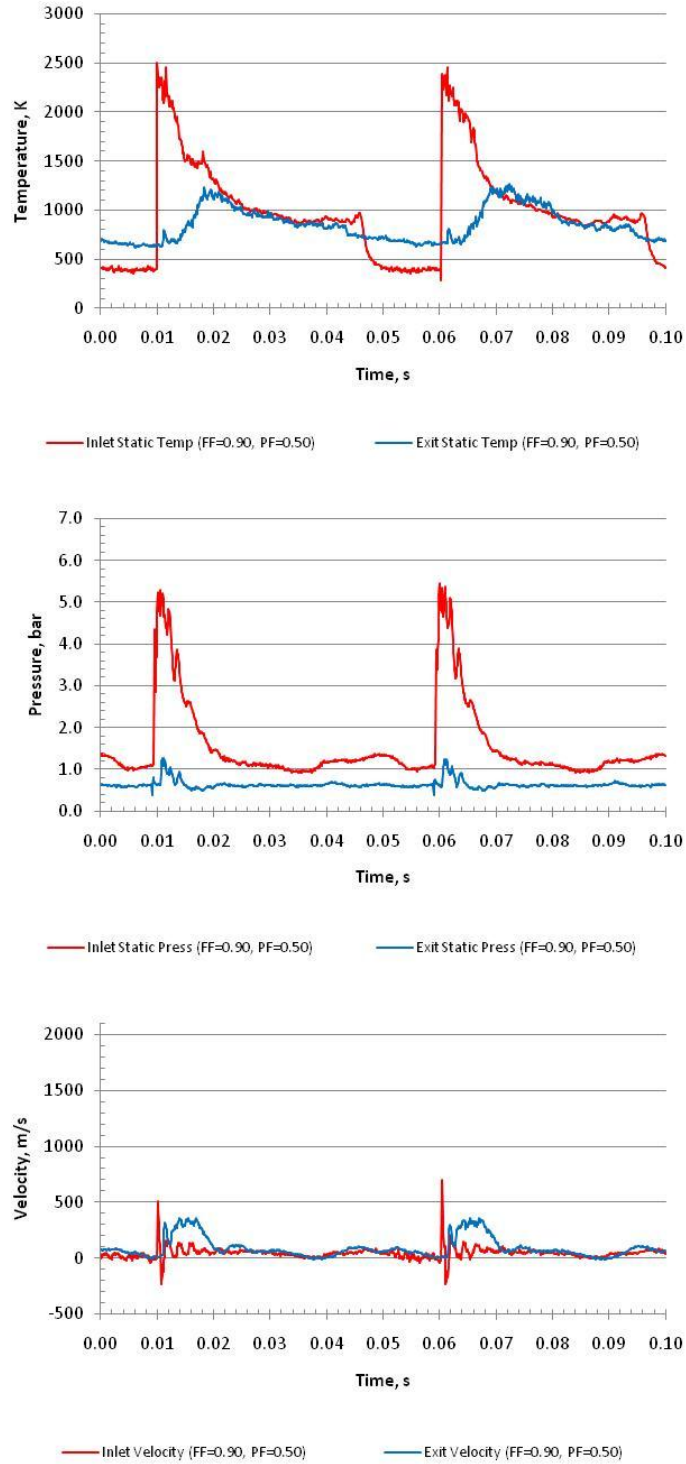


**Figure 147. Time-resolved turbine inlet and exit flowfield properties with 20 Hz ethylene-fueled PDC with 0.90 fueled fraction and 0.50 purge fraction**

## Appendix K: Alternate Unsteady Turbine Efficiency Results

The results presented here are from variations in the Eq. (4) formulation on page 14 for instantaneous turbine efficiency using data collected with the 30 Hz hydrogen-fueled PDC with 0.75 fueled and purge fractions.

### Instantaneous Turbine Efficiency

One such variation accounted for heat transfer effects, substituting Eqs. (16) and (20) on page 21 for inlet and exit total enthalpy rate, respectively, into Eq. (4), including station numbers consistent with Fig. 6 on page 19. The instantaneous power term in Eq. (79) includes the instantaneous power to the compressor from Eq. (27) on page 23, as well as the instantaneous change in rotational energy of the wheel assembly, using Eq. (78) on page 186 and the manufacturer's moment of inertia,  $3.2\text{E-}5 \text{ kg m}^2$ . Due to the periodic nature of the rotor speed, the initial rotor speed was obtained from the final point of the data set.

$$\eta_{\text{turb, instant}} \equiv \frac{\dot{W}_{\text{out}}}{\dot{H}_{t,1} - (\psi)(\dot{H}_{t,1} - \dot{H}_{t,4} - \dot{W}_{\text{out}}) \left( 1 - \left( \frac{P_{t,\text{out}}}{P_{t,\text{in}}} \right)^{\frac{\gamma-1}{\gamma}} \right)} \quad (79)$$

$$\dot{W}_{\text{out}} = \dot{W}_{\text{compr}} + \frac{d(\text{KE}_{\text{rot}})}{dt} \quad (80)$$

$$\frac{d(\text{KE}_{\text{rot}}(t))}{dt} = \frac{\frac{1}{2}I(\omega(t))^2 - \frac{1}{2}I(\omega(t + \Delta t))^2}{\Delta t} \quad (81)$$

Figure 148 includes results over 14 sequential cycles at 30 Hz, using the instantaneous efficiency formulation proposed in Eq. (79) with  $\psi = 0.75$ . For a significant portion of the cycle time, instantaneous efficiency is non-physical exceeding 100% or below 0%; however, the cycle average instantaneous efficiency is 8%. The large positive and negative spikes are associated with moments during the detonation cycle when total enthalpy rate and total pressure are nearly the same at the inlet and exit. The negative values occur at moments when exit total enthalpy rate exceeds that of the inlet.

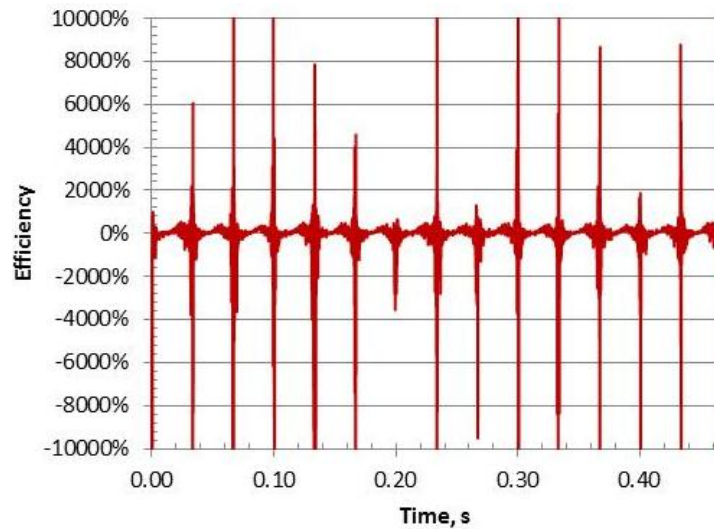


**Figure 148. Time resolved turbine efficiency with 30 Hz hydrogen-fueled PDC with 0.75 fueled and purge fractions and  $\psi = 0.75$ , using Eq. (79)**

Figure 149 shows ensemble averaged turbine efficiency over 14 sequential cycles at 30 Hz, including ensemble averaged time-resolved efficiency points, represented by squares, within 0% to 100%. Reasonable magnitudes for ensemble averaged time-resolved efficiency occurred during the fire phase due to total pressure ratios significantly greater than unity. There are a few random moments during the purge phase when ensemble averaged efficiency is of reasonable magnitude; however, these moments occur

when the total enthalpy rate and total pressure are nearly the same at the inlet and exit with a low signal-to-noise ratio such that there is little confidence the points represent actual efficiency.

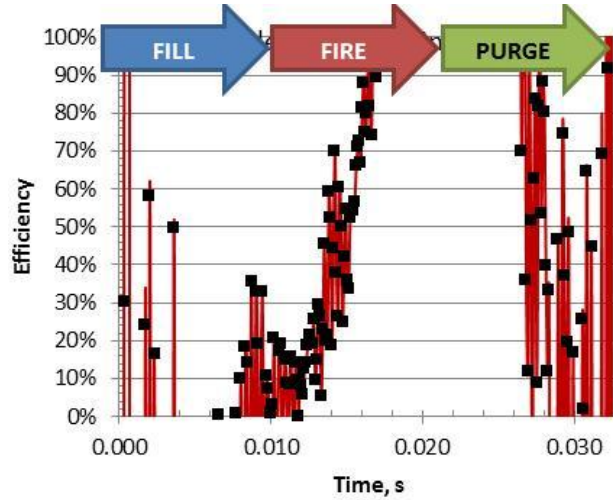


**Figure 149. Ensemble averaged turbine efficiency over 14 cycles with 30 Hz hydrogen-fueled PDC with 0.75 fueled and purge fractions and  $\psi = 0.75$ , using Eq. (79)**

### Mean Effective Instantaneous Turbine Efficiency

Another variation of the Eq. (4) formulation for instantaneous turbine efficiency included a moving average for mean effective inlet and exit total pressure and specific heat. The development of the formulation began with Eq. (79) and included mass average total pressure and specific heat over a time window.

$$\eta_{turb, instant, eff} \equiv \frac{\dot{W}_{out}}{\dot{H}_{t,1} - (\psi)(\dot{H}_{t,1} - \dot{H}_{t,4} - \dot{W}_{out}) \left( 1 - \left( \frac{P_{t,out}}{P_{t,in}} \right)^{\frac{\gamma-1}{\gamma}} \right)} \quad (82)$$

$$P_t \equiv \frac{\int_{window} (\dot{m}P_t) dt}{\int_{window} (\dot{m}) dt} \quad (83)$$

$$\frac{\gamma - 1}{\gamma} \equiv \frac{R}{c_{p,avg}} \equiv R \left[ \frac{1}{2} \left( \frac{\int_{window} (\dot{m}c_p)_1 dt}{\int_{window} (\dot{m})_1 dt} + \frac{\int_{window} (\dot{m}c_p)_4 dt}{\int_{window} (\dot{m})_4 dt} \right) \right]^{-1} \quad (84)$$

Figure 150 shows the effect of window size on cycle average turbine efficiency over 14 cycles, using the instantaneous efficiency formulation proposed in Eq. (82) with  $\psi = 0.75$ . The magnitude of average turbine efficiency was nearly asymptotic with a window size greater than 113. Figures 151 and 152 show time-resolved efficiency, using Eq. (82) with a window size of 113 points. Time-resolved turbine efficiency was non-physical for a significant portion of the cycle time. Reasonable magnitudes for time-resolved turbine efficiency occurred during periods with large peaks in inlet total enthalpy rate. Time average efficiency was 21%. The general shape of the time-resolved turbine efficiency was similar to that of the turbine power from Eq. (80), indicating a strong relationship between instantaneous turbine efficiency and turbine power.

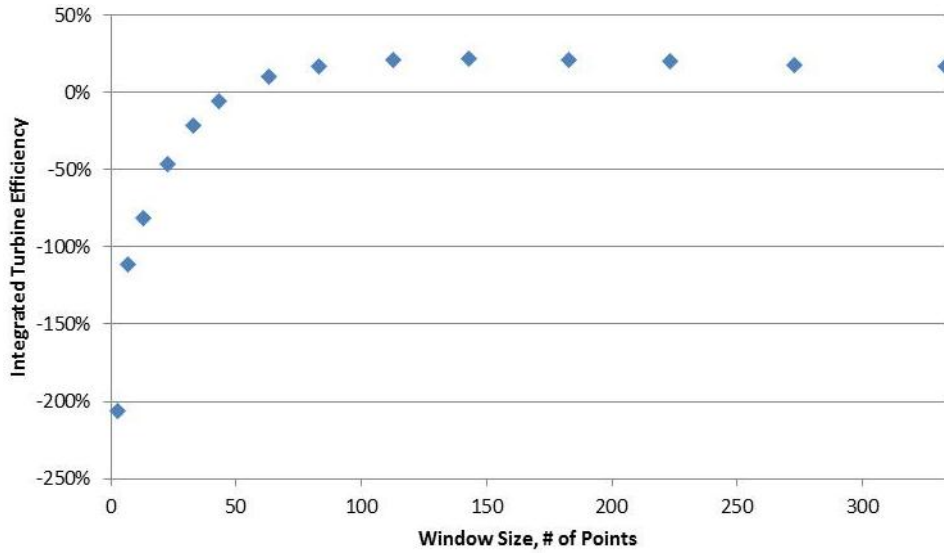


**Figure 150.** Cycle average turbine efficiency over 14 cycles with 30 Hz hydrogen-fueled PDC with 0.75 fueled and purge fractions and  $\psi = 0.75$ , using Eq. (82)

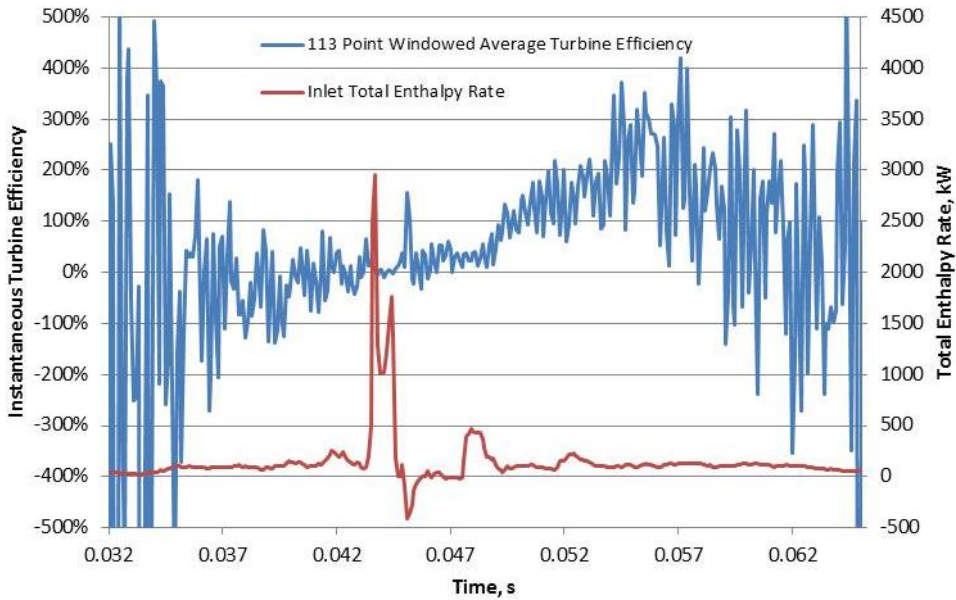


**Figure 151.** Time-resolved turbine efficiency and inlet total enthalpy rate over one cycle with 30 Hz hydrogen-fueled PDC with 0.75 fueled and purge fractions and  $\psi = 0.75$ , using Eq. (82)

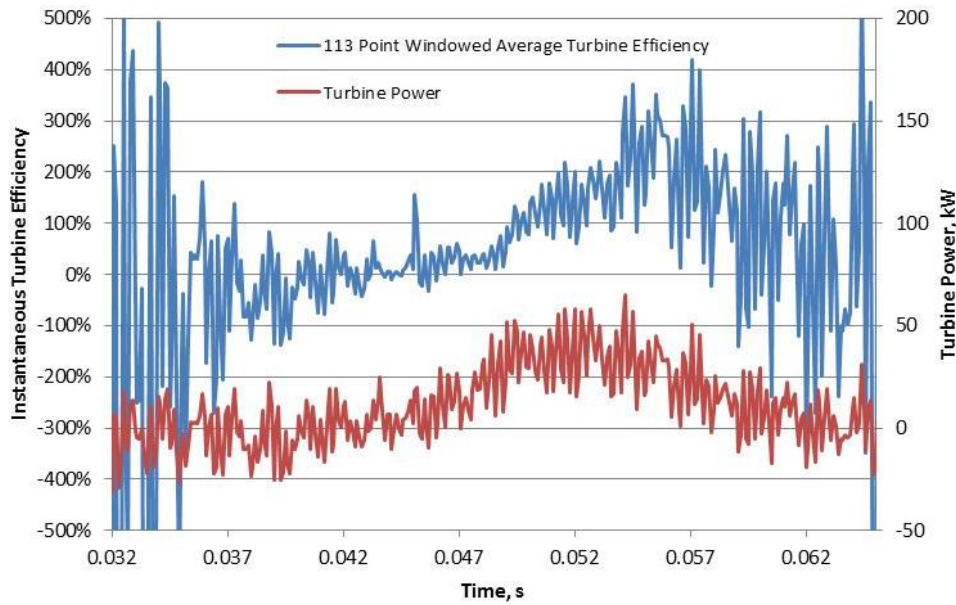


**Figure 152. Time-resolved turbine efficiency using Eq. (82) and turbine power using Eq. (80) for one cycle with 30 Hz hydrogen-fueled PDC with 0.75 fueled and purge fractions and  $\psi = 0.75$**

### Summary and Conclusions

The various formulations proposed here for instantaneous turbine efficiency are impractical for the instrumentation arrangement in this study. Non-physical values for instantaneous efficiency include magnitudes significantly above 100% and significantly below 0%. Large excursions in instantaneous efficiency result from moments when total enthalpy rate and total pressure are nearly equal at the inlet and exit. Negative values for instantaneous turbine efficiency result when exit total enthalpy rate at a moment exceeds that of the inlet. To properly characterize instantaneous efficiency and avoid non-physical results, the instrumentation arrangement would need to track each fixed mass from the inlet, through the turbine, and to the exit and account for the difference in flowfield and mechanical response times to the pulsed detonations.

## Appendix L: Turbine Inlet Rayleigh Line Flow Analysis

The Rayleigh line flow analysis presented here is an alternative to the proposed constant pressure heat transfer model in Eq. (29) on page 24. In this analysis and for comparison purposes, the inlet transfer fraction parameter is 100% ( $\psi = 1$ ). The total amount of heat transfer from the First Law analysis between turbine inlet and exit measurement locations is the same regardless of the heat transfer model, as shown in Eq. (13) on page 20; however, in the Rayleigh model, total pressure changes in proportion to the momentum imparted by heat transfer. The Rayleigh analysis is used to determine the total pressure at the turbine inlet, at station 2 in Fig. 153, downstream from the inlet measurement location at station 1. The resulting total pressure is used in the denominator of the pressure ratio in the Eq. (29) formulation for turbine efficiency. The analysis begins by calculating instantaneous Mach number at station 1 from measurements of velocity and temperature, as shown in Eq. (85), where specific heat is calculated for air as a function of temperature.

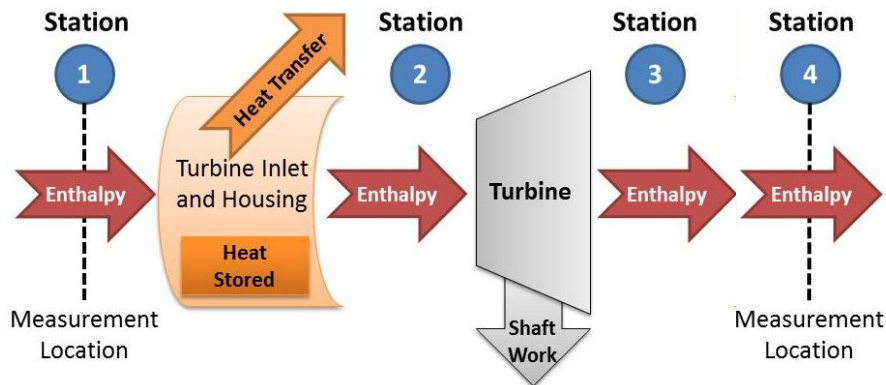


**Figure 153. Schematic of unsteady model for Rayleigh analysis of a pulsed detonation driven turbine**

$$M_1(t) = \frac{v_1(t)}{a_1(t)} = \frac{v_1(t)}{\sqrt{\gamma_1(t)RT_1(t)}} \quad (85)$$

$$\gamma_1(t) = c_{p,1}(t)(c_{p,1}(t) - R) \quad (86)$$

The instantaneous ratio of total temperature at station 1 and a reference condition where Mach number is unity,  $T_t^*$ , is calculated as function of Mach number and ratio of specific heat at station 1.

$$\frac{T_{t1}(t)}{T_t^*} = \frac{(1 + \gamma_1(t))^2 M_1(t)^2 \left(1 + \frac{\gamma_1(t) - 1}{2} M_1(t)^2\right)}{(1 + \gamma_1(t) M_1(t)^2)^2 \left(1 + \frac{\gamma_1(t) - 1}{2}\right)} \quad (87)$$

The instantaneous total temperature at station 2 is calculated from total temperature at station 1 and the cycle-average heat transfer from Eq. (13) and cycle-average mass flow rate and specific heat. The use of cycle-average properties is a limitation in this analysis, as instantaneous heat transfer is not known.

$$T_{t,2}(t) = T_{t,1}(t) - \frac{\overline{\dot{Q}_{out}}}{(\overline{\dot{m}}_1)(c_{p,1})} = T_{t,1}(t) - \frac{(\overline{\dot{H}}_{t,1} - \overline{\dot{H}}_{t,4} - \overline{\dot{W}}_{turb})}{(\overline{\dot{m}}_1)(c_{p,1})} \quad (88)$$

The instantaneous ratio of total temperature at station 2 and a reference condition where Mach number is unity,  $T_t^*$ , is calculated from total temperature relationships between stations 1 and 2, as well as the reference condition where Mach number is unity.

$$\frac{T_{t2}(t)}{T_t^*} = \frac{T_{t1}(t)}{T_t^*} \frac{T_{t2}(t)}{T_{t1}(t)} \quad (89)$$

The analysis proceeds with iterations of  $M_2$ , assuming that  $\gamma_1$  and  $\gamma_2$  are equal, until the calculation for total temperature ratio from Eq. (90) is equal to that of Eq. (89).

$$\frac{T_{t2}}{T_t^*}(t) = \frac{(1 + \gamma_2(t))^2 M_2(t)^2 \left(1 + \frac{\gamma_2(t) - 1}{2} M_2(t)^2\right)}{\left(1 + \gamma_2(t) M_2(t)^2\right)^2 \left(1 + \frac{\gamma_2(t) - 1}{2}\right)} \quad (90)$$

Stations 1 and 2 static pressure ratios, shown in Eqs. (91) and (92), are then calculated using Mach numbers at the respective stations and the ratio of specific heats.

$$\frac{P_1}{P^*}(t) = \frac{1 + \gamma_1(t)}{1 + \gamma_1(t) M_1(t)^2} \quad (91)$$

$$\frac{P_2}{P^*}(t) = \frac{1 + \gamma_2(t)}{1 + \gamma_2(t) M_2(t)^2} \quad (92)$$

Static and total pressures at station 2 are then calculated using Eqs. (93) and (94) with ratios to the reference condition, the measured static pressure at station 1, and Mach number and ratio of specific heats at station 2.

$$P_2(t) = \frac{P_2}{P^*}(t) \frac{P^*}{P_1}(t) P_1(t) \quad (93)$$

$$P_{t,2}(t) = P_2(t) \left(1 + \frac{\gamma_2(t) - 1}{2} M_2(t)^2\right)^{\frac{\gamma_2(t)}{\gamma_2(t) - 1}} \quad (94)$$

Station 2 total pressure is then used to calculate mean effective isentropic turbine efficiency using Eq. (29) on page 24.

## Bibliography

- Akbari, P., Szpynda, E., and Nalim, M. R.. "Recent Developments in Wave Rotor Combustion Technology and Future Perspective: A Progress Review." *43rd AIAA/ASME/SAE/ASEE Joint Propulsion Conference*. AIAA2007-5055, Cincinnati OH, 8-11 July, 2007.
- Andrus, I., and King, P. I. "Evaluation of a High Bypass Turbofan Hybrid Utilizing a Pulse Detonation Combustor." *43rd AIAA/ASME/SAE/ASEE Joint Propulsion Conference*. AIAA2007-5074, Cincinnati OH, 8-11 July, 2007.
- Austin, J. M., and Shepherd, J. E. "Detonations in Hydrocarbon Fuel Blends." *Combustion and Flame*, pp. 73-90, 2003.
- Austin, J. M., Pintgen, F., and Shepherd, J. E. "Lead Shock Oscillation and Decoupling in Propagating Detonations." *43rd Aerospace Sciences Meeting*. AIAA2005-1170, Reno NV, 10-13 January, 2005.
- Austin, J. M., Pintgen, F., and Shepherd, J. E. "Reaction Zones in Highly Unstable Detonations." *Proceedings of the Combustion Institute* 30. pp. 1849-1857, 2005.
- Baker, W. E., Cox, P. A., Westine, P. S., Kulesz, J. J., and Strehlow, R. A. *Explosion hazards and evaluation*. Elsevier Scientific Publishing Co., New York NY, 1983.
- Baptista, M., Rasheed, A., Badding, B., Velagandula, O., and Dean, A. J. "Mechanical Response in a Multi-tube Pulsed Detonation Combustor-Turbine Hybrid System." *44th AIAA Aerospace Sciences Meeting*. AIAA2006-1234, Reno NV, 9-12 January, 2006.
- Bauer, P. A., Brochet, C., and Presles, H. N. "The Influence of Initial Pressure on Critical Diameters of Gaseous Explosive Mixtures." *Progress in Astronautics and Aeronautics*. vol. 94, pp. 118-129, 1984.
- Bauer, P. A., Presles, H. N., Heuze, O., and Brochet, C. "Measurement of Cell Lengths in the Detonation Front of Hydrocarbon Oxygen and Nitrogen Mixtures at Elevated Initial Pressures." *Combustion and Flame*. vol. 64, pp. 113-123, 1986.
- Blunck, D., Kiel, B., Goss, L., and Lynch, A. "Spatial Development and Temperature of Spark Kernels Exiting into Quiescent Air." Submitted to *AIAA Journal*. 2010.
- Bussing, T., and Pappas, G. "An Introduction to Pulse Detonation Engines." *32nd AIAA Aerospace Sciences Meeting*. AIAA94-0263, Reno NV, 10-13 January, 1994.

- Bykovskii, F. A., S. A. Zhdan, and E. F. Verdernikov. "Continuous Spin Detonations." *AIAA Journal of Propulsion and Power*. vol. 22, no. 6, pp. 1204-1216, November-December, 2006.
- Caldwell, N., Glaser, A., Gutmark, E. "Performance Measurements of a Pulse Detonation Engine Array Integrated with a Turbine," *42nd AIAA/ASME/SAE/ASEE Joint Propulsion Conference*. AIAA-2006-4307, July, 2006.
- Caldwell, N., Gutmark, E. "Performance Analysis of a Hybrid Pulse Detonation Combustor/Gas Turbine System," *44th AIAA/ASME/SAE/ASEE Joint Propulsion Conference*. AIAA-2008-4880, July, 2008.
- Catchpole, B. C., and Runacres, A. *Constant Volume Gas Turbine Experiments with Gaseous Fuel in a Rotating Pocket Combustor*. Aeronautical Research Laboratories, Department of Defence, Mechanical Engineering Note, ARL/ME 353, Melbourne Australia, October, 1974.
- Coleman, M. L. *Overview of Pulse Detonation Propulsion Technology*. Chemical Propulsion Information Agency, CPTR 70, Columbia MD, 2001.
- Daniau, E., Falempin, F., and Zhdan, S. "Pulsed and Rotating Detonation Propulsion Systems: First Step Toward Operational Engines." *AIAA/CIRA 13th international Space Planes and Hypersonic Systems and Technologies Conference*. AIAA2005-3233, Capua, 16-20 May, 2005.
- Dean, A. J. "A Review of PDE Development for Propulsion Applications." *45th AIAA Aerospace Sciences Meeting*. AIAA2007-0985, Reno NV, 8-11 January, 2007.
- Dean, A. J. "Recent Developments in Approaches to Pulsed Detonation Propulsion (Invited)." *39th AIAA/ASME/SAE/ASEE Joint Propulsion Conference*. AIAA2003-4510, Huntsville AL, 21-23 July, 2003.
- Deng, J., Zheng, L., Yan, C., Jiang, L., Xiong, C., and Li, N. "Experimental Investigations of a Pulse Detonation Combustor-Turbine Hybrid System." *47th AIAA Aerospace Sciences Meeting*. AIAA2009-0506, Orlando FL, 5-8 January, 2009.
- Dunlap, R., Brehm, R. L., and Nicholls, J. A. *A Preliminary Study of the Application of Steady-State Detonative Combustion to a Reaction Engine*. Project 2284, AFOSR TN 57-657, Ann Arbor MI, 1957.
- Dyer, R. S., and Kaemming, T. A. "The Thermodynamic Basis of Pulsed Detonation Engine Thrust Production." *38th AIAA/ASME/SAE/ASEE Joint Propulsion Conference*. AIAA2002-4072, Indianapolis IN, 7-10 July, 2002.

- Fickett, W., and Davis, W. C. *Detonation Theory and Experiment*. Dover Publications Inc., Mineola NY, 2001.
- Friedman, R. *Journal of the American Rocket Society*. vol. 24, p. 349, November, 1953.
- Fritsch, G., and Giles, M. "Second Order Effects of Unsteadiness on the Performance of Turbomachines." *ASME International Gas Turbine and Aeroengine Congress*. 92-GT-389, June 1992.
- Gamezo, V. M., Ogawa, T., and Oran, E. S. "Deflagration-to-Detonation Transition in Premixed H<sub>2</sub>-Air in Channels with Obstacles." *45th AIAA Aerospace Sciences Meeting*. AIAA2007-1172, Reno NV, 8-11 January, 2007.
- Glaser, A. J., Caldwell, N., and Gutmark, E. "A Fundamental Study on the Acoustic Behavior of Pulse Detonation Engines." *45th AIAA Aerospace Sciences Meeting*. AIAA2007-0444, Reno NV, 8-11 January, 2007.
- Glaser, A. J., Caldwell, N., and Gutmark, E. "Experimental Investigation into the Acoustic Performance of a Pulse Detonation Engine with Ejector." *43rd AIAA Aerospace Sciences Meeting*. AIAA2005-1345, Reno NV, 10-13 January, 2005.
- Glaser, A. J., Caldwell, N., and Gutmark, E. "Performance of an Axial Flow Turbine Driven by Multiple Pulse Detonation Combustors." *45th AIAA Aerospace Sciences Meeting*. AIAA2007-1244, Reno NV, 8-11 January, 2007.
- Glassman, I. *Combustion*. 3rd Edition. Academic Press, San Diego CA, 1996.
- Greitzer, E., Epstein, A., Giles, M., McCune, J., and Tan, C. *Unsteady Flow Phenomena in Turbomachines*. AFOSR TR 93-0194, January 1993.
- Guirao, C. M., Knystautas, R., Lee, J., Benedick, W., and Berman, M. "Hydrogen-Air Detonations." *19th Symposium (Int.) on Combustion*. pp. 583-590, 1982.
- Hayashi, A. K., Kimura, Y., Yamada, T., Yamada, E., Kindracki, J., Dzieminska, E., Wolanski, P., Tsuboi, N., Tangirala, V., Fujiwara, T. "Sensitivity Analysis of Rotating Detonation Engine with a Detailed Reaction Model." *47th AIAA Aerospace Sciences Meeting*. AIAA2009-0633, Orlando FL, 5-8 January, 2009.
- Heiser, W. H., and Pratt, D. T. "Thermodynamic Cycle Analysis of Pulse Detonation Engines." *AIAA Journal of Propulsion and Power*. vol. 18, no. 1, January-February, 2002.
- Helfrich, T. M. *Cycle Performance of a Pulse Detonation Engine with Supercritical Fuel Injection*. MS Thesis, Air Force Institute of Technology, WPAFB OH, 2006.

- Helfrich, T. M., King, P. I., Hoke, J. L., and Schauer, F. R. "Effect of Supercritical Fuel Injection on the Cycle Performance of a Pulse Detonation Engine." *42nd AIAA/ASME/SAE/ASEE Joint Propulsion Conference*. AIAA2006-5133, Sacramento CA, 9-12 July, 2006.
- Helman, D., Shreeve, R. P., and Eidelman, S. "Detonation Pulse Engine." *22nd AIAA/ASME/SAE/ASEE Joint Propulsion Conference*. AIAA1986-1683, Huntsville AL, 16-18 June, 1986.
- Hofer, D. C., Tangirala, V. E., and Suresh, A. "Performance Metrics for Pulse Detonation Combustor Turbine Hybrid Systems." *47th AIAA Aerospace Sciences Meeting*. AIAA2009-0292, Orlando FL, 5-8 January, 2009.
- Hoffman, N. *Reaction Propulsion by Intermittent Detonative Combustion*. Ministry of Supply, Volkenrode Translation, 1940.
- Hoke, J. L., Bradley, R. P., and Schauer, F. R. "The Effect of the Dynamic Filling Process on PDE Performance and Nozzle Selection." *51st JANNAF Propulsion Meeting*. Lake Buena Vista FL, 2002.
- Hoke, J., Bradley, R., Stutrud, J., and Schauer, F. "Integration of a Pulsed Detonation Engine with an Ejector Pump and with a Turbo-charger as Methods to Self-Aspirate." *40th AIAA Aerospace Sciences Meeting*. AIAA2002-0615, Reno NV, 14-17 January, 2002.
- Holzwarth, H. *The Gas Turbine*. Charles Griffin and Co., Ltd, London England, 1912.
- Hopper, D. *Direct Initiation of Multiple Tubes by Detonation Branching*. PhD Dissertation, Air Force Institute of Technology, WPAFB OH, 2008.
- Kentfield, J. A. C. "Progress Towards a Pressure-Generating Combustion Chamber for Gas Turbines." *First International Symposium on Pulsating Combustion*. Paper no. 11, England, 1971.
- Kentfield, J. A. C., Rehman, M., and Marzouk, E. S. "A Simple Pressure Gain Combustor for Gas Turbines." *ASME Journal of Engineering for Power*. vol. 99, no. 2, pp. 153-158, April, 1977.
- Kentfield, J. A. C., Rehman, A., and Cronje, J.. "The Performance of Pressure-Gain Combustors without Moving Parts." *AIAA Terrestrial Energy Systems Conference*. AIAA79-0998, Orlando FL, 4-6 June, 1979.
- Kentfield, J. A. C., and O'Blenes, M. J. "Small Gas Turbine Using a Second-Generation Pulse Combustor." *AIAA Journal of Propulsion and Power*. vol. 6, no. 2, pp. 214-220, March-April, 1990.

- Knystautas, R., Guirao, C., Lee, J. H., and Sulmistras, A. "Measurements of Cell Size in Hydrocarbon-Air Mixtures and Predictions of Critical Tube Diameter, Critical Initiation Energy, and Detonability Limits." *Progress in Astronautics and Aeronautics*. vol. 94, pp. 23-37, 1984.
- Kojima, T., Tsuboi, N., Taguchi, H., Kobayashi, H., Sato, T., Daimon, Y., Inaba, K. "Design Study of Turbine for Pulse Detonation Combustor." *43rd AIAA/ASME/SAE/ASEE Joint Propulsion Conference*. AIAA2007-5081, Cincinnati OH, 8-11 July, 2007.
- Krzycki, L. J. *Performance Characteristics of an Intermittent-Detonation Device*. U.S. Naval Ordnance Test Station, Navweps Report 7655, China Lake CA, 1962.
- Kuo, K. K. *Principles of Combustion*. John Wiley and Sons, New York, NY, 1986.
- Lyle, K., Jeffries, J., and Hanson, R. "Diode-Laser Sensor of Air-Mass Rate 1: Design and Wind-Tunnel Validation." *AIAA Journal*. vol. 45, no. 9, pp. 2204-2212, 2007.
- Marzouk, E. S., and Kentfield, J. A. C. "Pressure-Gain Combustion, A Means of Improving the Efficiency of Thermal Plant." *Proceedings of the 9th Intersociety Energy Conversion Engineering Conference*. pp. 1125-1131, San Francisco CA, August, 1974.
- Mattingly, J. D. *Elements of Gas Turbine Propulsion*. McGraw-Hill, Inc., New York NY, 1996.
- Mattison, D. W., Brophy, C. M., Sanders, S. T., Ma, L., Hinckley, K. M., Jeffries, J. B., and Hanson, R. K. "Pulse Detonation Engine Characterization and Control Using Tunable Diode Laser Sensors." *AIAA Journal of Propulsion and Power*, vol. 19, No. 4, pp. 568-572, 2003.
- Meier, GEA. "New Optical Tools for Fluid Mechanics." *8th International Symposium on Flow Visualization*. Sorrento Italy, 1-4 September, 1998.
- Meyer, T. R., Hoke, J. L., Brown, M. S., Gord, J. R., and Schauer, F. R. "Experimental Study of Deflagration-to-Detonation Enhancement Techniques in a H<sub>2</sub>/Air Pulsed Detonation Engine." *38th AIAA/ASME/SAE/ASEE Joint Propulsion Conference*. AIAA2002-3720, Indianapolis IN, 2002.
- Mikutsu, Y., Araki, N., and Hayashi, A. K. "Detailed Study of the Structure Near Hot Spots in Hydrogen-Air Detonation." *Proceedings of the 17th International Colloquium on the Dynamics of Explosions and Reactive Systems*. Heidelberg Germany, 1999.

- Miser, C. L. *Pulse Detonation Engine Thrust Tube Heat Exchanger for Flash Vaporization and Supercritical Heating of JP-8*. MS Thesis, Air Force Institute of Technology, WPAFB OH, 2005.
- Nango, A., Inaba, K., Kojima, T., and Yamamoto, M. "Aerodynamic Effect of Turbine Blade Geometry in Pulse Detonation Combustor." *45th AIAA Aerospace Sciences Meeting*. AIAA2007-1176, Reno NV, 8-11 January, 2007.
- Nango, A., Inaba, K., Kojima, T., and Yamamoto, M. "Numerical Study of Detonation Interaction with a Single-Stage Axial Turbine." *46th AIAA Aerospace Sciences Meeting*. AIAA2008-0985, Reno NV, 7-10 January, 2008.
- Nicholls, J. A., and Morrison, R. B. *Detonative Combustion*. Project M898, Ann Arbor MI, 1952.
- Nicholls, J. A., Wilkinson, H. R., and Morrison, R. B. *Intermittent Detonation as a Thrust-Producing Mechanism*. Wright Aeronautical Division, Curtiss-Wright Corporation, Project 2318, Wood-Ridge NJ, 1955.
- Oran, E. S., and Khokhlov, A. M. "Deflagrations, Hot Spots, and the Transition to Detonation." *Proceedings of the 17th International Colloquium on the Dynamics of Explosions and Reactive Systems*. Heidelberg Germany, 1999.
- Oran, E. S., Young, T. R., Picone, J. P., Boris, J. M., and Edwards, D. H. *A Study of Detonation Structure: The Formation of Unreacted Gas Pockets*. Naval Research Laboratory Memorandum Report 4866, Washington DC, 1982.
- Oro, J., Marigorta, E., Diaz, K., and Ballesteros-Tajadura, R. "Forced and Unforced Unsteadiness in an Axial Turbomachine." *Experimental Thermal and Fluid Science*. vol. 33, no. 3, pp. 449-459, March, 2009.
- Panzenhagen, K. L. *Detonation Branching in a PDE with Liquid Hydrocarbon Fuel*. MS Thesis, Air Force Institute of Technology, WPAFB OH, 2004.
- Petters, D. P., and Felder, J. L. "Engine System Performance of Pulse Detonation Concepts Using the NPSS Program." *38th AIAA/ASME/SAE/ASEE Joint Propulsion Conference*. AIAA2002-3910, Indianapolis IN, 7-10 January, 2002.
- Pintgen, F., and Shepherd, J. E. "Stereoscopic Imaging of Transverse Detonations in Diffraction." *5th Pacific Symposium on Flow Visualization and Image Processing*. Australia, 27-29 September, 2005.
- Pintgen, F., Eckert, C. A., Austin, J. M., and Shepherd, J. E. "Direct Observations of Reaction Zone Structure in Propagating Detonations." *Combustion and Flame* vol. 133, no. 3, pp. 211-229, 2003.

- Pintgen, F., Austin, J. M., and Shepherd, J. E. *Detonation Front Structure: Variety and Characterization*. Torus Press, Moscow Russia, 2003.
- Porowski, R., and Teodorczyk, A. "Cellular Structure of Detonation Wave for Hydrogen-Methane-Air Mixtures." *European Combustion Meeting*. 2009.
- Raffel, M., Richard, H., and Meier, GEA. "On the Applicability of Background Oriented Optical Tomography for Large Scale Aerodynamic Investigations." *Experimental Fluids* 28. pp. 477-481, 2000.
- Rasheed, A., Tangirala, V. E., Vandervort, C. L., Dean, A. J., and Haubert, C., "Interactions of a Pulsed Detonation Engine with a 2D Turbine Blade Cascade," *42nd AIAA Aerospace Sciences Meeting*. AIAA-2004-1207, Reno NV, 5-8 January, 2004.
- Rasheed, A., Furman, A., and Dean, A. J. "Experimental investigations of an Axial Turbine Driven by a Multi-tube Pulsed Detonation Combustor System." *41st AIAA/ASME/SAE/ASEE Joint Propulsion Conference*. AIAA2005-4209, Tucson AZ, 10-13 July, 2005.
- Richard, H., Rein, M., Kompenhans, J., and Meier, GEA. "Demonstration of the Applicability of a Background Oriented Schlieren (BOS) Method." *10th International Symposium on Applications of Laser Techniques to Fluid Mechanics*. Lisbon Portugal, 10-13 July, 2000.
- Rolling, A. J. *Alternative Pulse Detonation Engine Ignition System Investigation through Detonation Splitting*. MS Thesis, Air Force Insitute of Technology, WPAFB OH, 2002.
- Rouser, K. P., King, P. I., Schauer, F. R., Hoke, J. L., and Sondergaard, R. "Parametric Study of Unsteady Turbine Performance Driven by a Pulse Detonation Combustor." *46th AIAA/ASME/SAE/ASEE Joint Propulsion Conference*. AIAA-2010-6536, Nashville TN, July 25-28, 2010.
- Rouser, K. P., King, P. I., Schauer, F. R., Hoke, J. L., and Sondergaard, R. "Performance Evaluation of an Unsteady Turbine Driven by a Pulsed Detonation Combustor." *ASME Internation Gas Turbine Institute Turbo Expo 2011*. GT-2011-45396, Vancouver Canada, June 6-10, 2011.
- Rouser, K. P., King, P. I., Schauer, F. R., Hoke, J. L., Goss, L. P., and Sondergaard, R. "Time-Accurate Flow Field and Rotor Speed Measurements of a Pulsed Detonation Driven Turbine." *49th AIAA Aerospace Sciences Meeting*. AIAA-2011-0577, Orlando FL, January 4-7, 2011.

- Rouser, K. P., King, P. I., Schauer, F. R., Sondergaard, R., and Hoke, J. L. "Unsteady Performance of a Turbine Driven by a Pulse Detonation Engine." *48th AIAA Aerospace Sciences Meeting*. AIAA-2010-1116, Orlando FL, 4-7 January, 2010.
- Sakurai, T., Obara, T., Ohyagi, S., Murayama, M. "Experimental Study of Pulse Detonation Turbine Engine toward Power Generator." *Proceedings of the 20th International Colloquium on the Dynamics of Explosion and Reactive Systems*. Montreal Canada, 2005.
- Schauer, F., Stutrud, J., Bradley, R., Katta, V., and Hoke, J. "Detonation Initiation and Performance in Complex Hydrocarbon Fueled Pulsed Detonation Engines." *50th JANNAF Propulsion Meeting*. paper I-05, Salt Lake City UT, 11-13 July, 2001.
- Schauer, F., Stutrud, J., Bradley, R., Katta, V., and Hoke, J. "Detonation Studies and Performance Results for a Research Pulse Detonation Engine." *Proceedings of the International Colloquium on Advances in Confined Detonations*. Moscow Russia, 2002.
- Schauer, F., Bradley, R., and Hoke, J. "Interaction of a Pulsed Detonation Engine with a Turbine." *41st AIAA Aerospace Sciences Meeting*. AIAA2003-0891, Reno NV, 6-9 January, 2003.
- Sharma, O., Pickett, G., and Ni, R. "Assessment of Unsteady Flows in Turbines." *ASME Journal of Turbomachinery*. vol. 114, no. 1, pp. 79-90, 1992.
- Shultz-Grunow, F. *Gas-Dynamic Investigations of the Pulse-Jet Tube, Parts I and II*. National Advisory Committee for Aeronautics TM No. 1131, Washington DC, 1947.
- Sieverding, C. H., Ottolia, D., Bagnera, C., Comadoro, A., Brouckaert, J.-F., and Desse, J.-M. "Unsteady Turbine Blade Wave Characteristics." *ASME Journal of Turbomachinery*. vol. 126, pp. 551-559, October 2004.
- Sinibaldi, J. O., Brophy, C. M., Li, C., and Kailsanath, K. "Initiator Detonation Diffraction Studies in Pulsed Detonation Engines." *37th AIAA/ASME/SAE/ASEE Joint Propulsion Conference*. AIAA2001-3466, Salt Lake City UT, 8-11 July, 2001.
- Slack, J. D. *Branch Detonation of a Pulse Detonation Engine with Flash Vaporized JP-8*. MS Thesis, Air Force Institute of Technology, WPAFB OH, 2007.
- Snyder, P. H., Alparslan, B., and Nalim, M. R. "Gas Dynamic Analysis of the CVC, A Novel Detonation Cycle." *38th AIAA/ASME/SAE/ASEE Joint Propulsion Conference*. AIAA2002-4069, Indianapolis IN, 7-10 July, 2002.

- Suresh, A., Hofer, D. C., Tangirala, V. E., "Turbine Efficiency for Unsteady, Periodic Flows." *47th AIAA Aerospace Sciences Meeting*. AIAA-2009-0504, Orlando FL, 5-8 January, 2009.
- Tsuji, T., Shirakawa, S., Yoshihashi, T., Obara, T., and Ohyagi, S. "Interaction Between Two Cylinders in a Pulse Detonation Engine." In *Advancements in Energetic Materials and Chemical Propulsion*, by K. K. Kuo and K. Hori, Begel House Inc., pp. 1035-1046, 2008.
- Tsukui, A., Matsumomo, K., Kasahara, J., and Kojima, T.. "Research on Interaction Between an Intermittent Flow and a PDE Turbine." *47th AIAA Aerospace Sciences Meeting*. AIAA2009-0295, Orlando FL, 5-8 January, 2009.
- Tucker, K. C. *A Flash Vaporization System for Detonation of Hydrocarbon Fuels in a Pulse Detonation Engine*. PhD Dissertation, Air Force Institute of Technology, WPAFB OH, 2005.
- Van Zante, D., Envia, E., and Turner, M. G.. "The Attenuation of a Detonation Wave by an Aircraft Engine Axial Turbine Stage." *18th AIAA International Symposium on Air-Breathing Engines*. AIAA2007-1260, Beijing China, 2-7 September, 2007.
- Venkatakrishnan, L., and Meier, GEA. "Density Measurements Using the Background Oriented Schlieren Techniques." *Experimental Fluids* 37. pp. 237-247, 2004.
- Vilimpc, V., Goss, L., and Sarka, B. "Spatial Temperature-Profile Measurements by the Thin Filament Pyrometry Technique." *Optics Letters*. vol. 13, pp. 93-95, 1988.
- Welch, G. E., Paxson, D. E., Wilson, J., and Snyder, P. H. *Wave-Rotor-Enhanced Gas Turbine Engine Demonstrator*. National Aeronautics and Space Administration TM-1999-209459, Cleveland OH, 1999.
- Werner, S. P. *Initiator Diffraction Limits for Pulse Detonation Engine Operation*. MS Thesis, Naval Postgraduate School, Monterey CA, 2002.
- Wilson, D. G. *The Design of High-Efficiency Turbomachinery and Gas Turbines*. The MIT Press, Cambridge MA, 1993.
- Wilson, J., and Fronek, D. "Initial Results from the NASA-Lewis Wave Rotor Experiment." *29th AIAA/ASME/SAE/ASEE Joint Propulsion Conference*. AIAA1993-2521, Monterey CA, 28-30 June, 1993.
- Wintenberger, E., and Shepherd, J. E. "Thermodynamic Analysis of Combustion Processes for Propulsion Systems." *42nd AIAA Aerospace Sciences Meeting*. AIAA2004-1033, Reno NV, 5-8 January, 2004.

- Yi, T., Jing, L., Turangan, C., Khoo, B. C., and Wolanski, P. "Effect of Nozzle Shapes on the Performance of Continuously Rotating Detonation Engine." *48th AIAA Aerospace Sciences Meeting*. AIAA2010-0152, Orlando FL, 4-7 January, 2010.
- Zhu, Y. J., Chao, J., and Lee, J. H. S. "An Experimental Investigation of the Propagation Mechanism of Critical Deflagration Waves that Lead to the Onset of Detonation." *Proceedings of the Combustion Institute 31*. pp. 2455-2462, 2007.
- Zipkin, M. A., and Lewis, G. W. *Analytical and Experimental Performance of an Explosion-Cycle Combustion Chamber for a Jet-Propulsion Engine*. National Advisory Committee for Aeronautics TN No. 1702, Washington DC, 1948.

<b>REPORT DOCUMENTATION PAGE</b>				<i>Form Approved OMB No. 074-0188</i>	
<p>The public reporting burden for this collection of information is estimated to average 1 hour per response, including the time for reviewing instructions, searching existing data sources, gathering and maintaining the data needed, and completing and reviewing the collection of information. Send comments regarding this burden estimate or any other aspect of the collection of information, including suggestions for reducing this burden to Department of Defense, Washington Headquarters Services, Directorate for Information Operations and Reports (0704-0188), 1215 Jefferson Davis Highway, Suite 1204, Arlington, VA 22202-4302. Respondents should be aware that notwithstanding any other provision of law, no person shall be subject to a penalty for failing to comply with a collection of information if it does not display a currently valid OMB control number.</p> <p><b>PLEASE DO NOT RETURN YOUR FORM TO THE ABOVE ADDRESS.</b></p>					
<b>1. REPORT DATE (DD-MM-YYYY)</b> 14-06-2012		<b>2. REPORT TYPE</b> <b>Doctoral Dissertation</b>		<b>3. DATES COVERED (From – To)</b> Sep 2008 – Jun 2012	
<b>4. TITLE AND SUBTITLE</b>  Unsteady Specific Work and Isentropic Efficiency of a Radial Turbine Driven by Pulsed Detonations				<b>5a. CONTRACT NUMBER</b>	
				<b>5b. GRANT NUMBER</b>	
				<b>5c. PROGRAM ELEMENT NUMBER</b>	
<b>6. AUTHOR(S)</b>  Rouser, Kurt P., Lieutenant Colonel, USAF				<b>5d. PROJECT NUMBER</b>	
				<b>5e. TASK NUMBER</b>	
				<b>5f. WORK UNIT NUMBER</b>	
<b>7. PERFORMING ORGANIZATION NAMES(S) AND ADDRESS(S)</b> Air Force Institute of Technology Graduate School of Engineering and Management (AFIT/EN) 2950 P Street, Building 640 WPAFB OH 45433-7765				<b>8. PERFORMING ORGANIZATION REPORT NUMBER</b>  AFIT/DS/ENY/12-25	
<b>9. SPONSORING/MONITORING AGENCY NAME(S) AND ADDRESS(ES)</b> Air Force Research Laboratory Propulsion Directorate, Turbine Engine Division, Combustion Branch (AFRL/RZTC) Attn: Dr. Frederick R. Schauer 1790 Loop Road North DSN: 785-6462 WPAFB OH 45433 Email: Frederick.schauer@wpafb.af.mil				<b>10. SPONSOR/MONITOR'S ACRONYM(S)</b> AFRL/RZTC	
				<b>11. SPONSOR/MONITOR'S REPORT NUMBER(S)</b>	
<b>12. DISTRIBUTION/AVAILABILITY STATEMENT</b> APPROVED FOR PUBLIC RELEASE; DISTRIBUTION UNLIMITED					
<b>13. SUPPLEMENTARY NOTES</b> This material is declared a work of the U.S. Government and is not subject to copyright protection in the United States.					
<b>14. ABSTRACT</b> There has been longstanding government and industry interest in pressure-gain combustion for use in Brayton cycle based engines. Theoretically, pressure-gain combustion allows heat addition with reduced entropy loss. The pulsed detonation combustor (PDC) is a device that can provide such pressure-gain combustion and possibly replace typical steady deflagration combustors. The PDC is inherently unsteady, however, and comparisons with conventional steady deflagration combustors must be based upon time-integrated performance variables. In this study, the radial turbine of a Garrett automotive turbocharger was coupled directly to and driven, full admission, by a PDC in experiments fueled by hydrogen or ethylene. Data included pulsed cycle time histories of turbine inlet and exit temperature, pressure, velocity, mass flow, and enthalpy. The unsteady inlet flowfield showed momentary reverse flow, and thus unsteady accumulation and expulsion of mass and enthalpy within the device. The coupled turbine-driven compressor provided a time-resolved measure of turbine power. Peak power increased with PDC fill fraction, and duty cycle increased with PDC frequency. Cycle-averaged unsteady specific work increased with fueled fraction and frequency. An unsteady turbine efficiency formulation is proposed, including heat transfer effects, extensively weighted total pressure ratio, and ensemble averaging over multiple cycles. Turbine efficiency increased with frequency but was lower than the manufacturer reported conventional steady turbine efficiency.					
<b>15. SUBJECT TERMS</b> pulsed detonation, unsteady turbine, detonation driven turbine, turbine efficiency, pulsed detonation combustor					
<b>16. SECURITY CLASSIFICATION OF:</b>			<b>17. LIMITATION OF ABSTRACT</b>  UU	<b>18. NUMBER OF PAGES</b> 263	
REPORT U	ABSTRACT U	c. THIS PAGE U		<b>19a. NAME OF RESPONSIBLE PERSON</b> Paul I. King (ENY)	
			<b>19b. TELEPHONE NUMBER (Include area code)</b> (937) 255-3636, ext 4628; email: Paul.King@afit.edu		

Standard Form 298 (Rev: 8-98)

Prescribed by ANSI Std. Z39-18